THE EFFECT OF CURRENT REVERSAL ON COATED TITANIUM ELECTRODES

by

Francis Elnathan

A dissertation submitted to the faculty of
The University of Utah
in partial fulfillment of the requirements for the degree of

Doctor of Philosophy

Department of Metallurgical Engineering

University of Utah

May 2012

The University of Utah Graduate School

STATEMENT OF DISSERTATION APPROVAL

The dissertation of **Francis Elnathan**

has been approved by the following supervisory committee members:

Michael S. Moats	, Chair	**08/16/2011** Date Approved
Jan D. Miller	, Member	**08/16/2011** Date Approved
Henry White	, Member	**08/16/2011** Date Approved
Michael L. Free	, Member	**08/16/2011** Date Approved
Sivaraman Guruswamy	, Member	**08/16/2011** Date Approved

and by **Jan D. Miller** , Chair of the Department of **Metallurgical Engineering**

and by Charles A. Wight, Dean of The Graduate School.

ABSTRACT

Coated titanium electrodes have applications in the electrochemical industry, including water treatment and swimming pool chlorination. Current/polarity reverse electrolysis is a technique used for "self-cleaning" of the coated titanium anodes employed in water disinfection and treatment. However, the literature holds very little information about the effects of polarity reversal on these anodes. The present work appears to be the first to investigate coated titanium anodes in polarity reversal in a systematic method. Two commercial titanium electrodes (RuTi and IrTa) were studied. Polarity reversal was the main electrochemical technique employing a current density of 1200 A/m^2, except when current density was studied. The effects of NO_3^-, SO_4^{2-}, ClO_4^-, HPO_4^{2-}, CO_3^{2-}, Mg^{2+} and Ca^{2+} on electrode lifetime were examined.

Analysis of the electrochemical results showed that plateau time (τ_P), for gas evolution, is highly important to the lifetime of the coated titanium anodes. The effects of three electrolysis variables on the coated titanium anode life were examined. Current density was observed to have an inverse relationship with anode life while reversal cycle time had a direct relation with lifetime. NaCl concentration had no discernible effect. In general, the RuTi electrode exhibited longer lifetimes than IrTa except for a few specific conditions. The influence of the concentration of five anions (NO_3^-, SO_4^{2-}, ClO_4^-, HPO_4^{2-}, and CO_3^{2-}) was determined. Changing the composition and concentration of anions

affected the lifetimes of the two electrodes, especially nitrate, hydrogen phosphate and carbonate. The lifetime of IrTa was highest in nitrate, and increased as a function of nitrate concentration. The service life of RuTi was highest in hydrogen phosphate, and increased with increasing hydrogen phosphate concentration. Lifetime of both anodes decreased with increasing carbonate ions.

The effects of Mg^{2+} and Ca^{2+} on electrode lifetime were examined with three anions (NO_3^-, HPO_4^{2-}, $ClO4^-$) electrolytes. While there were numerous effects and interactions between Mg^{2+} or Ca^{2+} and anions on lifetime, these effects were found to mainly affect the amount of time the electrodes spent in the charging and discharging reactions. The times related to gas evolution (which is the plateau time, τ_P) were found to be strikingly similar. The charging times (τ_C), which are related to adsorption and desorption of species, were not also any significantly different.

Coating dissolution, substrate and/or coating passivation mechanisms were identified as being responsible for coated titanium anode failure in current reverse and hard water electrolysis. IrTa is believed to have failed predominantly by the dissolution mechanism in nitrate, hydrogen phosphate and perchlorate. RuTi failed predominantly by substrate and/or coating passivation in hydrogen phosphate, nitrate and carbonate. Anode failure is believed to be the result of plateau (τ_P) and charging (τ_C) reactions occurring at the coating/electrolyte and/or substrate/coating interface. The τ_P and τ_C are useful determinants for the process of anode failure.

DEDICATED TO GOD THE FATHER, GOD THE SON AND GOD THE HOLY GHOST

TABLE OF CONTENTS

LIST OF FIGURES

Figure **Page**

LIST OF TABLES

Table **Page**

ACKNOWLEDGEMENTS

I would like to express my deepest gratitude to my adviser, Dr. Michael S. Moats, for his guidance, untiring efforts to make this work excellent, and continuous financial support throughout the work.

I would also like to thank Dr. Jan D. Miller, Dr. Michael L. Free, Dr. Sivaraman Guruswamy, and Dr. Henry White for their useful discussion and serving on my supervisory committee.

I would like to thank Alexander Derrick for his help in the laboratory. I am grateful to Mr. Richard Kus and Dr. Oladapo Eso for their assistance with XRF and SEM/EDS data. I would also like to thank Mrs. Miller and Dorrie for their prayer support during my time in graduate school. I also thank Karen and Kay for their help.

Finally I would like to thank my heavenly Father for sustaining and encouraging me these past seven years in graduate school. I would have abandoned the program without your encouragement. I appreciate it Dad.

CHAPTER 1

INTRODUCTION

1.1 General Background

The demand for clean water for both domestic and industrial use is ever increasing for safety and efficient operation of industrial equipment reasons. Furthermore, public and private swimming pools for leisure and recreational purposes are also increasing in modern times with the attendant increased demand for pool disinfection. At present, periodic current/polarity reversal of coated titanium electrodes (CTEs) is a technique used in the water treatment and swimming pool disinfection industries, yet there is little information in the open literature about the effect of the reversal on CTE lifetime except for the work of Kraft [1] and Morimitsu et al. [2].

The work of Kraft and Morimitsu et al. was limited to only one electrolyte; Berlin water and sodium sulfate in sulfuric acid, respectively. The contrast between the present work and the work of Kraft and Morimitsu et al. will be discussed in the last section of this chapter. The present work will examine the reasons for failure of CTEs during current reversal electrolysis in various electrolytes. The sections following will discuss general concepts related to CTEs.

1.2 Coated Titanium Electrodes (CTEs)

Coated titanium electrodes (CTEs) [3-6] have been used in the electrochemical industry for decades, being particularly popular for chlorine and oxygen evolution reactions. Their applications have been extended to other industries over time; an example is the medical industry where they are used as implants. CTEs are made by coating titanium substrates with oxides of precious metals mixed with nonprecious metal oxides.

Though CTEs [3-6] have exhibited longer lifetimes than the graphite anodes they replaced in the chlor-alkali industry, they still have inherent stability problems. Attempts over the years have been to make durable and longer lasting CTEs at cheaper cost. To achieve this, various concentration combinations of precious and nonprecious metals and preparation procedures have been developed.

Coated titanium electrodes are characterized by a conducting substrate coated with an activated oxide layer which usually catalyzes a particular electrochemical reaction. The catalysts are typically platinum group metal oxides (such as RuO_2 and IrO_2) mixed with other nonprecious metal components, sometimes referred to as additives (such as TiO_2 and Ta_5O_5). The conducting substrate is mainly commercially pure Ti [3], although other substrates have been investigated [4].

Depending upon operating conditions in chlor-alkali production, graphite anodes of improved quality have a life span of at most 2 years for chlorine generation, while CTEs [1, 5] have demonstrated lifetimes of over 20 years. Unlike the graphite anodes, CTEs allow for lower cell voltages, longer lifetimes and improved product quality. This

is largely due to the dimensional tolerance of the Ti substrate and the stability of the coating in the harsh chlorine-alkali electrolytic environment [6-9].

The graphite [3, 10, 11] electrode has the same overpotential for anode chlorine evolution as CTEs. Graphite was consumed during the anodic reactions by the O_2 present in Cl_2. The consumption of the graphite widened the electrode gap thus increasing the ohmic drop (IR) between the electrodes. Consequently, power/energy consumption and the associated costs for the graphite anodes were high due to their consumption and instability.

CTEs [9] may operate under different conditions, varying from mild conditions (acid-water electrolysis, metal electrowinning, cathodic protection, electro-organic synthesis, etc.) to very severe conditions, such as fast electroplating processes operating at high current densities.

1.2.1 History and Development

Since the CTE was developed, it has undergone compositional modifications for durability, efficiency and cost effective reasons. The chlorine-alkali electrolysis cells used graphite or lead anodes since the process began in the early 1900s [12-18]. CTEs were developed in the 1960s to replace the graphite anodes which were problematic for chlorine-alkali electrolysis [3]. The coated titanium electrode [3] was invented in the 1960s by H. B. Beer. Table 1 summarizes contributors and important historical dates in the development of the CTEs.

Table 1 Historical development of the coated titaniumelectrode (CTE) [12, 18].

Year	Mixed Metal Oxide Anode (CTE) Developed	Reference
1958	Rhodium electrodeposited on titanium	Beer
1958	Platinum electrodeposited on titanium	Cotton et al.
1960	Paint/thermal decomposition method of coating	Angell et al
1965	First mixed metal oxide coatings	Beer
1967	Second mixed metal oxide coatings	Beer
1968	First titanium based electrodes (70:30 wt% Pt:Ir coated) in commercial chlor-alkali cells	Beer
1974	First nonprecious metal alloys (Co-Mo)	Jaksic
1984	Titanium-based anodes in electro-galvanizing	
1986	Titanium-based anodes in the cathodic protection of rebar in concrete	
2008	Titanium-based anodes in copper electrowinning	Sandoval et al.

1.2.1.1 Energy Consumption

As electrical power consumption and cost are critical factors in industrial applications, it is worth considering the power consumed by an electrolysis cell. The consumption of electric power (P) is proportional to VI, where V is voltage/potential applied to the electrolysis cell and I is the current flowing through the cell, considered considered to be a measurement of the rate of production of the electrochemical products. Thus for a given current in the cell, it is necessary to minimize the voltage, V to reduce energy cost. V is made of the components as indicated equation in 1 [13].

$$V = E + \eta + V_{\Omega} + V_S \quad (1)$$

where

E is the equilibrium potential of the electrode reactions

η is the sum of the anodic and cathodic overpotentials

V_{Ω} is the ohmic drop (IR) between the electrodes and the connections

V_s is a measure of the electrode's stability

The terms in equation 1 can be defined by equations 2-4.

$$E = E^{o} + \frac{2.303RT}{nF} \log \frac{\prod a_{products}}{\prod a_{reactants}} \quad (2)$$

where

E is the equilibrium electrical potential or voltage at which the reaction is occurring. E is defined by the Nernst equation.

E^o is the standard potential or voltage (at 1 atmosphere and 298 K)

R is the gas constant

T is the temperature, K

n is the number of electrons transferred in the reaction

F is the Faraday constant

$a_{products}$ is the activity of products

$a_{reactants}$ is the activity of reactants

Overpotential, η is related to electrocatalysis at constant current. η is a measure of the potential above the potential E at which the reaction is occurring at a specific rate. Therefore, the value of η can be decreased by improving the electrocatalytic activity of an electrode. Overpotential, η is the kinetic term in equation 1 and is determined by the rate of the reaction assuming mass transport effects are negligible. The overpotential (η) can be obtained from Butler-Volmer equation given in equation 3.

$$i = i_o\left(\exp\left[\frac{\alpha nF\eta}{RT}\right] - \exp\left[-\frac{(1-\alpha)nF\eta)}{RT}\right]\right) \quad (3)$$

where

i is the rate at which the electrochemical reaction takes place

i_o is the exchange current density

α is the transfer coefficient

η is the overpotential

The stability of the electrode, V_s can be obtained from equation 4.

$$V_s = V_t - V_{o.}. \quad (4)$$

where

V_t is the electrode potential at time = t

V_o is the initial electrode potential

Generally V_s measures the change in V with time as the electrode coating degrades. V_s is usually zero for fresh electrodes and increases with electrochemical reaction time.

For practical purposes, the aim is to keep V as small as possible at a constant current density. In materials evaluation and selection for coating purposes V is considered to include all the parameters listed in equation 1. In practice, it is expedient to develop electrodes that minimize V over their lifetimes than one that is simply electrocatalytically active in nature [9, 14, 11-21].

1.2.2 Electrocatalysis and Materials Selection for Ti Coated Oxide Electrodes

Electrocatalysis [22] is the study of how reactions occurring at electrodes may be accelerated at a constant potential, and this often requires that the surface of the electrodes has to be modified in some fashion. An electrode [23] is considered more electrocatalytic than another when at constant overpotential (η), a given reaction proceeds faster on the former than the latter. The electrocatalytic material is the most important component of a composite anode. It accounts for the catalysis of a specific electrochemical reaction on its surface. The electrocatalytic material behaves as an electronic interface between the substrate and the electrolyte [24].

It is generally accepted that a good catalyst [25-27] for the oxygen evolution reaction (OER) must have a relatively high electronic conductivity, high affinity for adsorbed hydroxide intermediates and the electrode must be resistant to corrosion. Noble metals oxides and their alloys have been investigated considerably. Noble metal oxides of

Ru, Ir, Rh, etc. are considered to be good electrocatalysts for the OER. However, noble metal oxide coatings can dissolve when exposed to the harsh industrial conditions such as higher current densities (30 mA cm^{-2}), strong acids (pH < 2) and aggressive chloride environments.

The objective of electrocatalysis is to establish a predictive basis for the design and optimization of catalysts. Predictions can be formulated only if the factors that are responsible for the electrocatalytic properties are known. Electronic and geometric factors are usually recognized to govern catalysis. The appropriate selection [4, 23] of electrode materials is therefore prerequisite to optimization of the parameters involved in the electrolysis process.

The most important industrial requirements for an electrode coating material are [23]:

1. Long-term stability (both mechanically and chemically)
2. Good electrocatalytic properties
3. Available at low cost
4. High surface area
5. High electrical conductivity
6. Minimal trapping of gas bubbles
7. Selective for designated reactions
8. Safe to handle

It is important [28] that an industrial coating material meets the requirements listed. However, it is highly unlikely a coating material will have all the characteristics required. In practice, a coating material with optimum properties for a given application will be

selected. Thus, a coating with optimum activity, stability and low cost will usually be selected.

Transition metal oxides with metallic or quasi-metallic conductivity are materials that tend to meet most of the requirements for a coating [23]. It has been established that the performance of some precious metal oxides is far better than their corresponding precious metals [3]. Conducting oxides or semiconducting oxides that can be doped are usually added to the active coating to stabilize it. Ta_2O_5, TiO_2, ZrO_2, SnO_2 are examples of such stabilizing oxides [29]. The electrocatalytic activity of oxide electrode coatings is controlled by factors such as, chemical nature of the catalyst, morphology, stoichiometry, band structure of the oxide, surface electronic structure, etc. These may be grouped into chemical (based on chemical composition) and structural (based on morphological features) factors [23].

1.2.3 Types of Coated Titanium Electrodes

Precious metal oxides used for making coated titanium electrodes are expensive materials. The amount used in practice is however minimized by "activating the electrodes" in the preparation process. In the activation process, a few micrometers of oxide layer are deposited on metallic support (usually Ti) by the thermal decomposition method [6, 23]. Oxides are seldom used alone in practical applications; usually they are doped or mixed with less active oxides of higher chemical stability [23, 30]. CTEs may be broadly grouped into three types according to reports in the literature. They are grouped based on certain characteristics they share in common [24].

1.2.3.1 Group 1 CTEs

One of these groups is Ti coated oxide electrodes, categorized under group 1. They are normally prepared by thermal decomposition of the desired metal salt on a Ti substrate [31-33]. This is achieved thermochemically by dissolving the suitable metals salts in a solvent (alcohol or acidified water). The solution is then applied to the prepared Ti substrate by dip coating or brush painting [3] or spin coating [31]. The solvent is evaporated and the remaining material is decomposed to form the metal oxide on the Ti [3]. Other methods of making Ti coated oxide electrodes have been reported. For example, Ribeiro et al. have reported that electrodes prepared by the Pechini-Adams method (decomposition of polymeric precursor) were 100% better in performance than those prepared by the thermal decomposition [31-33].

Generally the group 1 CTEs have a corrosion resistant valve metal as a substrate, which is usually commercially pure Ti. The substrate is coated with an electrocatalytic layer of a noble metal (Ru, Ir, Pd etc), a noble metal oxide (RuO_2, IrO_2, PdO_2 etc), a valve metal oxide (TiO_2, Nb_2O_5, Ta_2O_5 etc), or a mixture of them. The group 1 CTEs are the most investigated in the literature [3, 5, 7, 9, 12-14, 25, 34-66] and patent literature [3, 68-80].

Group 1 CTE are prepared by pretreating the surface of the substrate by degreasing, chemical etching or sandblasting to increase the surface area and enhance adhesion of the coating. Pretreated Ti substrate can be painted, dip-coated or spin-coated. Precious metal loadings in coatings usually range from 0.1-3 mg cm^{-2}. Electroplating [76-77], sputtering [25, 35] and electroless deposition [74] are other deposition techniques that can be employed for coating the electrode. Conductive polymers have also been

investigated as substrates for the CTE [63-65]. The coating is hot pressed unto the polymer substrate. CTEs prepared using conductive polymer as substrate is cheaper [63], but has not found wide commercial acceptance.

1.2.3.2 Group 2 CTEs

The group 2 CTEs is made by introducing an intermediate layer (which can be valve metal oxide or a conducting polymer) between the substrate and the electrocatalytic coating. The Group 2 CTEs are the next most researched group after group 1 according to the open literature [25, 78-88] and patent literature [85-89].

The protective intermediate layer between the substrate and the electrocatalytic coating can be deposited using the standard thermal decomposition of chlorides salts [3].The intermediate layer can also be deposited by the Pechini-Adams method (decomposition of polymeric precursors) [90] or galvanostatic anodization of the substrate [70-71, 74] or by any suitable deposition method [91]. The protective intermediate layer is expected to act as barrier to reduce diffusion of oxygen to the substrate surface. This extends the coating's life by slowing TiO_2 thickening, which causes increase resistance leading to voltage escalation [24].

1.2.3.3 Group 3 CTEs

The group 3 CTEs comprise of compacted powder electrode containing a homogeneous mixture of electrocatalyst and valve metal particles. The group 3 CTEs constitute the least studied [24] group. The electrode can be made by mixing sintered powders containing at least one valve metal as a substrate (90 %wt) with at least one

oxide of metals such as: Cr, Mn, Re, Fe, Co, Ni, Ca, Ag, Au, Zn, Cd, Ge, Sn and Pb [25]. Other ways of making this group of electrodes are available [92]. This type of CTE is not commonly used in practice.

1.2.4 Composition and Structure of Oxides

Oxides formed by the thermal decomposition [4] of suitable precursors are usually non-stoichiometric. The composition of the oxide formed depends on the calcination temperature. Oxides formed may contain some residual impurities from the precursors. The amount of residual impurities is a function of the temperature of decomposition. For example, RuO_2 obtained from $RuCl_3$ is usually defective in oxygen while it contains residual chlorine. Chlorine is also found in RhO_x obtained from $RhCl_3$ [93]. The chlorine residual content has been reported to decrease as the calcination temperature is increased [9]. IrO_2, however, tend to contain an excess of oxygen [94]. This is also observed in Co_3O_4 [95]. While RuO_2 and IrO_2 exhibit metallic conductivity [96], almost all other oxides are semiconductors, some of them with insulating properties (e.g., TiO_2, Ta_2O_5).

Stoichiometry is approached as the calcinations temperature is increased. That is, stoichiometric oxides are likely to be formed at higher calcination temperatures. Thus, the temperature of calcination and the nature of the precursor appear to be the primary factors influencing the properties of the resulting oxide. At low calcination temperatures amorphous or microcrystalline oxides are formed. The particle size and the crystallinity increase as the calcination temperature is raised [95, 96]. These tend to have an effect on physical parameters (such as surface area and morphology) and the electronic factors [4,

97]. As the nature of the precursor is changed, both micro-composition and particle size can vary at the same calcination temperature [98]. Both have an effect on the electrocatalytic activity of the oxide [9].

1.3 Interfacial Phenomena: The Interface between Conducting Phases

The CTEs under study in the present work are going to be examined in various electrolytes. The reactions occurring at the coating/electrolyte and coating/substrate interface are critically important to the lifetimes and failure mechanisms of the electrodes. It is therefore necessary to briefly review occurrences at interfaces. The interface [99] between any pair of conducting phases exerts a potential difference whose magnitude is a function of both the composition and nature of the phases. Examples of interfaces for which this phenomenon is of practical importance are:

1. solid/electrolyte solution interface,
2. solid/solid interface,
3. electrolyte solution/electrolyte solution interface, and
4. solution of lower concentration/semi-permeable membrane/solution of higher concentration interfaces.

The potentials observed at the interfaces are due to the electrical double layer (EDL). The EDL arises due to an excess of charge at the interface which may be ions, electrons or oriented dipoles. The structure of the EDL is responsible for the properties of any given interface.

1.3.1 Oxide Electrode/Electrolyte Interfaces

When a metal is immersed in an electrolyte [100], a potential is set up across the two phases (at the electrode/electrolyte interface) and a double layer (DL) develops at the interface. There are reasons why the potential difference occurs across the interface of the two phases. The most common one is charge transfer across the interface. Thus, charge separation occurs because of electron transfer across the interface. The charge [9] on the electrode's surface is balanced by a region of opposite charge in the electrolyte adjacent to the electrode surface. The other reasons [100] for the occurrence of the potential difference are due to surface-active groups in the ionizable electrolyte and the orientation of permanent or induced dipoles.

The DL [100] at the interface between two phases has electrical, compositional, and structural characteristics. The electrical and compositional characteristics deal with the excess charge densities on each phase. The structural characteristic deals with the distribution of the constituents (ions, electrons, dipoles, and neutral molecules) in the two phases, including the interfacial region. The properties [6] of the DL play an important role in the exchange of charged species at the interface and adsorption of charged chemical species on the electrode.

1.3.2 Basic Electrical Double Layer (EDL) Theory

In order to maintain electro-neutrality [101] at the interface between the two phases, the oxide electrode's surface charge is balanced by an equal and opposite charge in the aqueous phase. This compensating charge is created by unequal adsorption of the electrolyte ions. The distribution of the aqueous charge density and the consequent

variation in the electrostatic potential has become known as the "theory of the electric double layer". Figure 1 shows a schematic diagram of the EDL.

The evolution of the theoretical aspects of the structure of the double layer, as applied to the CTE oxide electrode/electrolyte interfaces, across which charge transfer reactions occur is briefly reviewed to understand the relevance of reactions occurring at interface of the EDL [100].

1.3.2.1 Parallel-Plate Condenser Model: Helmholtz Model

The Helmholtz model [102] was the first type of model proposed for the structure of the double layer (DL) at an electrode/electrolyte interface. It is comparable to a capacitor with two layers of charge of opposite sign and separated by a fixed distance. It is assumed that electrons are in the metal and positive ions in the solution. The potential drop across the interface will be linear and the capacitance (C) of the double layer is treated as a parallel-plate capacitor, given by equation 5.

$$C = \frac{\varepsilon}{4\pi d} \tag{5}$$

where ε is the dielectric constant in the medium between the plates and d is the distance between them [100].

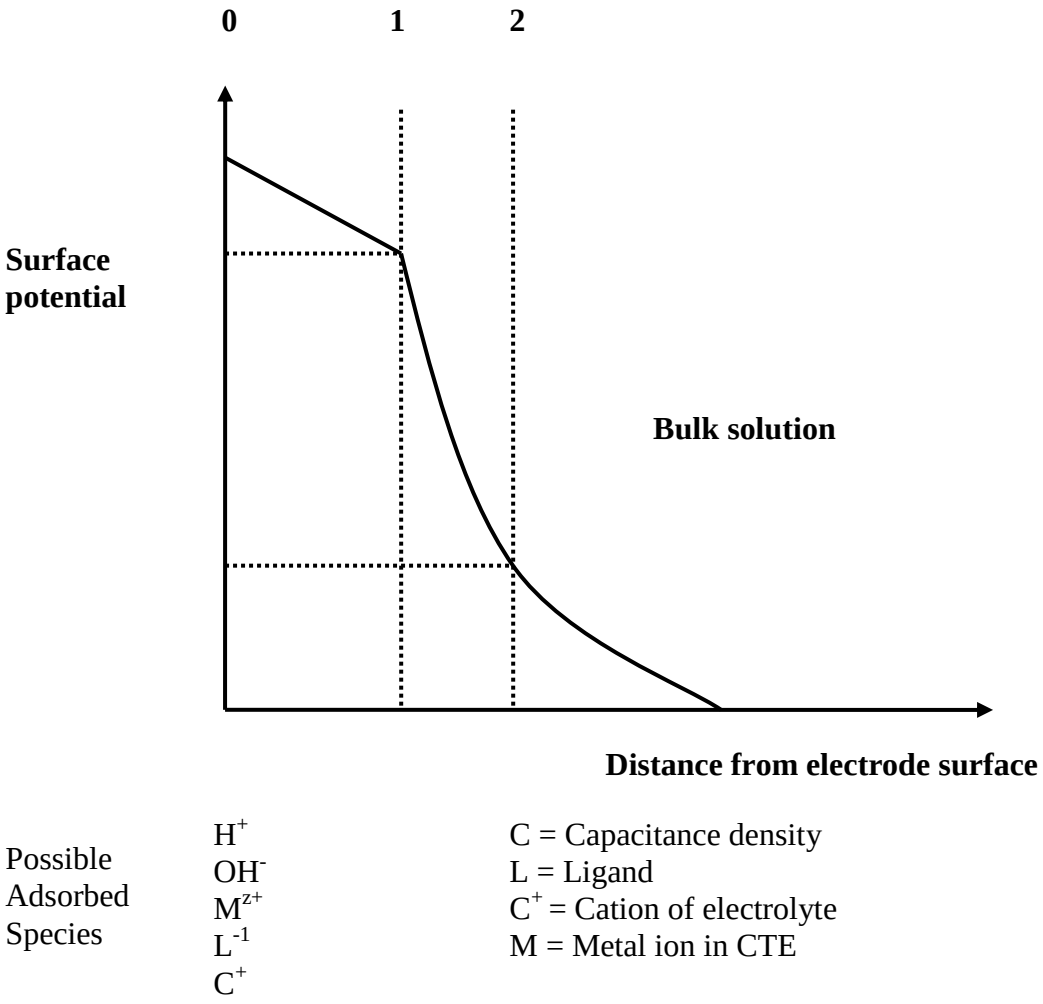

Figure 1 Schematic of EDL, where: 0 is the electrode surface, 1. Inner Helmholtz layer (IHP) with adsorbed ions and solvent molecules, 2. Outer Helmholtz layer (OHP), 3. Diffuse layer or bulk solution with solvated ions.

1.3.2.2 Diffuse-Layer Model: Gouy-Chapman Model

According to Gouy [100] and Chapman [104], ions in the electric double layer are subjected to electrical and thermal fields. This allows Maxwell-Boltzmann statistics to be applied to the charge distribution of ions as a function of distance away from the metal surface similar to the distribution of negatively charged ions surrounding a positive ion. The analysis in both cases is similar except that for the ion-ion case there is spherical symmetry, while the electrode/electrolyte layer is planar. For this model, the diffuse charge (Q_D) and the capacitance (C) are given by equations 6 and 7.

$$Q_D = \left\{\frac{2kTn_O\varepsilon}{\pi}\right\}^{1/2} \sinh\left(\frac{e_O V}{2kT}\right) \tag{6}$$

$$C = \left\{\frac{n_O \varepsilon e_O^{\,2}}{2\pi kT}\right\}^{1/2} \cosh\left(\frac{e_O V}{2kT}\right) \tag{7}$$

where n_o is the number of ions of positive and negative sign per unit volume in the bulk of the electrolyte and V is the potential drop from the metal to the bulk of the electrolyte. K is the Boltzmann constant, T is the Kelvin temperature, and e is the charge. According to this model, the capacitance is a minimum at V = 0 and rises to very high values symmetrically and parabolically on either side of V [100].

1.3.2.3 Compact Diffuse-Layer Model: Stern Model

The Stern model [105] is a hybrid of the Helmholtz and Gouy-Chapman models. First, ions are considered to have finite size and are located at a finite distance from the electrode. Second, the charge distribution in the electrolyte is divided into two contributions: (i) as in the Helmholtz model charge is immobilized close to the electrode, and (ii) as in the Gouy- Chapman model, charge diffusely spread out in the solution. Thus,

$$Q_M = Q_S = Q_H + Q_G \tag{8}$$

where Q_M is the charge on the metal. Qs is the total charge on the solution side (of opposite sign) comprising the Helmholtz fixed charge, Q_H, and the Gouy-Chapman diffuse charge, Q_G.

The double layer capacitance across this electrode/electrolyte interface is given by equation 9.

$$\frac{1}{C} = \frac{1}{C_H} + \frac{1}{C_G} \tag{9}$$

where C_H and C_G are the contributions of the Helmholtz and Gouy-Chapman capacitances, which are in series. Thus, the double-layer structure approaches that of the Gouy-Chapman model for two reasons. First, in concentrated electrolytes the value of $1/C_H$ is considerably greater than that $1/C_G$. This model is very similar to that of Helmholtz. Second, in extremely dilute solution, where $1/C_G \gg 1/C_H$ and thus, $C = C_G$ [100].

1.3.2.4 Triple-Layer Model: Esin and Markov, Grahame, and Devanathan Model

The Esin and Markov [106], Grahame [107], and Devanathan [108] model takes into consideration that ions can be dehydrated in the direction of the metal and specifically adsorbed on the electrode. Thus, an inner layer between the electrode surface and the Helmholtz layer further modifies the structure of the double layer. This inner layer is the locus of centers of unhydrated ions strongly attached to the electrode. For this case, Devanathan derived the relation in equation 10.

$$\frac{1}{C} = \frac{1}{C_1} + \left(\frac{1}{C_2} + \frac{1}{C_3}\right)\left(1 - \frac{D_{q1}}{D_{qM}}\right) \tag{10}$$

where C_1 and C_2 are the integral capacities of the space between the electrode and the inner Helmholtz plane (IHP) and between the inner and outer Helmholtz planes (OHP), respectively; C_3 is the differential capacity of the diffuse double layer, and (D_{q1}/D_{qM})

represents the rate of change of the specifically adsorbed charge with charge on the metal. Some [100] interesting analyses may be obtained from equation 10:

1. If (D_{q1}/D_{qM}) is zero, the expression for the capacity (C) is equivalent to that for three capacitors in series, that is, inner Helmholtz, outer Helmholtz, and Gouy. Hence, this model is referred to as the triple-layer model.

2. The capacity is a minimum when D_{q1}/D_{qM} is zero, because the latter can have only positive values.

3. If D_{q1}/D_{qM} exceed unity, the differential capacity attains large values. When C tends to infinity, the electrode becomes nonpolarizable.

4. The minimum in the capacity is in the vicinity of the potential of zero charge.

1.3.2.5 Surface Charge

Most substances [109, 110] in contact with an aqueous medium acquire a surface electric charge due to a redistribution of charge in the interfacial region. This process is described as the formation of an electrified interface or electrical double layer. Several types of redistribution of charge are possible:

(1). Ionization of ionogenic groups, e.g., proteins acquire their charge mainly by ionization of -COOH and $-NH_2$ groups to give $–COO^-$ and $-NH_3^+$;

(2). Unequal dissolution of oppositely charged ions of which the solid phase may be composed, e.g., AgI;

(3). Unequal adsorption by the solid phase of ions of opposite charge;

(4). Adsorption and orientation of dipolar molecules.

1.3.3 Capacitance and Pseudocapacitance of Coated Titanium Electrodes

The CTE/electrolyte interface acts as a DL that stores charges, thus behaving as a capacitor (pseudocapacitor). Electrochemical capacitors or supercapacitors are energy-storage devices which have high power density and long cycle life. Charge-storage mechanisms proposed for electrochemical capacitors include the DL capacitance and pseudocapacitnace. DL capacitance is due to the separation of charge at the electrode/electrolyte interface while pseudocapacitance is caused by faradaic reactions occurring at or near the surface of the electrode over some potential range.

Electrode materials with high specific surface areas such as carbon and transition metal oxides are considered suitable materials for these charge-storage devices. Carbon-based systems function as DL capacitors due to their high specific surface areas. Transition metal oxides (including hydrous oxides and nitrides) and conductive polymers are considered to be excellent electrode materials for supercapacitors where their charge-storage mechanisms are based predominantly on pseudocapacitance. Presently, hydrous ruthenium oxides (RuO*x*·*n*H2O) is considered a suitable electrode materials for use in electrochemical capacitors because of their excellent quasi-metallic conductivity and high pseudocapacitance.

Pseudocapacitance arises on electrodes (such as CTEs) when the application of a potential induces faradaic current from reactions such as electrosorption or the oxidation/reduction of electroactive materials. Conducting metal oxides such as RuO_2 (or IrO_2) exhibit pseudocapacitance through a coupled proton-electron transfer in aqueous solutions following equation 11.

$$RuO_2 + \delta H^+ + \delta e^- \leftrightarrow RuO_{2-\delta}(OH)_\delta \quad (11)$$

Redox processes observed during potential cycling of, for example, RuO_2 which involve its II, III, and IV oxidation states, yield high currents and the pseudocapacitance measured often exceeds that of the DL capacitance by a factor of ten. While DL charging can occur on high surface area RuO_2, the redox processes and proton transfer reactions giving rise to pseudocapacitance are predominant in the charging mechanisms [6, 11, 22, 100, 109, 111-114].

1.3.4 Theoretical Models for the Oxide/Solution Interface Region

The oxide/solution interface is a complex region. It is significantly different from the classical electrochemical double layer systems such as the Hg/solution or AgI/solution interfaces [101, 111-114]. Some of the features exhibited at the oxide/solution interface include, for example, the presence of an extended space charge layer in semiconducting oxides and the presence of a reversible double layer within the compact Helmholtz region which is due to the transfer of potential determining H^+ or OH^- ions across the interface occurring via a variety of adsorption and dissociation reactions at a hydroxylated oxide surface.

Several theories have been posited for the structure of the oxide/solution interface [101]. These theories can generally be grouped into two main categories: (a) classical and (b) nonclassical models.

1.3.4.1 Classical Models

The Gouy-Chapman-Stern-Grahame (GCSG) model [111, 115, 116] is considered as the classical approach to interfacial behavior. The GCSG model has been used extensively to describe the Hg/solution and AgI/solution interfaces. Three planes of charge have been proposed in the formulation of the model:

(1) the plane of surface charge, i.e., that of the adsorbed potential determining ions;

(2) the plane of the centers of specifically adsorbed ions, the inner Helmholtz plane (IHP),

(3) the outer Helmholtz plane (OHP)

Blok and de Bruyn [117] developed the basic GCSG model for the oxide/solution interface Levine and Smith [118] extended the basic model by allowing for non-Nernstian behavior of the surface potential and for discreteness-of-charge effects on the adsorption process. Levine and Smith obtained theoretical (or calculated) charge-capacitance and potential-pH curves which were in reasonable agreement with published experimental data.

Wright and Hunter [119-120] used the simple GCSG model to interpret the zeta potential behavior of oxides. They compared theoretical potential concentration variations at fixed electrolyte pH and obtained a general trend. However, calculated surface charge densities were much less than those found experimentally.

GCSG-based models can qualitatively account for observed interfacial properties provided certain values are chosen for various fundamental parameters (examples, specific adsorption potential and inner layer integral capacity) which are associated with each model. However, Healy et al. [101] have pointed out that it is not at all certain that

the values assigned to some of these parameters (especially a rather large inner layer integral capacitance) are reasonable.

Furthermore, explanations proposed to account for the magnitude of these parameters have not as yet received experimental verification. However, the major defect associated with the GCSG-based models is that the surface charge values observed in certain cases exceed that developed due to the ionization of all surface hydroxyl groups [111, 121].

1.3.4.2 Nonclassical Models

A number of nonclassical models have been proposed to explain the very high surface charge densities observed at the oxide/solution interfaces. These models include the porous double layer [122-125] model, the gel layer [126-128] model, the transition layer [129-130] model and the polyelectrolyte or site-binding [131-133] model.

1.3.4.2.1 Porous Double Layer (PDL) Model

In the porous double [122-125] layer (PDL) model, it is assumed that the oxide surface is porous to both potential-determining ions and counter-ions. That is, the two separated planes of adsorbed ions and counter-ions of the GCSG model are replaced by a model in which the counter-ions reside in the same region as the potential-determining ions. This scenario accounts qualitatively for the general trends observed in interfacial properties.

First, the more permeable the surface layer is the higher the charge density that can be accommodated in the region. Second, because sorption is not restricted to the

oxide surface itself, charge densities exceeding those corresponding to the ionization of the total number of hydroxyl groups on the surface are reasonable.

Finally, because counter-ions may also penetrate the surface to a certain extent, charge densities and zeta potential values at the solution side of the interface remain low. The PDL model can, therefore, generally account for the experimentally observed low electrokinetic potentials and colloidal stability provided that the degree of counter-ion penetration is extensive.

1.3.4.2.2 Gel Layer Model

Perram et al. proposed an alternative gel layer model [126-128] for the oxide/solution interface. These workers based their analysis on the assumption that there is a homogeneous gel-like layer (which is formed from a hydrolyzed oxide material) of definite thickness (2-5 nm) at the interface containing metal hydroxyl groups M(OH)n into which various ions can adsorb.

The gel-layer model accounts for the high surface charge in terms of ion penetration into subsurface regions of the oxide. Daghetti et al. [134] have noted that the gel model is consistent with experimental facts; however, Smith et al. [135] have contended that the presence of the gel layer has not been confirmed by radiotracer experiments.

1.3.4.2.3 Transition Layer Model

Dignam [129-130] combined the basic ideas of the porous and hydrolyzed gel-like layer theories to propose a transition layer model for the oxide/solution interface. The

fundamental feature of this model is that it has a transition layer (atomic dimensions) within which equilibrium exists between the oxide and aqueous ionic species.

1.3.4.2.4 Polyelectrolyte Model

Yates et al. [131-133], and Davis et al. [133] formulated the polyelectrolyte or site-binding model for the oxide/solution interface. The oxide surface in the model is represented by a two-dimensional array of positive, negative, and neutral discrete charged sites exhibiting acid-base properties. Potential determining ions and counter-ions are then considered to react or bind with the acid-base sites. It is assumed that the adsorbed supporting electrolyte cations and anions are distributed in two ways.

First, as interfacial ion pairs formed with oppositely charged surface groups. Secondly, as a diffuse layer to balance the remaining surface charges not yet neutralized. In this model the high surface charge and low zeta-potential are rationalized in terms of ion-pair formation between surface ionized groups and counter ions. In order to obtain reasonable correlation with experimental data Yates et al. [132] assumed a rather high inner zone (IHP) capacity and a rather low outer zone (OHP) capacity.

1.3.5 Coated Titanium Electrode Stability

The need for a stable electrode for the chlorine-alkali industry led to the invention of the CTE [3], and so the importance of electrode coating stability can not be overemphasized. The stability of an electrode may be defined in terms of its lifetime. It measures the time it takes for the coated oxide electrode to be deactivated or fail in the electrolysis cell. For coated titanium electrodes, stability is the ability of the electrode to

function effectively in the application (desired reaction) for which it was designed for longer periods. For example, the stability of RuO_2 and IrO_2-based electrodes may be defined in terms of their ability to evolve chlorine and/or oxygen at a relatively constant cell potential and current in chloride and /or acid solutions over long periods of time.

In general, electrode deactivation/ failure [23] is regarded as the rapid increase in cell potential when operating at constant current density or the rapid decrease in current density when operating at constant cell potential. The former definition is adopted for this work. Thus, the electrode is considered to have reached deactivation /failure threshold when at a constant current density, the cell voltage begins to rise rapidly from the onset voltage. For CTEs, failure [21] of the oxide electrode can occur at substrate/coating interface or the coating/electrolyte interface.

The failure/deactivation mechanisms [9, 21, 23, 91, 136, 137] attributed to the CTE are suggested to be broadly influenced by the factors discussed in the next sections. The factors which govern the beginning of a particular deactivation mechanism can be either external (related to the process) or internal to the electrode. The latter, if identified, can be minimized by a proper fabrication of the electrode itself.

1.3.5.1 Dissolution

Dissolution of the electrocatalytic coating can lead to electrode failure. An increase [9, 21, 23, 91, 136, 137] in the anode current density due to partial removal/wear of coating from the substrate is dissolution. The pH of electrolytes and electrolyte impurities also influences coating dissolution.

In highly oxidizing environments, RuO_2 is unstable, and tend to oxidize to higher oxidation states. In acidic electrolytes, RuO_2 tend to oxidize to soluble RuO_3 (+6 oxidation state) or to volatile RuO_4 (+8 oxidation state). In alkaline electrolytes, RuO_2 tend to oxidize to volatile RuO_4 or to perruthenate species (+7 oxidation state, e.g., $KRuO_4$). These processes lead to the dissolution of the active material in the coating, thus leading to coating failure. The presence of TiO_2 in the coating reduces dissolution; however, this may cause passivation leading to selective dissolution of Ru ions at the surface. RuO_2 is stable for ClERs but unstable under oxidizing conditions for OERs as Ru is believed to oxidize to higher volatile oxidation state.

Slow dissolution rate has been reported for IrO_2 under chlorine evolution conditions in straight polarity [137]. Deactivation [4] of IrTa electrode is reported to be related to long term polarization at higher overpotentials of IrO_2. This can be caused by IrO_2 oxidizing to a higher valent state of +6 (IrO_4^{2-}) or decomposing to IrO_3. IrO_2, however, is much more stable than RuO_2 under oxidizing conditions. Thus, commercial anodes used for oxygen evolution utilize IrO_2 based coating instead of RuO_2.

1.3.5.2 Passivation

Passivation failure [9, 21, 23, 91, 136, 137] is caused by the formation of a non-conductive oxide layer at the substrate/ coating interface resulting in increased resistance of the electrode and passivation of the interface. For porous coatings, oxygenated species are able to penetrate to the underlying Ti substrate causing the formation of TiO_2 at the substrate/coating interface. This causes an ohmic drop at the interface thereby increasing resistance at the interface. Factors governing coating porosity include film thickness,

composition and method of coating preparation. The substrate/coating interface can also be passivated. The TiO_2 usually present on the Ti substrate becomes doped by the RuO_2 (or IrO_2) during the coating process. If the doping is insufficient due to low RuO_2 (IrO_2) content, then the potential drop that occurs during current flow across TiO_2 causes it to grow thereby passivating the interface. Passivation of the substrate/coating can be minimized by etching the Ti substrate with about 60% H_2SO_4 to form Ti hydride at the Ti surface.

1.3.5.3 Surface Deposits

Failure can be caused by the deposition [9, 21, 23, 91, 136, 137] of foreign materials (MnO_2, Fe_2O_3, oxysalts, etc) on the surface of the coating. This leads to blinding of the active coating area, poisoning, or passivation of the coating. The effective surface area of the coating under consideration is reduced thus increasing the effective current density for the active coating. This method of coating deactivation can be common in industrial practice. This can be mitigated by periodically cleaning the electrode.

1.3.5.4 Substrate Attack

Substrate attack failure [9, 21, 23, 91, 136, 137] is caused by undesired ions (such as F^-) in the electrolyte that penetrate the coating to the substrate leading to corrosion and eventual spalling of the coating. Excessive porosity of the coating must be minimized. Therefore the electrochemical stability (measured in terms of breakdown corrosion potential) of materials selected for coating preparation should be known. Materials

selected should have a break down potential of 2-3 volts above the working electrode potential to avoid corrosion problems.

1.3.5.5 Mixed Failure

This mechanism [137] is the most probable to lead to electrode failure in practice. For example, a poor electrode design can lead to uneven current distribution across the coating, combined with the presence of undesirable ions (high F^- levels), can lead to the total deactivation of CTEs, in the parts where the current density is high. The result is the corrosion of the base metal, with the local loss of active coating. This is a typical example of CTEs, considered to be deactivated even if 90% of the surface is still active. Problems of uneven current distribution are frequently treated on an empirical basis, by means of various kinds of masking, but finite element analysis is now widely adopted, in order to obtain a better electrode design.

1.4 Applications of Coated Titanium Electrodes

CTEs have applications in many electrochemical industries apart from the chlor-alkali industry for which they were initially invented. Some of the applications are summarized in Table 2. As there is not much information in the open literature about the current reversal (CR) process, the applications of CTEs relevant to this work are briefly reviewed in the next sections.

Table 2 Applications of CTEs by continuous electrolysis (CE) and current reversal electrolysis (CRE).

Application	**Product**	**Reference**
Chlorine/Oxygen/chlorate electrolysis by CE	Chlorine/oxygen/chlorate/ ClO^-/HClO	1-2, 9, 139
Waste water treatment by CRE	Portable for water discharge into watershed by removal of toxic pollutants	1-2, 140-150
Sea water electrolysis by CE and CRE	ClO^-, HClO/Water devoid of saline products	1-2, 9, 140-150
Electrowinning	Cu, Zn, Co, Ni, etc	9, 137,151
Electro-synthesis of organics	Acids, aldehydes, ketones reduced to alcohols, hydrodimerization of acrylo-nitrile	9, 137
Electroplating	Sn or Zn plated of steel strips, Cu-foil	9, 137
Pool chlorination by CE and CRE	HClO, ClO^-	1, 140-150
Water treatment by CRE	Removal of Ca^{2+} , Mg^{2+}, Mn^{2+} ions	1, 140-150

1.4.1 Chlorine, Oxygen, and Chlorate Production on Coated Titanium Electrodes

The schematic diagram shown in Figure 2 depicts the electrolytic process for the production of chlorine, hypochlorite ions/hypochlorous acid, and chlorate. The production of Cl_2, ClO^-/HClO and ClO_3^- is based on the direct discharge of chlorine electrochemically on the anode, which then initiates the formation of the desired product based on solution chemistry.

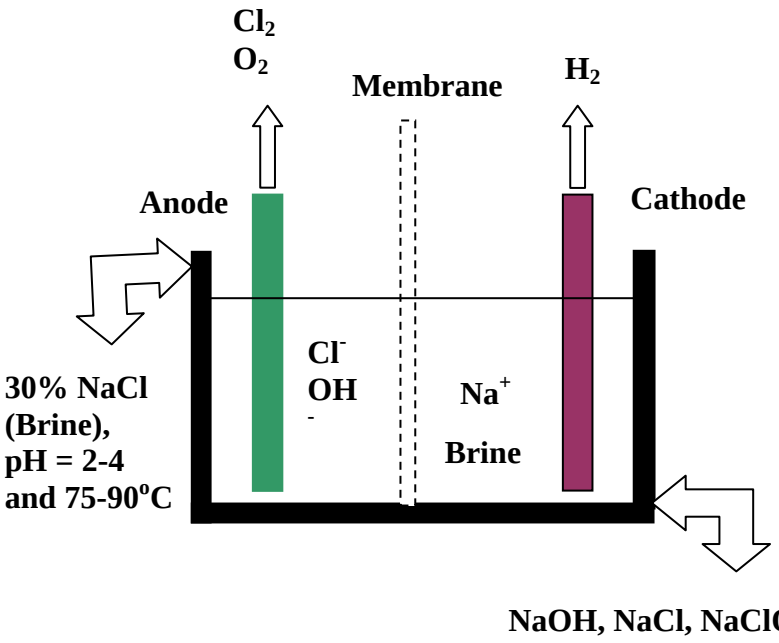

Figure 2 Schematic diagram showing chlorine, hypochlorite/hypochlorous, and chlorate production.

In Cl_2 production, an aqueous solution of about 30% brine (NaCl), having a pH of 2-4 and a temperature of 75-90^{o}C is usually circulated through the electrochemical cells.

A direct electric current is passed through the brine to discharge Cl_2 at the CTE as shown in equation 12. O_2 evolution, as in many anodic processes, is an unavoidable side reaction occurring at the anode with Cl_2. It is also the most common anodic reaction associated with processes occurring in aqueous solutions (such as water electrolysis and electrowinning) as given in equation 13 [3, 4, 23, 152, 153-154].

$$2Cl^{-}_{(aq)} = Cl_{2(g)} + 2e^{-} \qquad (12)$$

$$2H_2O_{(l)} = O_{2(g)} + 4H^+_{(aq)} + 4e^- \quad (13)$$

RuO_2-TiO_2 coated titanium electrodes are among the best anodes for Cl_2 evolution for the following reasons [155-157]:

1. They do not undergo passivation easily;

2. They have little dissolution problems since the reaction occurs at low overpotential; and

3. They are not easily wetted by Hg in Hg cells and so Cl_2 gas is readily released to avoid gas entrapment and coating wear.

In dilute chloride solutions at higher pH, the efficiency of Cl_2 evolution decreases as a result of occurrences of the following side reactions [158-161]:

$$Cl_{2(g)} + H_2O_{(l)} = HClO_{(l)} + H^+_{(aq)} + Cl^-_{(aq)} \quad (14)$$

$$12HClO_{(l)} + 6H_2O_{(l)} = 4ClO_3^-{}_{(aq)} + 8Cl^-_{(aq)} + 24H^+_{(aq)} + 3O_{2(g)} + 12e^- \quad (15)$$

Consequently Cl_2 evolution efficiency depends on electrolyte concentration and composition, current density, nature of electrode and temperature [23].

In chlorate electrolysis [9, 139], chlorine is produced at the CTE from chloride ions. The chlorine molecules then hydrolyze and subsequently form the chlorate product

by chemical oxidation. The chlorate production process can be described by equations 16-19.

$$2Cl^-_{(g)} = Cl_{2(g)} + 2e^- \quad (16)$$

$$Cl_{2(aq)} + H_2O_{(l)} = HClO_{(aq)} + Cl^-_{(aq)} + H^+_{(aq)} \quad (17)$$

$$HClO_{(aq)} = H^+_{(aq)} + ClO^-_{(aq)} \quad (18)$$

$$2HClO_{(aq)} + ClO^-_{(aq)} = ClO_3^-{}_{(aq)} + 2H^+_{(aq)} + 2Cl^-_{(aq)} \quad (19)$$

The electrical supply and arrangement of the chlorate electrochemical cell systems appear similar to those used in chlorine plants except the cells are undivided. Comparison of the processes of generation of chlorine and chlorate suggests that the reactions occurring on the CTEs appear to have commonalities. For example, in either case, the reactions occurring on the CTEs have oxygen evolution as a side reaction, accompanied by dissolution of the anode electrode.

The O_2 evolution reaction can occur favorably in both acidic and alkaline media on RuO_2-TiO_2 anodes. RuO_2-TiO_2 based anodes are however unstable for O_2 evolution as

they exhibit much shorter lifetimes in such applications due to coating dissolution. Alkaline media would have been the preferred option for practical applications; however, the media tend to attack the RuO_2-TiO_2 anodes. Thus, the acidic solution option is preferred for O_2 evolution on RuO_2 based anodes. O_2 evolution is reported to decrease as chloride concentration increases. Furthermore, at low current density, O_2 evolution decreases as RuO_2 in the active layer decreases. The shorter lifetimes of RuO_2 based anodes for O_2 evolution are attributed to the oxidation of Ru (from +4, RuO_2) to soluble RuO_3 (+6) or to the highly volatile oxidation states of RuO_4 (and +8) respectively [4, 9, 21-23, 138, 162].

IrO_2-Ta_2O_5 based anodes are efficient for O_2 evolution when compared to RuO_2 based anodes due to their relative stability, and are often used for high current density applications [21, 32]. IrO_2 has therefore become an indispensable active component for high performance anodes because of its good activity for O_2 evolution and better corrosion resistance in aggressive media than other precious metal oxides [29]. It has been suggested that, because of the better resistance of IrO_2 to corrosion than RuO_2, introduction of optimized quantities of IrO_2 into RuO_2-based CTEs improves or eliminates the pseudo-passivation which occurs in chlorine and chlorate electrolysis on RuO_2-based electrodes [163-166].

1.4.2 Electrochemical Water Disinfection Using Coated Titanium Electrodes (CTEs)

Electrochemical water disinfection using CTEs is among many methods employed in the treatment of domestic (drinking and swimming pool chlorination) and

industrial water. In electrochemical water disinfection, the disinfecting species, mainly hypochlorite ions and hypochlorous acid can be generated on-site, thereby avoiding the strict regulations involved with storage and transporting of hazardous materials, such as chlorine gas.

Electrochemical water disinfection [1, 167-169] is based on the chloride content of the water to be treated for generation of the disinfecting species, except in swimming pool chlorination where NaCl has to be added periodically. NaCl concentration in swimming pool water is usually between 2-5 g/L. For the disinfection process to be effective, water containing high chloride concentration, such as sea water (containing about 19 g/L choride ions) is recommended. For water containing low chloride concentration (drinking water), it has been found that less than 100 mg/L chloride concentration is sufficient to effectively disinfect the water.

The disinfecting [1, 167-169] hypochlorite and hypochlorous species are produced at the anode. Cl_2 hydrolyzes in water to form the hypochlorous acid. Hypochlorous acid and hypochlorite ions then form a pH dependent equilibrium. The mechanistic steps for the formation of the disinfecting species follow equations 20-22.

$$2Cl^-_{(g)} \rightarrow Cl_{2(g)} + 2e^- \quad (20)$$

$$Cl_{2(g)} + H_2O_{(l)} \rightarrow HClO_{(aq)} + HCl_{(aq)} \quad (21)$$

$$HClO_{(aq)} = ClO^{-}{}_{(aq)} + H^{+}{}_{(aq)} \quad (22)$$

Chloride ions consumed by the electrochemical chlorine production during the water disinfection process are reformed. In the treatment of low chloride concentration water (drinking water), the current efficiency of the CTE material for the production of the free chlorine must be as high as possible to compensate for the low chloride water content.

In practical applications, CTEs are inserted into the water system (e.g. swimming pool chlorination or hypochlorite generation from sea water for the prevention of power plant biofouling of the cooling water system) to be treated. Coated titanium electrodes can be used as both anode and cathode.

1.4.3 Hard Water Treatment Using Coated Titanium Electrodes (CTEs)

In water electrolysis such as swimming pool chlorination and water treatment (sea and brackish water), hard water (Ca and Mg) deposits build-up on the cathode. Over time, the deposits can cause increases in the operating cell voltage, thus decreasing cell efficiency.

Various techniques have been proposed for the removal of the cathode scale deposits from hard water treatment systems. These include: mechanical brushing, acid washing (dissolve scales), periodic air blasting, and periodic current/polarity reversal (dissolve/displaces scales). The proposed techniques have all presented their own deficiencies. However, the technique whereby the polarities of the electrodes are periodically reversed in the hard water treatment system is used commercially though it

has its own challenges (shorter lifetimes depending on conditions applied). It is cost effective, has little or no downtime for cleaning purposes and has the ability to withstand corrosion related problems [140-150].

In the current reversal application [1, 167-169], usually, two or more electrodes are introduced into the water system to be disinfected. A d.c voltage is applied on the electrodes with periodic polarity reversal to clean the cathode of the hard water scales deposited on it. The scale deposits are thin films of hydroxides and /or compounds of calcium and/or magnesium that form on the cathode during disinfection and chlorination (water-electrolysis) process. During the water-electrolysis [1, 167-169], the film scale deposits (consisting mainly of $Ca(OH)_2$, $CaCO_3$ and $Mg(OH)_2$) forms on the cathode surface due to the local increase in pH caused by the evolution of hydrogen (equation 23). However, the pH on the anode surface decreases due to the evolution of oxygen (equation 24).

$$2H_2O_{(l)} + 2e^- = H_{2(g)} + 2OH^-_{(aq)} \quad (23)$$

$$2H_2O_{(l)} + 4e^- = O_{2(g)} + 4H^+_{(aq)} \quad (24)$$

This technique [1, 167-169] is used for the removal of cathode scale deposits by periodically reversing polarity of the electrodes. When the polarity of the electrodes are reversed, the former cathode with scale deposits acts as the anode and, with continued

electrolysis, a local pH decrease at the anode surface occurs. This leads to dissolution of the scale deposits on the anode surface according to equations 25 and 26.

$$Ca(OH)_{2(s)} + 2H^{+}_{(aq)} = Ca^{2+}_{(aq)} + 2H_2O_{(l)} \quad (25)$$

$$Mg(OH)_{2(s)} + 2H^{+}_{(aq)} = Mg^{2+}_{(aq)} + 2H_2O_{(l)} \quad (26)$$

1.5 Research Objectives

The main reason for pursuing this work is the lack of information in the open literature (apart from the work of Kraft and Morimitsu et al.) regarding the effect of current reversal on coated titanium lifetimes, even though is used in industry. The other reason is that the work of both Kraft and Morimitsu et al. was limited in scope and characterization methods used to evaluate failed anodes. The work of Kraft and Morimitsu et al. was limited to only one electrolyte; Berlin water and sodium sulfate in a sulphuric acid solution, respectively.

The present work will examine two commercial CTEs in solutions containing five different anions to evaluate their effects on the electrode life. Furthermore, the effect of three electrolysis parameters (current density, reversal time and NaCl concentration) will be examined. In addition, water hardness (Ca and Mg) effects in three supporting anions

on CTE lifetime will be studied.

Finally, the anodes will be characterized methodically (employing physical and electrochemical techniques) in current reversal and hard water electrolysis to determine the lifetime patterns and failure mechanisms of the CTEs. Table 3 compares the work of Kraft and Morimitsu et al. based on current density, current reversal time and electrode separation distance.

Table 3 Comparison of published work on current reversal electrolysis.

Coating	**Electrolyte**	**Reversal time (min)**	**Current density (Am^{-2})**	**Electrode separation distance (mm)**	**Lifetime**	**Reference**
IrO_2	Berlin water	30	200	4	2.4 months	Kraft [1]
RuO_2	Berlin water	30	200	4	3 months	Kraft [1]
IrO_2-RuO_2	Berlin water	30	200	4	Nearly 1 year	Kraft [1]
Platinized Ti	Berlin water	30	200	4	8 years and running	Kraft [1]
IrO_2-Ta_2O_5	Na_2SO_4 and H_2SO_4	10	200	Not stated	1-2 months	Morimitsu et al. [2]

CHAPTER 2

EXPERIMENTAL

2.1 Samples and Sample Preparation

Commercially prepared electrode samples of RuO_2-TiO_2 and IrO_2-Ta_2O_5 coated on Ti substrates were used for all experiments. The RuO_2-TiO_2 coating was reported to have a ruthenium loading as metal of 3.2 g/m^2. The IrO_2-Ta_2O_5 was reported to iridium loading as metal of 10.8 g/m^2. The anode electrodes were provided coated on grade 1 Ti sheets. Samples from the sheets were sheared to produce 1 cm x 1 cm samples for the experiments.

2.2 Chemicals and Electrolyte Preparation

2.2.1 Chemicals

ACS reagent grade chemicals were used for the preparation of the synthetic supporting electrolytes for the experiments. The different anion sources used for current reversal testing were obtained from Na_2SO_4, $NaNO_3$, Na_2CO_3, $NaClO_4$ and Na_2HPO_4. Calcium ($CaCl_2.2H_2O$) and magnesium ($MgCl_2.6H_2O$) salts were used to simulate hardness in the hard water experiments.

2.2.2 Electrolytes for Current Reversal (CR) Testing

Supporting electrolytes for CR testing were usually prepared to 1 L with 18.2 MΩcm of DI water. In the CR experiments, different anions ($SO4^{2-}$, NO^{3-}, ClO_4^-, HPO_4^{2-} and CO_3^{2-}) with different concentrations (0.3, 0.6, 0.9 and 1.2M) were used. For these tests, a fixed amount of 0.043M (2.5gpl) of NaCl was usually added to each electrolyte. The concentrations and compositions of electrolytes were maintained as standard procedure for all the CR experiments. However, in verifying the effect of chloride concentration on lifetime, different amounts (0.009, 0.043 and 0.08M) of NaCl were added to 1.2M Na_2SO_4.

The chloride concentration selected was typical of concentration used for swimming pool disinfection. The sodium salts were used as supporting electrolytes to reduce the solution resistance in the electrochemical cell. In addition, the effect of the anions and their concentrations on the lifetimes of coated Ti electrodes was investigated.

2.2.3 Electrolytes for Simulated Hard Water Testing

For the simulated hard water experiments, $NaNO_3$, $NaClO_4$ and Na_2HPO_4 were used as supporting electrolytes. Salts of calcium ($CaCl_2.2H_2O$) and magnesium ($MgCl_2.6H_2O$) were used to simulate hardness in the electrolytes. Different molar concentrations (0.3, 0.6, 0.9 and 1.2M) of the supporting electrolytes were used for the hard water experiments.

2.3 Preparation of Electrodes

A standardized method of electrode preparation was adopted for all the electrochemical experiments and characterization procedures. The area of both working electrodes (WE) and counter electrodes (CE) was maintained at 1 cm^2 unless otherwise stated. Electrodes were spot welded to grade 2 Ti rods to provide electrical contact.

The backsides of the electrodes had no precious metal coatings and were covered with non-conducting Teflon film and vinyl tape to avoid possible current flow from the surface to be tested. Electrodes were rinsed thoroughly with deionized (DI) water before usage. A typical diagram of WE/CE welded to Ti rod is shown schematically in Figure 3.

2.4 Current Reversal (CR) and Simulated Hard Water Experiments

Current reversal and simulated hard water tests were conducted to observe the effect that periodic CR as well as Ca^{2+} and Mg^{2+} ions have on the lifetimes of the DSA electrodes under study. Periodic current reversal and hard water lifetime tests were performed in a two-electrode cell with a capacity of 1.2 L. The electrolyte under study was prepared to 1 L in the two-electrode cell. The working and counter electrodes were sometimes made of the same type of CTE material. In other instances, the WE and CE were made of different CTE material.

The coated surfaces of the electrodes under study were positioned parallel to each other in the electrochemical cell with a spacing of 10 cm as shown in Figure 4. Experiments were conducted at room temperature (25 ± 3^oC) and pressure conditions. Figure 5 shows a schematic diagram of a two electrode cell. The working electrode (WE)

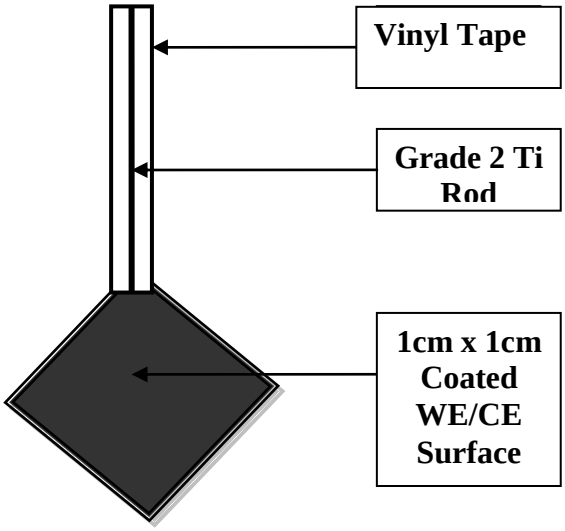

Figure 3 Schematic diagram of typical WE/CE used for the electrochemical experiments.

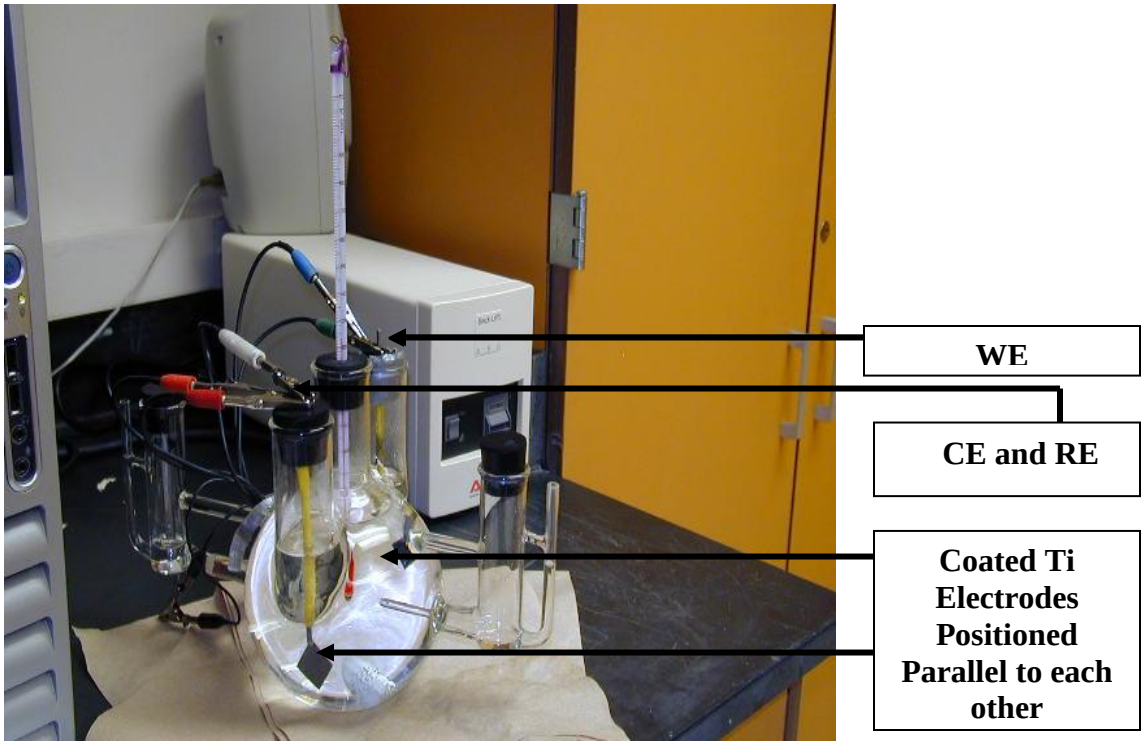

Figure 4 Setup for current reversal and simulated hard water testing.

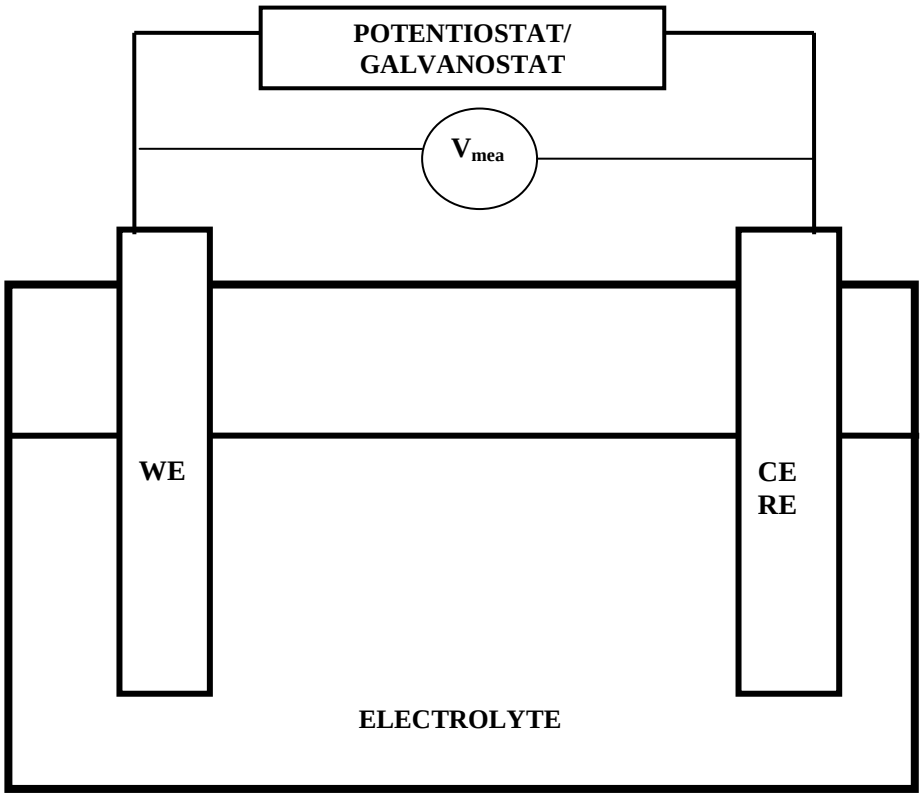

Figure 5 Schematic diagram of a two-electrode cell.

leads are connected to the anode while the counter electrode (CE) and reference electrode (RE) leads are connected to the cathode.

2.5 Experimental Control and Data Acquisition

A Gamry Potentiostat/Galvanostat PCI4/750 instrument with Virtual Front Panel 600 (VFP 600) software was used for experimental control and data acquisition for both current reversal and hard water lifetime tests.

2.5.1 Current Reversal Data Acquisition and Control

The VFP 600 software allowed for some parameters to be fixed while monitoring parameters of interest under study. In the CR experiments, the current density, current reversal frequency and data acquisition rate were fixed while cell voltage was monitored. Data acquisition for the experiments was set at 1 Hz and the electrical signal selected was of square wave form.

A current density of 1200 A m^{-2} was used for most of the experiments. However, to study the effect of current density (anode and cathode current densities on lifetime were also investigated) on lifetime and coating failure, other current densities were employed. Due to time constraints, a current density of 1200 A m^{-2} was selected to enable experiments to be completed on time in a laboratory setting while also allowing for compositional changes in the CTE under study to be evaluated upon failure.

A fixed concentration of 0.043 M NaCl was added to supporting electrolytes for CR experiments, except when studying the effect of chloride concentration on the lifetimes of the working electrodes, where other chloride concentrations were employed. Again, a constant current reversal frequency of 0.1 Hz was employed for the CR experiments, however, when studying the effect of current reversal frequency (current reversal cycle length) on lifetime; other current reversal frequencies were used. A summary of the CR experimental design is given in Table 4.

The failure of a CTE may be marked by the rapid increase in the potential of the coating when operating at constant current density or the rapid decrease in current when applying a constant voltage. For the CR work, CTE failure was defined as being 2 V increase from the onset/startup cell voltage. Most of the CR experiments were conducted

Table 4 Experimental design for current reversal tests.

Parameters studied	**Current density (A m^{-2})**	**Chloride concentration (M)**	**Current reversal frequency (cycle length)**	**Concentration of supporting electrolyte of Na (M)**
Effect of current density on lifetime	900	0.043	0.1	1.2 M $SO4^{2-}$
	1200	0.043	0.1	1.2 M $SO4^{2-}$
	1500	0.043	0.1	1.2 M $SO4^{2-}$
Effect of chloride concentration on lifetime	1200	0.043	0.1	1.2 M $SO4^{2-}$
	1200	0.009	0.1	1.2 M $SO4^{2-}$
	1200	0.08	0.1	1.2 M $SO4^{2-}$
Effect of current reversal frequency on lifetime	1200	0.043	0.1	1.2 M $SO4^{2-}$
	1200	0.043	0.01	1.2 M $SO4^{2-}$
	1200	0.043	0.02	1.2 M $SO4^{2-}$
Effect of SO_4^{2-} anion on lifetime	1200	0.043	0.1	0.3 M
	1200	0.043	0.1	0.6 M
	1200	0.043	0.1	0.9 M
	1200	0.043	0.1	1.2 M
Effect of HPO_4^{2-} anion on lifetime	1200	0.043	0.1	0.3 M
	1200	0.043	0.1	0.6 M
	1200	0.043	0.1	0.9 M
	1200	0.043	0.1	1.2 M
Effect of ClO_4^- anion on lifetime	1200	0.043	0.1	0.3 M
	1200	0.043	0.1	0.6 M
	1200	0.043	0.1	0.9 M
	1200	0.043	0.1	1.2 M
Effect of CO_3^{2-} anion on lifetime	1200	0.043	0.1	0.3 M
	1200	0.043	0.1	0.6 M
	1200	0.043	0.1	0.9 M
	1200	0.043	0.1	1.2 M
Effect of NO_3^- anion on lifetime	1200	0.043	0.1	0.3 M
	1200	0.043	0.1	0.6 M
	1200	0.043	0.1	0.9 M
	1200	0.043	0.1	1.2 M

in triplicates to determine reproducibility of the results.

2.5.2 Simulated Hard Water Data Acquisition and Control

Hard water experiments, experimental control and data acquisition were conducted as the current reversal tests using the VFP 600 software on the Gamry Potentiostat/Galvanostat instrument. Some parameters were fixed while parameters under investigation (cell voltage) were monitored. $NaNO_3$, $NaClO_4$ and Na_2HPO_4 were used as supporting electrolytes while $CaCl_2.2H_2O$ and $MgCl_2.6H_2O$ were used to simulate hardness in the electrolytes.

Chloride concentration was fixed at 0.043 M by the addition of NaCl when needed. A summary of the fixed and variable parameters for the hard water experiments is shown in Table 5. Data acquisition for the experiments was set at 1 Hz and the electrical signal chosen was a square wave form. Coating failure for the hard water tests was defined as 2 V increase in cell voltage from the startup voltage. Experiments were conducted in triplicates to determine reproducibility of the results.

2.6 Characterization Techniques

Electrochemical and physical properties of the CTEs were characterized. CTE samples were characterized to elucidate information and explanations for observations made in the current reversal and hard water electrolysis experiments, and to also determine the mechanism of failure for the CTEs. The electrochemical techniques employed were cyclic voltammetry (CV), galvanostatic electrochemical impedance spectroscopy (EIS) and chronopotentiometry (CP). The physical techniques used were X-

Table 5 Experimental design for simulated hard water tests.

Parameter under study	**Concentration of Ca^{2+} ions in solution (mg/l)**	**Concentration of Mg^{2+} ions in solution (mg/l)**	**Current density (A m^{-2})**	**Current reversal frequency (Hz)**	**Concentration of supporting electrolyte (M)**
Effect of very hard water on lifetime	857	857	1200	0.1	0.3-1.2
Effect of hard water on lifetime Hard	425	425	1200	0.1	0.3-1.2
Effect of moderately hard water on lifetime	265	161, 265	1200	0.1	0.3-1.2

ray fluorescence (XRF), scanning electron microscopy (SEM) and energy dispersion spectroscopy (EDS).

2.6.1 Electrochemical Characterization

CV experiments were conducted using a Gamry PCI4/750 Potentiostat/Galvanostat instrument. CTEs were prepared as described in section 2.3. Experiments were performed at room temperature and pressure conditions. CV experiments were conducted in a three-electrode cell as shown schematically in Figure 6. The measured potential ($V_{measured}$) is obtained from the potential measured between the working electrode (CTE) and saturated Ag/AgCl reference electrode.

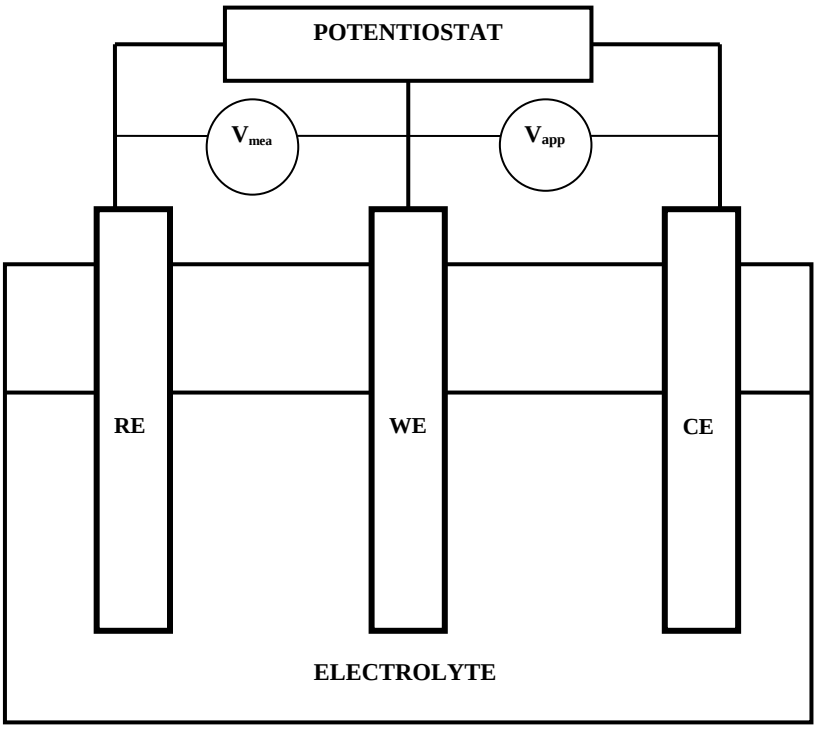

Figure 6 Schematic diagram of a three-electrode cell.

2.6.1.1 Cyclic Voltammetry

CV experiments were conducted on fresh, tested (current reversal testing was done at various time intervals before coating failure) and failed (after current reversal lifetime testing) samples. The RE was saturated Ag/AgCl, the CE was platinum wire and WE was the CTE (IrTa and RuTi).

CV experiments were performed in 1.2 M supporting electrolytes of Na_2SO_4, $NaNO_3$, $NaClO_4$, Na_2HPO_4 and Na_2CO_3 dependent on electrolyte used in lifetime testing. A fixed amount of 0.043M (2.5gpl) of NaCl was added to each electrolyte. The potential was scanned from 0.2 V to 0.6 V (and 0.2 V to 0.9 V for some CV tests) versus Ag/AgCl at a scan rate of 100 mVs^{-1}.

2.6.1.2 Chronopotentiometry

Chronopotentiometry was conducted in simulated hard water to observe the effect of electrolyte composition and concentration on the deposition of Ca and Mg ions on CTEs. A constant current of -0.12 A was maintained for the duration of experiments. Potential was then measured as a function of time. The working electrode was the CTE under study while the counter electrode was another CTE with a much longer lifetime than the one under study.

2.6.2 Physical Characterization

XRF and SEM/EDS techniques were employed to evaluate the elemental and chemical composition as well as the surface morphology of the CTE coating before and after testing. Again, as with the electrochemical techniques, fresh, tested and failed CTE coated samples were tested. Samples for XRF and SEM/EDS analysis were run in the same supporting electrolytes as discussed under CV and EIS.

2.6.2.1 X-ray Fluorescence

XRF analysis was performed on CTE samples using a Jordan Valley Applied Research (JVAR) Model3600 instrument. Comparison of the net intensities generated during XRF analysis of the CTE samples allows for the amount of precious metal (Ir and Ru) and base metals (Ta and Ti) present in the fresh, tested and failed samples to be computed.

2.6.2.2 Scanning Electron Microscopy (SEM) and Energy Dispersion Spectroscopy (EDS)

Surface morphological features and elemental composition of coatings were investigated by SEM/EDS analysis. SEM/EDS analysis of CTE samples was done by a Hitachi S 3400. Samples were analyzed at a potential of 30 kV and a magnification of 500X.

CHAPTER 3

RESULTS

Two commercially prepared anode electrode samples of RuO_2-TiO_2 (RuTi) and IrO_2-Ta_2O_5 (IrTa) coated on Ti substrates were investigated in a laboratory controlled environment. The effect of current reversal on these coated titanium electrodes (CTEs) and the mechanism of their failure are presented and discussed.

3.1 Typical Profiles of CTE Undergoing Current Reversal

As the electrochemical cell under goes current reversal, the cell polarity reverses periodically. A plot of an example of the cell voltage profile versus a short time is shown in Figure 7. The example shown is for a 0.1 Hz cycle for 120 seconds. Figure 8 presents a magnified square wave for 0.1 Hz cycle. That is the current flows in the positive direction for 5 seconds. This can be seen by the positive cell voltage. Then the current is reversed for 5 seconds and the cell polarity becomes negative. As the direction of the current is reversed, the cell voltage does not immediately reach a maximum in absolute value terms.

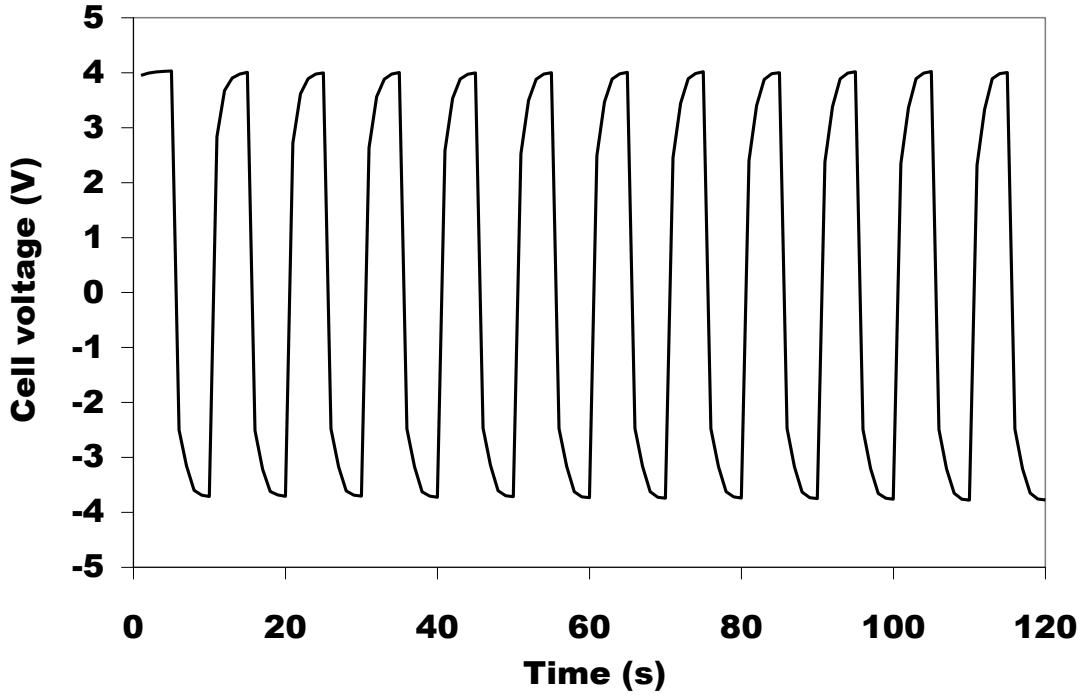

Figure 7 Example of cell voltage response to an applied square current wave vs. time at 0.1 Hz cycle for 120 seconds.

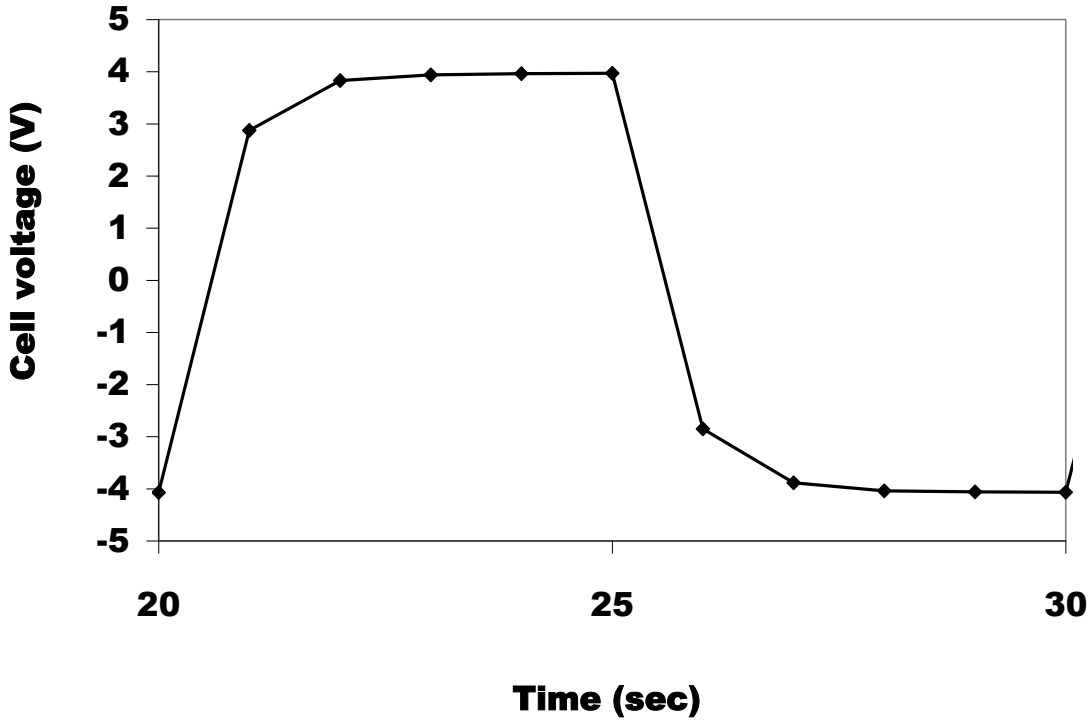

Figure 8 Example of first cycle is cell voltage response vs. time at 0.1 Hz per cycle.

Initially, a low cell voltage is observed. As the coated titanium electrodes employed typically exhibit large [170] pseudocapacitance due to their high surface areas and proton [171] insertion. This lower temporary cell voltage can be explained by the surface charge of the electrode changing with minimal faradic reactions occurring. After the surface is fully charged then faradic reactions occur with the evolution of oxygen and chlorine at the anode and hydrogen evolution at the cathode.

The primary focus of this study is the examination of lifetime in relation to the failure time (τ) for the two anode electrodes examined. The failure time for the anodes was set at an absolute value of 2 V above the initial cell voltage when current was flowing in either the positive or negative direction. Figure 9 shows an example of cell voltage versus time plot for an accelerated lifetest under current reversal conditions. A voltage "band" in the cell voltage plot is observed and will be described in more detail under Chapter 4. The band is believed to be caused by pseudocapacitance effects of the coatings.

As seen in Figure 9, the cell voltage undergoes three regions of voltage changes before electrode failure. The first region (I) is where there is a drop in voltage at the start of each current reversal cycle. The second region (II) is when the maximum voltage of each voltage starts to rise in a fairly constant manner with time. The third region (III) is when voltage rises sharply as the electrode approaches the failure time. These three regions of voltage changes will be discussed in detail in Chapter 4.

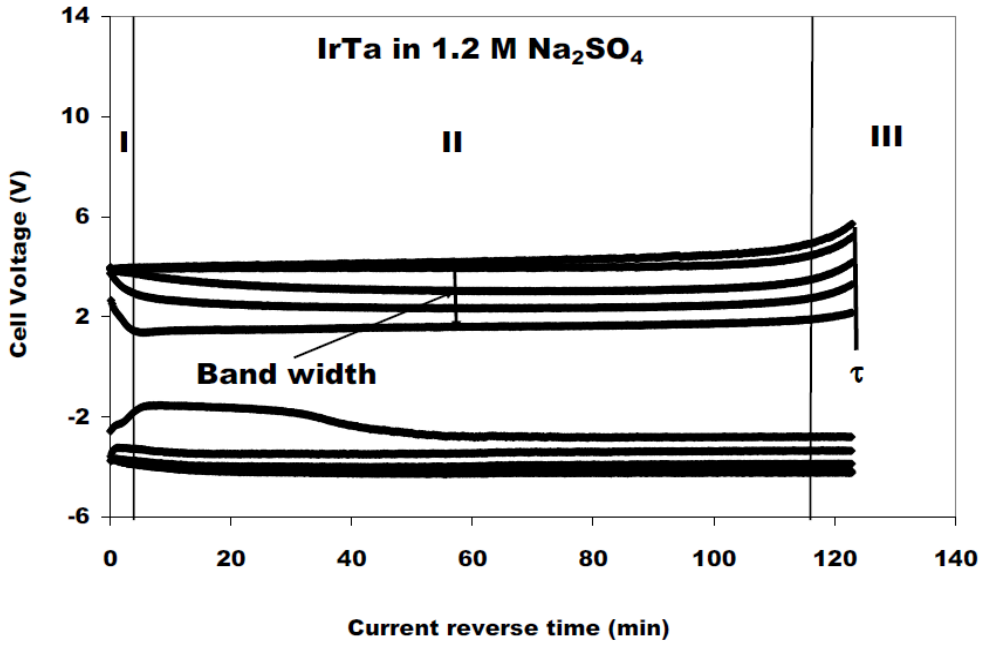

Figure 9 Cell voltage vs. lifetime for IrO_2-Ta_2O_5 anode at 1200 A/m^2, 1.2 M Na_2SO_4, 0.043 M NaCl, 0.1 Hz reversal frequency.

3.2 Iridium Dioxide-Tantalum Pentaoxide (IrO_2-Ta_2O_5) Electrode

IrTa anodes were examined under electrolysis conditions with periodic current reversal. The effect of some electrolysis parameters on the anode's life was investigated in synthetic electrolytes. In addition, the effects of five anions (SO_4^{2-}, NO_3^-, ClO_4^-, HPO_4^{2-}, CO_3^{2-}) added with sodium on the anodes were studied. Finally, hard water (Ca and Mg) effects on lifetime of IrTa anode were evaluated.

3.2.1 Effects of Current Reversal Electrolysis Parameters on Lifetime of IrO_2-Ta_2O_5 Electrode

3.2.1.1 Current Density

Current density plays an important role in the chlor-alkali and swimming pool industries as lifetimes of the CTEs employed in chlorine generation depend upon it [172, 173]. In the swimming pool industry, chlorine generators have been developed that run at current densities ranging from 300 to 620 A/m^2 [173, 174]. If the chlorine generator is self-cleaning, then the lifetime of the CTE is reduced. Three current densities were selected for study. The magnitude of the current densities selected was such as to accelerate failure of the CTEs in a laboratory setting.

The effect of the current density on IrTa anode lifetime is shown in Figure 10. The plot shows that increasing the current density leads to decreasing lifetime of the IrTa anode. The reasons for failure will be discussed in Chapter 4.

To further understand if failure is predominately controlled by the anodic or cathodic current density during current reversal testing, experimental conditions were modified to study an asymmetric current wave. While examining the effect of anodic current density on the working electrode, the cathodic current density was maintained at 1200 A/m^2. Likewise while studying the cathodic current density, the anode current density was set to 1200 A/m^2. The counter electrode was changed to a RuO_2-TiO_2 coated electrode of twice the surface area of the working electrode to insure that failure occurred on the working electrode which was IrO_2-Ta_2O_5.

The effects of anodic and cathodic current densities on lifetime are shown in Figure 11. Lifetime increases as either anodic or cathodic current density is reduced. As

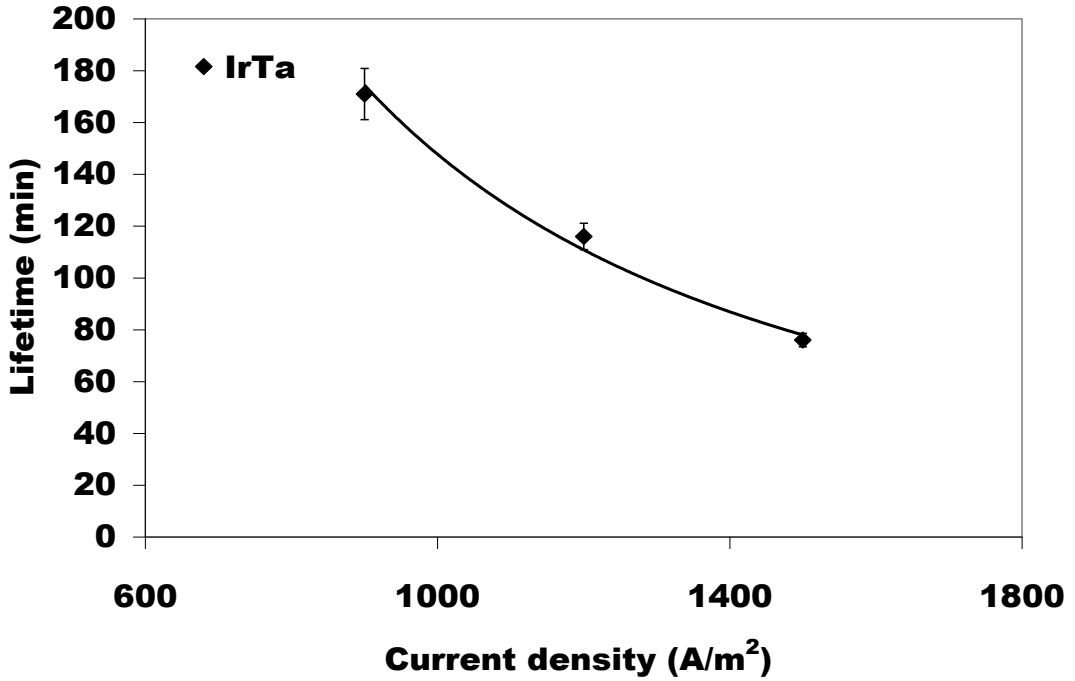

Figure 10 Effect of current density on IrO_2-Ta_2O_5 electrode lifetime in 1.2 M Na_2SO_4, 0.043 M NaCl, 0.1 Hz.

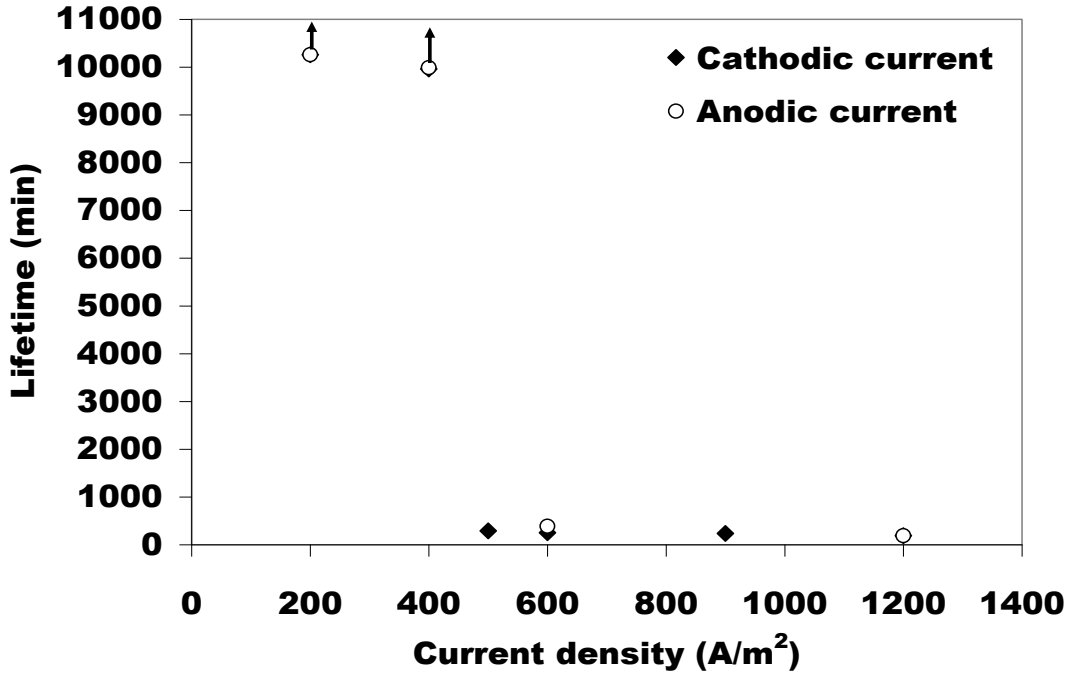

Figure 11 Effect of anodic and cathodic current densities on IrO_2-Ta_2O_5 electrode lifetime in 1.2 M Na_2SO_4, 0.043 M NaCl, 0.1 Hz.

seen in Figure 11, the experiments performed at low current density had long lifetimes and were stopped before failure occurred. This seems to suggest that CTEs are likely to last much longer at lower current densities even with periodic current reversal. The results seem to indicate that reducing the anodic or cathodic current density has similar effects on lifetime.

3.2.1.2 Current Reversal Frequency

Lifetimes of CTEs are known to last longer when used in continuous anodic or cathodic [2] electrolysis applications as compared to periodic current reversal. As the main focus of this work was to evaluate the effects of current reversal on CTEs, it was necessary to investigate the effects of the frequency of reversal on these anodes. For most of this work the reversal cycle time or frequency was 10 seconds or 0.1 Hz. This means that, the working electrode in the electrochemical cell under study behaves as an anode for 5 seconds recording positive voltages and currents. Then the polarity of the working electrode changes to become a cathode for the next 5 seconds recording negative voltages and currents. To investigate the effect of current reversal cycle frequency on lifetime of CTEs, four current reversal cycle times were considered. Reversal cycle times (or frequencies) of 10 sec (0.1 Hz), 50 sec (0.02 Hz), 100 sec (0.01 Hz) and 30 minutes (0.0006 Hz) were used. The plot in Figure 12 displays the results of the reversal cycle frequency versus current reversal time. The plot reveals that increasing the current reversal cycle time from 10 to 1800 seconds (0.1 to 0.0006 Hz) leads to longer lifetimes for IrTa. In fact, a dramatic increase in the lifetime of IrTa is observed as the reversal cycle time was increased to 30 minutes. This suggests that CTEs used for self-cleaning

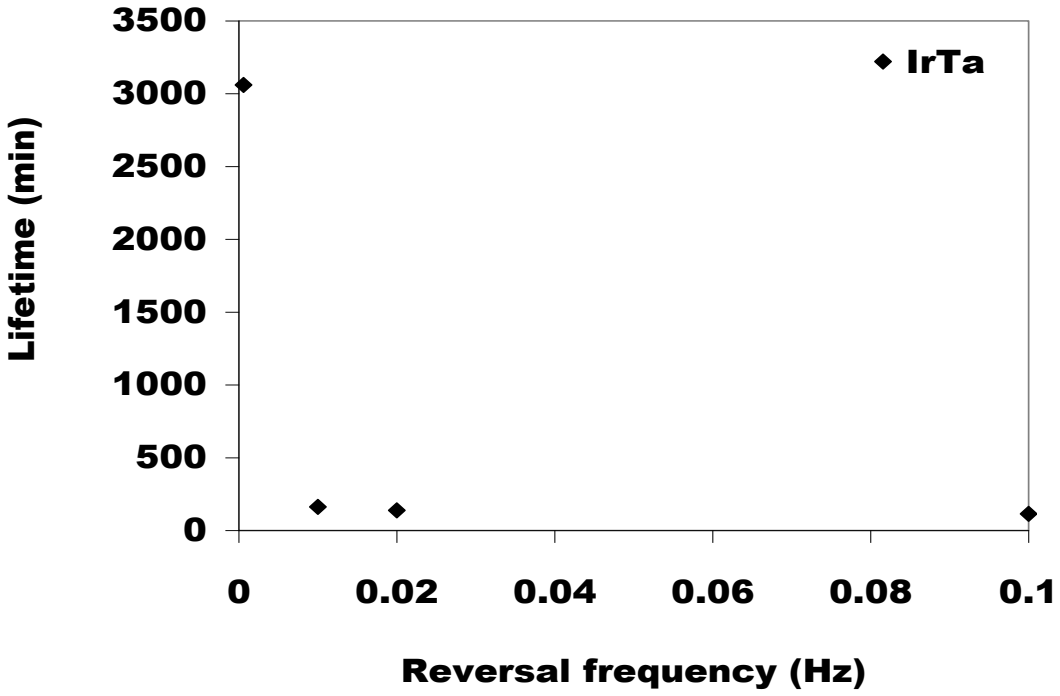

Figure 12 Effect of current reversal cycle time on IrO_2-Ta_2O_5 electrode lifetime at 1200 A/m^2, 1.2 M Na_2SO_4, 0.043 M NaCl.

applications need an optimal current reversal cycle frequency.

3.2.1.3 Sodium Chloride Concentration

As salt (NaCl) is used for water disinfection, it seemed useful to investigate the effect of chloride concentration on lifetime of IrTa anode. Synthetic electrolyte of 1.2 M Na_2SO_4 mixed with three different concentrations of NaCl were investigated. The NaCl concentrations range selected was typical for the salt water swimming pool disinfection [1]. Concentrations of 0.009, 0.043 and 0.077 M NaCl were used. NaCl had minimal effect on the lifetime of IrTa over the range of salt concentration investigated as indicated

in Figure 13. Hine [175] et al. has reported a positive correlation between CTEs lifetime and NaCl concentration under continuous electrolysis and much higher chloride concentrations. The insignificant influence of NaCl concentration on IrTa life appears to be due to the low concentration values of NaCl.

3.2.2 Effect of Electrolyte Composition and Concentration

The effects of electrolyte concentration and composition during current reversal electrolysis on the lifetime of IrTa anode were examined. Synthetic supporting electrolyte concentrations of 0.3, 0.6, 0.9 and 1.2 M of anions were used. 0.043 M of NaCl was added to all the electrolytes studied. In this investigation current reversal cycle frequency was 0.1 Hz. Figure 14 displays the effect of supporting electrolyte anion species and concentration on lifetime of IrTa anode. The plot reveals that with increasing nitrate concentration, longer lifetimes are produced and were the longest lifetime found for IrTa electrodes. Hydrogen phosphate produced the lowest lifetime at the four concentration levels examined. IrTa anode life appeared not to change with increasing hydrogen phosphate concentration. Lifetime appears to decrease with increasing carbonate and sulphate concentrations. Lifetime does not appear to change as a function of concentration for perchlorate ions. It is clear from the observations made that electrolyte composition and concentration affects the life of IrTa. Four out of the five electrolytes examined influences IrTa anode life to some degree; however, IrTa life is most significantly affected in nitrate ions. The cause for these failures will be discussed in Chapter 4.

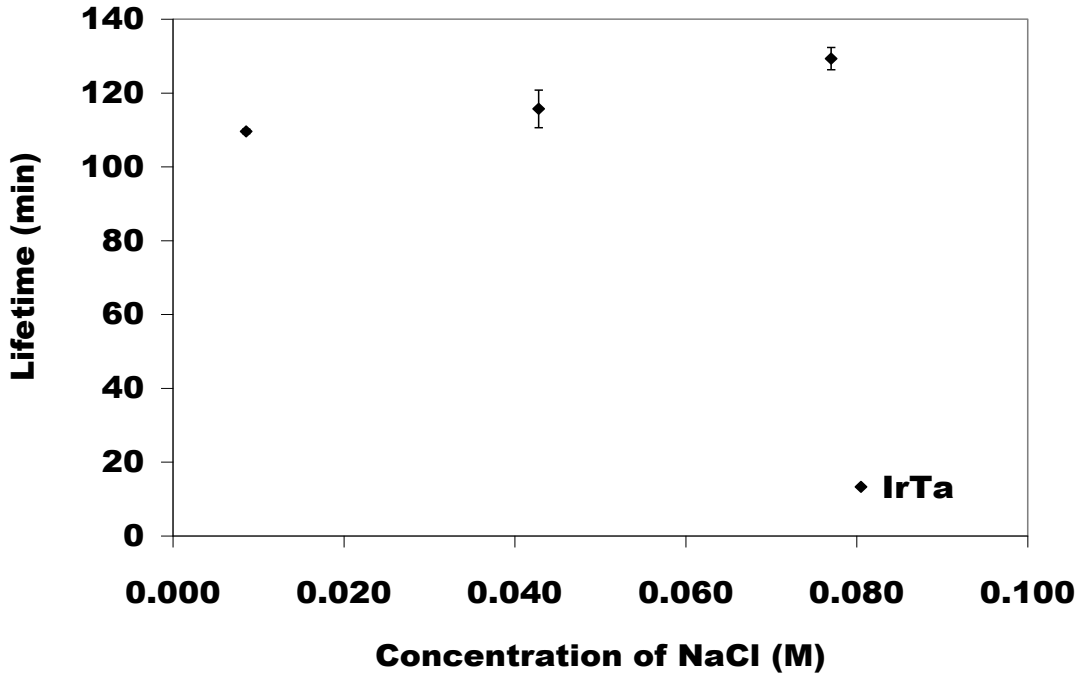

Figure 13 Effect of sodium chloride concentration on IrO_2-Ta_2O_5 electrode lifetime at 1200 A/m^2, 1.2 M Na_2SO_4, 0.1 Hz.

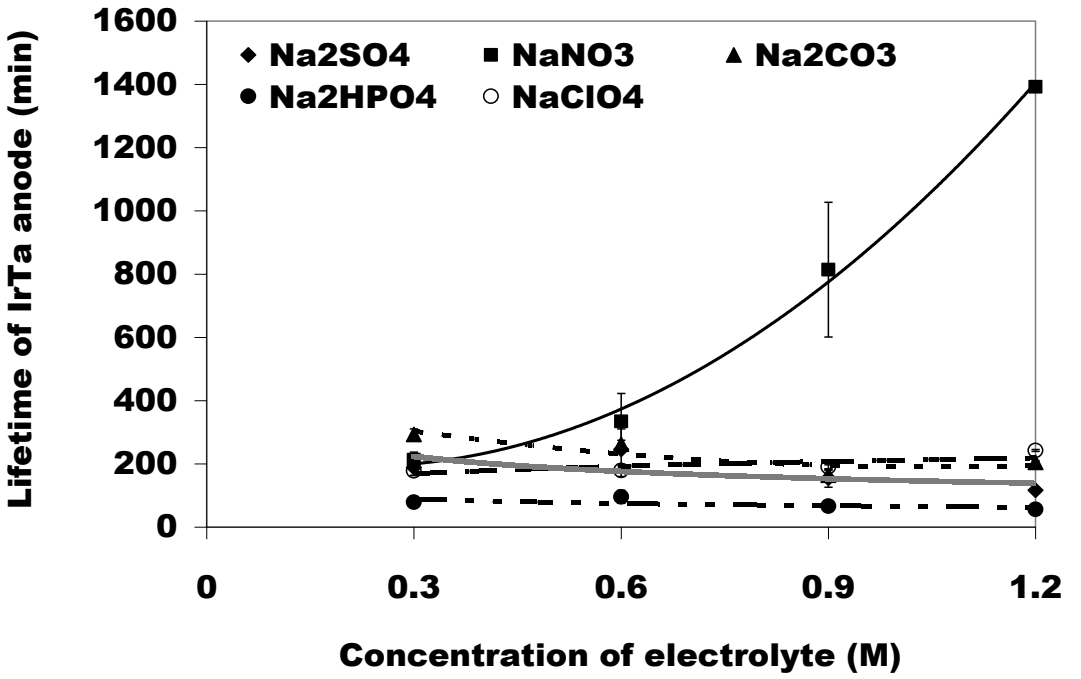

Figure 14 Effect of electrolyte composition and concentration on IrO_2-Ta_2O_5 electrode lifetime at 1200 A/m^2, 0.043 M NaCl, 0.1 Hz cycle.

3.2.3 Effect of Water Hardness on Lifetime of IrO_2-Ta_2O_5

Water hardness was simulated by introducing calcium or magnesium ions in soluble synthetic supporting electrolytes of sodium nitrate, sodium hydrogen phosphate and sodium perchlorate to study its effect. According to the U. S. Geological Survey guidelines [176] for the classification of water hardness in the U.S, 0-60 mg/L is considered as soft water, 61-120 mg/L as moderately hard, 121-180 mg/L as hard, and greater than 180 mg/L as very hard water. The water hardness investigated in this work was modified from [176-178] and ranged from slightly hard water (140-210 mg/L) to very hard water (greater than 830 mg/L). The concentrations selected were to acceleratefailure of the oxide electrodes in the laboratory setting. The concentration of Ca ions examined was between 265 to 857 mg/L and Mg ions concentration examined was between 161 to 857 mg/L. It was expected from conversations with a CTE supplier that the harder the water, the shorter will be the lifetime of the coated titanium electrode.

Representative samples of cell voltage versus time plots for accelerated lifetests of IrTa anodes in $NaNO_3$ with Ca and Mg ions are shown in Figures 15 and 16 respectively. Again the voltage bands are observed in the plots. This is believed to be caused by pseudocapacitive effects of the coatings as mentioned in preceding sections. Obviously, the band for Mg ions is much longer than observed for Ca ions. This will be discussed in Chapter 4.

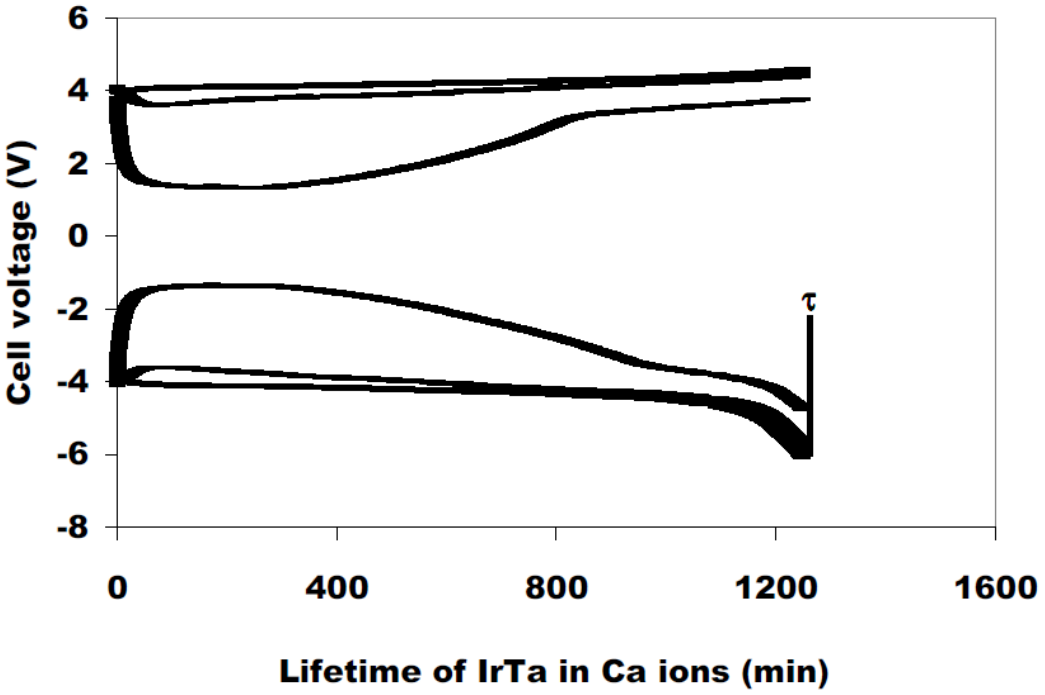

Figure 15 Cell voltage vs lifetime for IrO_2-Ta_2O_5 electrode at 1200 A/m^2, 857 mg/L Ca ions, 1.2 M $NaNO_3$, 0.026 M Cl^-, 0.1 Hz reversal frequency.

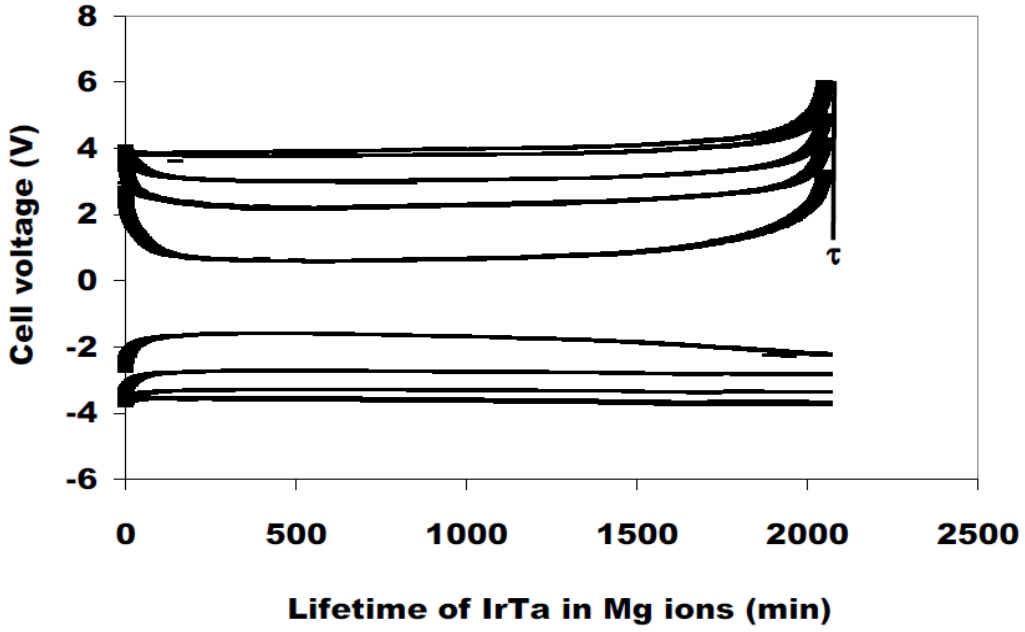

Figure 16 Cell voltage vs lifetime for IrO_2-Ta_2O_5 electrode at 1200 A/m^2, 857 mg/L Mg ions, 1.2 M $NaNO_3$, 0.026 M Cl^-, 0.1 Hz reversal frequency.

3.2.3.1 Effect of Calcium and Magnesium Ions on IrO_2-Ta_2O_5 Lifetime in $NaNO_3$

The effect of calcium and magnesium ions on the lifetime of IrTa anode was determined in 0.3, 0.6, 0.9 and 1.2 M $NaNO_3$ concentrations. Total chloride concentration was maintained at 0.043 M in the electrolytes. The effect of both Ca and $NaNO_3$ concentrations on IrTa are shown in Figure 17. The general trend observed is that the lifetime of IrTa electrode increased as the concentration of $NaNO_3$ was increasing regardless of Ca concentration. The lifetime of IrTa appears to be affected by Ca concentration discernibly only in the 0.6 and 0.9 M nitrate at 857 mg/L Ca concentrations.

In the presence of Mg ions, the lifetime of IrTa changes as shown in Figure 18. As observed in the plot, there was an initial increase in lifetime of IrTa electrode from the 0 to 161 mg/L Mg ions concentrations (highest lifetime for IrTa) before a subsequent decline in lifetime with increasing Mg. Again, the lifetime of IrTa increases with increasing $NaNO_3$ concentration regardless of Mg concentration.

Obviously the compositions and concentrations of sodium nitrate supporting electrolyte and Mg ions appear to influence the lifetime of the IrTa anode while Ca concentration had minimal effect on IrTa life.

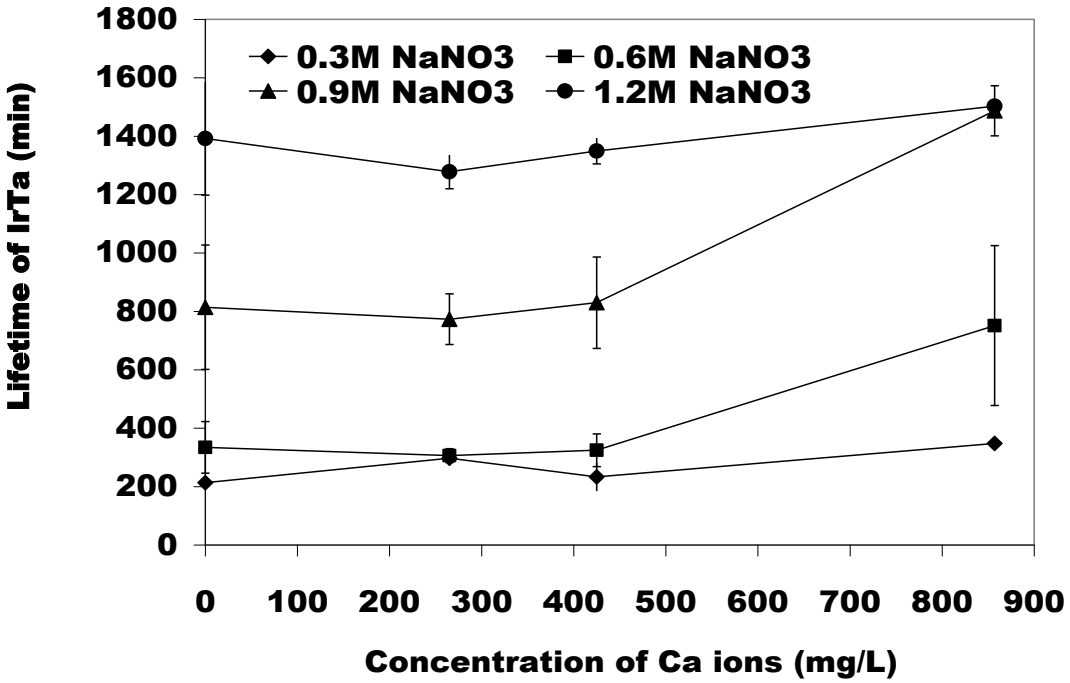

Figure 17 Effect of Ca and sodium nitrate concentrations on IrO_2-Ta_2O_5 electrode lifetime at 1200 A/m^2, 0.026 M Cl^-, 0.1 Hz cycle.

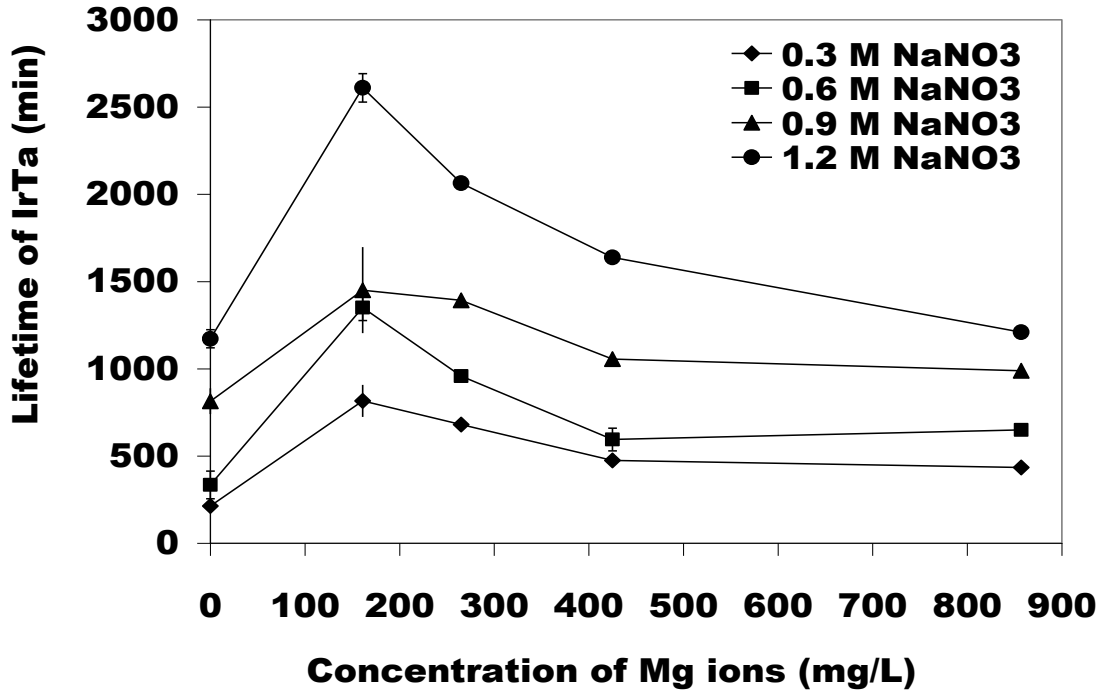

Figure 18 Effect of Mg and sodium nitrate concentrations on IrO_2-Ta_2O_5 electrode lifetime at 1200 A/m^2, 0.026 M Cl^-, 0.1 Hz cycle.

3.2.3.2 Effect of Calcium and Magnesium Ions on IrO_2-Ta_2O_5 Lifetime in $NaClO_4$

The same electrolysis conditions were used for IrTa electrode testing in sodium perchlorate ($NaClO_4$) supporting electrolyte as described in the previous section. The effects of Ca, Mg ions concentrations and $NaClO_4$ concentrations are shown in Figures 19 and 20, respectively. Figure 19 reveals that lifetime of IrTa increases with the addition of Ca ions followed by a decrease with increasing Ca ions concentration. The plot also shows that lifetime of IrTa increases as perchlorate ion concentration increases in the presence of higher Ca ions cocentrations. Figure 19 also shows that IrTa anode had longer lifetimes at 265 and 425 mg/L Ca ions concentrations (at the different perchlorate concentrations examined) than in the 0 mg/L Ca ions concentrations. The lifetimes of IrTa anode in the presence of Ca and nitrate ions are higher than the lifetimes of IrTa in Ca and perchlorate ions.

The lifetimes for IrTa in Mg and perchlorate solutions are shown in Figure 20. Small amounts of Mg (161 mg/L) increases lifetime significantly. Lifetime of IrTa is observed to increase to a maximum at 161 mg/L Mg and then decreases with increasing Mg concentration. Perchlorate ions appear to influence IrTa lifetime at 161 and 857 mg/L Mg concentrations. While lifetime of IrTa is seen to increase with increasing perchlorate ions concentration at the 161 mg/L Mg ions concentration, IrTa lifetime is observed to decrease with increasing perchlorate ions concentration at the 857 mg/L Mg ions concentration.

As can be seen from the discussion, the lifetime of IrTa appears to be affected to some degree by the composition and concentration of perchlorate, Ca and Mg ions.

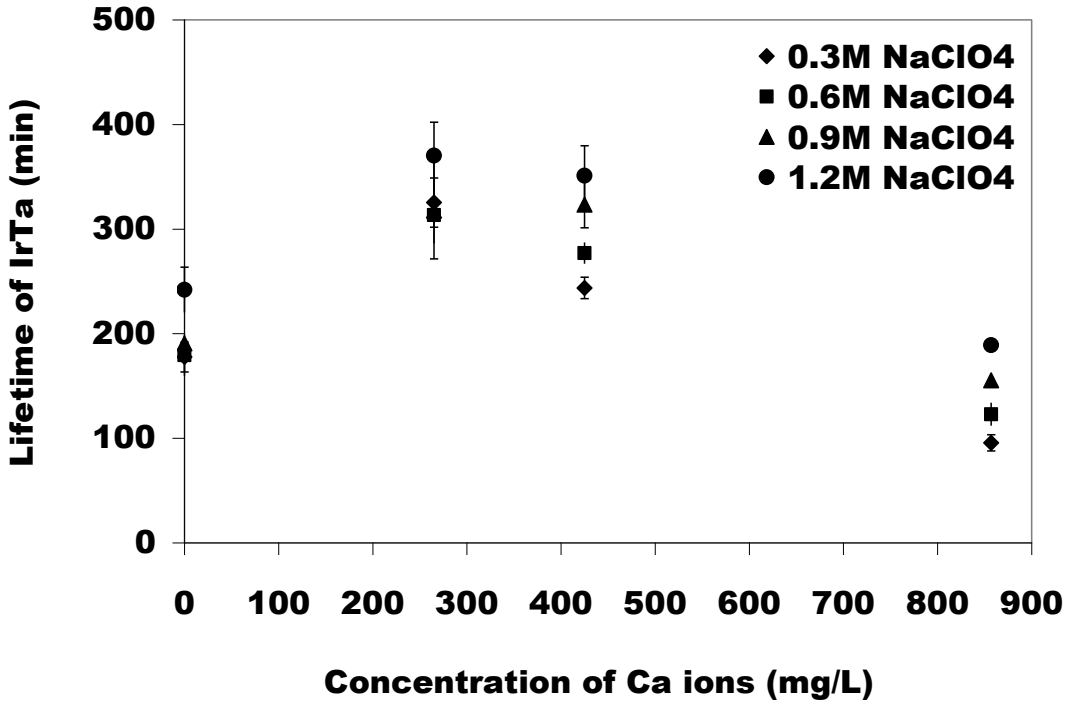

Figure 19 Effect of Ca and sodium perchlorate concentrations on IrO_2-Ta_2O_5 electrode lifetime at 1200 A/m^2, 0.026 M Cl^-, 0.1 Hz cycle.

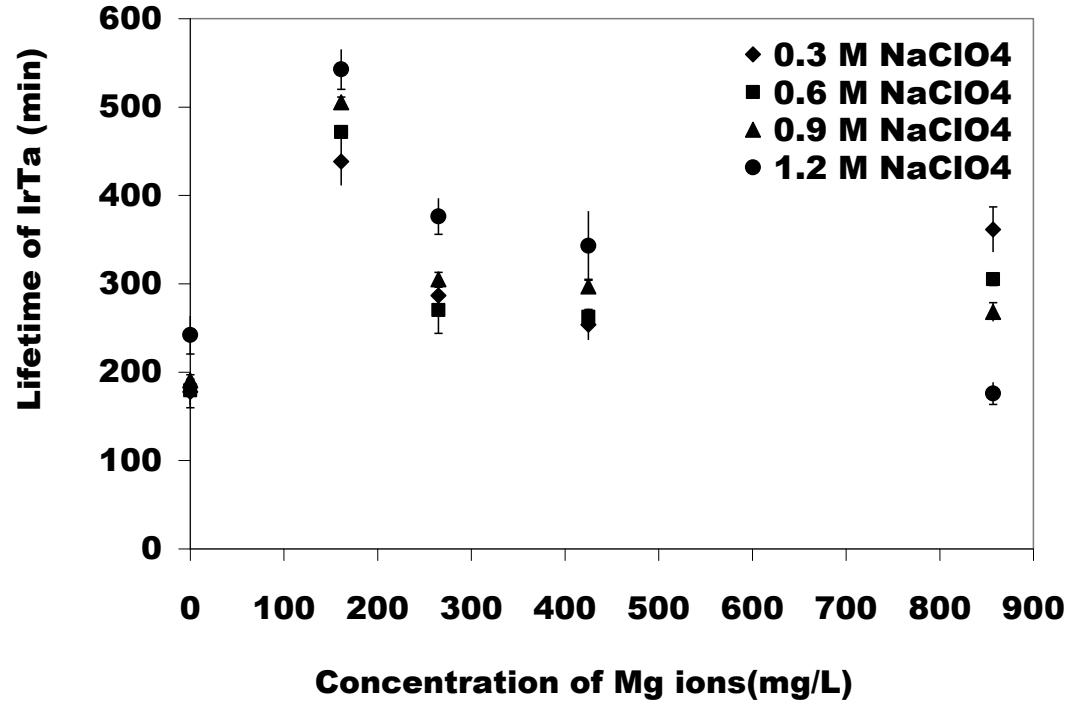

Figure 20 Effect of Mg and sodium perchlorate concentrations on IrO_2-Ta_2O_5 electrode lifetime at 1200 A/m^2, 0.026 M Cl^-, 0.1 Hz cycle.

3.2.3.3 Effect of Calcium and Magnesium Ions on IrO_2-Ta_2O_5 Lifetime in Na_2HPO_4

The effect of Ca and Mg ions on IrTa electrode using Na_2HPO_4 as supporting electrolyte was examined using the same conditions as described in Section 3.2.3.1. The effects of Ca and Mg ions on IrTa lifetimes are presented in Figures 21 and 22, respectively. The lifetime of IrTa rises (from 0-425 mg/L Ca ions concentration) and then declines (at 857 mg/L Ca ions concentration) as concentration of Ca ions increases. The lifetime of IrTa increases as the Na_2HPO_4 concentration increases at low (265mg/L) to medium (425 mg/L) concentration of Ca ions, but at the high (857 mg/L) Ca ions concentration, Na_2HPO_4 concentration appears not to affect the life of IrTa.

In the presence of Mg and hydrogen phosphate ions, IrTa anode life as seen in Figure 22 appears to have a maximum at 161 mg/L Mg and then declines to 425 mg/L Mg. The concentration of hydrogen phosphate ions appear not to distinctly influence the lifetime of IrTa except at the high (857 mg/L) concentration of Mg ions, where lifetime appears to decrease as hydrogen phosphate concentration increases. The lifetimes of the IrTa electrode appear higher in the presence of Ca and Mg ions than in only hydrogen phosphate ions. It appears the Ca and Mg concentrations interact with the hydrogen phosphate supporting electrolyte, to some extent and influence the life of IrTa.

3.2.4 Physical Characterization

To understand the mechanism of failure of the CTEs in current reversal, fresh and tested CTE samples were characterized using physical and electrochemical methods.

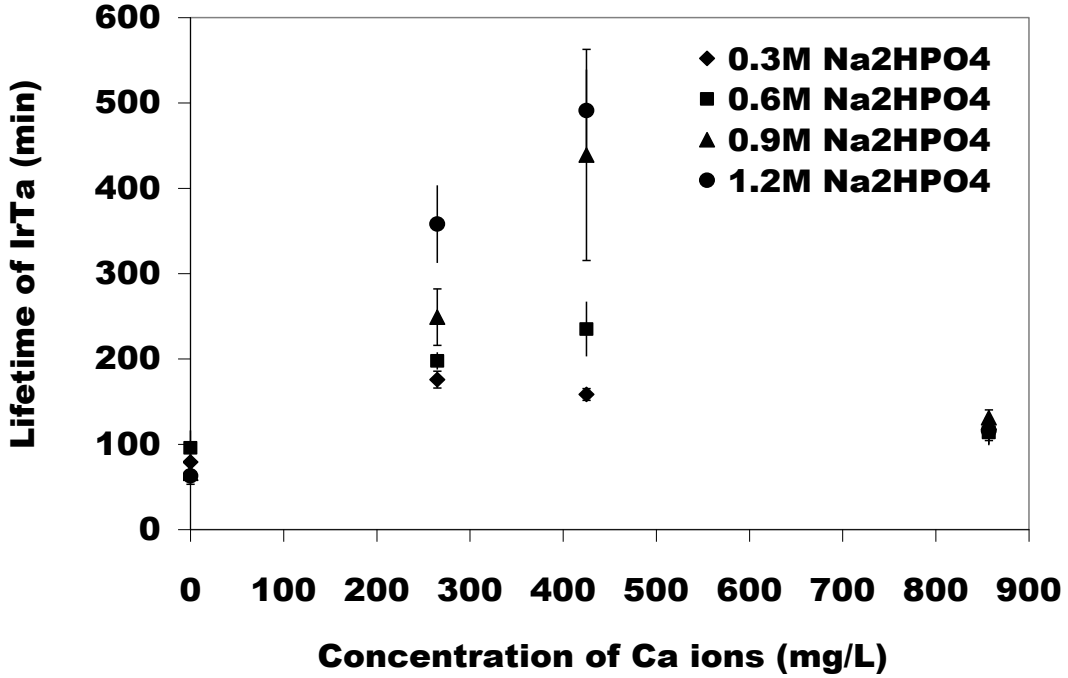

Figure 21 Effect of Ca and disodium hydrogen phosphate concentrations on IrO_2-Ta_2O_5 electrode lifetime at 1200 A/m^2, 0.026 M Cl^-, 0.1 Hz cycle.

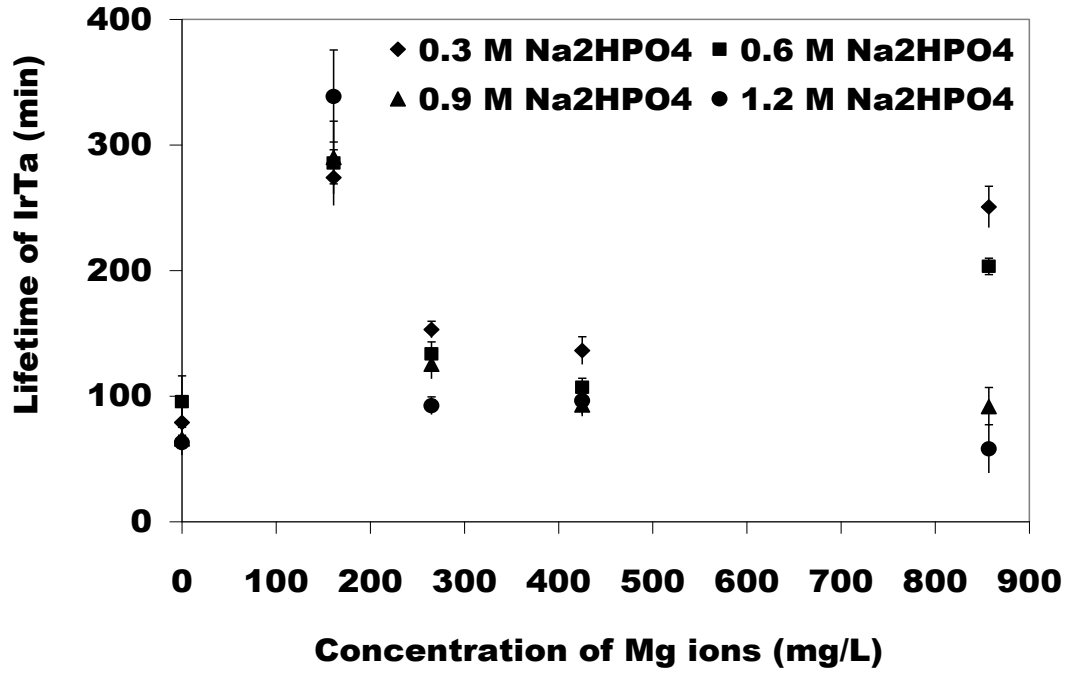

Figure 22 Effect of Mg and disodium hydrogen phosphate concentrations on IrO_2-Ta_2O_5 electrode lifetime at 1200 A/m^2, 0.026 M Cl^-, 0.1 Hz cycle.

Tested samples are specimens that have been operated for various periods of times under current reversal and hard water electrolysis conditions. First, the results from physical characterization will be presented, followed by the electrochemical characterization results.

3.2.4.1 X-ray Fluorescence (XRF) Analysis

XRF was employed to measure the quantity of metal constituents present in the fresh and tested CTEs. In XRF, the quantity of an element is related to the measured x-ray intensities. As no calibration curves existed, percentages were examined to determine if changes were occurring with time of operation.

The percent of the initial intensity of Ir, Ta and Ir/Ta are plotted against normalized time in Figures 23 to 25, respectively. As the times to failure were dramatically different in some supporting electrolytes, samples were operated to similar percentage of the failure time in each electrolyte. Thus, the results are plotted versus the normalized current reversal time (t) to the failure time (τ_f) in that particular electrolyte. The normalized time allows for a more uniform comparison of the CTEs to be made in the different electrolytes examined.

The initial percentage of XRF intensities for Ir and Ta are observed to be over 100% for some of the short time cycles in Figures 23 and 24. This observation seems to be as a result of the uneven spread of the IrTa coating on the Ti substrate. Even so, it is pretty clear that Ir and Ta intensities decrease with increasing normalized time (t/τ_f) in all the electrolytes.

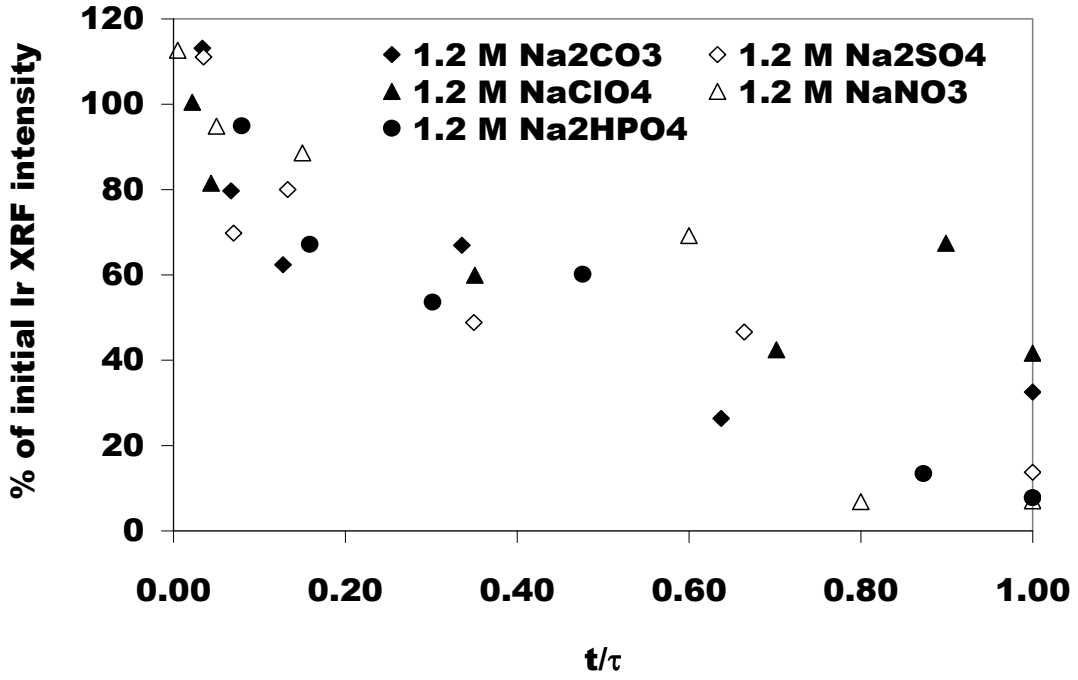

Figure 23 XRF values of % Ir vs t/τ for IrO_2-Ta_2O_5 anode in different electrolytes at 1200 A/m^2, 0.043 M NaCl, 0.1 Hz cycle.

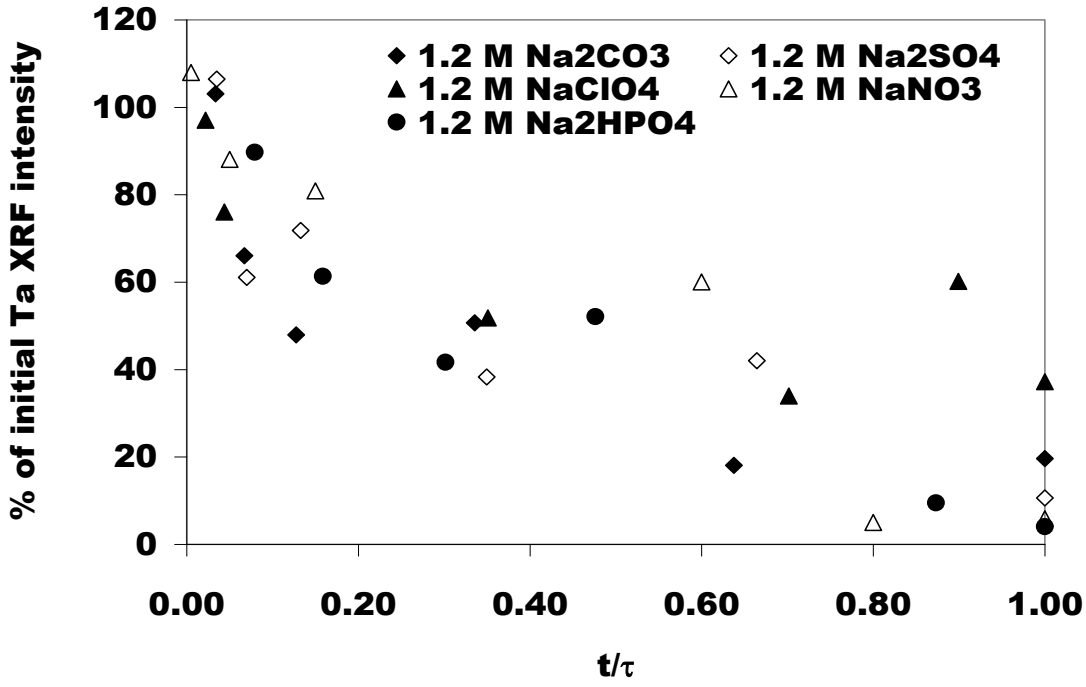

Figure 24 XRF values of % Ta vs t/τ for IrO_2-Ta_2O_5 anode in different electrolytes at 1200 A/m^2, 0.043 M NaCl, 0.1 Hz cycle.

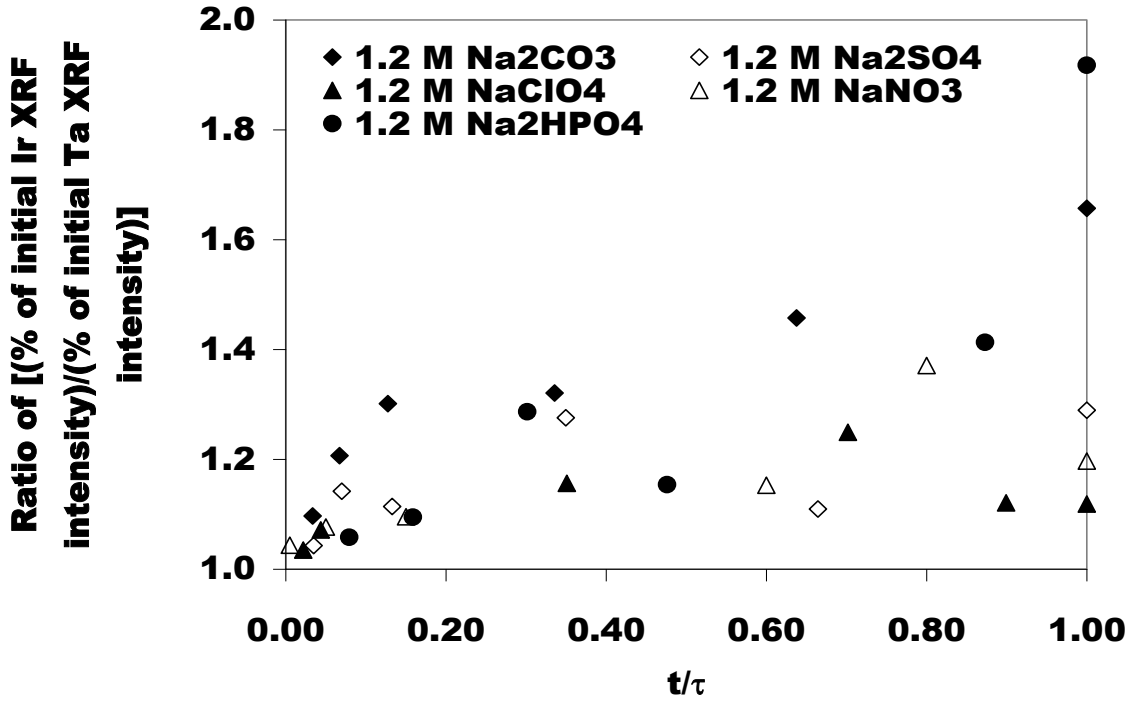

Figure 25 XRF values of Ir:Ta ratio vs t/τ for IrO_2-Ta_2O_5 anode in different electrolytes at 1200 A/m^2, 0.043 M NaCl, 0.1 Hz cycle.

This suggests that both Ir and Ta are dissolving. All of the electrolytes produce similar shaped curves; for example approximately 60 % of the Ir remains at approximately 40 % of the time to failure regardless of the supporting electrolyte. XRF intensities data for the fresh and tested samples appear to corroborate this theory.

Figure 25 shows the relative dissolution rate of Ir to Ta in the coating. Values greater than 1 indicate that Ta is consumed at a relatively faster rate that Ir in the IrTa coating at any given t/τ_f. Ta may be dissolving to a greater extent in some electrolytes (CO_3^{2-}) than others (ClO_4^-).

Finally, the scattered nature of the data near failure as observed in Figures 23 to 25, appears again to be due to uneven distribution of IrO_2-Ta_2O_5 coating on the Ti substrate of the electrodes examined. In some instances, tested samples reported higher intensities than the fresh samples analyzed. The problem may have been exacerbated as electrodes were sheared to 1 cm x 1 cm before use.

3.2.4.2 Energy Dispersive Spectroscopy (EDS) and Scanning Electron Microscopy (SEM) Analysis

3.2.4.2.1 EDS Examination of IrO_2-Ta_2O_5 from Current Reversal Electrolysis

Fresh IrTa electrode samples and IrTa samples operated for various times in current reversal electrolysis were also evaluated by EDS analysis. The EDS values for IrTa examined in the five electrolytes ($NaNO_3$, $NaClO_4$, Na_2CO_3, Na_2SO_4, and Na_2HPO_4) are presented in Table 6. The EDS results corroborate the XRF results in that Ir and Ta are dissolving. As current reversal time increases, the amounts of Ir and Ta in the IrO_2-Ta_2O_5 coated electrode decreases.

The ratio of Ir to Ta appear to corroborate the fact that Ta is consumed a little faster than Ir. Failure mechanism for the IrTa electrodes seems to start with dissolution of Ir and Ta, thus exposing the Ti substrate to the electrolyte for possible initiation of the passivation mechanism. The exposure of Ti is indicated by the increase in At % Ti with current reversal time. While oxygen values are reported, standardless EDS results are notoriously erroneous. The true values for oxygen are expected to be much higher as the coating is IrO_2-Ta_2O_5.

Table 6 EDS values from current reversal electrolysis for IrO_2-Ta_2O_5 anode in different electrolytes at 1200 A/m^2, 0.043 M NaCl, 0.1 Hz cycle.

Electrolyte	CR Time (min)	At % Ir	% Ir Error	At % Ta	% Ta Error	At % Ti	% Ti Error	At % O	% O Error	Ratio of Ir:Ta
$NaNO_3$	0	63.19	2.61	16.52	1.42	7.31	2.19	12.97	0.84	79:21
	5	58.92	2.95	13.74	1.52	10.06	3.05	14.74	1.07	81:19
	50	55.47	2.81	12.05	1.39	16.92	3.93	15.82	0.96	82:18
	150	51.49	2.78	8.18	1.44	20.63	3.23	16.61	1.30	86:14
	600	45.51	2.52	5.74	1.24	29.70	4.96	18.17	0.99	89:11
	800	7.21	1.07	1.37	0.46	53.73	9.96	36.14	1.29	84:16
	1392	5.74	1.14	0.93	0.53	55.76	9.56	35.76	1.15	86:14
$NaClO_4$	0	63.19	2.61	16.52	1.42	7.31	2.19	12.97	0.84	79:21
	5	57.55	2.90	15.33	1.60	8.66	2.81	15.83	1.08	79:21
	30	41.46	2.31	9.04	1.15	29.29	5.14	18.36	0.93	82:18
	80	46.45	2.43	10.68	1.24	23.09	4.47	17.81	0.96	81:19
	160	46.88	2.33	10.25	1.16	23.87	4.32	16.42	0.86	82:18
	205	38.88	2.27	8.00	1.10	28.78	5.22	21.10	1.02	83:17
	242	3.66	0.73	0.84	0.37	59.00	9.03	35.44	1.02	81:19
Na_2CO_3	0	63.19	2.61	16.52	1.42	7.31	2.19	12.97	0.84	79:21
	5	56.28	3.12	13.85	1.65	9.49	3.23	14.83	1.12	80:20
	10	50.42	2.62	10.86	1.30	18.28	4.06	15.42	0.94	82:18
	19	38.28	2.33	7.19	1.08	31.84	5.71	18.03	0.93	84:16
	50	30.49	2.45	4.18	1.15	41.65	5.04	17.64	0.97	88:12
	95	18.48	1.49	2.96	0.57	53.13	6.33	19.37	2.19	86:14
	205	10.48	1.95	1.33	0.70	61.57	7.24	25.48	1.03	89:11
Na_2SO_4	0	63.19	2.61	16.52	1.42	7.31	2.19	12.97	0.84	79:21
	5	61.27	2.98	15.74	1.61	7.94	2.66	14.38	1.03	80:20
	10	45.15	2.48	10.15	1.25	26.90	5.01	17.11	0.94	82:18
	19	51.25	2.57	11.74	1.31	20.08	4.13	16.31	0.94	81:19
	50	31.20	2.04	6.40	0.98	40.59	6.40	20.98	0.92	83:17
	95	31.50	2.05	6.47	0.99	39.73	6.33	21.15	0.93	83:17
	116	10.50	1.12	1.80	0.49	54.85	7.60	29.82	0.89	85:15
Na_2HPO_4	0	63.19	2.61	16.52	1.42	7.31	2.19	12.97	0.84	79:21
	5	59.57	3.18	15.46	1.72	7.83	2.86	13.87	1.09	79:21
	10	41.35	2.65	8.24	1.26	18.74	4.71	23.62	1.34	83:17
	19	40.02	2.55	7.75	1.20	28.40	5.29	19.85	1.09	84:16
	30	43.94	2.59	8.18	1.19	25.14	5.16	19.23	1.07	84:16
	55	10.36	1.32	1.25	0.49	55.06	9.06	31.08	1.08	89:11
	63	4.82	0.90	0.54	0.32	60.40	9.78	32.98	1.05	90:10

3.2.4.3 Scanning Electron Microscopic (SEM) Analysis of IrO_2-Ta_2O_5 Electrode

3.2.4.3.1 Characteristic Features of IrTa Anode

SEM images showing the surface morphology (micrograph A) and the coating thickness (micrograph B) for a fresh IrTa electrode are presented in Figure 26. The fresh IrTa coating (micrograph A) has dried mud micro-cracks on the surface interconnecting to form a network, surrounded by compact areas as expected from the literature [179-180]. The surface morphology exhibited by IrTa anode is characteristic of CTEs prepared by thermal decomposition. This surface feature [181-184] is suggested to be a result of the stresses generated by the differential thermal expansion and cooling of the coating. Micrograph B in the plot shows IrTa with an average coating thickness of 44 μm and the coating has a reported iridium loading as metal of 10.8 g/m^2.

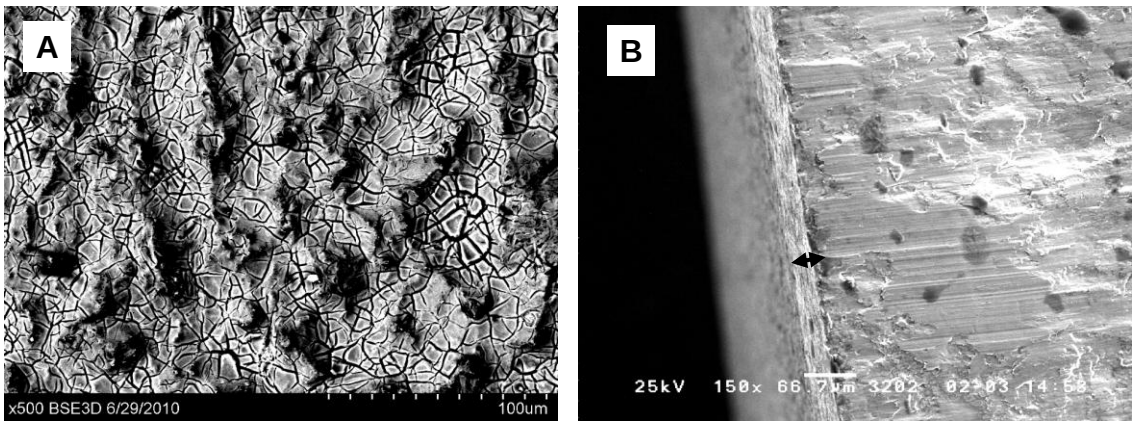

Figure 26 SEM images showing the surface a fresh IrTa sample (image A) and a cross section of IrTa coating to reveal its thickness (image B).

3.2.4.3.2 SEM Micrographs of IrO_2-Ta_2O_5 in Various Electrolytes under Current Reversal Electrolysis

SEM micrographs were taken to give a pictorial account of the IrTa electrode failure process with increasing current reversal time. Representative sample plots are shown in Figures 27 to 29. IrTa anode had the longest lifetime in $NaNO_3$ supporting electrolyte. The IrTa coating starts degrading extensively in nitrate ions in micrograph D (150 min) as seen in Figure 27. It appears micrographs F (800 min) and G (1392 min) for the most part are showing the Ti substrate. The observation shows that IrTa failure in nitrate ions was greatly influenced by coating dissolution. The XRF and EDS showed residual IrTa on the substrate after electrode failure, which seem to suggest that passivation may have likely occurred.

IrTa had the shortest lifetime in Na_2HPO_4 electrolyte. And as revealed in Figure 28, extensive coating degradation started at micrograph C (10 min). It appears the Ti substrate was exposed from micrographs E (30 min) to G (63 min) the failure point. Coating consumption, it appears was highly influential in IrTa failure in hydrogen phosphate ions.

The SEM images shown in Figures 27 to 29 seem to support the theory that electrode degradation is caused by dissolution and then passivation. This dissolution process is particularly evident in Figure 29 for Na_2SO_4 electrolytes where the micrographs appear to show a gradual coating removal prior to electrode failure.

The SEM results seem to corroborate the XRF and EDS results for IrTa electrode examined under current reversal electrolysis in the five electrolytes. Failure of IrTa

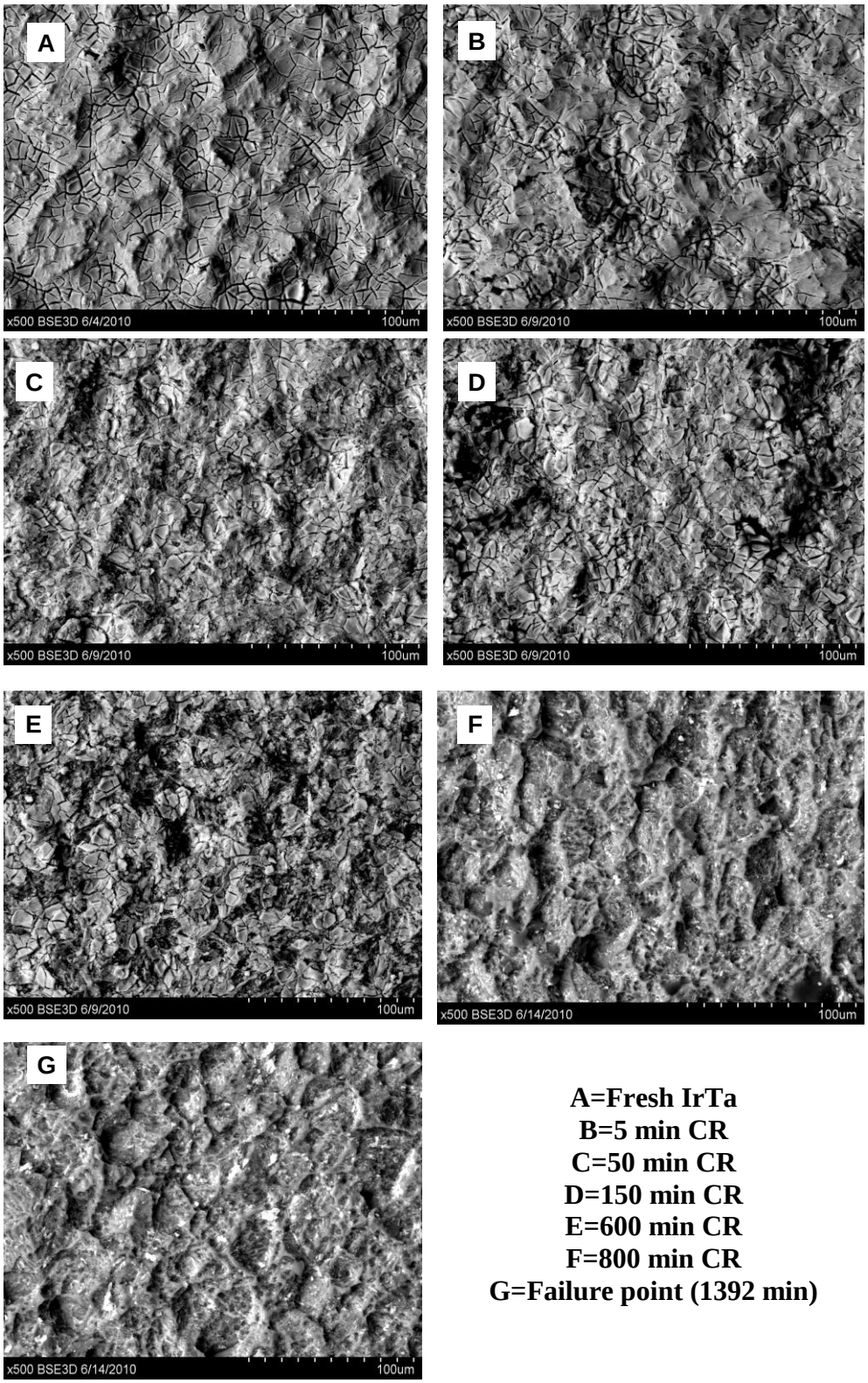

Figure 27 SEM micrographs of IrO_2-Ta_2O_5 as a function of operation time in 1.2 M $NaNO_3$ at 1200 A/m^2, 0.043 M NaCl, 0.1 Hz cycle.

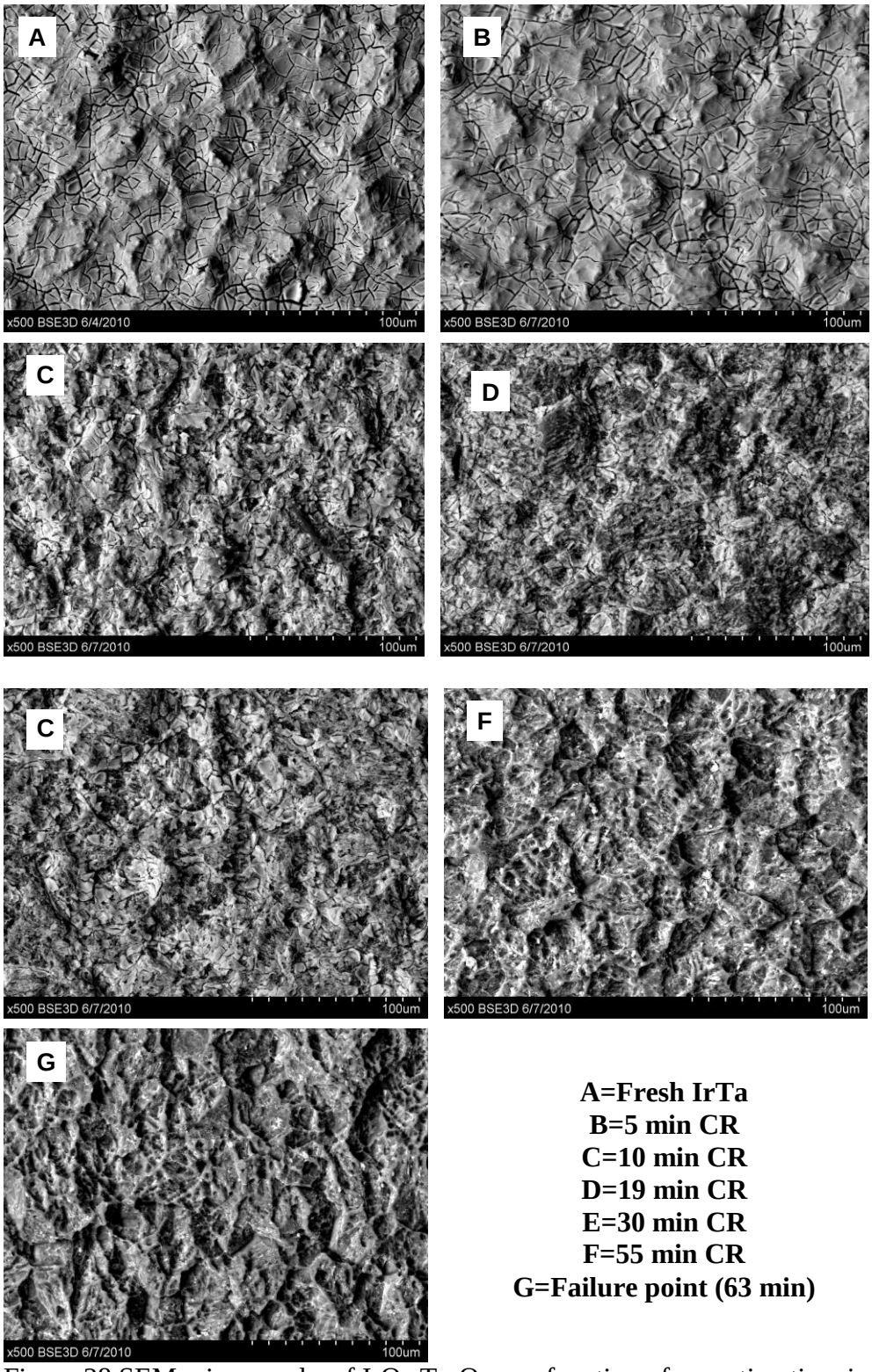

Figure 28 SEM micrographs of IrO_2-Ta_2O_5 as a function of operation time in 1.2 M Na_2HPO_4 at 1200 A/m^2, 0.043 M NaCl, 0.1 Hz cycle.

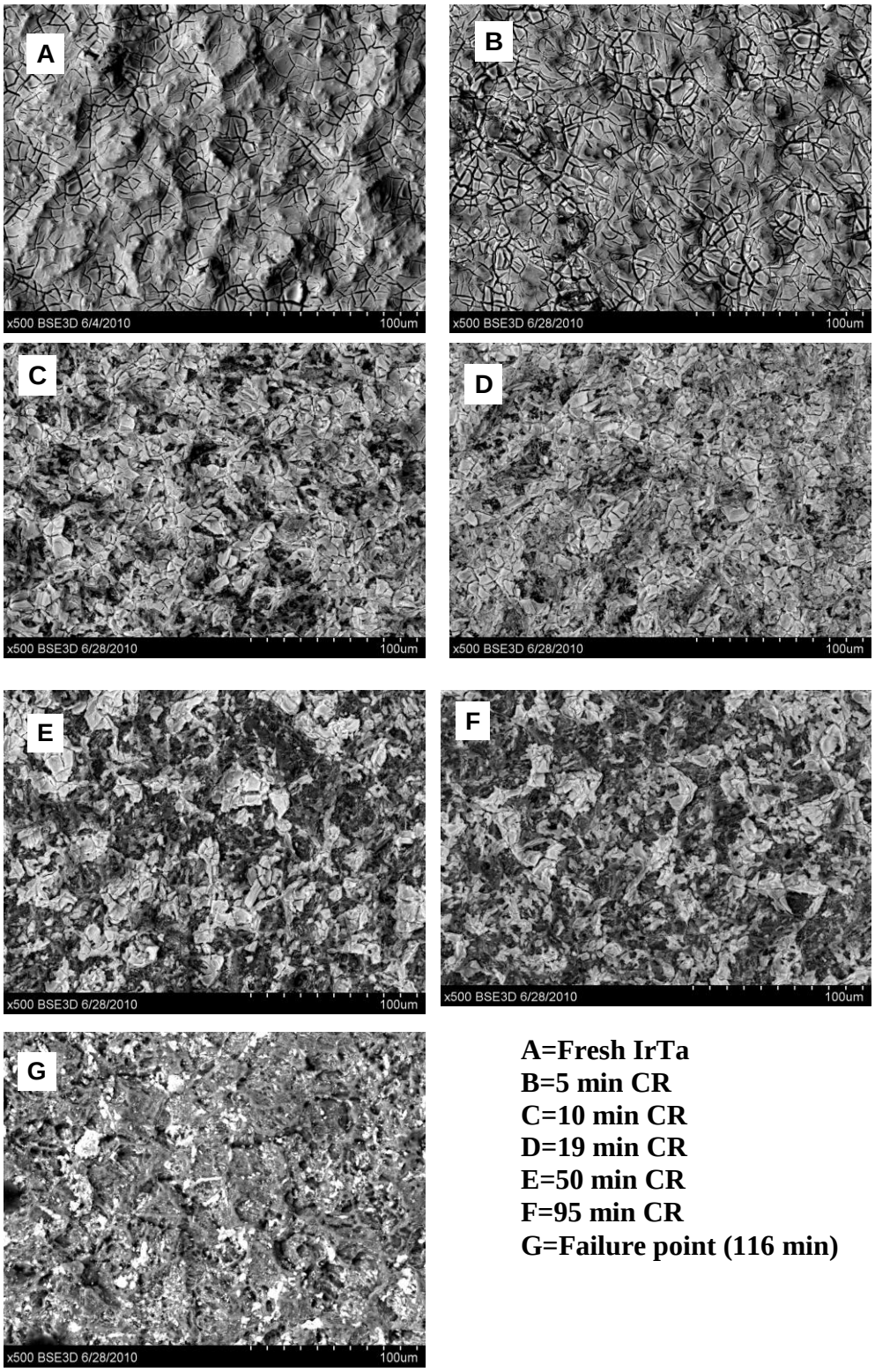

A=Fresh IrTa
B=5 min CR
C=10 min CR
D=19 min CR
E=50 min CR
F=95 min CR
G=Failure point (116 min)

Figure 29 SEM micrographs of IrO_2-Ta_2O_5 as a function of operation time in 1.2 M Na_2SO_4 at 1200 A/m^2, 0.043 M NaCl, 0.1 Hz cycle.

electrode in the electrolytes appears to be caused by the systematic dissolution of Ir and Ta from the coating. The electrolyte in the electrolysis cell is then able to make contact with the exposed surface area of the Ti substrate, subsequently causing deactivation of the electrode by the formation of a passivating layer at the substrate/coating interface.

3.2.4.3.3 SEM and EDS Analysis of IrO_2-Ta_2O_5 in Hard Water from Chronopotentiometry

CTEs investigated were expected to have shorter lifetimes in the hard water tests than in the current reversal electrolysis tests (without hard water ions). However, the electrodes appear to last longer in the presence of Ca and Mg ions for certain conditions. Analysis by EDS of IrTa electrode indicated that Ca and Mg were not deposited during the hard water experiments at current reversal cycle frequency of 0.1 Hz (10 seconds).

Chronopotentiometry was therefore used to determine whether or not Ca or Mg was deposited on the CTEs during the hard water tests, and at what time does deposition occur. In the determination of Ca or Mg deposition during the hard water experiments, IrTa was examined in 1.2 M $NaNO_3$ at different chronopotentiometric times, in the presence of 857 mg/L Ca and Mg ions. The chronopotentiometric time was increased in a stepwise fashion. The At % of Ca and Mg measured on IrTa using EDS versus time are shown in Figure 30. As the amounts of Ca and Mg deposited are less 5 % and no visual evidence was detected, the chronopotentiometric experiments showed Ca and Mg deposits did not occur in nitrate electrolytes within 25 minutes of direct electrolysis. This seems to confirm that Ca and Mg deposits were not forming during the hard water current reversal experiments.

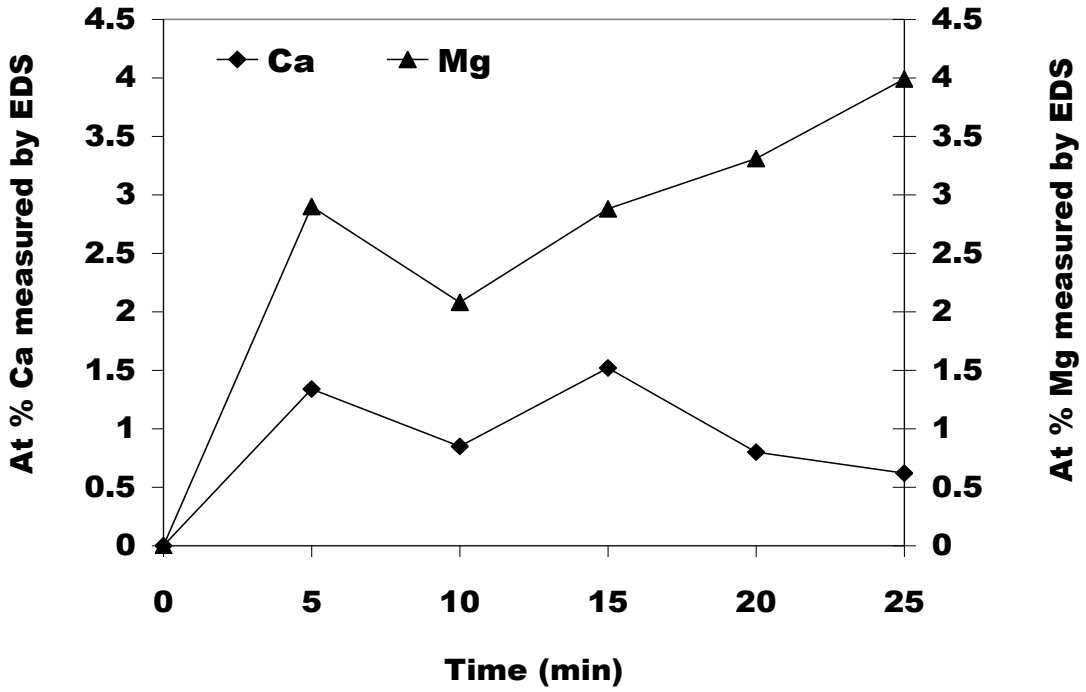

Figure 30 EDS values for Ca and Mg deposition from chronopotentiometry on IrTa electrode in 1.2 M $NaNO_3$, 857 mg/L Ca and Mg ions, -1200 A/m^2, 0.026 M Cl^-.

3.2.5 Electrochemical Charaterization

3.2.5.1 Cyclic Voltammetry (CV)

The voltammetric behavior of IrTa electrode was examined in the five electrolytes with sodium salts, before (fresh electrode), after various amounts of current reversal testing, and after electrode failure. CV voltage limits were selected such that gas (Cl_2, O_2, and H_2) evolution did not occur. Typical voltammograms for IrTa samples are given in Figure 31A. Voltammetric charge determined from the CV curves is plotted versus current reversal time in Figure 31B. Voltammograms were also determined for IrTa in the other supporting electrolytes. These voltammograms showed similar behavior and their

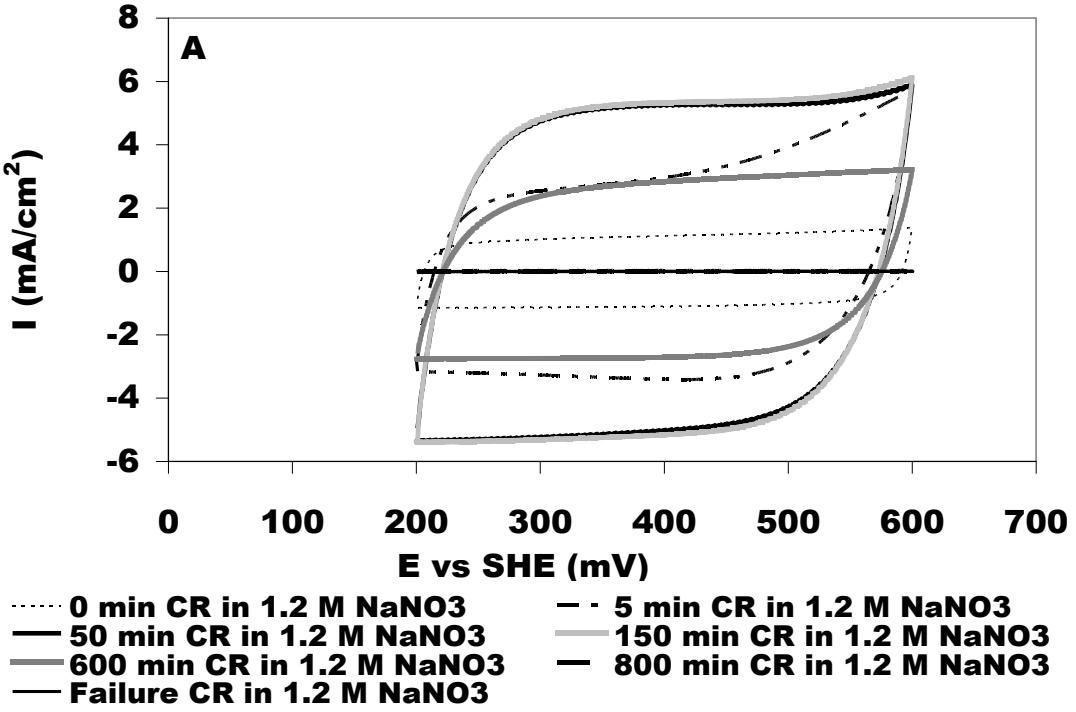

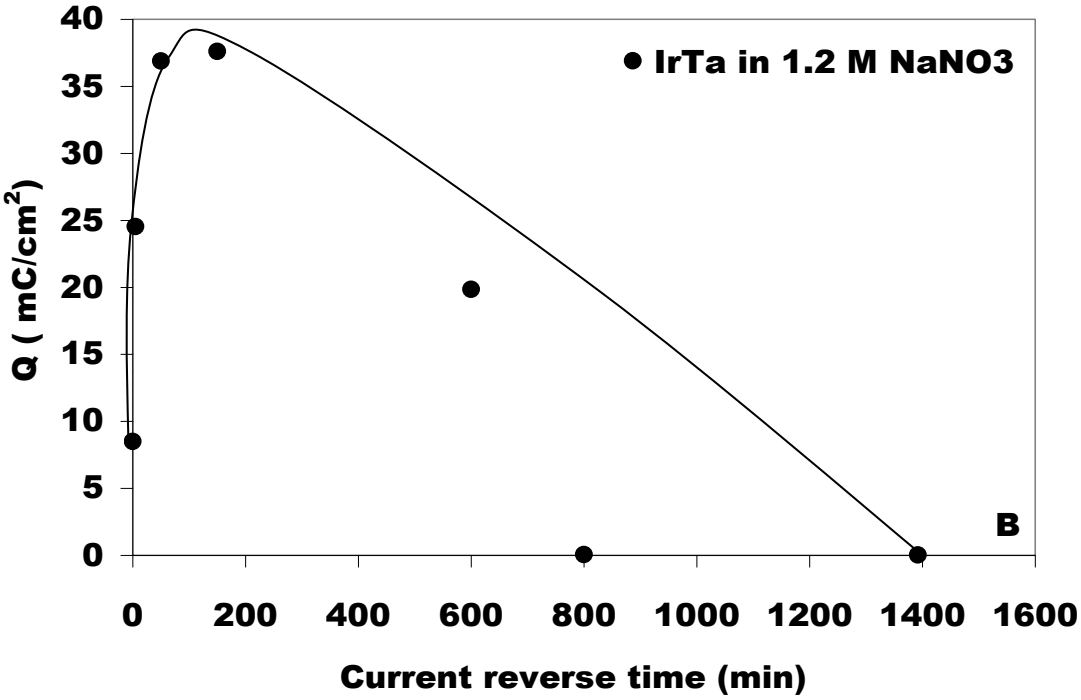

Figure 31 Cyclic voltammograms and charge plots (A) Cyclic voltammograms at 100 mV s^{-1} in 1.2 M $NaNO_3$, 0.043 M NaCl (B) Charge vs current reversal time for IrO_2-Ta_2O_5.

curves show similar trends as can be seen in Figures 33A and 33B and 34A and 34B, respectively.

The CV curves demonstrate the pseudocapacitive behavior of the IrTa oxide electrode [185-189], changing reversibly as the direction of potential cycling is changed. This is supported by the broad nature of peak currents exhibited by all the curves. The peaks observed between the potentials 200 to 400 mV at the different current reversal times are characteristic of solid state redox transition of Ir(III)/Ir(IV) [185-189]. From Figure 32A, it can be seen that as current reversal time increases the current densities (between 200- 400 mV) for individual CV curves also increases to a maximum (around 360 mV and 5.24 mA/cm^2) before declining. Furthermore, from Figure 31B, charge (Q) increases to a maximum (150 minutes and 38 mC/cm^2) value before declining with increasing current reversal time.

Previous research has shown the charge is directly related to the effective surface area of the electrodes coating [185-189]. Thus, the charge is seen to decrease as the number of active sites (effective area) on the coating decreases. Similarly, the pseudocapacitance of the coating which also depends on faradaic charge transfer reactions (charging effects at the coating interface) occurring on the high area IrTa surface/electrolyte interface also rises to a maximum and then declines. This is consistent with reports in the literature [189] that pseudocapacitive response reduces drastically as either Ir or Ru content in CTEs decreases below 10 atomic percent.

This seems to explain the profile of the curves shown in Figure 31A. The pseudocapacitance behavior observed in the plots can further be explained by viewing the

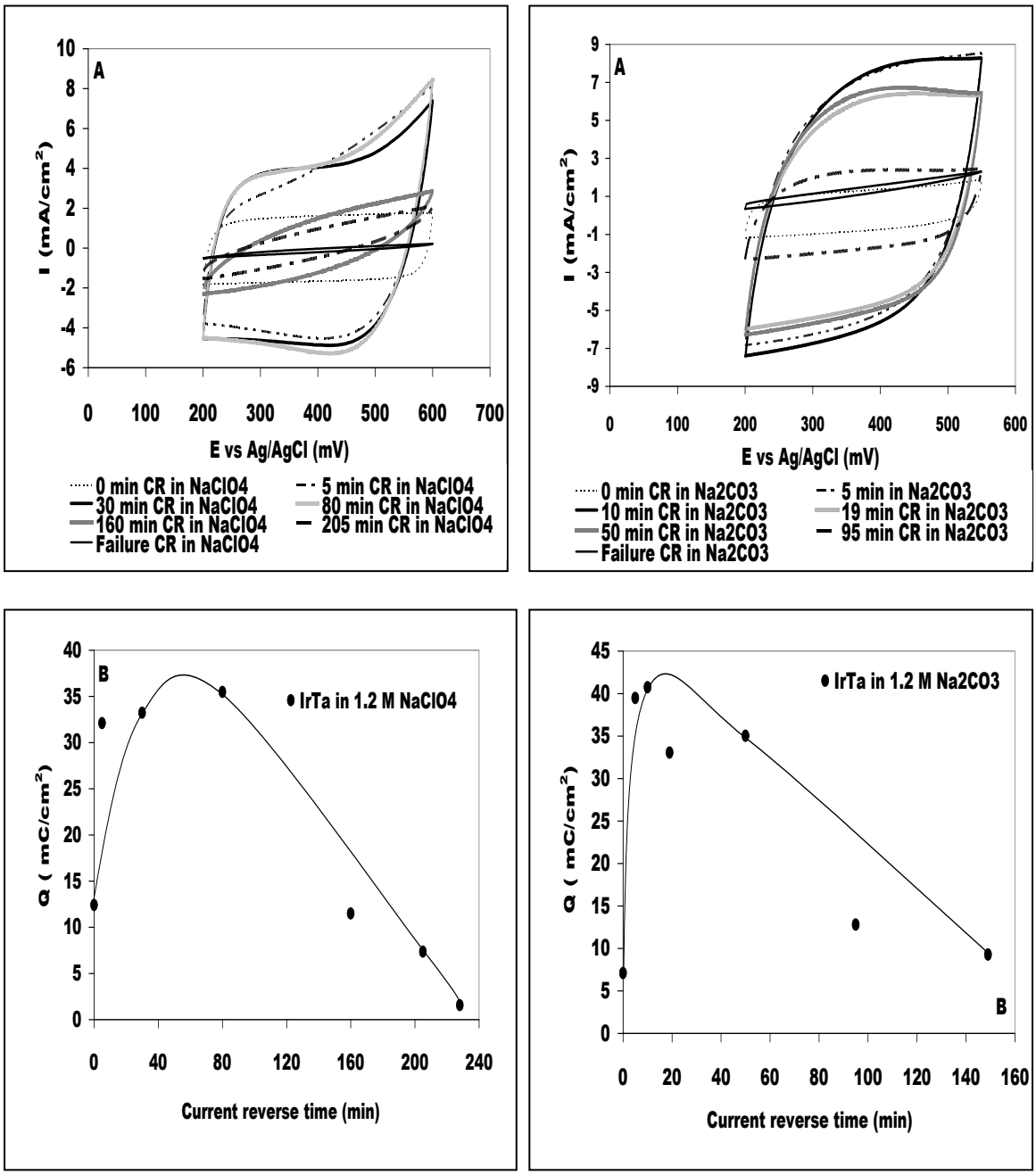

Figure 32 Cyclic voltammograms and charge plots. (A) Cyclic voltammograms at 100 mV s^{-1} and (B) Charge vs current reversal time for IrO_2-Ta_2O_5 in 1.2 M $NaClO_4$, and Na_2CO_3, 1200 A/m^2, 0.043 M NaCl, 0.1 Hz cycle.

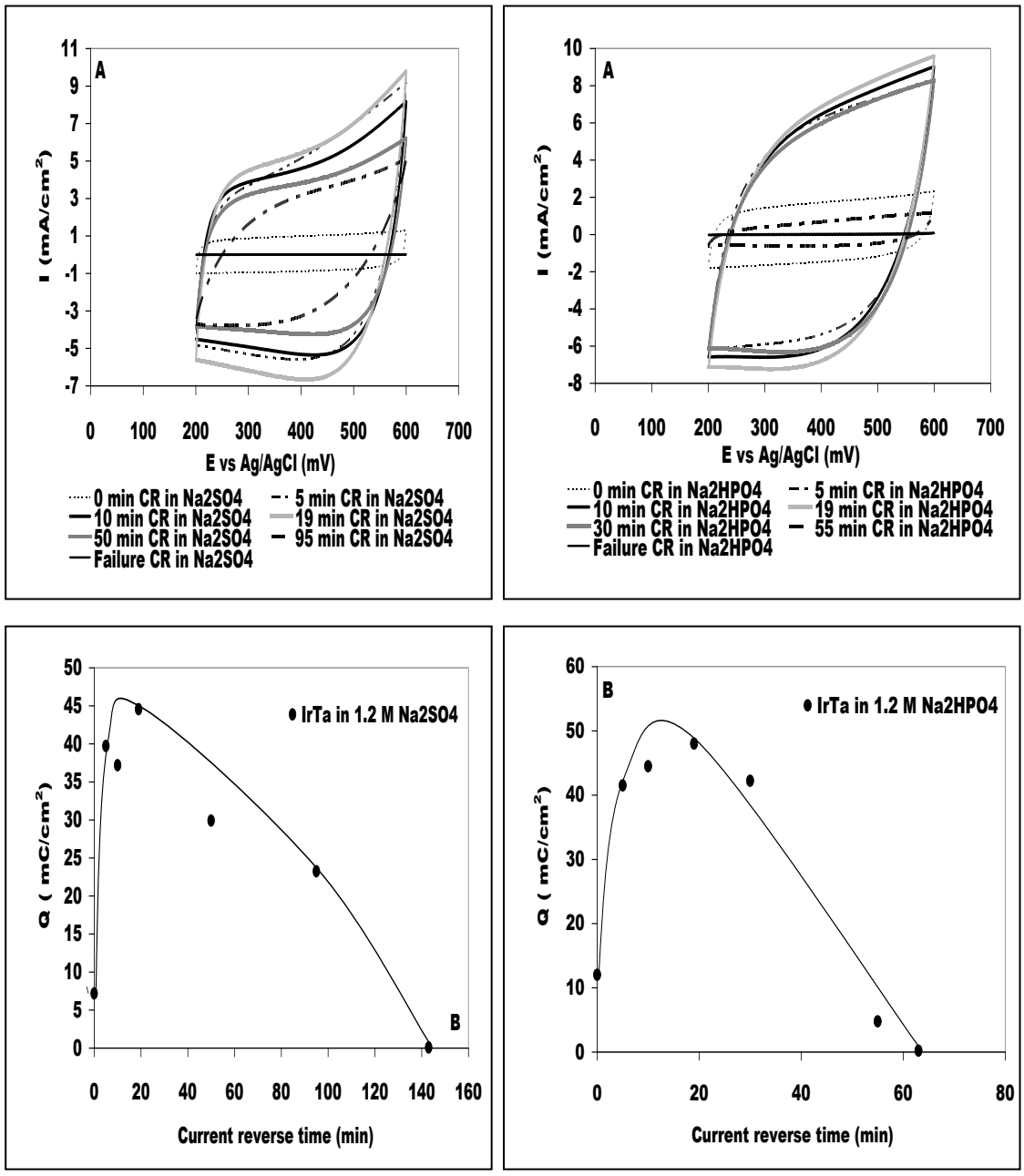

Figure 33 Cyclic voltammograms and charge plots (A) Cyclic voltammograms at 100 mV s^{-1} and (B) Charge vs current reversal time for IrO_2-Ta_2O_5 in 1.2 M Na_2SO_4, and Na_2HPO_4, 1200 A/m^2, 0.043 M NaCl, 0.1 Hz cycle.

IrTa coating/electrolyte interface acting as a double layer that stores charges, thus behaving as a capacitor (pseudocapacitor). As current reversal time was increasing voltammetric charge exchanged and/or accumulated at the interface also increased until effective coating area was reduced by coating dissolution and/or coating coverage, then charge declines. This will be discussed in detail in Chapter 4.

3.3 Ruthenium Dioxide-Titanium Dioxide (RuO_2-TiO_2) Electrode

The RuTi electrode was another CTE studied. It was examined in similar fashion as the IrTa electrode. RuTi was examined under current reversal and hard water electrolysis conditions. Representative samples of cell voltage versus time plots of RuTi electrode for accelerated lifetime tests under current reversal and hard water conditions are depicted in Figures 34 and 35. As with the IrTa electrode, three regions of cell voltage changes are also observed for RuTi electrode as can be seen in Figure 34. The first region (I) involves a drop in the initial cell voltage after each current reversal. This is followed by the second region (II) where voltage rises in a slow constant fashion to a maximum, and the third region (III) is when the voltage escalates indicating electrode failure.

As mentioned previously, the bands observed in the cell voltage time plots is believed to be due to pseudocapacitance effects and will be discussed in Chapter 4.

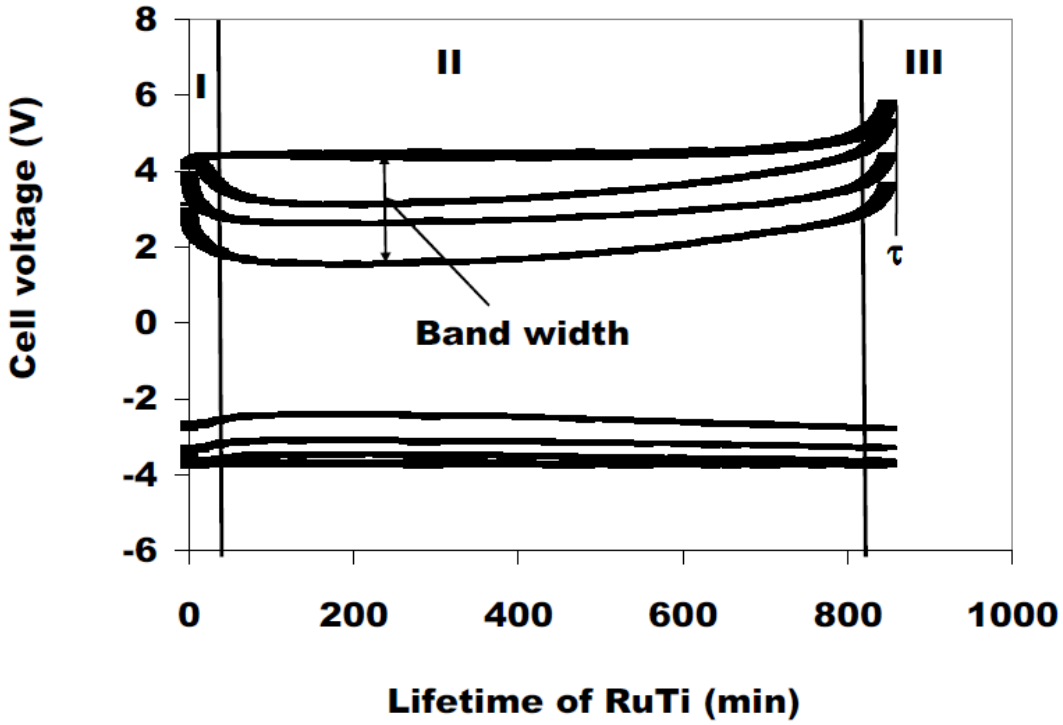

Figure 34 Cell voltage vs. time for RuO_2-TiO_2 electrode at 1200 A/m^2, 1.2 M Na_2HPO_4, 0.043 M NaCl, 0.1 Hz reversal frequency.

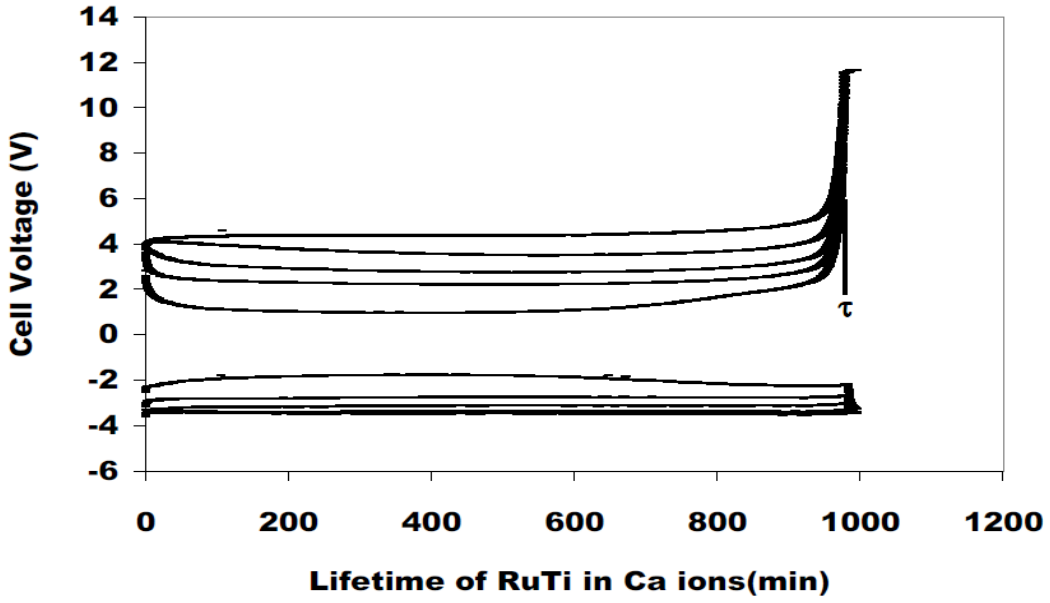

Figure 35 Cell voltage vs. time for RuO_2-TiO_2 electrode at 1200 A/m^2, 857 mg/L Ca ions, 1.2 M Na_2HPO_4, 0.026 M Cl^-, 0.1 Hz reversal frequency.

3.3.1 Effects of Current Reversal Electrolysis Parameters on Lifetimeof RuO_2-TiO_2 Electrode

3.3.1.1 Current Density

The influence of current density on RuTi electrode lifetime was examined in sodium sulfate. RuTi was studied at the same current densities selected as IrTa.The results of the investigation are presented in Figure 36. As can be seen from the plot the lifetime of RuTi is seen to increase as current density decreases. This trend is similar to the observation made for IrTa. The lifetime of RuTi was higher than IrTa at the three current densities examined in sulfate ions.

3.3.1.2 Current Reversal Frequency

RuTi was examined at the same four reversal cycle frequencies as IrTa in sodium sulfate. The relationship between RuTi lifetime and reversal cycle frequency is shown in Figure 37. As can be seen from the plot the lifetime of RuTi is observed to increase as reversal cycle frequency decreases, which is similar to the observation made for the IrTa electrode. The RuTi anode life was longer than IrTa lifetime at three (10, 50 and 100 seconds) of the four reversal cycle times examined. When the two electrodes were examined at 30 minutes reversal cycle time sulphate ions, IrTa anode life was longer than RuTi lifetime. Detailed comparison of RuTi and IrTa lifetimes will be made in Section 3.4.

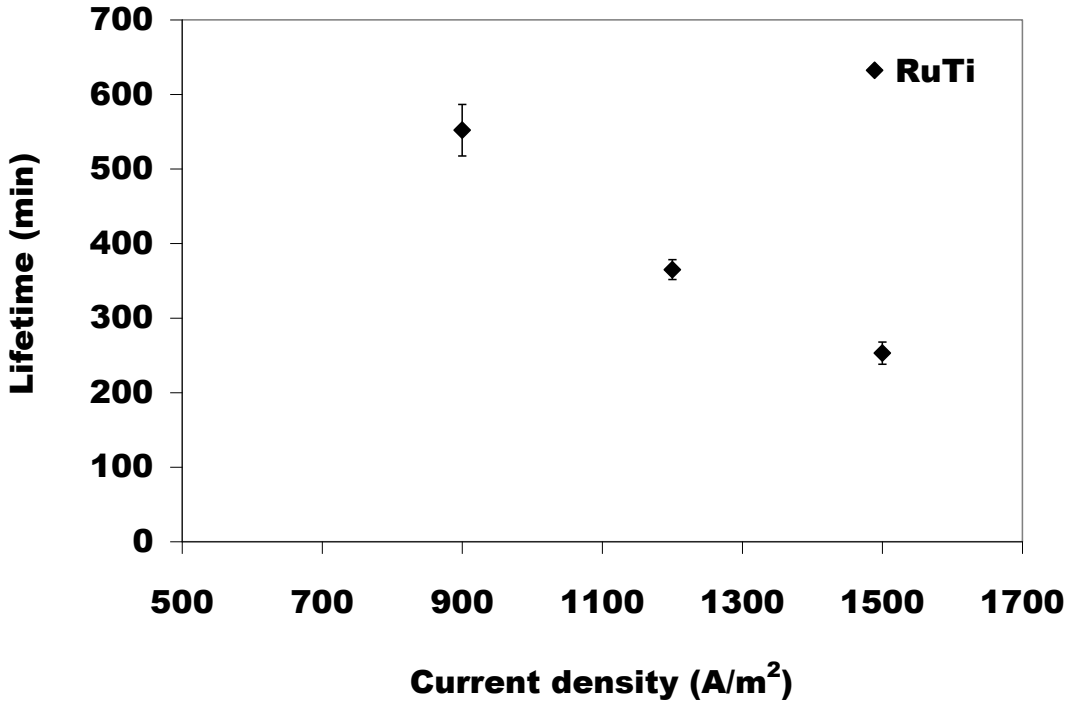

Figure 36 Effect of current density on RuO_2-TiO_2 electrode lifetime coating at 900, 1200 and 1500 A/m^2, 1.2 M Na_2SO_4, 0.043 M NaCl, 0.1 Hz reversal frequency.

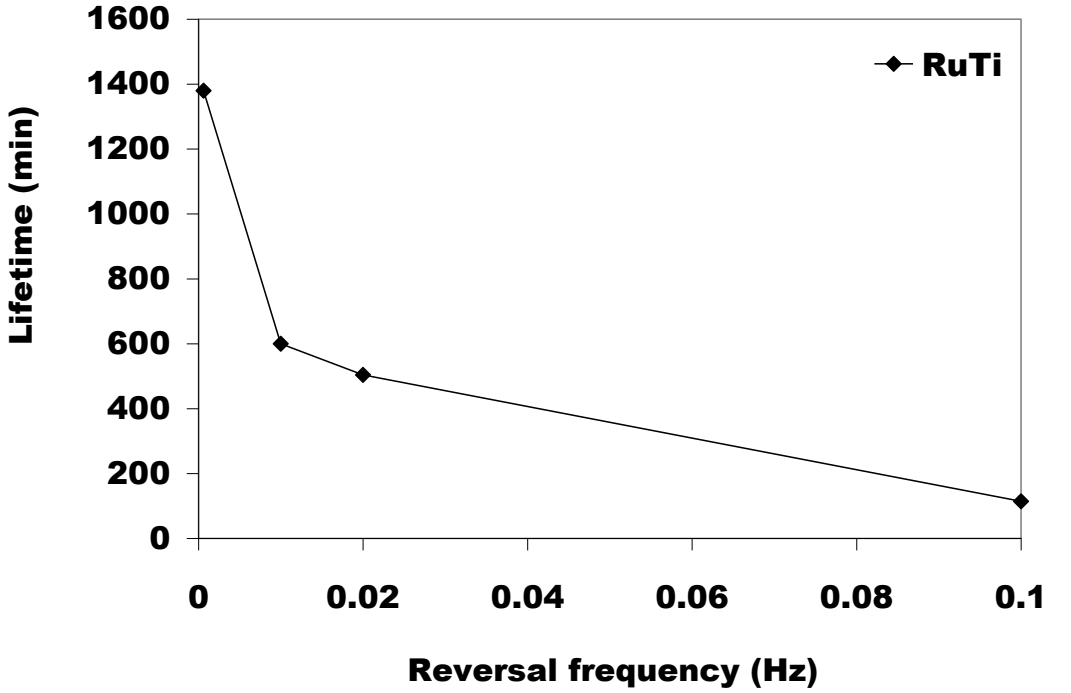

Figure 37 Effect of current reversal cycle time on RuO_2-TiO_2 electrode lifetime at 1200 A/m^2, 1.2 M Na_2SO_4, 0.043 M NaCl.

3.3.1.3 Sodium Chloride Concentration

The influence of sodium chloride concentration seems not to affect RuTi lifetime as seen in Figure 38. The concentration of NaCl used in the tests seems to be too low to significantly affect RuTi life.

3.3.2 Effect of Electrolyte Composition and Concentration

RuTi electrode was examined in the same electrolytes and at the same concentrations as was IrTa electrode. RuTi has the longest lifetime in higher concentrations of Na_2HPO_4 electrolyte as shown in Figure 39. The lifetime of RuTi increased with increasing hydrogen phosphate concentration. Lifetime decreases with increasing carbonate and perchlorate concentrations. Lifetime does not appear to change as a function of concentration for nitrate and sulfate ions. It is obvious that electrolyte composition and concentration affects the lifetime of RuTi anode in three out of the five electrolytes investigated. These trends are generally not the same as IrTa. For example, IrTa had the longest lifetime in nitrate ions, while RuTi anode had the longest lifetime in hydrogen phosphate ions.

3.3.3 Effect of Water Hardness on Lifetime of RuO_2-TiO_2

The influence of electrolyte composition and concentrations changes, and hard water composition and concentrations (Ca and Mg ions) appear not to affect the lifetime of RuTi electrode significantly. For this reason the results presented are for instances where trends were observed.

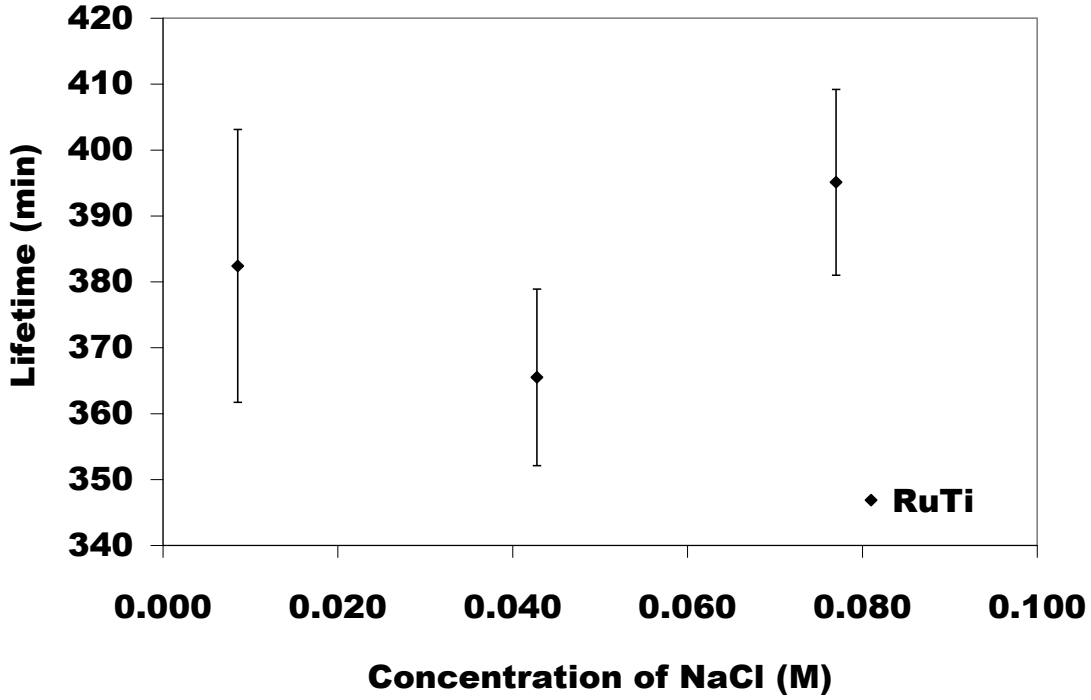

Figure 38 Effect of sodium chloride concentration on RuO_2-TiO_2 electrode lifetime at 1200 A/m^2, 1.2 M Na_2SO_4, 0.1 Hz.

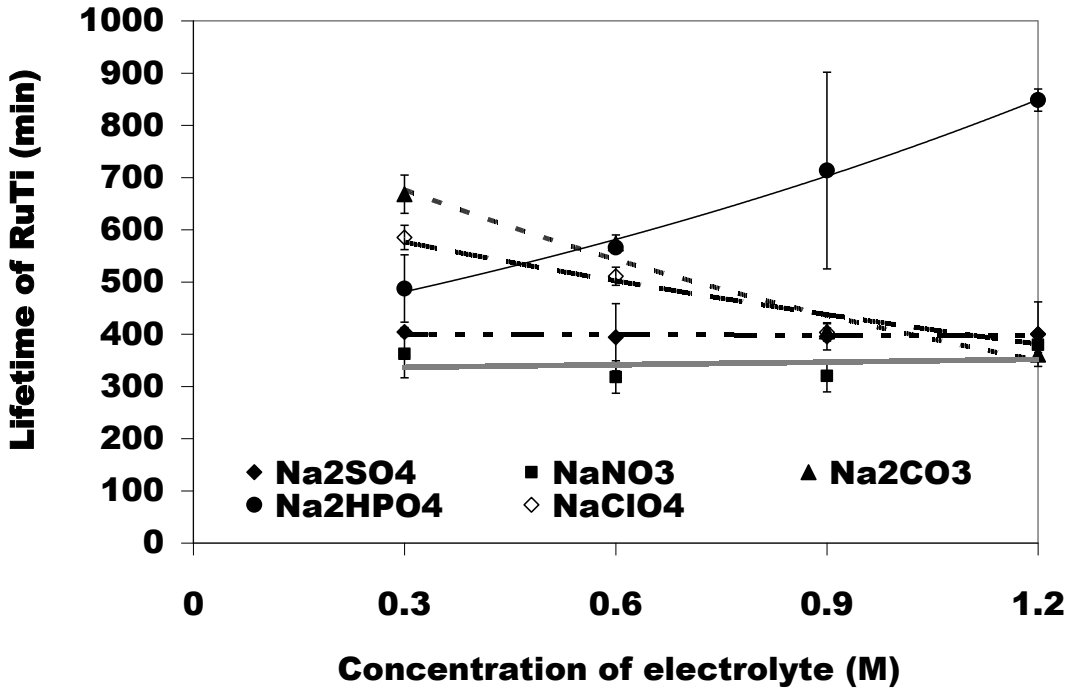

Figure 39 Effect of electrolyte composition and concentration on RuO_2-TiO_2 electrode lifetime at 1200 A/m^2, 0.043 M NaCl, 0.1 Hz cycle

3.3.3.1 Effect of Calcium Ions on RuO_2-TiO_2 Lifetime in $NaNO_3$

A representative sample plot of the effects of Ca and sodium nitrate on RuTi lifetime is displayed in Figure 40. The plot seem to indicate that nitrate and Ca ions affect RuTi life but not in a distinct manner. After an initial decrease in RuTi life from 0 to 265 mg/L Ca ions, lifetime then appears to increase with increasing Ca ions concentration. The dependence of RuTi anode life on nitrate ions at the different Ca hardness examined appears not to follow a consistent trend.

3.3.3.2 Effect of Calcium Ions on RuO_2-TiO_2 Lifetime in $NaClO_4$

The influence of Ca and perchlorate ions on RuTi lifetime is presented in Figure 41. In general, lifetime of RuTi appears to increase from 0 to 265 mg/L Ca, after which lifetime seem to decrease with increasing Ca concentration. Perchlorate ions concentration appears not to affect RuTi lifetime in a distinct manner.

3.3.3.3 Effect of Magnessium Ions on RuO_2-TiO_2 Lifetime in Na_2HPO_4

The relationship between Mg, hydrogen phosphate ions concentration and the lifetime of RuTi is displayed in Figure 42. Lifetime of RuTi appear to decrease as a function of Mg hardness. The influence of hydrogen phosphate ions on RuTi lifetime does not show a clear trend.

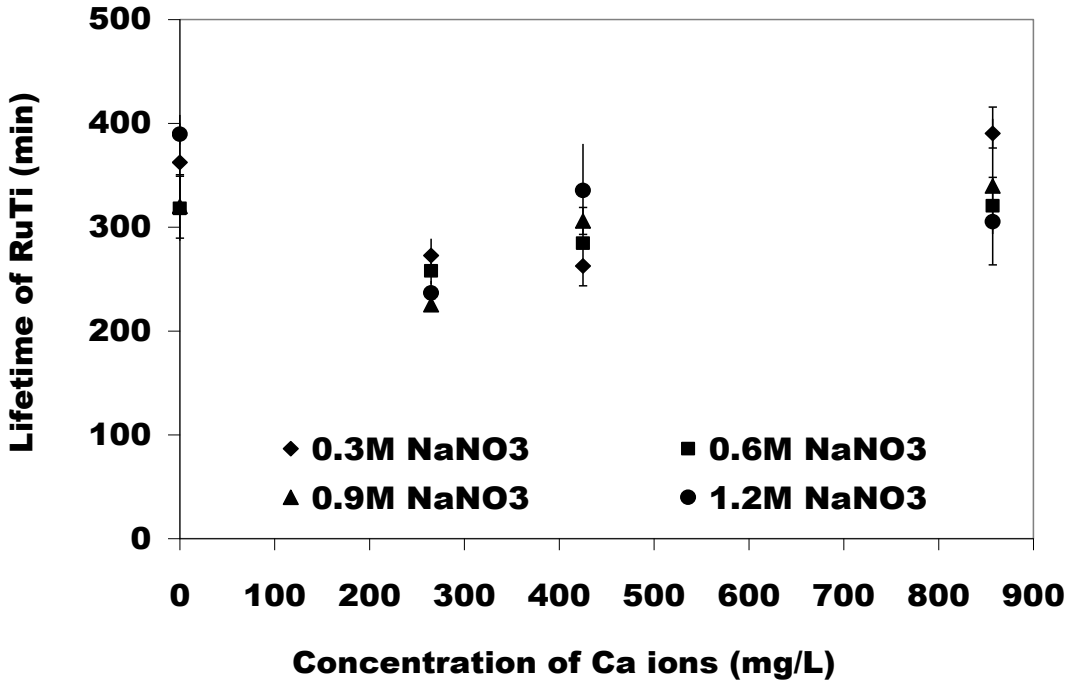

Figure 40 Effect of Ca and sodium nitrate concentrations on RuO_2-TiO_2 electrode lifetime at 1200 A/m^2, 0.026 M Cl^-, 0.1 Hz cycle.

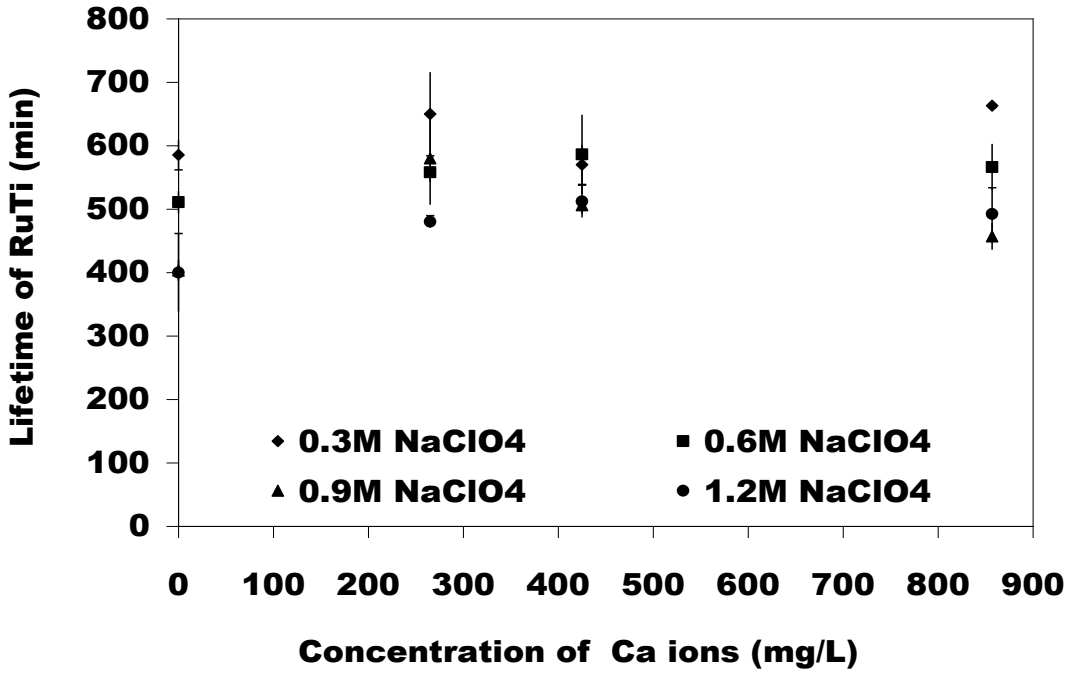

Figure 41 Effect of Ca and sodium perchlorate concentrations on RuO_2-TiO_2 electrode lifetime at 1200 A/m^2, 0.026 M Cl^-, 0.1 Hz cycle.

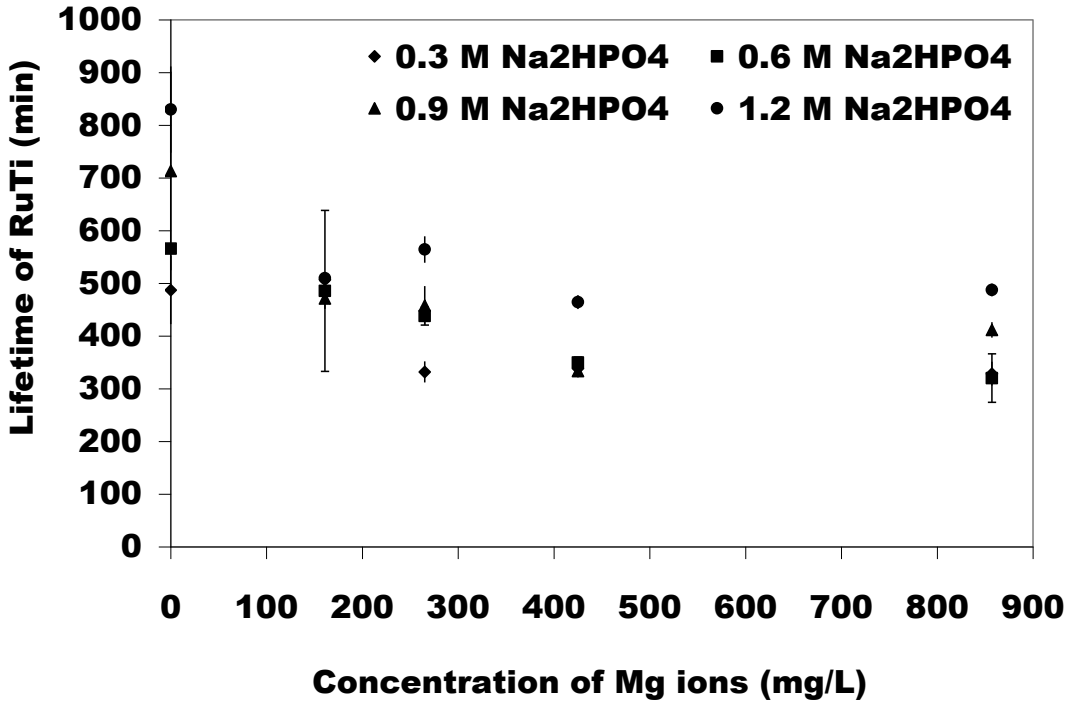

Figure 42 Effect of Mg and disodium hydrogen phosphate concentrations on RuO_2-TiO_2 electrode lifetime at 1200 A/m^2, 0.026 M Cl^-, 0.1 Hz cycle.

3.3.4 Physical Characterization

3.3.4.1 XRF Analysis

XRF was also employed to measure the quantity of metal constituents in the fresh and tested RuTi electrode. Percentages of initial intensities were examined to determine if changes were occurring with time of operation. As with the IrTa electrode, the RuTi electrode samples were also operated to similar percentage of the time to failure as the failure times were quite different in some of the supporting electrolytes. Hence, the results are plotted versus the normalized current reversal time. The percent of initial intensity of Ru and Ti plotted against the normalized time are given in Figures 43 and 44.

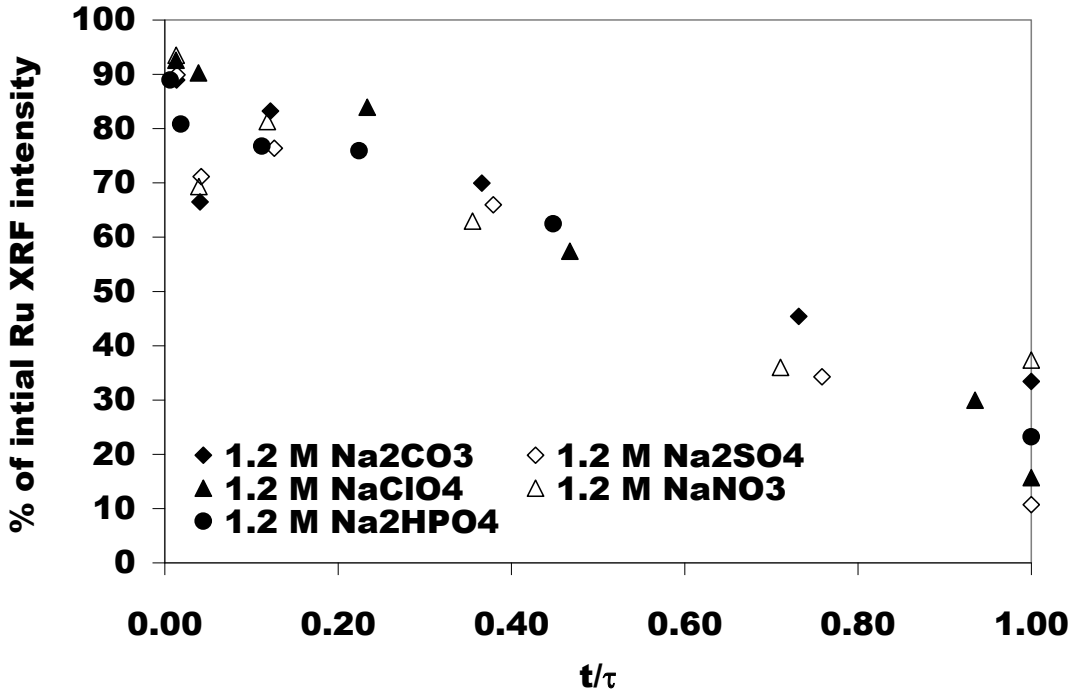

Figure 43 XRF values of % Ru vs t/τ for RuO_2-TiO_2 anode in different electrolyte at 1200 A/m^2, 0.043 M NaCl, 0.1 Hz cycle.

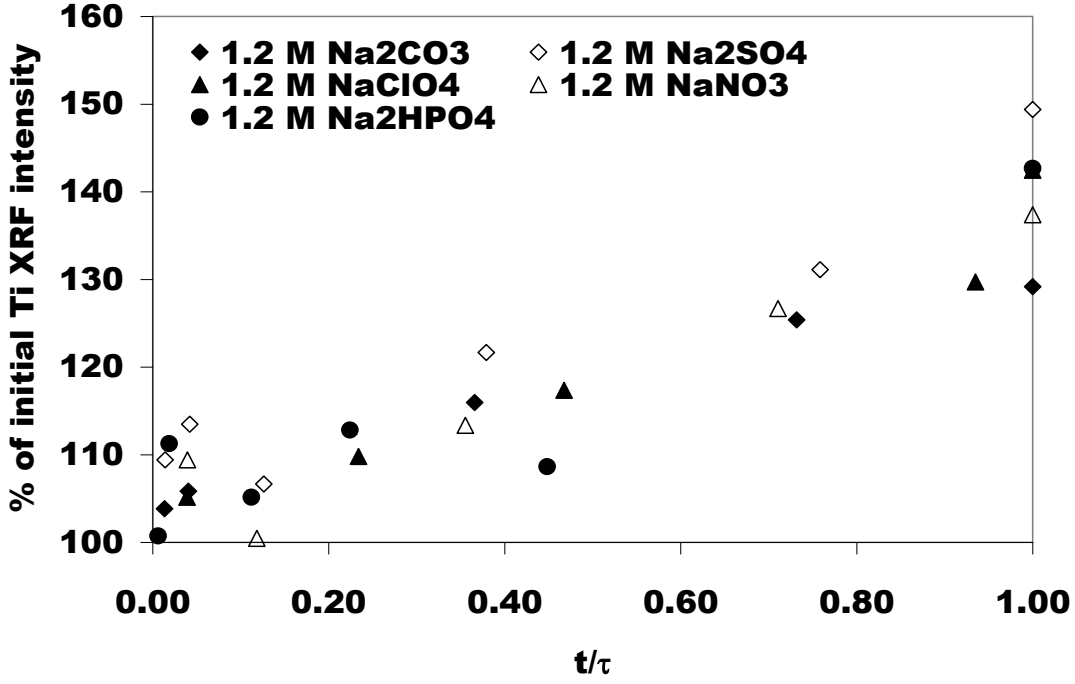

Figure 44 XRF values of % Ti vs t/τ for RuO_2-TiO_2 anode in different electrolytes at 1200 A/m^2, 0.043 M NaCl, 0.1 Hz cycle.

The percentage of initial Ru in RuTi is seen to decrease with increasing normalized current reversal time (t/τ). Where t is the current reversal time at which the electrode (RuTi) was examined and τ is the time to failure (τ_f) for the electrode in that particular electrolyte. This indicates that Ru is dissolving at the same rate with respect to the fraction of time to failure. Again, all the electrolytes produce similar shaped curves as observed for IrTa. For instance, approximately 60 % of the Ru remains at 40 % of the time to failure regardless of the supporting electrolyte.

Interestingly, the percent of initial Ti in RuTi is seen to be increasing with increase in t/τ. The over 100 % values recorded for Ti seems to indicate exposure of the Ti substrate to the electrolyte after dissolution has occurred. The exposure obviously influences electrode failure by the formation of a passivating layer at the substrate/coating interface as electrolyte makes contact with the substrate.

In summary, even though the times to failure appear to be different for RuTi in the different electrolytes, the curves seem to follow the same trend; indicating that RuTi may be failing by the same mechanisms in the electrolytes. Again, it seems clear from the observations that coating dissolution is a primary deactivating mechanism for the RuTi anode, after which the secondary mechanism of passivation of the exposed Ti substrate occurs.

3.3.4.2 EDS and SEM Analysis

3.3.4.2.1 EDS Analysis from Current Reversal Electrolysis

Fresh RuTi electrode samples and samples operated for various times in current reversal electrolysis were examined by EDS analysis. According to Table 7, the EDS data

for RuTi electrode corroborate the XRF results in that, atomic percent Ru decreases with current reversal time. Ti is seen to increase with time. It is also observed from Table 7 that Ru remained on RuTi electrode after failure in all of the electrolytes. RuTi had the longest lifetime in Na_2HPO_4 and yet 14 atomic percent Ru remained after failure. This seems to indicate that dissolution alone does not account for RuTi electrode failure. Atomic percent of Ti are observed to be increasing with current reversal time, indicating the electrolyte has greater reach of the substrate due to the loss of coating. Exposure of the Ti substrate to the electrolyte in the presence of H_2O ions can lead to the formation of a passivating layer at substrate/coating interface.

The fact that the RuTi electrode examined in the all the electrolytes had residual coating remaining after failure reinforces the hypothesis that a secondary passivating mechanism occurred leading to the eventual failure of the RuTi electrodes.

3.3.4.3 SEM Analysis of RuO_2-TiO_2 Electrode

3.3.4.3.1 Characteristic Features of RuTi Anode

SEM images showing the surface morphological features and coating thickness for fresh RuTi electrode are presented in Figure 45. The surface morphology of the fresh RuTi coating (micrograph A) is characterized by typical pronounced dried mud cracks. The presence of large "islands" is observed in some places on the coating [190-192].

Micrograph B shows the average coating thickness of 56 μm for the RuTi electrode. RuTi coating is reported to have a ruthenium loading as metal of 3.2 g/m^2. IrTa has an average coating thickness of 44 μm and has a reported iridium loading as metal of 10.8 g/m^2. The ratio of Ir:Ta is 70:30 At%. RuTi coating is 12 μm thicker than IrTa

Table 7 EDS values from current reversal electrolysis for RuO_2-TiO_2 anode in different electrolytes at 1200 A/m^2, 0.043 M NaCl, 0.1 Hz cycle.

Electrolyte	Current reversal Time (min)	Elements after Current reversal (At %)		
		Ru	Ti	O
Na_2HPO_4	0	30.98	39.17	29.86
	5	30.96	40.95	27.16
	15	27.33	43.98	27.99
	90	29.69	41.02	27.85
	180	26.17	39.13	30.03
	360	24.15	44.02	29.23
	848	14.01	48.77	34.61
$NaClO_4$	0	30.98	39.17	29.86
	5	29.23	40.49	30.09
	15	29.42	40.25	29.33
	90	30.22	41.22	28.09
	180	23.42	46.63	28.87
	360	15.95	52.55	30.94
	471	7.14	57.76	33.30
Na_2SO_4	0	30.98	39.17	29.86
	5	28.53	41.41	28.63
	15	24.80	44.42	30.43
	45	29.80	41.65	27.11
	125	25.99	43.09	28.82
	270	17.90	49.66	30.97
	400	3.99	61.16	32.32
$NaNO_3$	0	30.98	39.17	29.86
	5	30.46	38.48	27.85
	15	28.57	43.05	25.97
	45	29.59	39.68	27.10
	135	22.62	42.47	30.24
	270	16.94	48.97	30.48
	380	16.50	50.51	29.43
Na_2CO_3	0	30.98	39.17	29.86
	5	29.83	35.99	28.13
	15	28.50	37.97	28.98
	45	28.56	38.57	29.63
	135	26.19	42.05	29.26
	270	18.17	46.37	32.32
	361	14.61	45.93	33.64

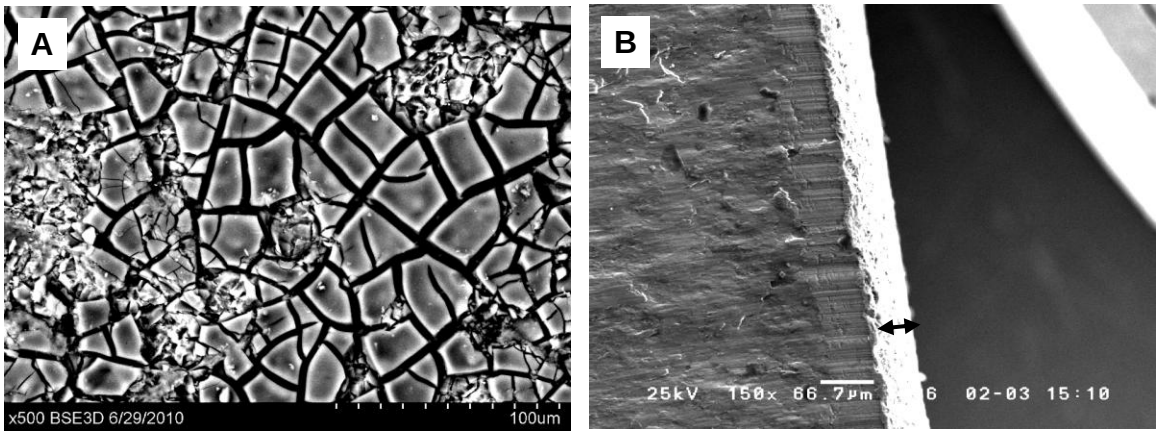

Figure 45 SEM images showing the surface of a fresh RuTi sample (micrograph A) and a cross section of the RuTi coating to reveal its thickness (micrograph B).

coating though RuTi has a third of precious metal in its coating when compared to IrTa. The much thicker RuTi (Ru:Ti is 30:70 At%) appear to be as a result of the increase in valve metal (Ti) component of the coating, which is 70 At%.

3.3.4.3.2 SEM Micrographs of RuO_2-TiO_2 in Various Electrolytes under Current Reversal Electrolysis

SEM representative micrographs showing RuTi electrode deactivation process with current reversal time are given in Figures 46 and 47 for Na_2HPO_4 and Na_2SO_4 electrolytes. The surface morphologies of fresh, examined and failed samples are shown in the figures. It is evident from the micrographs that the coating is systematically

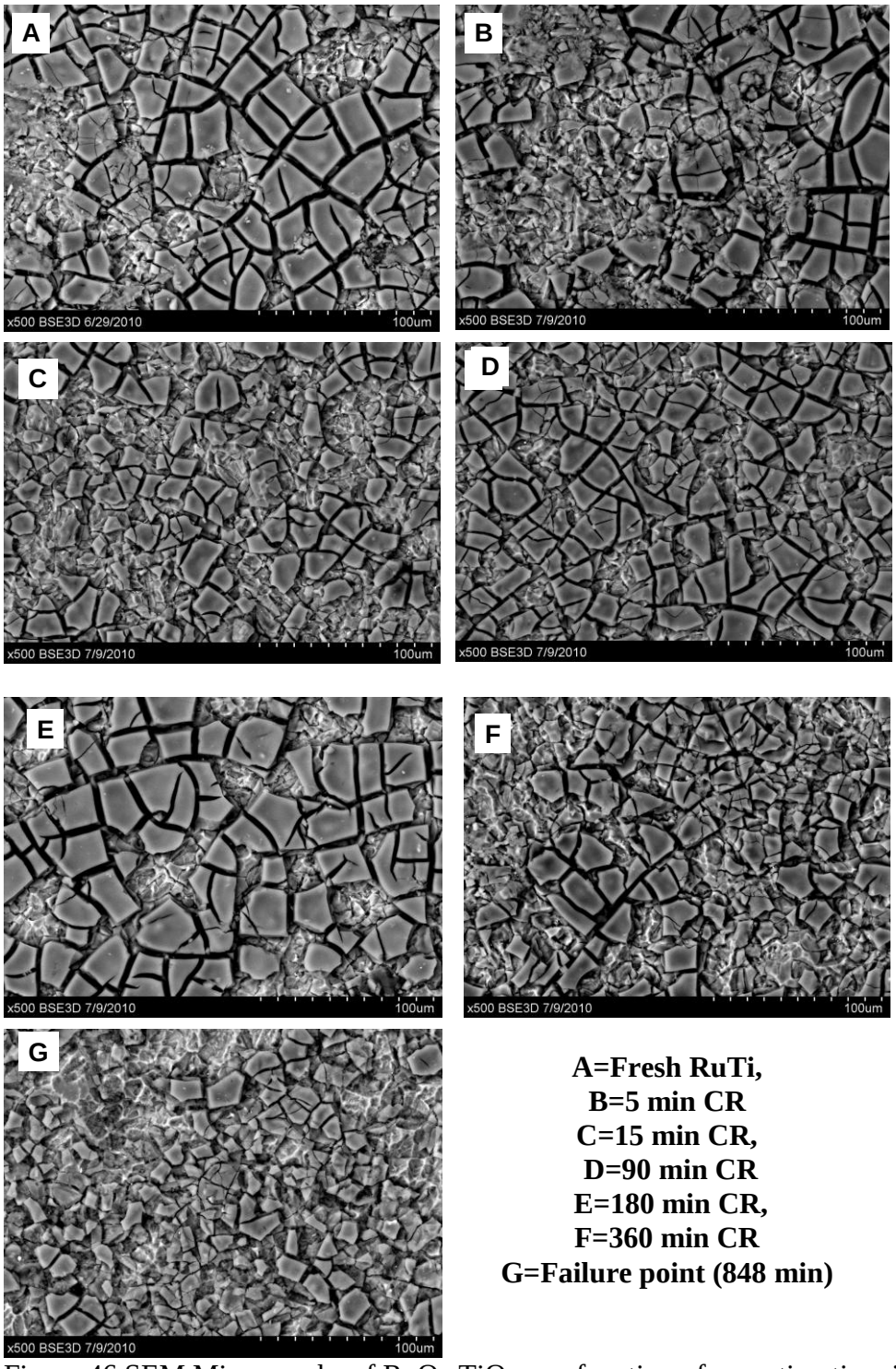

A=Fresh RuTi,
B=5 min CR
C=15 min CR,
D=90 min CR
E=180 min CR,
F=360 min CR
G=Failure point (848 min)

Figure 46 SEM Micrographs of RuO_2-TiO_2 as a function of operation time in 1.2 M Na_2HPO_4 at 1200 A/m^2, 0.043 M NaCl, 0.1 Hz cycle.

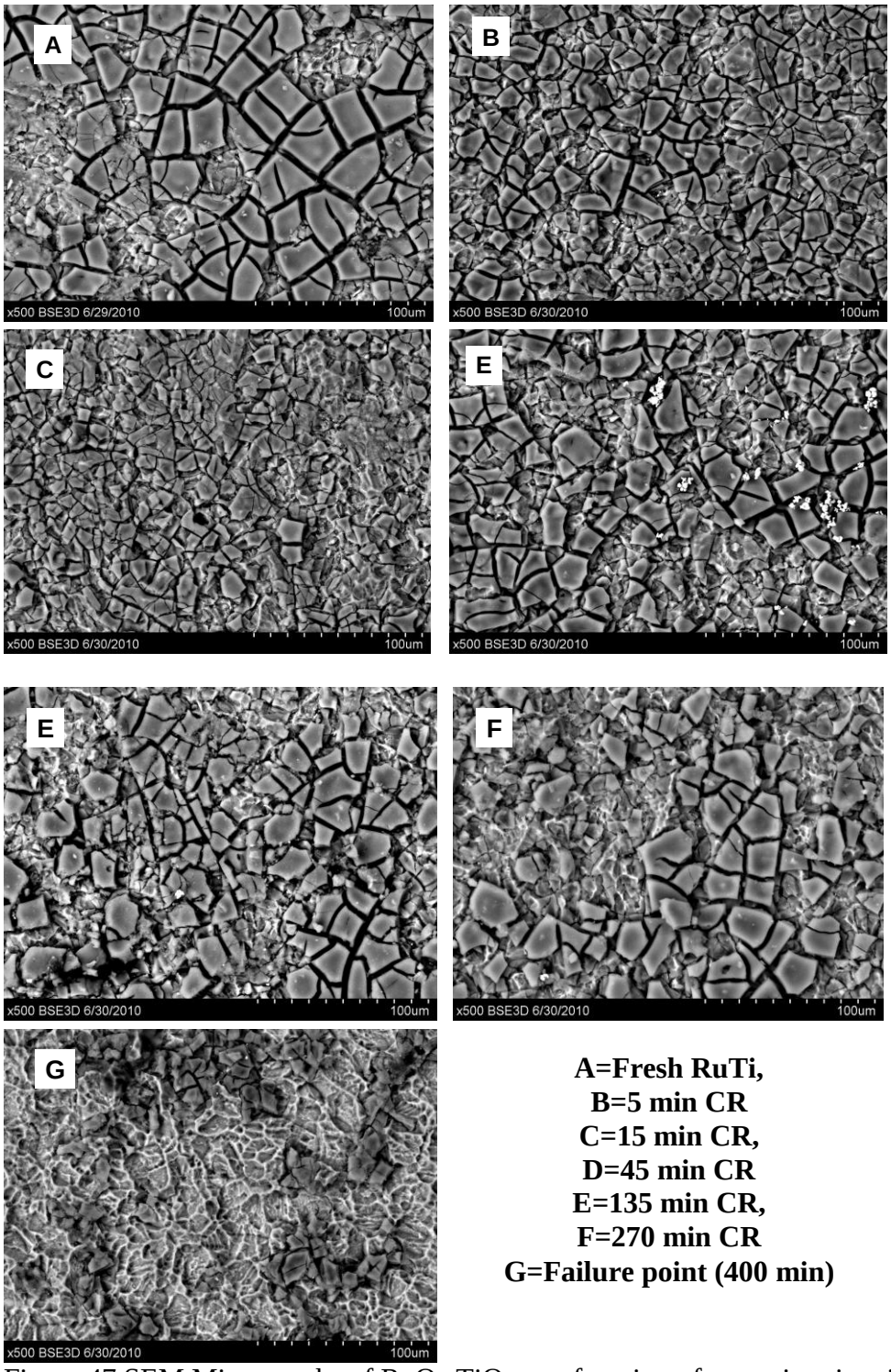

Figure 47 SEM Micrographs of RuO_2-TiO_2 as a function of operation time in 1.2 M Na_2SO_4 at 1200 A/m^2, 0.043 M NaCl, 0.1 Hz cycle.

removed from the electrode's surface with increasing current reversal time. The micrographs also reveal that residual coating remains on the electrode after failure has occurred. This is consistent with observations made in the XRF and EDS results. The RuTi electrode had 7 and 14 atomic percent of Ru remaining on it at failure in Na_2SO_4 and Na_2HPO_4 electrolytes. This observation appears to be supported by the images at the failure time (micrographs G) shown in the figures.

Again, the SEM images have shown that coating depletion occurred over the period of current reversal investigations. The sequence of RuTi deactivation is believed to be caused by the coating dissolution mechanism preceding the passivation mechanism leading to the electrode's failure.

3.3.4.3.3 SEM and EDS Analysis of RuTi in Hard Water from Chronopotentiometry

The purpose of employing the chronopotentiometric technique was to verify the deposition of Ca and Mg on the CTEs during the hard water investigations. Experimental conditions and procedures employed for IrTa were replicated for the RuTi anode. The amounts of Ca and Mg deposited during the chronopotentiometric investigations are shown in Figure 48. RuTi was examined in other anions (perchlorate and hydrogen phosphate) and will be discussed at the end of Chapter 3.

Clearly, the amount of Ca deposited was significantly greater than Mg, which is insignificant. The plot shows that significant deposition of Ca started after 15 minutes. This seems to suggest that in the hard water investigations, hard water scales would have deposited especially Ca in the presence of nitrate ions if the cycle time was increased to

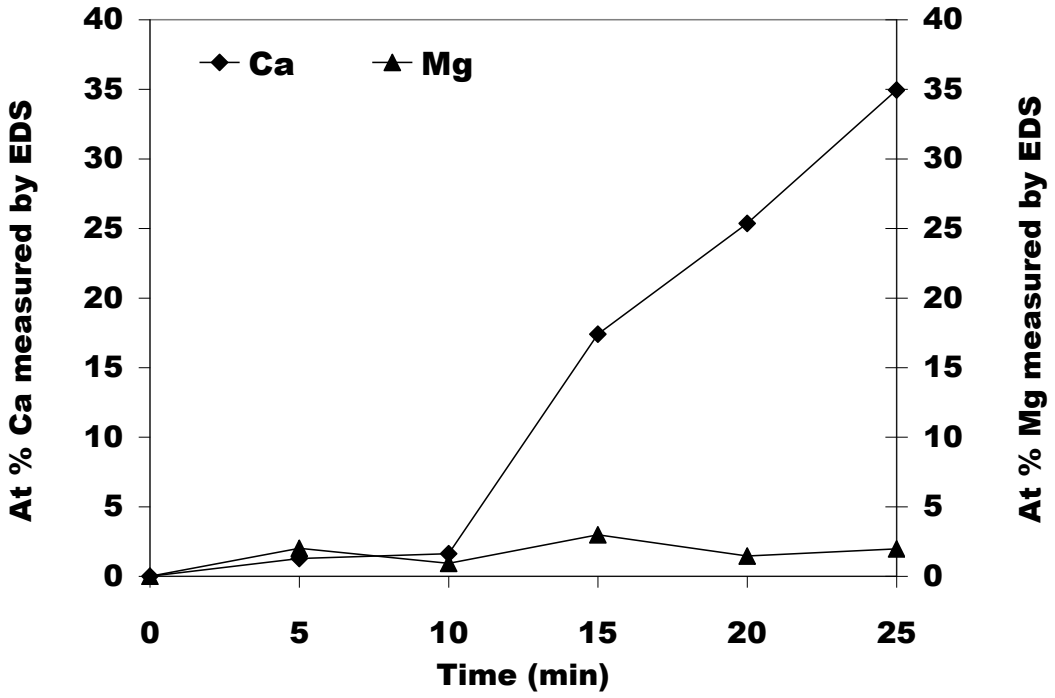

Figure 48 EDS values for Ca and Mg from chronopotentiometry on RuTi electrode in 1.2 M NaNO3, 857 mg/L Ca and Mg ions, -1200 A/m^2, 0.026 M Cl^-.

30 minutes. Thus, at a cycle time of 10 seconds (0.1 Hz), no Ca or Mg deposits are expected. This will be discussed in detail in Chapter 4.

3.3.5 Electrochemical Characterization

3.3.5.1 Cyclic Voltammetry

The behavior of RuTi electrode was examined by cyclic voltammetry in the five sodium electrolytes studied and the results are shown in Figure 49. Fresh, tested and deactivated electrode samples were evaluated. Typical cyclic voltammograms for the RuTi electrode are shown in Figure 49A. A representative plot of voltammetric charge

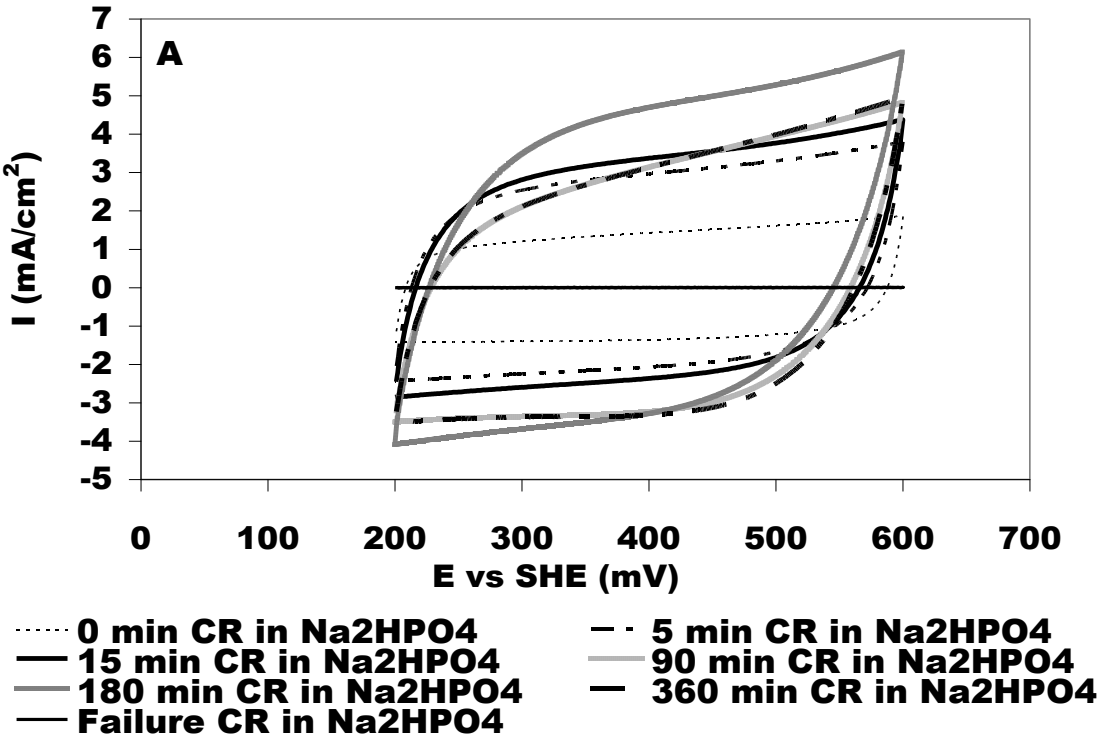

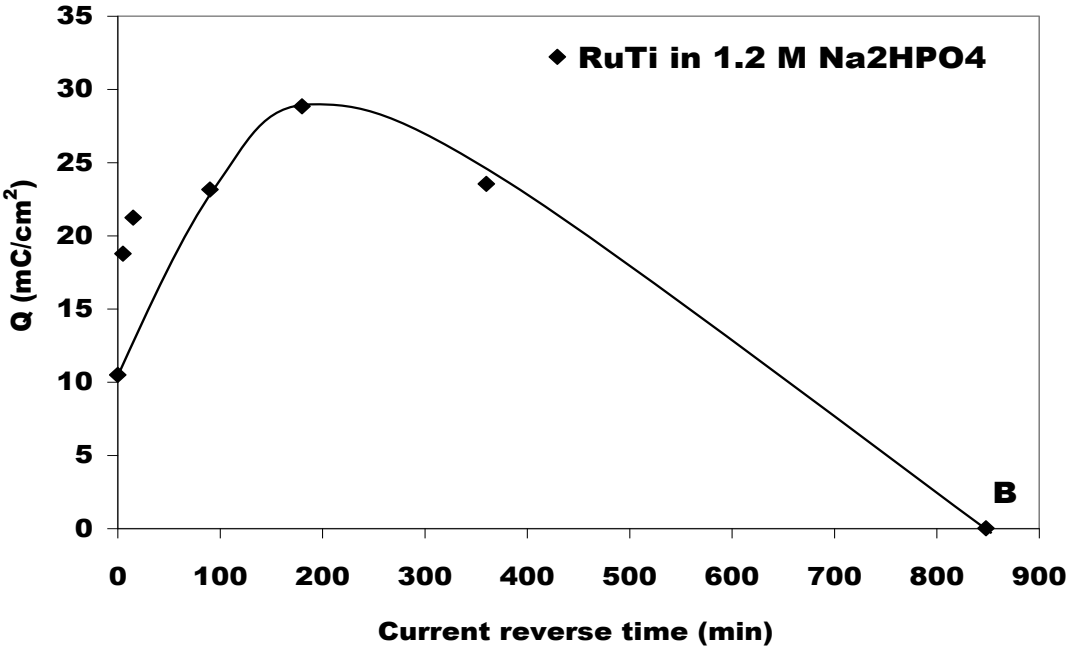

Figure 49 Cyclic voltammograms and charge plots. (A) Cyclic voltammograms at 100 mV s^{-1} in 1.2 M Na_2SO_4, 0.043 M NaCl (B) Charge vs. current reversal time for RuO_2-TiO_2.

versus current reversal time is given in Figure 49B. CV voltage limits were selected such that gas (Cl_2, O_2, and H_2) evolution did not occur.

The CV curves [186, 193] for RuTi also show broad peak currents between 200 to 400 mV potential range, and exhibit high redox reversibility and pseudocapacitance characteristics. Nonfaradaic charge transfer reactions occurring at the high surface area of RuTi electrode and electrolyte interface explains this pseudocapacitive behavior. The [194-195] peaks observed between 200 mV and 400 mV is associated with the solid state redox transition of Ru(III)/Ru(IV).

As current reversal time increases, the peak current densities for the individual CV curves also increases to a maximum (around 400 mV and 4.70 mA/cm^2) before declining, as seen in Figure 49A. This pattern and shape of curves was also observed for the RuTi examined in the other anion electrolytes (nitrate, carbonate, perchlorate and sulphate) as presented in Figures 50A and 50B and 51A and 51B, respectively. In like manner, the charge as shown in Figure 49B increases with increasing current reversal time to a maximum value (180 minutes and 29 mC/cm^2) and then declines.

The pseudocapacitive behavior at the RuTi coating/electrolyte interface is related to the charge, and the charge it appears depends on the effective area of the RuTi coating. And so as the effective coating area increases and then decreases, primarily by dissolution and then possibly surface coverage with adsorbed species, the charge and pseudocapacitance decrease as well.

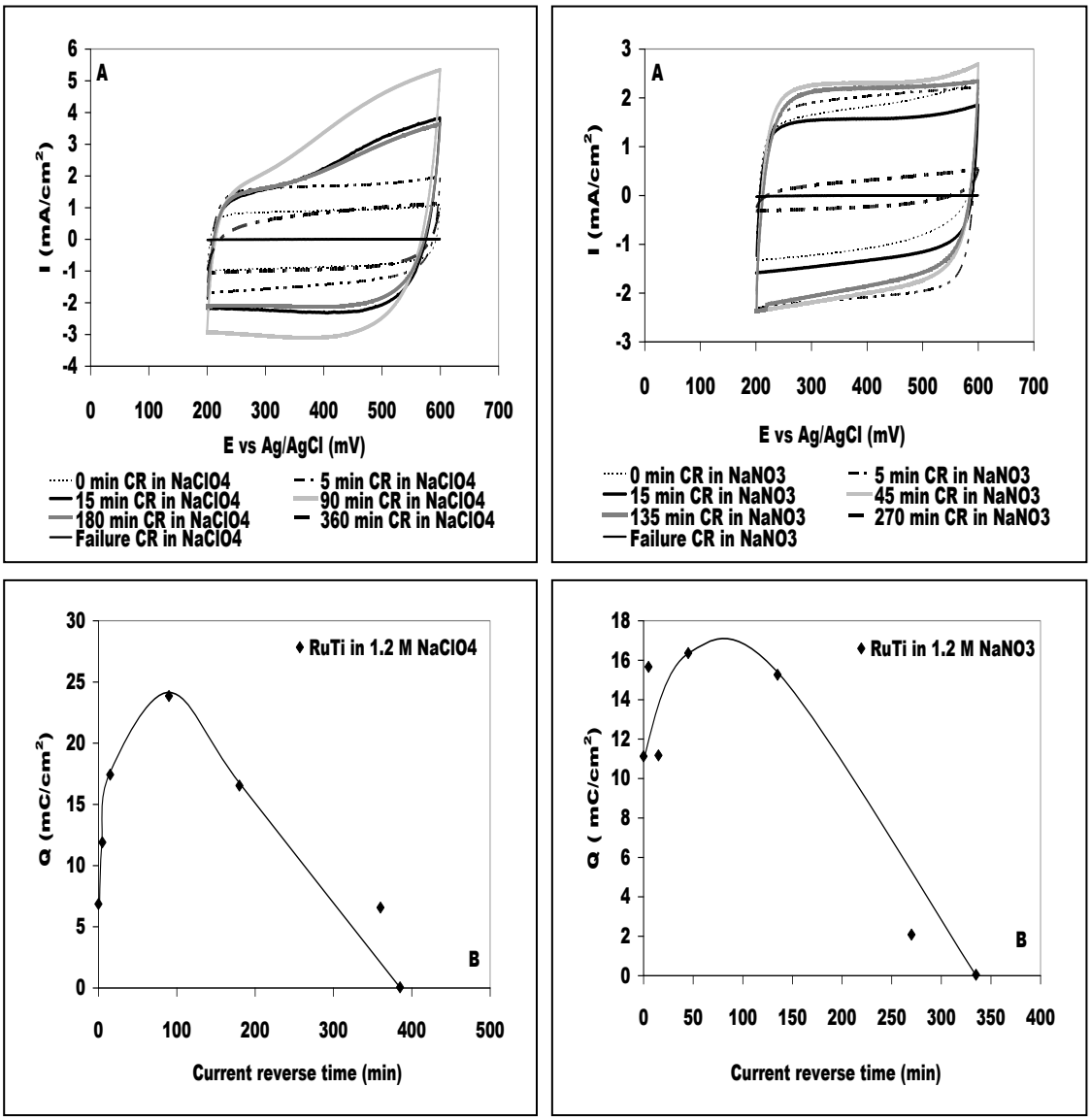

Figure 50 Cyclic voltammograms and charge plots. (A) Cyclic voltammograms at 100 mV s^{-1} and (B) Charge vs. current reversal time for RuO_2-TiO_2 in 1.2 M $NaClO_4$ and $NaNO_3$ 1200 A/m^2, 0.043 M NaCl, 0.1 Hz cyle.

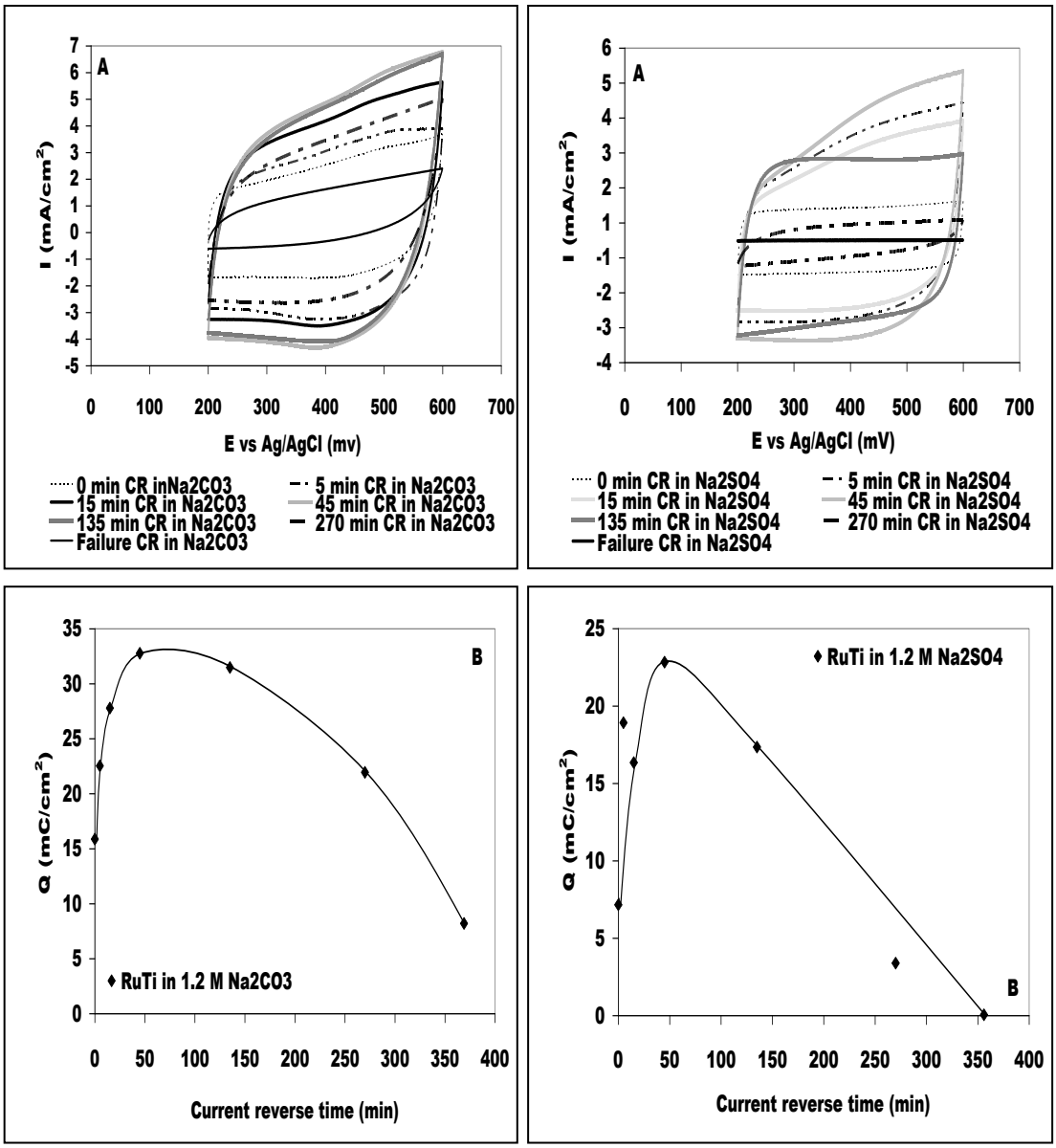

Figure 51 Cyclic voltammograms and charge plots. (A) Cyclic voltammograms at 100 mV s^{-1} and (B) Charge vs. current reversal time for RuO_2-TiO_2 in 1.2 M Na_2CO_3 and Na_2SO_4, 1200 A/m^2, 0.043 M NaCl, 0.1 Hz cycle.

3.4 Comparison of Coated Titanium Electrodes

The two electrodes (IrTa and RuTi) examined under current reversal and hard water electrolysis conditions are compared and discussed in the following sections.

3.4.1 Current Reversal Electrolysis

3.4.1.1 Factors Influencing Coated Titanium Electrode Failure in Sodium Sulfate

The effects of current density, current reversal cycle frequency and sodium chloride concentration on CTEs were investigated under current reversal conditions. Lifetime of the CTEs examined in 1.2 M Na_2SO_4 was found to decrease as a function of current density. The plot of lifetime versus current density is shown in Figure 52. RuTi anode had longer lifetimes at all the current densities examined than IrTa anode. Observations have been made by other researchers in continuous or straight polarity in Na_2SO_4 mixed with H_2SO_4 [2, 137, 196] that lifetime decreases with increasing current density. However, IrTa coatings tend to have longer lifetimes when the main anode reaction is oxygen evolution.

As current reversal cycle frequency is reduced, lifetime is prolonged for the CTEs. This can be seen in Figure 53. RuTi anode life is evidently longer than IrTa at to higher reversal cycle frequencies. However, when the reversal cycle frequency was further decreased to 5.6×10^{-4} Hz (30 minutes) the CTEs experienced dramatic increases in lifetimes. The IrTa lifetime was more than twice that of RuTi as observed in Figure 53.

A positive correlation has been reported [175, 197] between NaCl concentration and CTEs lifetime with straight polarity. CTE anode lifetimes with current reversal

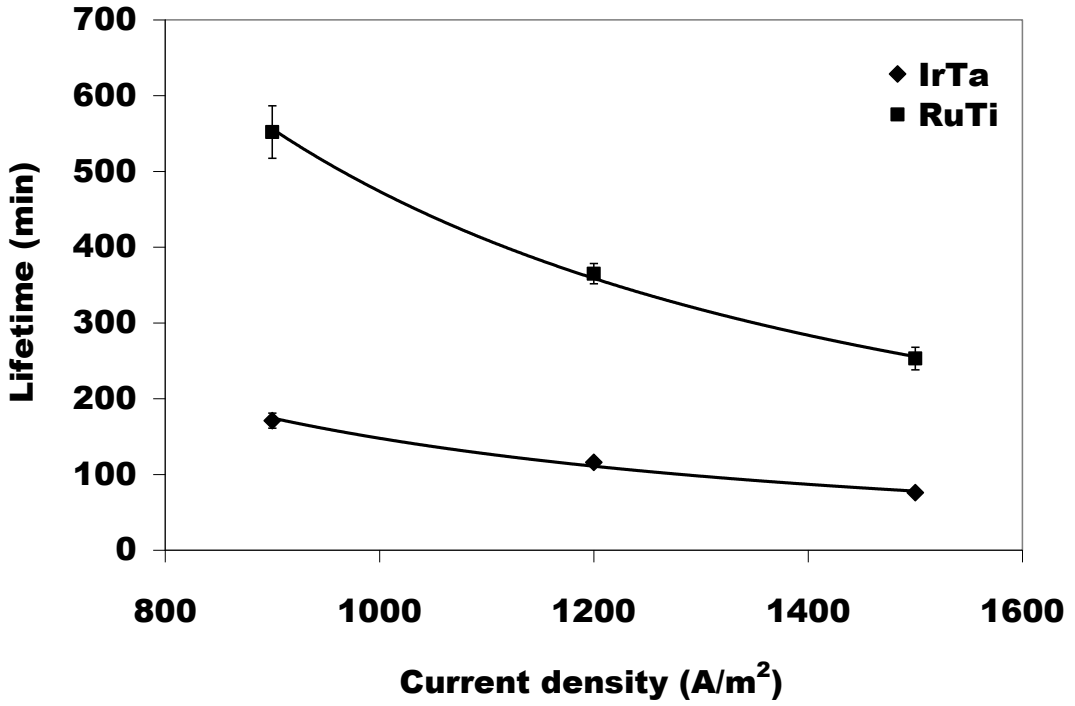

Figure 52 Effect of current density on CTEs in 1.2 M Na_2SO_4, 0.043 M NaCl, 0.1 Hz.

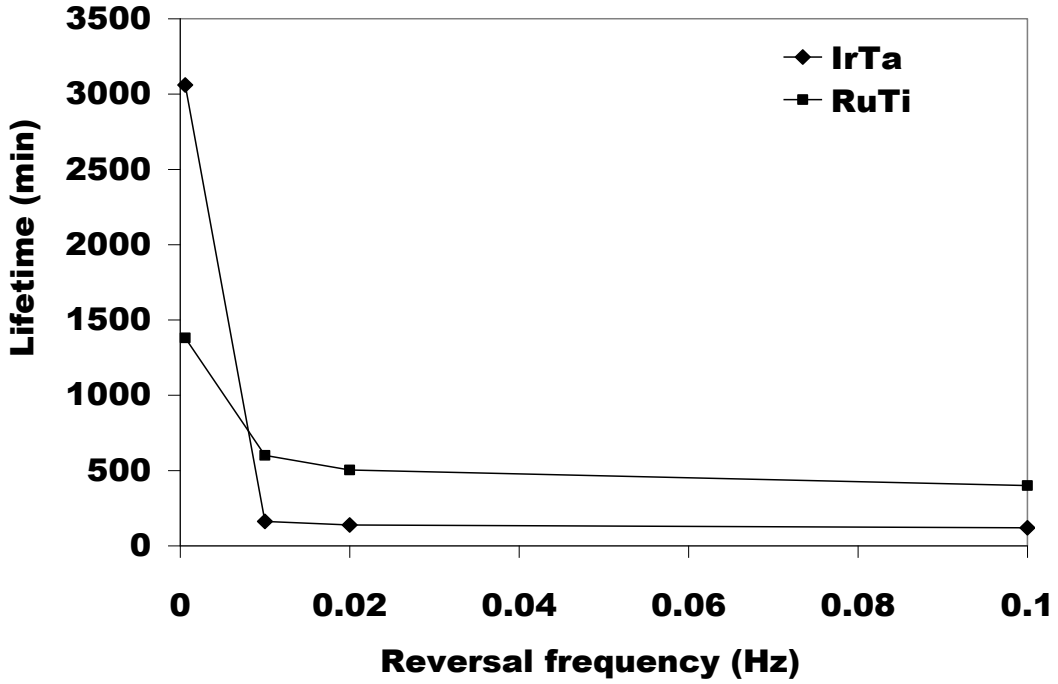

Figure 53 Current reversal cycle frequency vs. lifetime of IrTa and RuTi electrodes in 1200A/m^2, 1.2 M Na_2SO_4, 0.043 M NaCl.

exhibited no effect with changes in NaCl as shown in Figure 54. This may be related to the relative lower amounts of NaCl concentration used. As observed in the plot, RuTi electrode lasted longer than the IrTa anode at all the concentrations of NaCl examined.

3.4.1.2 Influence of Anion Composition and Concentration on Coated Titanium Electrodes

The effects of changes in anion composition and concentration on the lifetimes of IrTa and RuTi are presented in Figures 55 to 59. It can be seen in Figure 55 IrTa had the

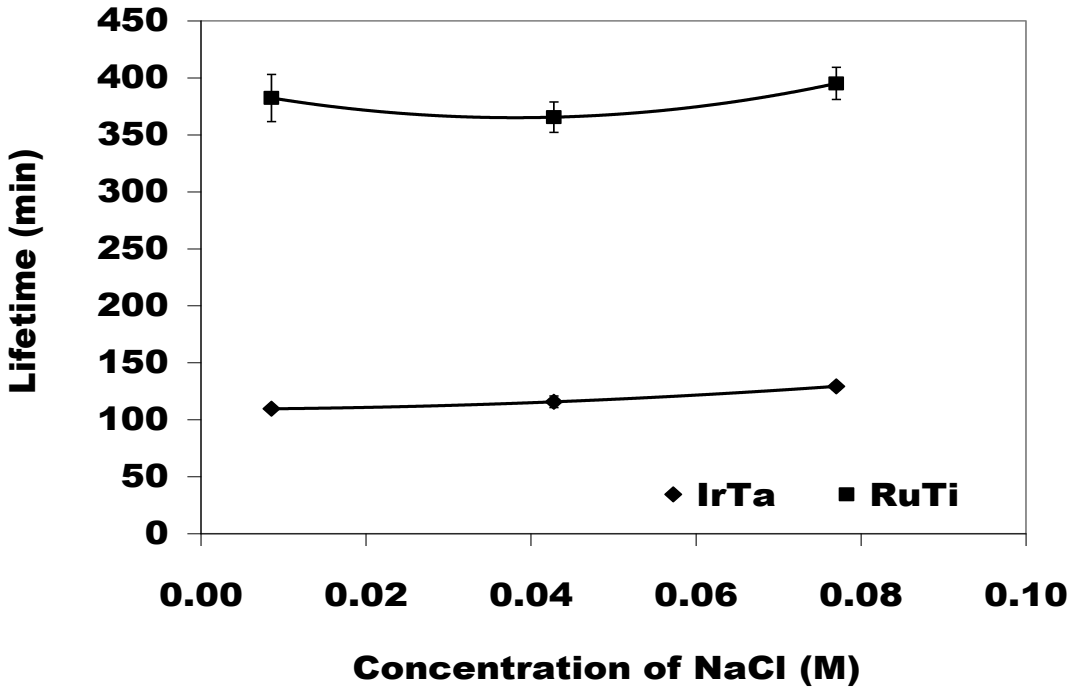

Figure 54 Effect of sodium chloride concentration on CTEs lifetime at 1200 A/m^2, 1.2 M Na_2SO_4, 0.1 Hz.

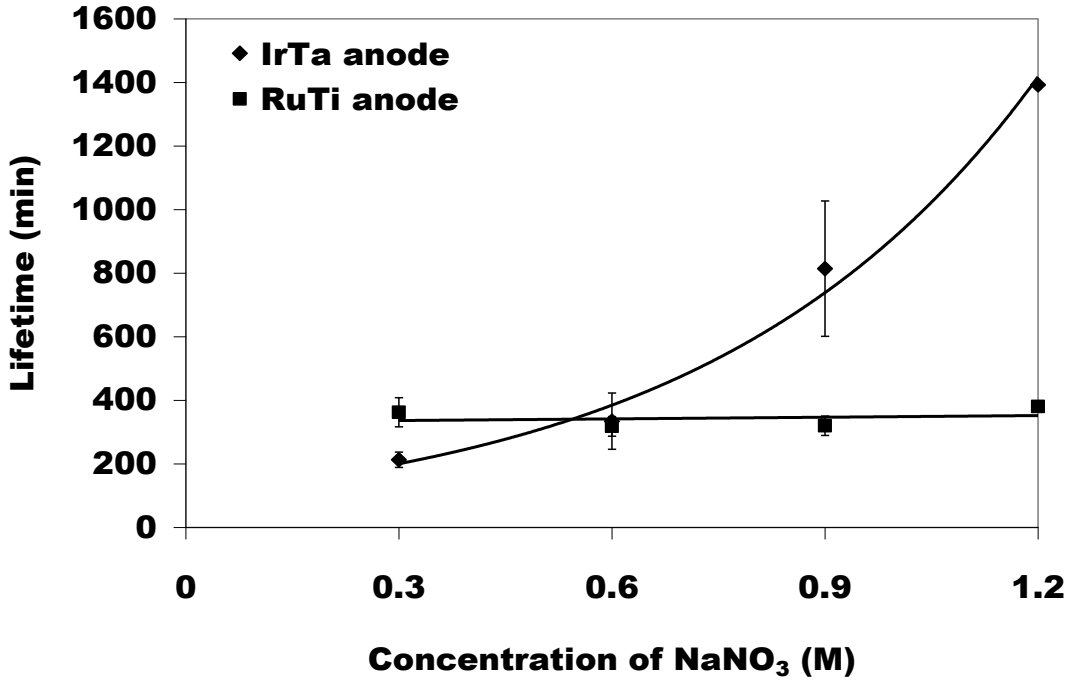

Figure 55 Effect of sodium nitrate concentration on CTEs lifetime at 1200 A/m^2, 0.043 M NaCl, 0.1 Hz.

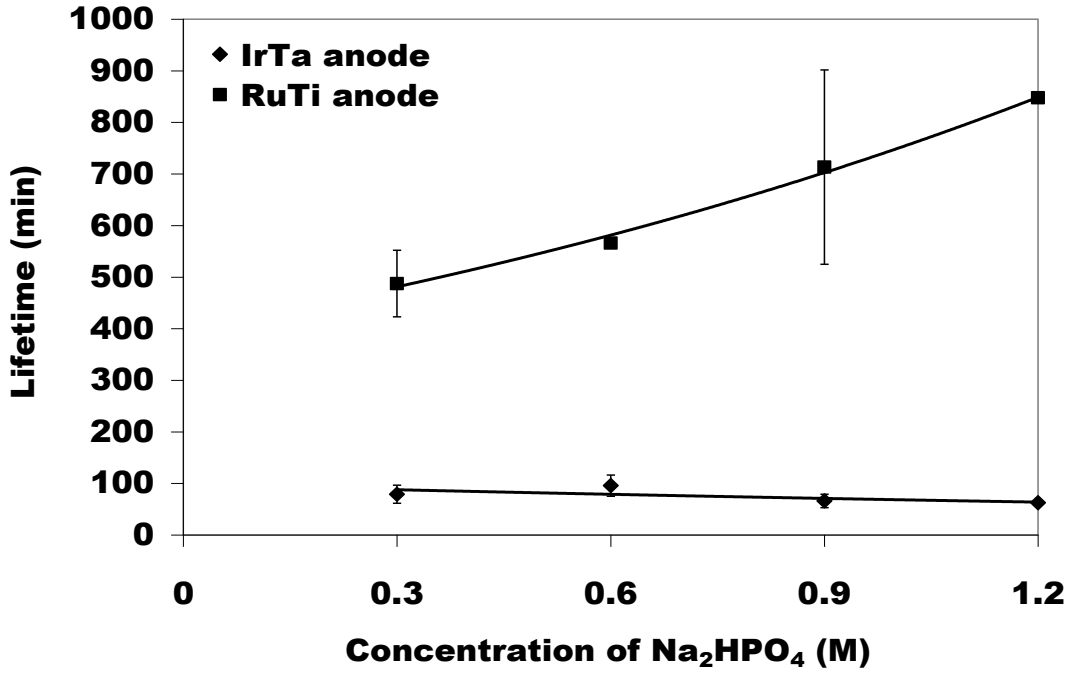

Figure 56 Effect of sodium hydrogen phosphate concentration on CTEs lifetime at 1200 A/m^2, 0.043 M NaCl, 0.1 Hz.

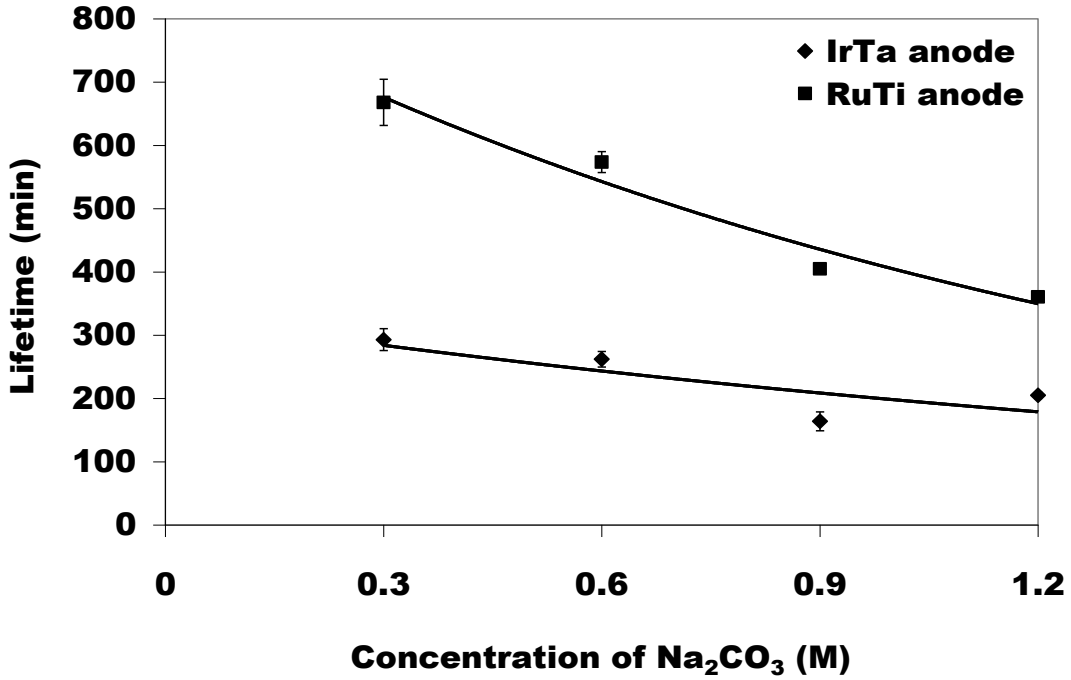

Figure 57 Effect of sodium carbonate concentration on CTEs lifetime at 1200 A/m^2, 0.043 M NaCl, 0.1 Hz.

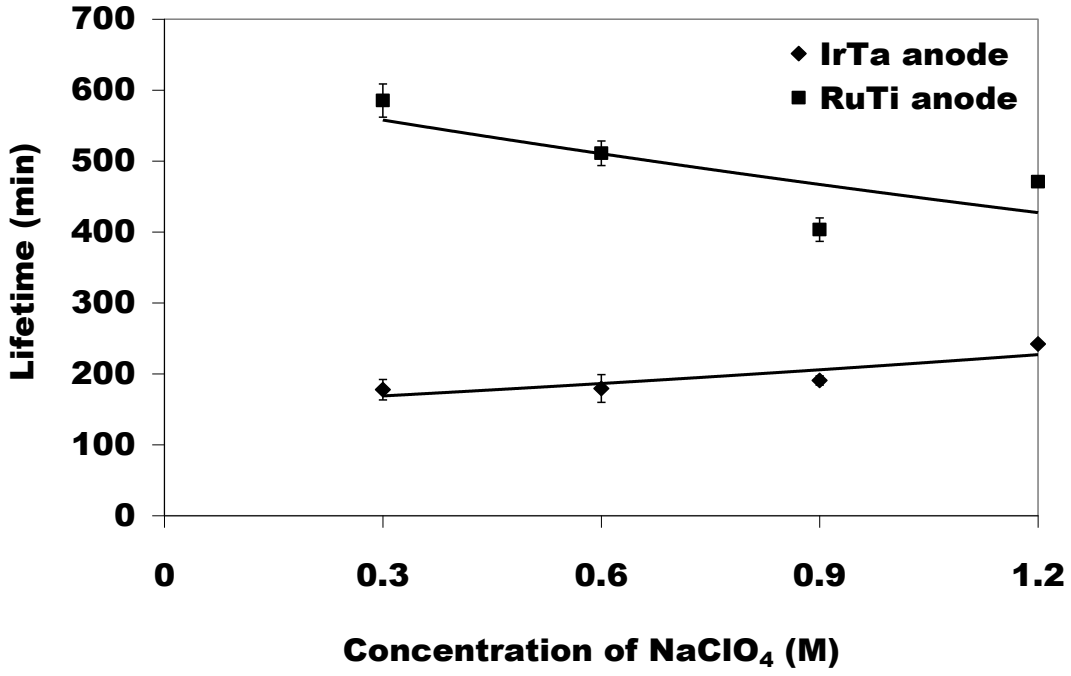

Figure 58 Effect of sodium perchlorate concentration on CTEs lifetime at 1200 A/m^2, 0.043 M NaCl, 0.1 Hz.

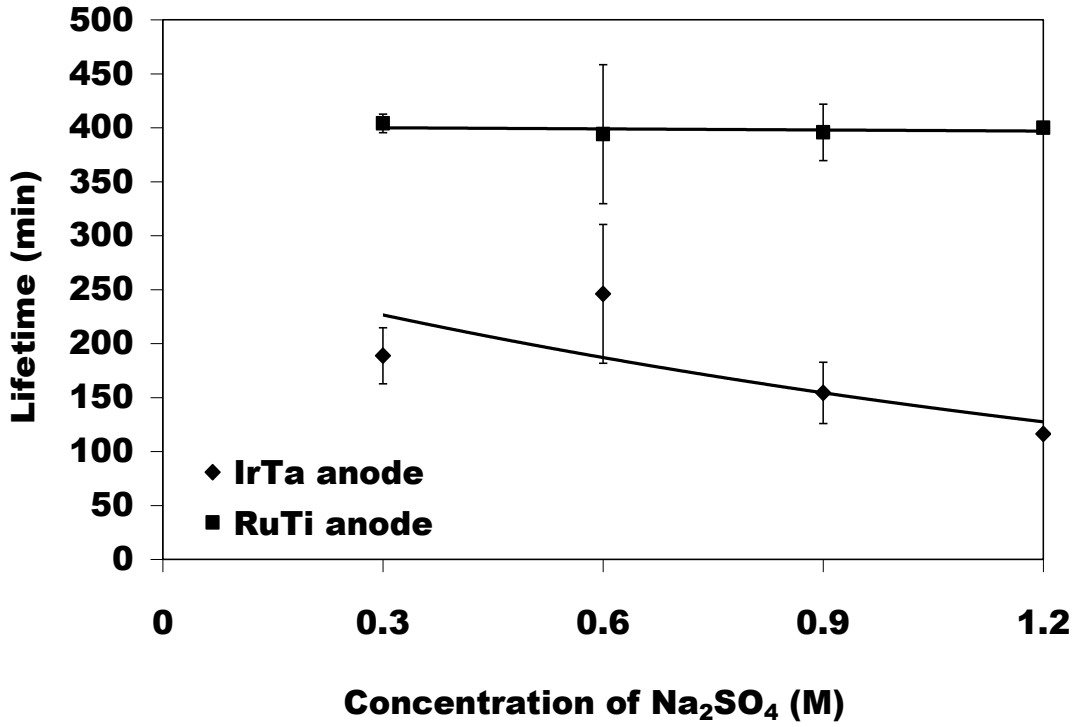

Figure 59 Effect of sodium sulphate concentration on CTEs lifetime at 1200 A/m^2, 0.043 M NaCl, 0.1 Hz.

longest lifetime in high concentrations of nitrate anions. RuTi had the longer lifetime in the other anions investigated as shown in Figures 55-59.

A positive correlation exists between IrTa lifetime and the concentration of nitrate anions. RuTi lifetime shows no correlation with nitrate concentration (Figure 55). In hydrogen phosphate anions, however, RuTi lifetime shows a positive correlation with hydrogen phosphate concentration. IrTa lifetime on the other hand exhibits no correlation with hydrogen phosphate anion concentration (Figures 56). Lifetime of both CTEs (Figures 57) appears to decrease as function of carbonate anions concentrations. Finally,

the lifetime of the CTEs appears not to change or only slightly decrease as either a function of perchlorate or sulphate anions (Figures 58 and 59).

A summary of the average current reversal lifetimes of IrTa and RuTi electrodes in the various anions is shown in Table 8. Lifetimes for each electrode are listed in declining order. Obviously, the CTEs (IrTa and RuTi) behaved differently in the different electrolytes examined. Clearly, composition and concentration of the supporting electrolyte can significantly influence the lifetimes of the electrodes. The sizes of the anions examined appear to have had no influence on lifetime as can be seen from Table 8, as there is no correlation between the anion size and lifetime of the CTEs.

In summary, IrTa had the longer lifetime in nitrate ions, and service life of IrTa increased as a function of nitrate concentration. RuTi had the longer lifetime in the other anions. RuTi lifetime increased as a function of hydrogen phosphate ions.

Table 8 Summary of lifetime for IrTa and RuTi in 1.2 M sodium anions

IrTa Anode		**RuTi Anode**		
Anion	**Lifetime (min)**	**Anion**	**Anion Size (pm)**	**Lifetime (min)**
NO_3^-	1392	HPO_4^{2-}	238	848
ClO_4^-	242	ClO_4^-	250	471
CO_3^{2-}	205	SO_4^{2-}	240	400
SO_4^{2-}	116	NO_3^-	179	380
HPO_4^{2-}	63	CO_3^{2-}	178	361

3.4.2 Current Reversal Electrolysis of Hard Water

Periodic polarity reversal [1, 146, 147] is among many techniques used in industry for water disinfection and treatment. During the electrolysis process, Ca and Mg ions in water are deposited on the cathode of the cell by precipitation, thereby increasing operating cell voltage and decreasing cell efficiency. When the polarity of the electrodes are reversed (initial cathode becomes anode), the deposits are removed. This is the concept behind the current reversal technique.

3.4.2.1 Factors Influencing CTE Failure in Hard Water Electrolysis

Water hardness was simulated by adding Ca and Mg ions to some electrolytes ($NaNO_3$, Na_2HPO_4, and NaClO4) to be examined. The influence of hard water concentration (Ca or Mg ions), electrolyte composition and reversal cycle frequency on the lifetime of electrodes were examined.

3.4.2.1.1 Effect of Reversal Frequency

The lifetimes of IrTa and RuTi anodes were compared at current reversal cycle times (or frequencies) of 10 sec (0.1 Hz) and 30 minutes (0.00056 Hz) in nitrate ions with Ca and Mg ions. Figure 60 reveals an obvious difference in the lifetimes of the two electrodes. The plot clearly indicates that increasing the reversal cycle time prolongs the CTEs lifetime, as polarity reversal [1, 146, 147] and indeed shorter polarity reversal cycle times reduces the service life of the CTEs. Chronopotentiometric measurements have

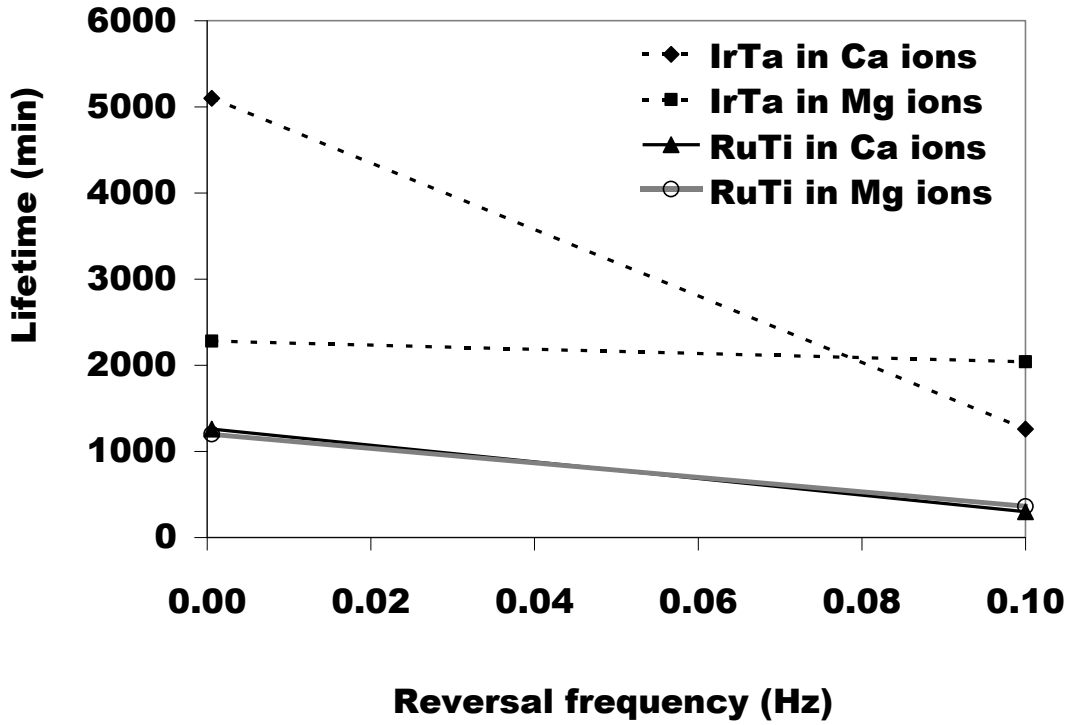

Figure 60 Effect of current reversal cycle time on CTE under current reversal and hard water conditions at 1200 A/m^2, 857 mg/L Ca and Mg ions, 1.2 M $NaNO_3$, 0.026 M Cl^-.

revealed that the amounts of Ca or Mg deposited on IrTa were insignificant. Ca deposited on RuTi was only significant after 15 minutes of testing time. The electrodes were examined at 30 minutes reversal cycle time to verify whether lifetimes would be prolonged or whether significant amounts of Ca and Mg will be deposited to accelerate failure.

As it can be seen in the plot of Figure 60 lifetimes of the electrodes increased as reversal cycle was increasing. This is particularly so for the IrTa electrode in Ca. The electrodes had longer lifetimes at 5.6×10^{-4} Hz than at 0.1 Hz. The lifetime of RuTi in the

presence of Ca and Mg ions appears identical. The lifetime of IrTa is significantly higher in Ca ions (85 hr) than in Mg ions (38 hr).

The lifetime of IrTa in 1.2 M $NaNO_3$ without the presence of Ca and Mg presence is 23 hours, far lower than the lifetime observed in the presence of hard water. The reason for this anomalous behavior is not understood, and should be pursued as future work. However, it can be hypothesize that, in the presence of nitrate ions, the Ca and Mg ions appear to provide protective covering so the CTE (especially the IrTa anode) do not fail as fast as they would otherwise do under current reversal electrolysis. This appears to suggest that CTEs can be used for self-cleaning applications provided reversal cycle frequency is optimized.

3.4.2.1.2 Effect of Hard Water and Type of Electrolyte on Lifetime

3.4.2.1.2.1 Effect of Calcium and Nitrate Ions

The effect of Ca ion concentration and nitrate concentration on the CTE life was evaluated. The expectation was that as hard water concentration increases lifetime of CTEs would decrease. This is not what has been observed in the present work for some of the electrolytes and hard water combinations. As shown in Figure 61A, the lifetime of IrTa in general appears to be increasing as a function of nitrate ions. The effect of Ca concentration on IrTa life is not discernible. IrTa life is higher than RuTi at all the Ca concentrations examined in nitrate supporting electrolyte. The lifetime of RuTi shown in Figure 61B appears to have no uniform trends with regards to nitrate or Ca concentrations.

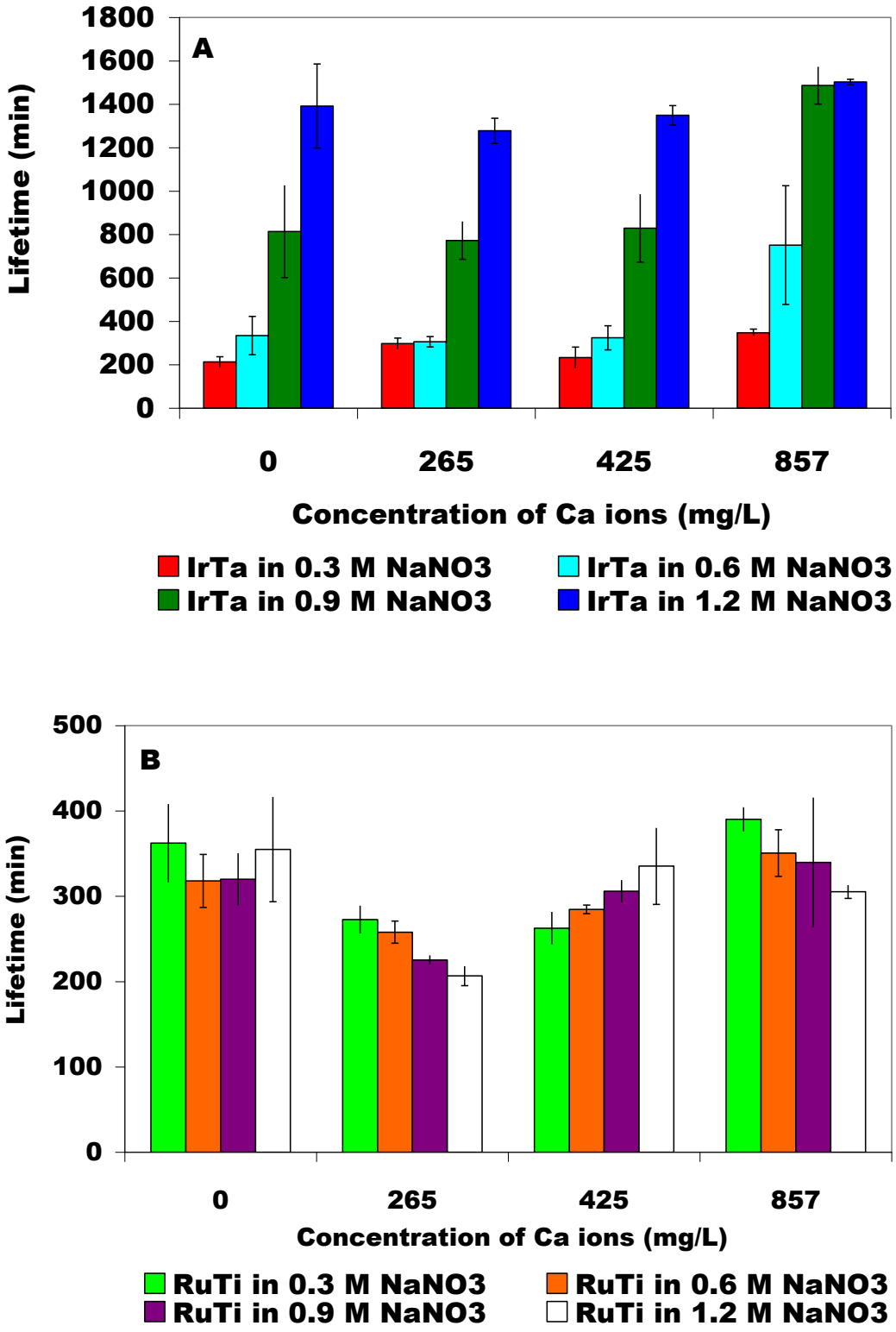

Figure 61 Effect of nitrate and Ca ions concentration on electrode lifetime at 1200 A/m^2, 0.026 M Cl^-, 0.1 Hz. Plot A for IrTa and B for RuTi.

In summary, nitrate concentration appears to influence IrTa life while Ca concentration does not do so in a discernible manner. Nitrate and Ca concentrations appear not to affect RuTi life.

3.4.2 1.2.2 Effect of Calcium and Hydrogen Phosphate Ions

The lifetime of RuTi was greater than IrTa in the presence of Ca and hydrogen phosphate ions, as shown in Figure 62. The lifetime of IrTa shown in Figure 62A appears to increase as a function of hydrogen phosphate ions at 265 and 425 mg/L Ca but then decrease at 857 mg/L Ca. The lifetime values for IrTa in Ca ions are greater than the values without Ca ions.

As seen in Figure 62B, hydrogen phosphate ions appear to influence RuTi life, however, not in clear distinct manner. Ca concentrations seem not to influence RuTi life since RuTi life at the different levels of Ca hardness examined appear similar apart from a few variations. Lifetime of RuTi is observed to increase as function of hydrogen phosphate ions in 0 mg/L Ca ions.

To summarize, Ca and hydrogen phosphate ions seem to affect IrTa life at low to medium Ca concentrations. The effects of hydrogen phosphate concentrations on RuTi life appear not to be distinct and the influence of Ca hardness on RuTi lifetime is not observed.

3.4.2.1.2.3 Effect of Calcium and Perchlorate Ions

The influence of composition and concentration of Ca and perchlorate ions on the lifetime of the CTEs is shown in Figure 63. The lifetime of RuTi anode as observed in

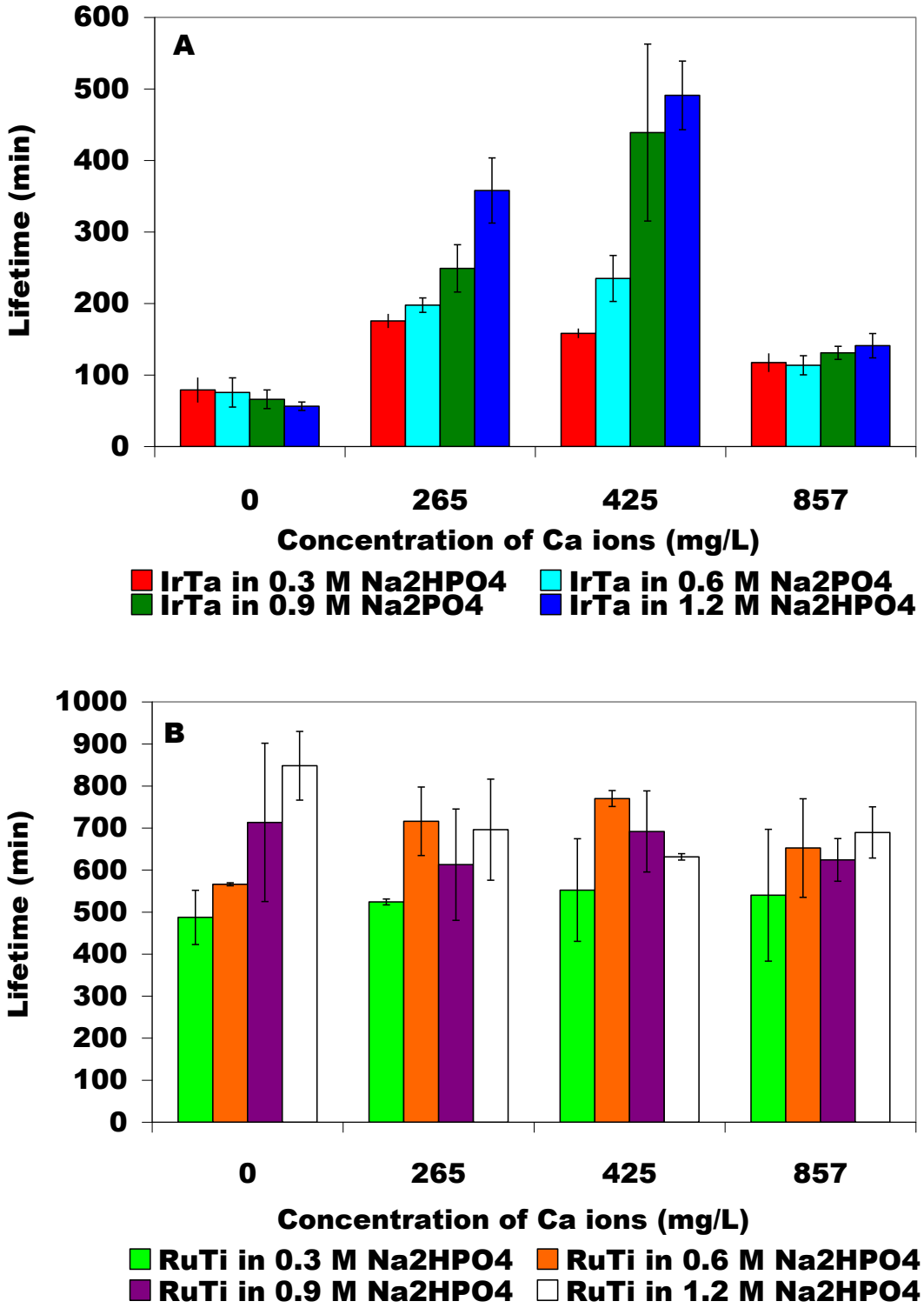

Figure 62 Effect of hydrogen phosphate and Ca ions concentration on electrode lifetime at 1200 A/m^2, 0.026 M Cl^-, 0.1 Hz. Plot A for IrTa and B for RuTi.

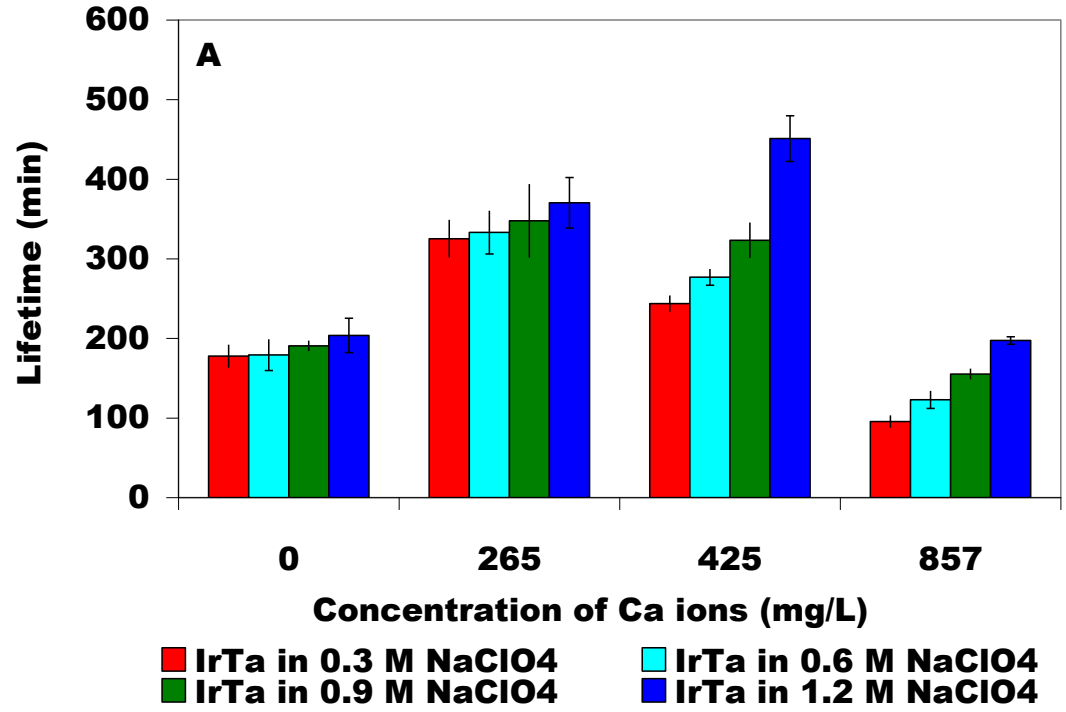

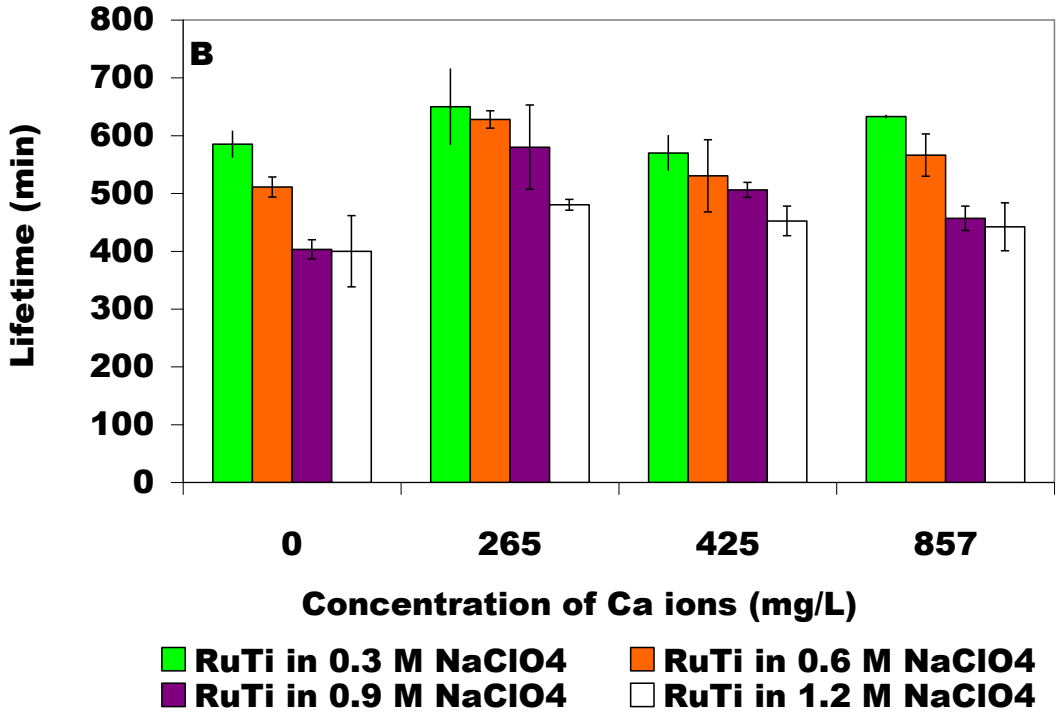

Figure 63 Effect of perchlorate and Ca ions concentration on electrode lifetime at 1200 A/m^2, 0.026 M Cl^-, 0.1 Hz. Plot A for IrTa and B for RuTi.

Figure 63B, is higher than IrTa anode life (Figure 63A) at all the concentrations of Ca and perchlorate ions examined. The lifetime of IrTa appears to increase with increasing perchlorate concentration, especially at the 425 and 857 mg/L Ca concentration. Lifetime of IrTa appear to generally increase and then decrease with increasing Ca concentration.

The service life of RuTi appears to decrease as a function of perchlorate ions. There appears to be no influence of Ca concentration on the lifetime of RuTi.

In summary, the concentration of Ca and perchlorate ions appears to have influence IrTa life. Perchlorate concentration seems to affect RuTi lifetime while Ca appears not do so.

3.4.2.1.2.4 Effect of Magnesium and Nitrate Ions

The influence of composition and concentration of Mg hardness and electrolyte on the CTE life was also investigated. The lifetime of IrTa appears longer than RuTi lifetime in Mg and nitrate ions. The lifetime of IrTa anode as shown in Figure 64A appears to be increasing with nitrate concentration. The lifetime of IrTa increases to a maximum at 161 mg/L Mg and then decreases with increasing Mg hardness.

As shown in Figure 64B, RuTi lifetime appears to be decreasing with increasing nitrate concentration at the 161 and 857 mg/L Mg. RuTi anode appears not to show a distinct pattern in lifetime with respect to Ca concentration.

To summarize, the concentration of nitrate and Mg seem to influence IrTa life. Nitrate concentration seems to affect RuTi life at the lowest and highest concentrations of Mg. Mg concentration not influence RuTi life.

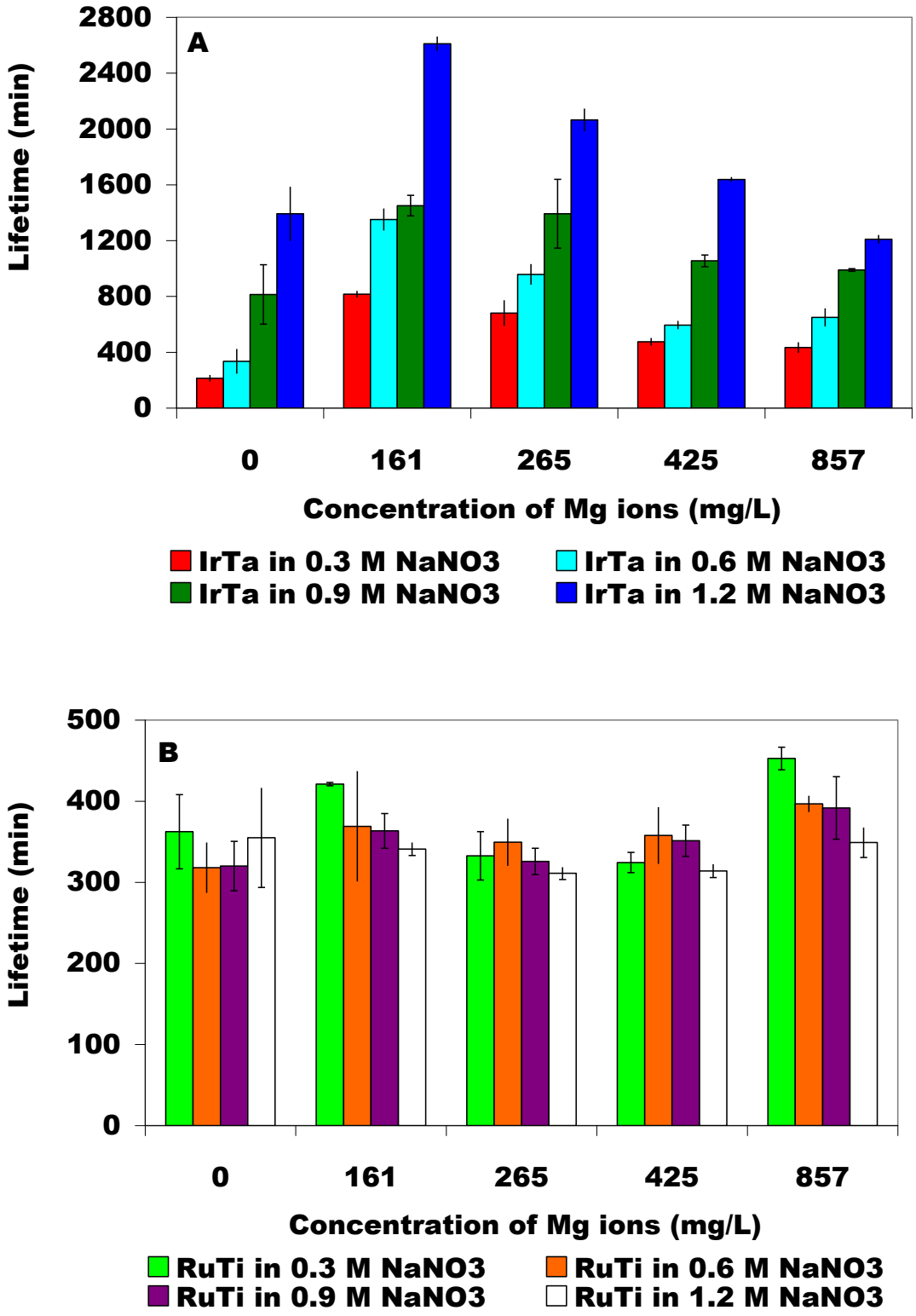

Figure 64 Effect of nitrate and Mg ions concentration on electrode lifetime at 1200 A/m^2, 0.026 M Cl^-, 0.1 Hz. Plot A for IrTa and B for RuTi.

3.4.2.1.2.5 Effect of Magnesium and Hydrogen Phosphate Ions

As observed in Figure 65, the lifetime of RuTi (Figure 65B) appears longer than IrTa life (Figure 65A) in Mg and hydrogen phosphate ions. The IrTa lifetime seems to decrease with increasing concentrations of hydrogen phosphate at 265 to 857 mg/L Mg concentrations. Lifetime of IrTa appears to increase with increasing hydrogen phosphate concentration at the 161 mg/L Mg. The lifetime of IrTa appears to increase to a maximum at 161 mg/L Mg and the decreases to a uniform lifetime with increasing Mg concentration. IrTa life in hard water seems higher than in the absence of water hardness. The general observation for the RuTi anode as seen in the plot is that Lifetime appears to increase as a function hydrogen phosphate concentration at 0 and 265 mg/L Mg. Mg concentration seems to have no effect on RuTi lifetime. RuTi life in the absence of hard water appears to be greater than in hard water.

In summary, the concentration of hydrogen phosphate and Mg ions appear to influence IrTa life. Mg concentration does not appear to affect RuTi life. Hydrogen phosphates effects are only observed at 0 and 265 mg/L Mg concentrations.

3.4.2.1.2.6 Effect of Magnesium and Perchlorate Ions

The lifetimes of the CTEs examined in perchlorate and Mg ions is presented Figure 66. RuTi life (Figure 66B) appears to be higher than IrTa life (Figure 66A) at all the levels of Mg hardness tested in perchlorate. IrTa anode life increases as a function of perchlorate ions at 161 to 425 mg/L Mg ions, but then decreases at 857 mg/L Mg. The lifetime of IrTa appears to increase to a maximum and then decrease to uniformity with increasing Mg concentration.

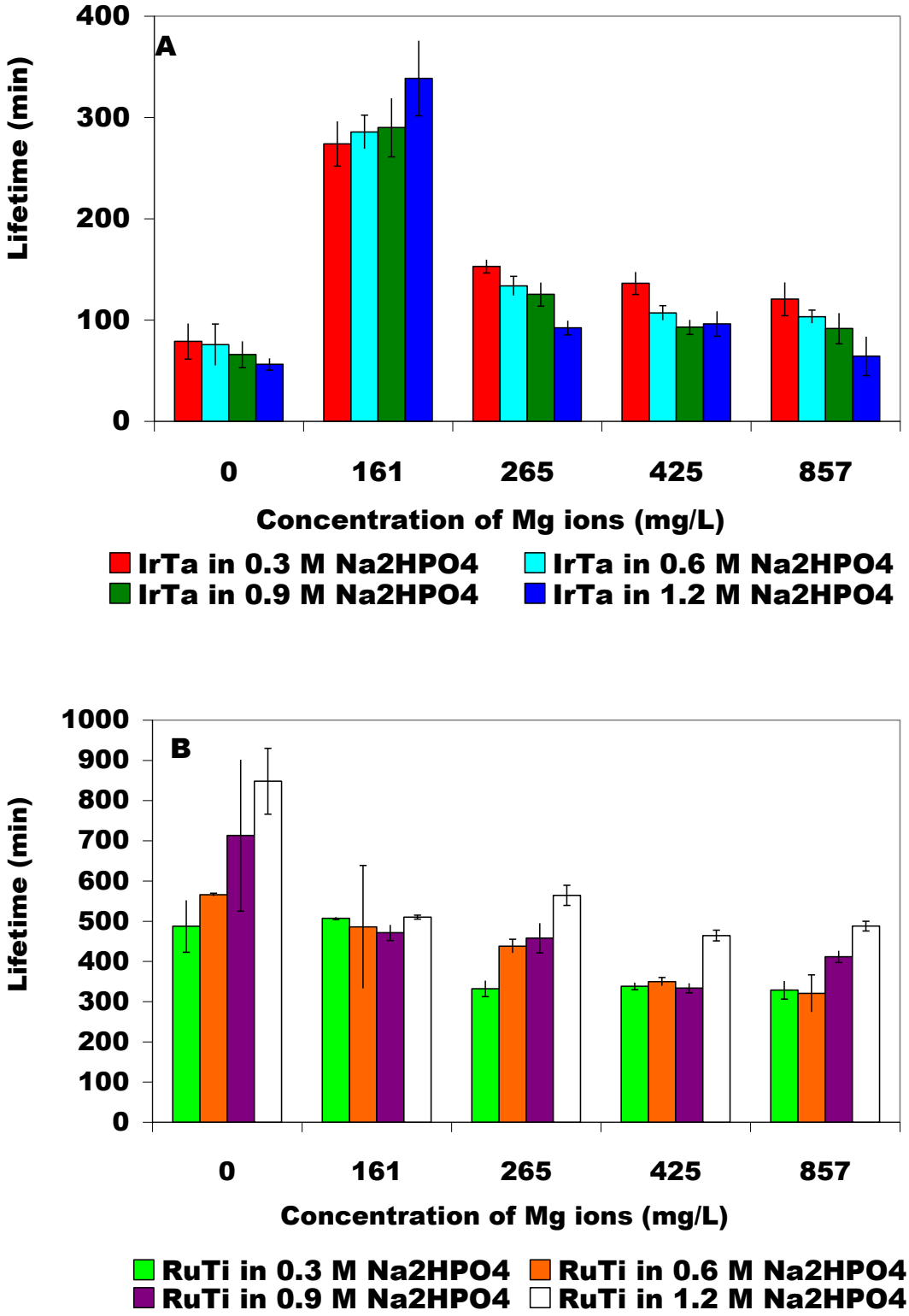

Figure 65 Effect of hydrogen phosphate and Mg ions concentration on electrode lifetime at 1200 A/m^2, 0.026 M Cl^-, 0.1 Hz. Plot A for IrTa and B for RuTi.

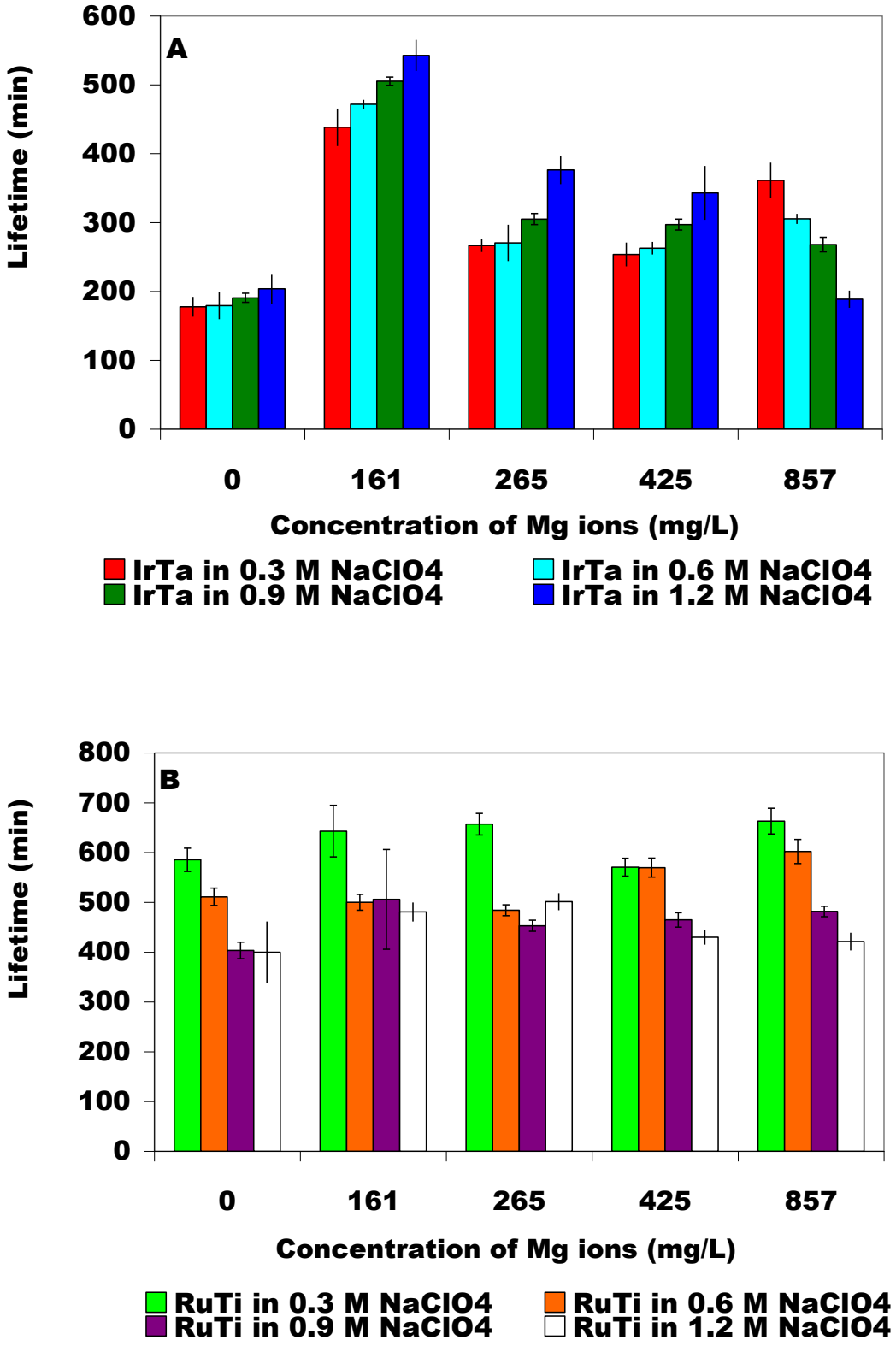

Figure 66 Effect of perchlorate and Mg ions concentration on electrode lifetime at 1200 A/m^2, 0.026 M Cl^-, 0.1 Hz. Plot A for IrTa and B for RuTi.

In general, the lifetime of RuTi appears to decrease as a function of perchlorate ions, especially at 857 mg/L Mg. RuTi life as it relates to Mg hardness appears to show no defined trend, as lifetime of RuTi appears to be similar with increasing Mg concentration. It therefore seems Mg ions may have no effect on RuTi anode life.

In summary, the concentration of perchlorate and Mg ions appear to influence IrTa lifetime. RuTi life appears not affected by increasing Mg concentration. Perchlorate ions appear to distinctly affect RuTi life only at 857 mg/L Mg concentration.

3.4.2.2 EDS and SEM Analysis from Chronopotentiometric Examination

From the few reports gleaned from the literature [1, 2, 146, 198] on current reversal, the two electrodes investigated were expected to have shorter lifetimes in the hard water tests than in the absence of water hardness (without hard water ions) under current reversal electrolysis. However, the electrodes appear to have similar or longer lifetimes in the presence of Ca and Mg ions. As this was an accelerated lifetests, parameters selected were to accelerate failure of the electrodes examined under laboratory conditions. Ca and Mg were observed not to have deposited on the CTEs in hard water as the current reversal cycle frequency of 0.1 Hz (10 seconds) appear to have been too short. This does not appear to be the case in practice. As reversal times of 1-10 minutes [2, 146] and 20-30 minutes [1, 198] for water treatment applications have been reported in the literature.

Chronopotentiometry was therefore used to determine whether or not Ca or Mg was deposited on the CTEs during the hard water tests in the three electrolytes ($NaNO_3$, Na_2HPO_4, and $NaClO_4$) examined. The tests were carried out for 1 hour in 1.2 M of of

the supporting electrolytes. The results are presented in Table 9. The table reveals that the amounts of Ca and Mg deposited on IrTa were insignificant. Similarly, the amounts of Ca and Mg deposited on RuTi were also insignificant, except for Ca in nitrate (425 mg/L) and Ca in hydrogen phosphate (425 and 857 mg/L) where the values seem high. Since the error values are also high for these observed deviations, it appears the recorded values may not represent their true values.

The results presented for the two sets (0-25 minutes and 1 hour) of chronopotentiometric times investigated reveals that Ca and Mg were deposited, however, in insignificant amounts. This, then, suggests that, the amounts of Ca and Mg

Table 9 EDS At % amounts of Ca and Mg deposited from chronopotentiometry for 1 hour in 1.2M electrolyte.

Electrolyte	**Hard water (mg/L)**	**Deposits on IrTa Anode**				**Deposits on RuTi Anode**			
		At % Ca	**Error**	**At % Mg**	**Error**	**At % Ca**	**Error**	**At % Mg**	**Error**
$NaNO_3$	265	0.59	0.34	2.02	0.8	0.75	1.12	2.79	3.29
	425	0.64	0.98	2.19	0.75	23.31	57.62	1	0.58
	857	1.19	0.94	2.99	1.42	1.15	1.62	0.37	0.25
$NaClO_4$	265	0.42	0.24	2.91	1.52	0.29	0.62	0.33	0.29
	425	1.13	0.58	3.74	2.85	0.16	0.3	0.52	0.43
	857	0.46	0.19	2.73	1.15	0.15	0.28	12.23	18.2
Na_2HPO_4	265	0.49	0.63	0.37	0.64	0.95	1.57	1.69	1.44
	425	0.42	0.89	1.9	1.16	36.89	78.97	2.12	2.2
	857	1.21	0.91	1.58	1.03	17.62	45.16	1.62	1.04

deposited during the hard water tests were minimal, and probably removed by the short polarity reversal times used as would be expected.

The CTE samples investigated by chronopotentiometry (CP) were also examined by SEM. The SEM images for IrTa and RuTi anodes examined in nitrate in the presence of Ca and Mg are shown in Figures 67 to 70. It is clear from the images that visible signs of granules of Ca deposition are seen on the RuTi anode at the 15 to 25 minutes time period (Figure 69). Mud-like coverings is also observed on the IrTa anode tested in Ca and Mg ions (Figures 67 and 68), and this is particularly visible at the 15 and 20 minutes time period.

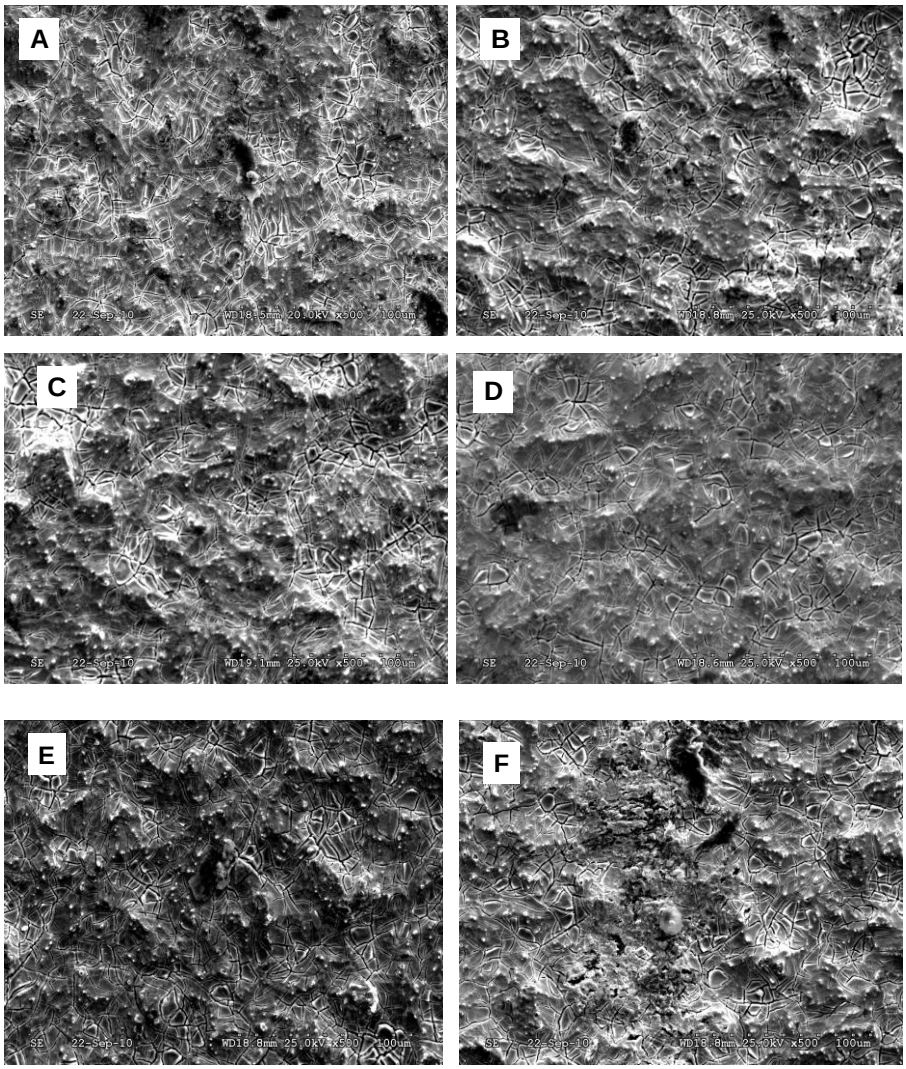

A= Fresh IrTa
B= 5 min
C= 10 min
D= 15 min
E= 20 min
F= 25 min

Figure 67 SEM micrographs of IrTa by chronopotentiometry as function of time of operation in 1.2 M $NaNO_3$, 857 mg/L Ca ions, -1200 A/m^2, 0.026 M Cl^-.

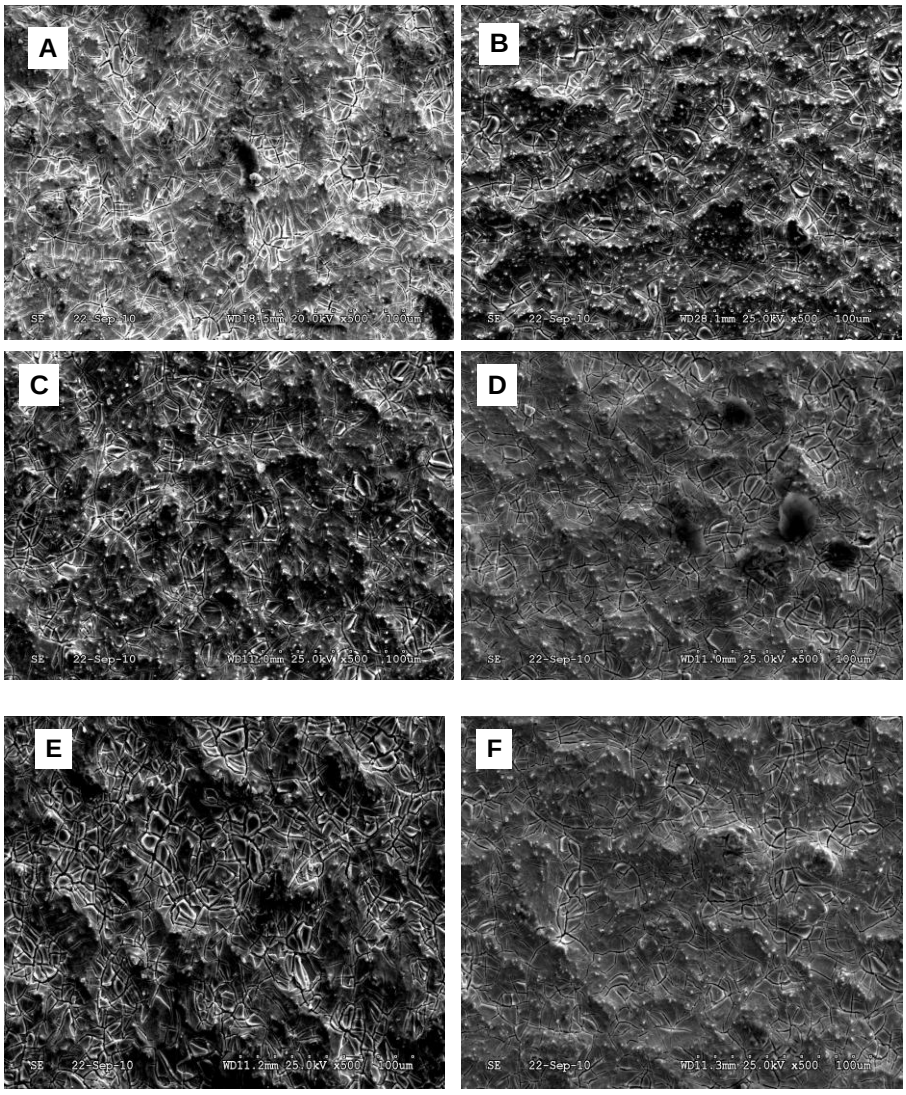

A= Fresh IrTa
B= 5 min
C= 10 min
D= 15 min
E= 20 min
F= 25 min

Figure 68 SEM micrographs of IrTa tested by chronopotentiometry as function of time of operation in 1.2 M $NaNO_3$, 857 mg/L Mg ions, -1200 A/m^2, 0.026 M Cl^-.

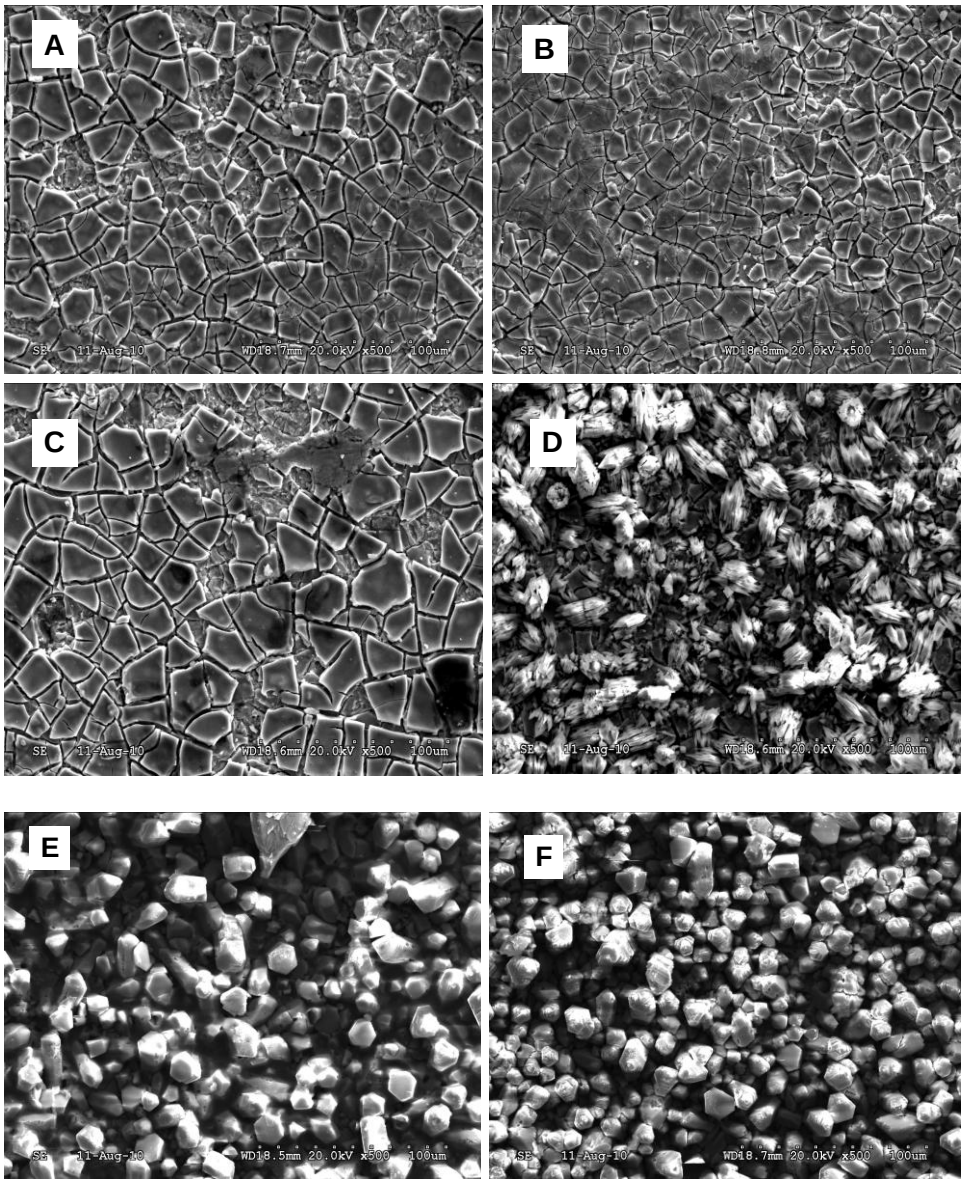

A= Fresh RuTi
B= 5 min
C= 10 min
D= 15 min
E= 20 min
F= 25 min

Figure 69 SEM micrographs of RuTi tested by chronopotentiometry as function of time of operation in 1.2 M $NaNO_3$, 857 mg/L Ca ions, -1200 A/m2, 0.026 M Cl^-.

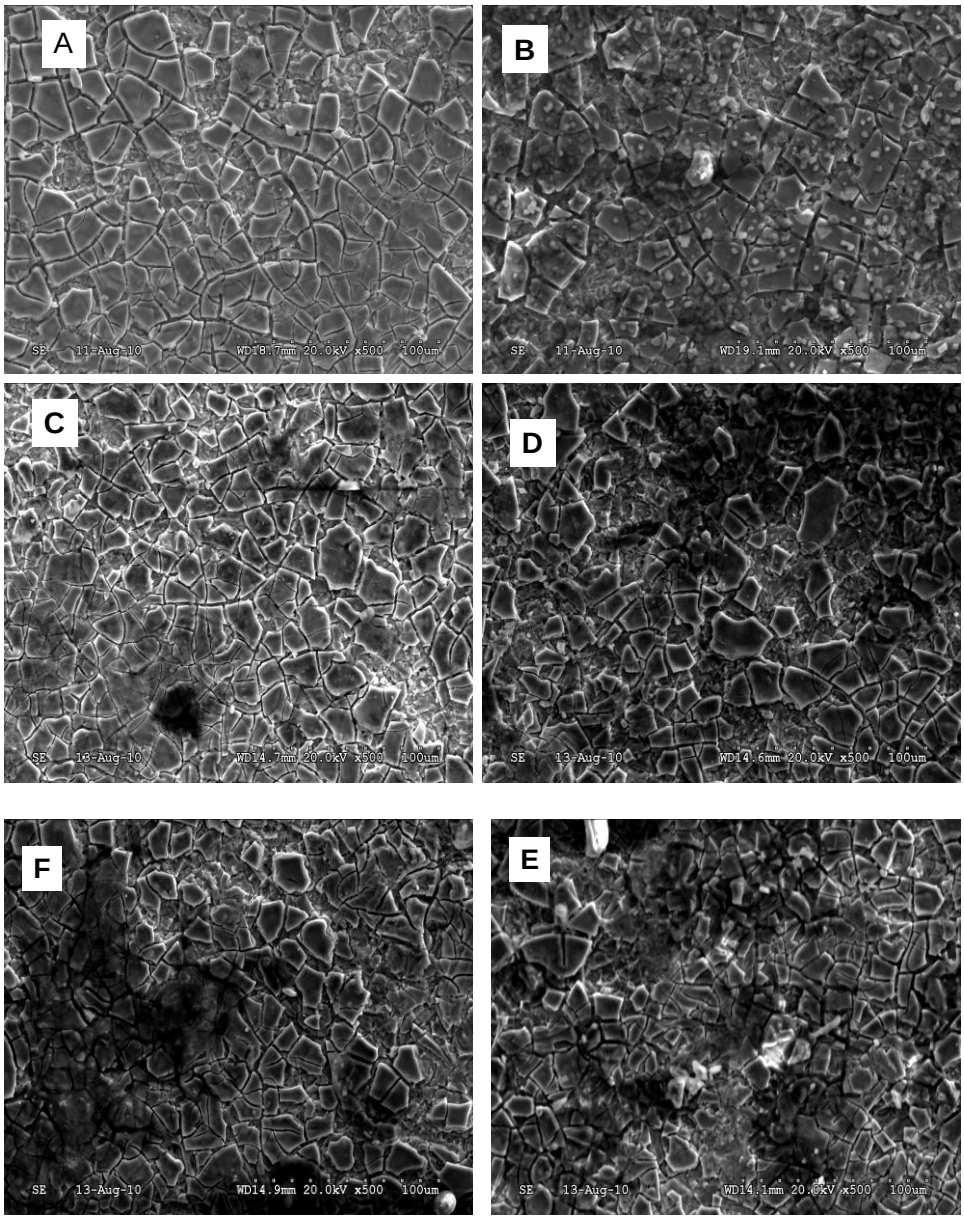

A= Fresh RuTi
B= 5 min
C= 10 min
D= 15 min
E= 20 min
F= 25 min

Figure 70 SEM micrographs of RuTi tested by chronopotentiometry as function of time of operation in 1.2 M $NaNO_3$, 857 mg/L Mg ions, -1200 A/m2, 0.026 M Cl^-.

CHAPTER 4

FAILURE ANALYSIS OF COATED TITANIUM ELECTRODES

The main aim of this work was to investigate the effects that periodic polarity reversal have on the lifetimes of coated titanium electrodes during the electrolysis of chloride containing water. The failure of the two commercial electrodes (IrTa and RuTi) examined under current reversal and hard water electrolysis conditions are thoroughly discussed. The mechanism of deactivation of the electrodes will be emphasized with supporting evidence and references where possible as there is not much information in the open literature about the current reversal technique even though it is been used widely in practice.

4.1 Current Reversal Electrolysis

Two types [199] of reactions take place at CTEs. The reactions can occur at substrate/coating and/or coating/electrolyte interfaces in the electrolysis cell, which ultimately results in electrode failure over time. These reactions may be classified broadly as faradaic and nonfaradaic reactions. Faradaic reactions are charge transfer reactions which leads to product formation in electrochemical cells, and in the present work the products formed are Cl_2, H_2 and O_2 gases. The nonfaradaic reactions involve

processes such as adsorption and/or desorption of species and/or complexes at the interfaces. Changes in potential, electrolyte composition and concentration, or electrode area causes nonfaradaic occurrences at the electrode/electrolyte interface.

The lifetimes and failure pattern observed for the electrodes investigated (in the different anions, hard water, and under three electrolysis variables) can be explained by faradaic and nonfaradaic [199] reactions occurring at the coating/electrolyte and/or substrate/coating interface. These reactions can cause coating dissolution, substrate passivation or coating passivation which ultimately leads to CTEs failure. Dissolution [2, 137] of CTEs can occur in either basic or acidic supporting electrolytes. Supporting electrolyte used in this investigation varied from neutral to basic. The Ti substrate in the CTEs can passivate in the presence of H_2O and/or oxygen due to formation of TiO_2. The effective coating area available for reaction can be reduced through coating passivation. Coating coverage can be caused by species and/or ion adsorption. The factors likely to have caused failure of the CTEs investigated are discussed in the sections following.

4.1.1 Failure Analysis of Coated Titanium Electrodes

4.1.1.1 Energy Dispersive Spectroscopic Analysis

EDS data for the CTEs show that the coating was probably dissolving with time. EDS values for IrTa and RuTi electrodes are shown in the plots in Figures 71 to 75. The plots of Figures 71 to 74 show the percentage amounts of Ir, Ta, Ru and Ti versus normalized current reversal time (the ratios of the current reversal time (t) to failure time

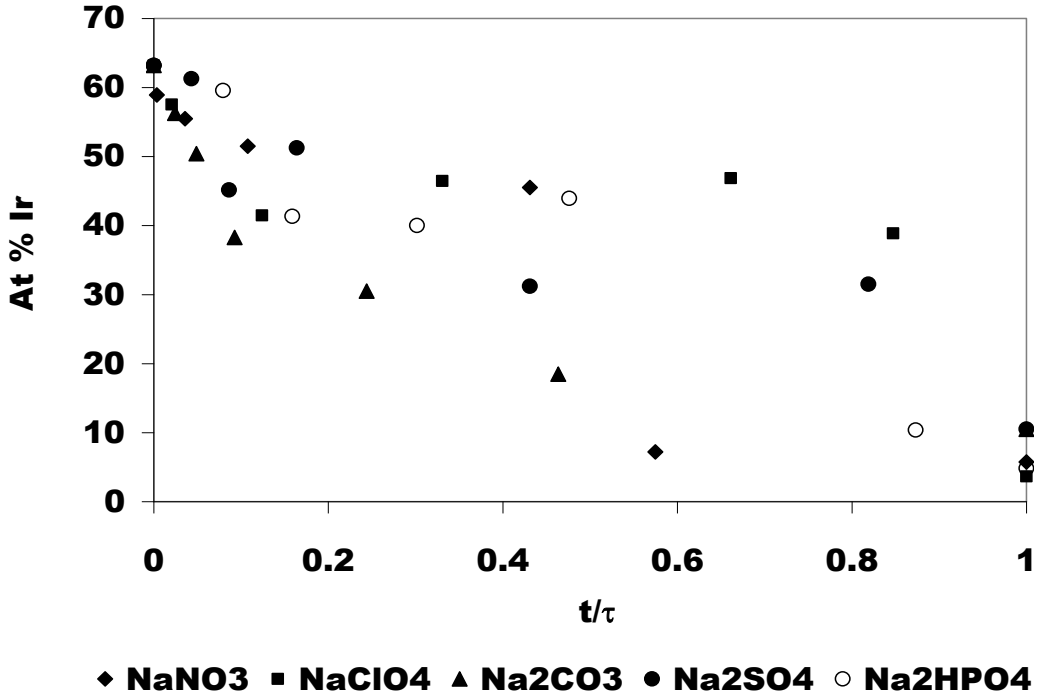

Figure 71 EDS values of At% Ir vs t/τ for IrO_2-Ta_2O_5 electrode in 1.2 M electrolytes, 1200 A/m^2, 0.043 M NaCl, 0.1 Hz cycle.

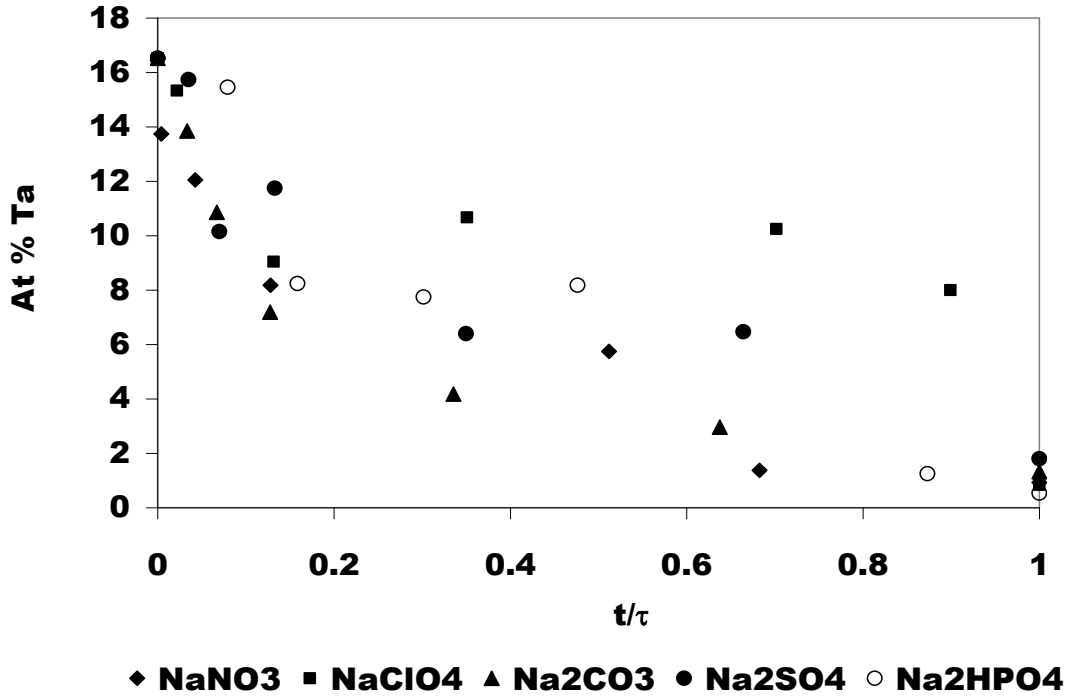

Figure 72 EDS values of At% Ta vs t/τ for IrO_2-Ta_2O_5 electrode in 1.2 M electrolytes, 1200 A/m^2, 0.043 M NaCl, 0.1 Hz cycle.

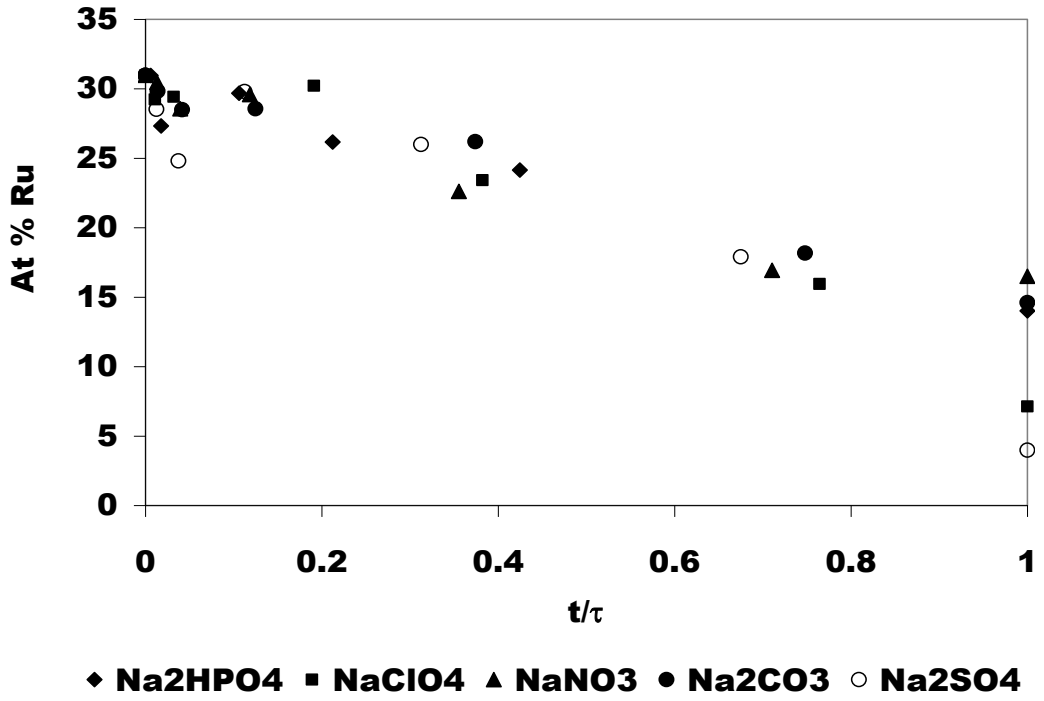

Figure 73 EDS values of At% Ru vs t/τ for RuO_2-TiO_2 electrode in1.2 M electrolytes, 1200 A/m^2, 0.043 M NaCl, 0.1 Hz cycle.

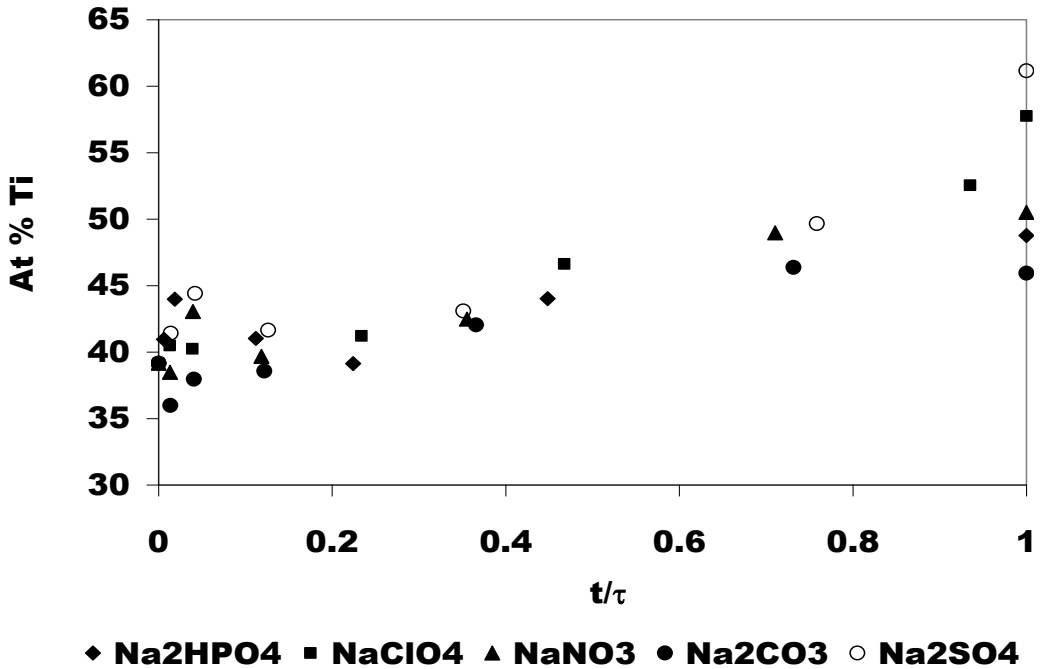

Figure 74 EDS values of At% Ti vs t/τ for RuO_2-TiO_2 anode in1.2 M electrolytes, 1200 A/m^2, 0.043 M NaCl, 0.1 Hz cycle.

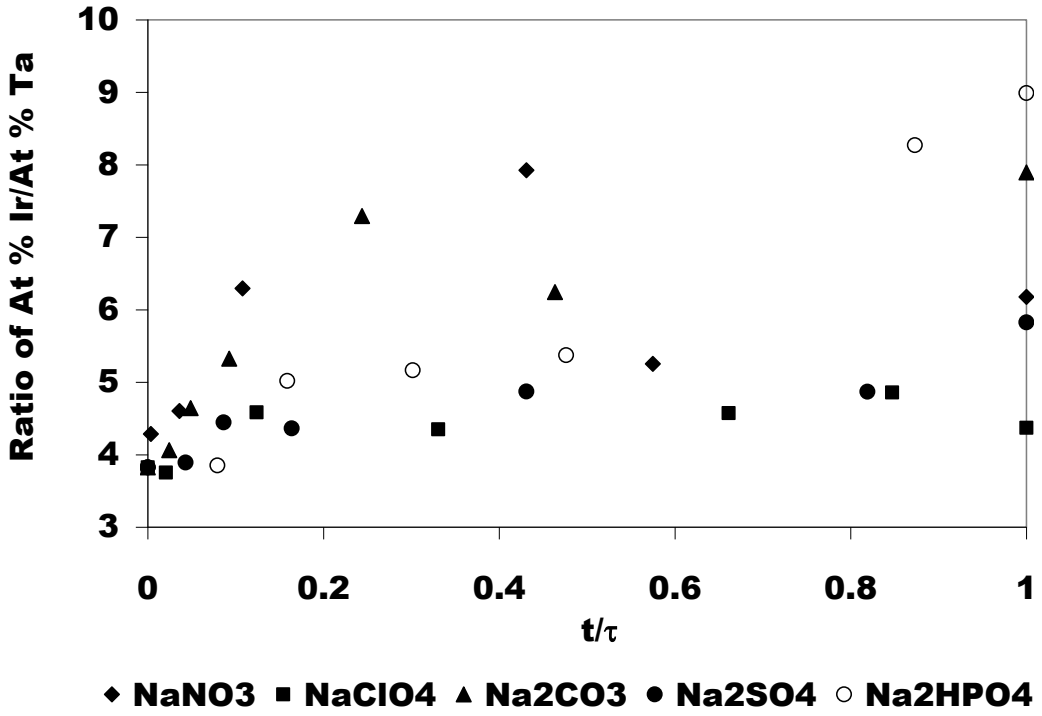

Figure 75 EDS values of Ir:Ta ratio vs t/τ for IrO_2-Ta_2O_5 anode in 1.2 M electrolytes, 1200 A/m^2, 0.043 M NaCl, 0.1 Hz cycle.

(τ)). The plot in Figure 75 show the dependence of the ratios of the precious metal component to the nonprecious metal component for IrTa versus normalized current reversal time (t/τ).

As can be seen in Figures 71 to 73, the percentage amounts of Ir, Ta and Ru decreased as a function of the normalized time. This indicates the dissolution (or consumption) of these elements from their respective oxide coatings. This observation (for Ir, Ta and Ru) from the EDS results is corroborated by the XRF results presented in Chapter 3. This reinforces the hypothesis that the coated titanium electrodes failed in part by a dissolution mechanism. The plot of Figure 74 shows the amount of Ti increasing as

a function of normalized time. This increase can be explained by the exposure of the Ti substrate to the SEM electron beam as the coating is dissolved. The Ti substrate gains more exposure as more coating is dissolved.

Figure 75 shows that Ta dissolves slightly faster than Ir as the Ir/Ta ratio increases. This same comparison can not be made for Ru/Ti ratio, as the At % of Ti values recorded by the electron beam for the RuTi electrode is likely to be influenced by exposed Ti substrate as the coating in RuTi dissolves.

All the electrolytes as evidenced by the plots appear to act in a similar manner when plotted against t/τ. This indicates that the coatings fail in a similar manner as a function of percent of lifetime. That is, in spite of the fact that the coatings have different failure times in all the electrolytes examined, their lifetimes in these electrolytes appear to be influenced by the same factors as revealed by the common pattern seen in their curves. Dissolution is thus far identified as a factor which contributed to coating failure of the two electrodes examined.

It is believed that since all the coating on the CTEs was not consumed in all the electrolytes (particularly for the RuTi electrode) suggests that dissolution alone can not account for the failure of the electrodes. Another deactivating factor such as passivation is believed to set in, as the exposed Ti substrate comes into contact with the electrolyte, leading to the eventual failure of the electrodes. These two factors (dissolution and/or passivation) may act sequentially or in combination to cause the failure of the CTEs.

In summary, it has been demonstrated by EDS analysis that dissolution occurs for each electrode in each electrolyte. The rate of dissolution differs by electrodes and electrolyte. As some coating is remaining at failure, passivation is also likely.

4.1.1.2 Scanning Electron Microscopic Analysis

The SEM micrographs shown in Chapter 3 for IrTa and RuTi revealed that the coating was dissolving gradually over time during current reversal electrolysis. Most of the micrographs showed the presence of residual coating even after the electrode's failure. Figure 76 presents representative micrographs of the surface morphological features of CTEs before and after failure in current reversal electrolysis.

The micrographs compare the surface features of fresh CTEs with tested CTEs in the electrolytes in which they had the longest and shortest lifetimes. The IrTa electrode had the longest lifetime (1392 min) in nitrate ions and the shortest lifetime (63 min) in hydrogen phosphate ions. Micrographs B and C for IrTa anode appear to show for the most part the Ti substrate with little residual coating at failure, suggesting that dissolution was the main cause of electrode failure. Micrographs B and C appear to show the rough surface Ti substrate. Micrograph A shows the surface morphological features typical of fresh IrTa, dried mud- like micro-cracks.

RuTi anode had the longest lifetime (848 min) in hydrogen phosphate ions and the shortest lifetime (361 min) in carbonate ions. As can be seen from micrographs E and F, the RuTi electrode appears to show the same amount of residual coating in hydrogen phosphate ions (micrograph E) as in carbonate ions (micrograph F). The fresh RuTi surface features as seen in micrograph D shows the characteristic mud-like cracks with "islands" observed in some places. Micrographs E and F for RuTi, however, appear to show features of larger areas of coating depletion and more uneven cracks in the residual coatings.

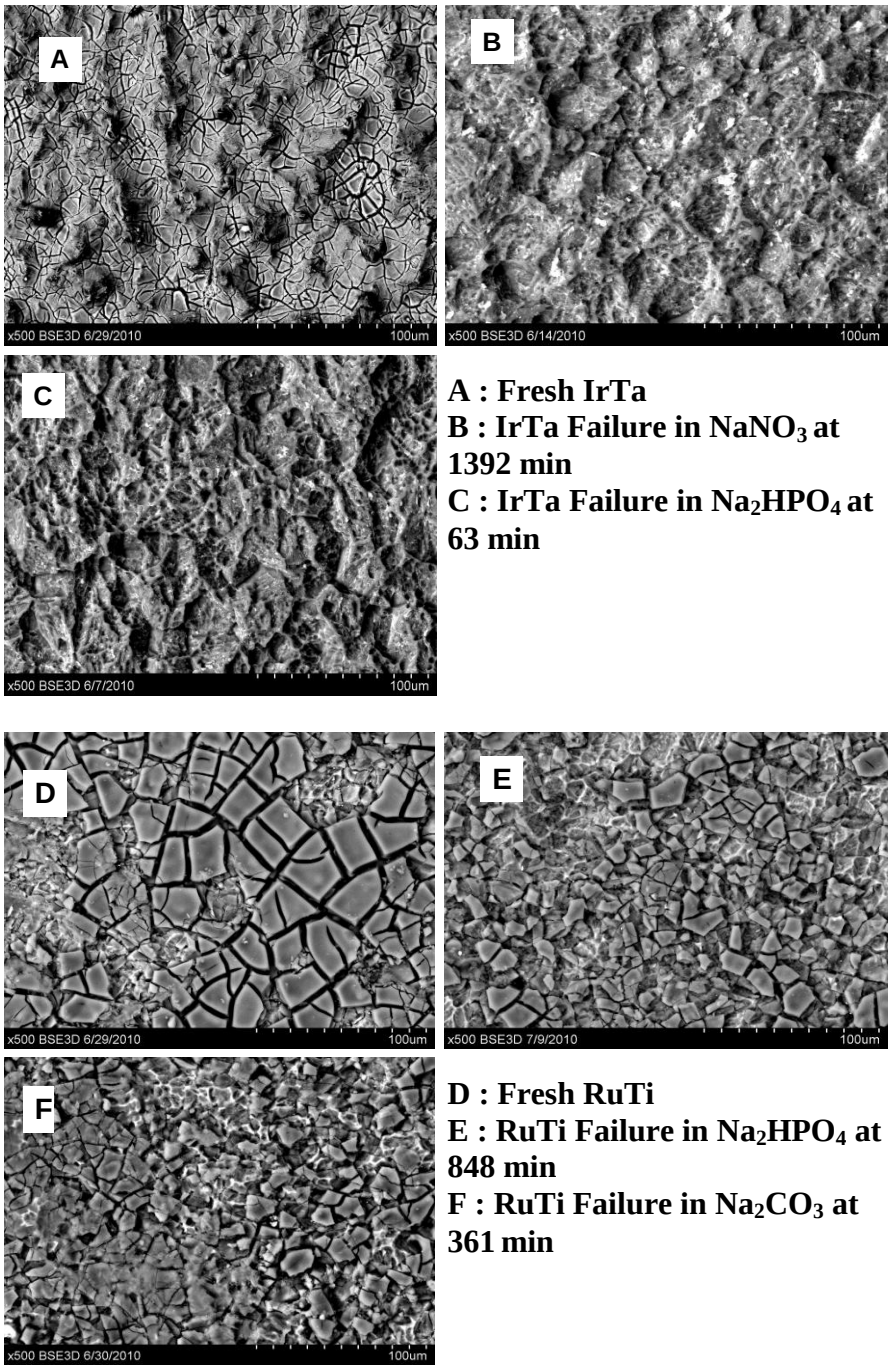

Figure 76 SEM micrographs depicting A/D: fresh CTEs, B/E: CTEs showing longest lifetime after failure, C/F: CTEs showing shortest lifetime after failure.

The micrographs shown in Chapter 3 and Figure 76 clearly reveal that coating dissolution occurs as a function of current reversal time. Micrographs of the failed electrodes show some amount of residual coating even after failure.

This suggests that coating dissolution is not the only mechanism that caused the electrodes examined to fail. The presence of the residual coating, clearly, indicates that passivation and/or adsorbed surface species mechanisms ultimately caused failure of the CTE. Other researchers have observed the same deteriorating effects with electrolysis time under straight polarity for IrTa [185] and RuTi [200]. The present work and the cited works show that CTEs will ultimately fail, whether employed in straight polarity or reverse polarity applications.

In summary, the micrographs presented and discussed indicate that CTEs dissolve overtime under current reversal electrolysis. The fact that residual coating was left after failure of some electrodes suggest that passivation and/or adsorbed surface species at the substrate and/or coating interfaces are mechanisms that contributed to electrode failure.

4.1.1.3 Equilibrium Stability Diagrams for Oxides of Iridium and Ruthenium

Dissolution is one of the mechanisms identified as been responsible for coating failure of the CTEs investigated. Coating stability can be examined using Eh-pH diagrams. Phase stability diagrams [201-203] have inherent limitations. They are valid only under equilibrium conditions, and the phases shown in the diagrams are regions for the dominant species. Other soluble species apart from the dominant one can also be present in a region. Stability diagrams do not provide information regarding the duration

for achieving the stated phase stability. In spite of the limitations mentioned, stability diagrams are able to predict the dominant species formed under equilibrium conditions

Equilibrium stability diagrams for Ir, Ru, Ta and Ti oxides are shown in Figures 77 to 80. The Eh-pH diagrams were developed by adopting some of the needed equilibrium equations from Pourbaix [201]. The CTEs were examined in 1.2 M of each of the five anions under current reversal conditions to determine their potentials versus Ag/AgCl reference electrode. The initial and final pHs were measured. The anode and cathode potentials were also determined. The measured final pH, anode and cathode potential values were then superimposed on the Eh-pH diagrams developed from the Pourbaix equilibrium equations.

From the SEM, EDS and XRF analysis, the failure of the CTEs involves dissolution. The anodic dissolution of the CTEs is a corrosion related reaction through oxidation of the metal components in the coatings [204-205], and since Eh-pH diagrams [202-203] are able to predict regions of corrosion for stable non-soluble species as well as stable soluble species, these diagrams were used to elucidate information to further explain the coating dissolution process. From Figures 77 to 80, the stable [202-203] non-soluble species are the uncharged oxides or metal (examples are Ir, IrO_2, IrO_3, Ru, RuO_2, Ta, Ta_2H, Ta_2O_5, TiH_2, Ti_5O_9, TiO_2) and stable soluble species are charged oxides (examples are IrO_4^{2-}, RuO_4^{2-}, TaO_2^{+}). RuO_4 is a stable gaseous species.

Straight polarization causes anodic oxidation and dissolution of coatings [204-205]. This dissolution may occur gradually over time. However, periodic polarity reversal of the electrodes exacerbates the dissolution problem through destabilization of the

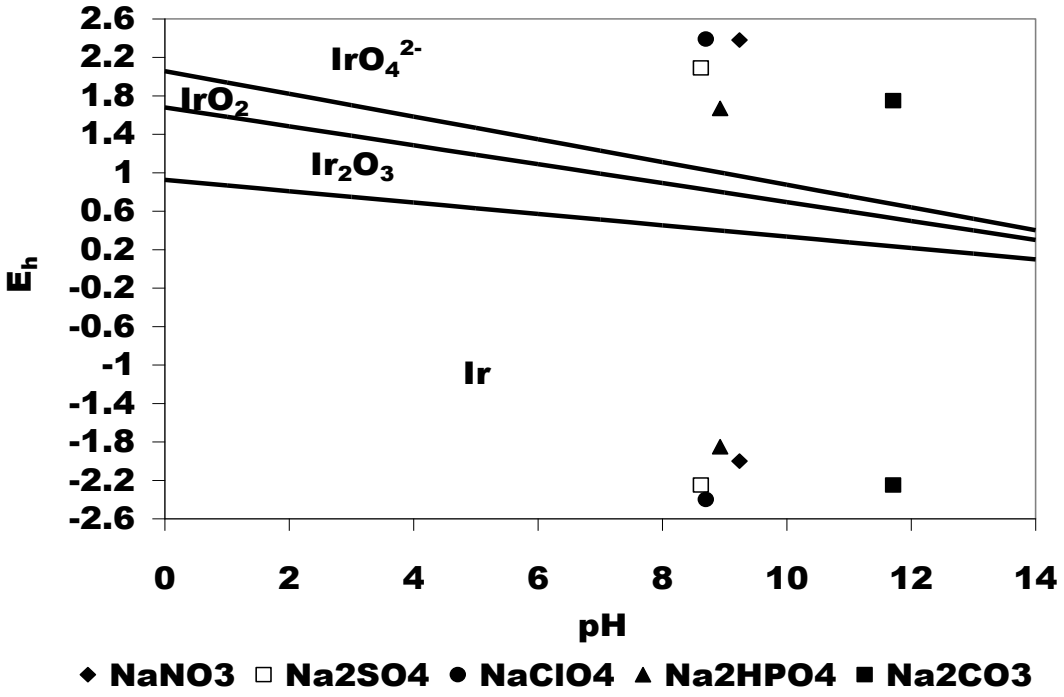

Figure 77 Stability diagram for oxides of iridium at 25°C, 1 atmosphere, 1.2 M electrolyte concentration.

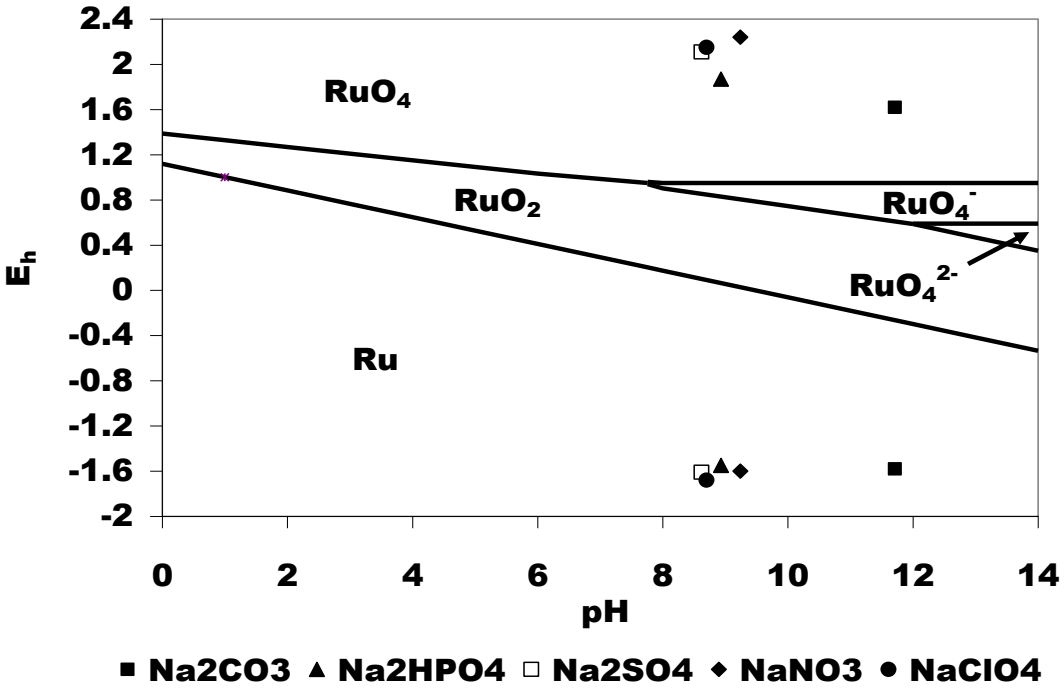

Figure 78 Stability diagram for oxides of ruthenium at 25°C, 1 atmosphere, 1.2 M electrolyte concentration.

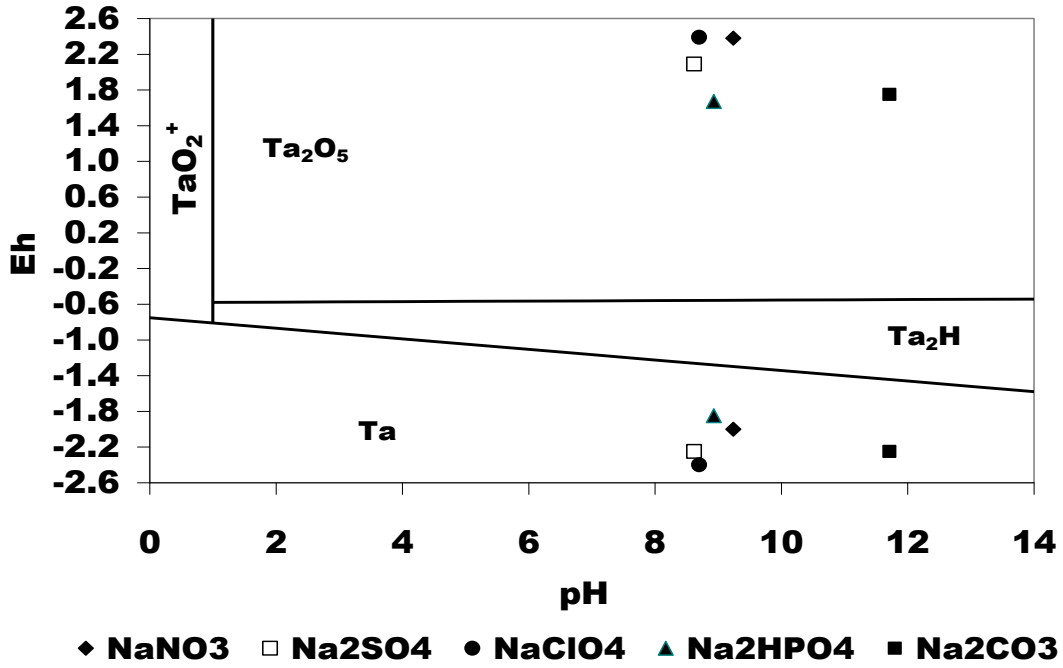

Figure 79 Stability diagram for oxides of tantalum at 25°C, 1 atmosphere, 1.2 M electrolyte concentration.

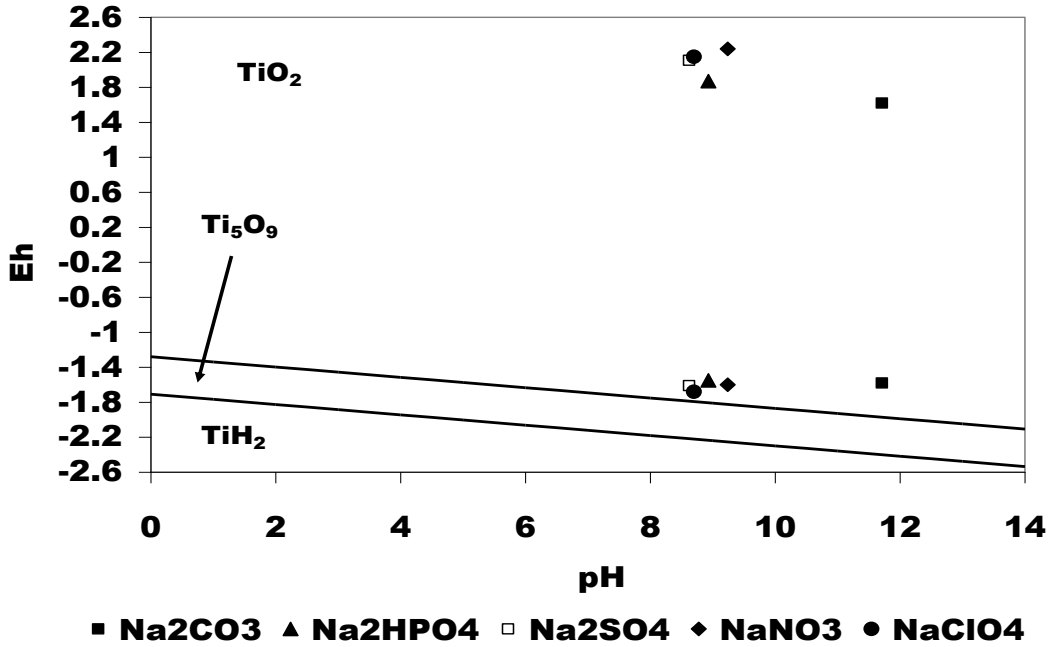

Figure 80 Stability diagram for oxides of titanium at 25°C, 1 atmosphere, 1.2 M electrolyte concentration.

coating and its properties. In the polarity reversal technique employed, the electrodes were switched every 5 seconds from highly reducing to highly oxidizing conditions and vice versa as seen in the plots, which damages [147] the coating of the CTEs and thus reduces electrode life.

Phase transitions of IrO_2, RuO_2, Ta_2O_5 and TiO_2 in the Eh-pH diagrams as shown in Figures 77 to 80 can lead to coating dissolution. The IrTa stability plot (Figure 77) shows that IrO_2 can be oxidized to a higher valent state of +6 (IrO_4^{2-}) at higher oxidizing potentials. The IrO_4^{2-} is a soluble species and can therefore dissolve, thus causing coating instability. IrO_2 can be reduced to Ir metal at higher reducing potentials. This may probably also cause the IrTa oxide coating to dissolve. IrTa coating [23] failure is reported to be related to long term polarization at higher overpotentials of IrO_2.

According to the Eh-pH plot for RuO_2, RuO_2 (Figure 78) can oxidize to the volatile RuO_4 at higher oxidizing potentials, which can cause instability, and thus coating dissolution. RuO_2 can be reduced to the Ru metal at higher reducing potentials and may in the process cause coating dissolution. According to [23], in the presence of acids RuO_2 oxidizes to volatile RuO_4. In alkali media, RuO_2 can oxidize to the ruthenates (RuO_4^{2-}) and perruthenates (RuO_4^{-}). The stability diagrams shown suggest that RuO_2 can oxidize to volatile RuO_4 in basic media and high potentials.

Ta_2O_5 is stable at higher oxidizing potentials as shown in Figure 79. Also transitions between Ta_2O_5 and TaO_2^{+} may be likely, which can lead to coating instability as TaO_2^{+} is soluble specie. Ta_2O_5 can be reduced to Ta at higher reducing potentials which may cause coating dissolution. The Eh-pH for TiO_2 is shown in Figure 80. There are several oxides of Ti having lines similar to the line between Ti_5O_9 and TiO_2, however,

only Ti_5O_9 was chosen in addition to the TiH_2 and TiO_2 to illustrate the possible stability regions of Ti oxide. As can be seen from the plot of Figure 80 TiO_2 seems stable at both higher oxidizing and reducing potentials. Since TiO_2 is uncharged nonsoluble specie suggest that it may not be affected by the electrolytes at these potentials. But when the Ti substrate oxidizes to any of the stable oxides shown in Figure 80 will form a passivating layer to deactivate the electrode with time as this will impede current flow.

Many factors [23, 137] including potential and pH are reported to influence the deactivation mechanisms of CTEs. As shown in Table 10, the lifetimes of the electrodes investigated do not show any distinct relationship between anodic and cathodic potentials to the initial and final pH of the electrolytes. The electrolytes studied fall in the basic range. Higher pH and dilute chloride concentrations [23] favors O_2 evolution over Cl_2 due to occurrence of side reactions. The presence of O_2 ions on the substrate surface causes it to passivate over time.

According to [137], phosphates selectively reacts with Ta under straight polarity conditions, it is therefore not surprising that IrTa lifetime in hydrogen phosphate ions is low. It is possible that Ta also selectively reacts with perchlorates, carbonates and sulfates given the relatively lower lifetimes observed for IrTa in these electrolytes when compared to the longer lifetime exhibited by IrTa in nitrate. Furthermore, sulfates, phosphates and chlorides have been reported [206] to have a retarding effect on lifetime when adsorbed on RuTi under straight polarization; it is therefore possible this same effect can occur under polarity reversal conditions.

Table 10 Potential, pH vs lifetime values from current reversal electrolysis for IrTa and RuTi anodes in 1.2 M electrolytes at 1200 A/m^2, 0.043 M NaCl, 0.1 Hz cycle.

IrTa Electrode					
Electrolyte	**Lifetime**	**Anode Potential**	**Cathode Potential**	**pH**	**pH**
	(min)	**V vs SHE**	**V vs SHE**	**Initial**	**Final**
$NaNO_3$	1392	2.38	-2	7.14	9.24
$NaClO_4$	242	2.39	-2.4	7.64	8.7
Na_2CO_3	205	1.75	2.25	11.71	11.71
Na_2SO_4	116	2.09	-2.25	6.99	8.62
Na_2HPO_4	63	1.67	-1.85	8.86	8.93
RuTi Electrode					
Na_2HPO_4	848	1.87	-1.55	8.86	8.93
$NaClO_4$	471	2.15	-1.68	7.64	8.7
Na_2SO_4	400	2.11	-1.61	6.99	8.62
$NaNO_3$	380	2.24	-1.6	7.14	9.24
Na_2CO_3	361	1.62	-1.58	11.71	11.71

4.1.1.4 Voltammetric Charge Analysis

Surface charges, Q, as measured by CV are plotted versus normalized current reversal time are shown in Figures 81 and 82 for the oxide electrodes. The two plots show that surface charge increases to a maximum in all the electrolytes before declining. This is not unexpected as surface charge is related to the effective surface area of the CTEs. Thus, as the current reversal time increases and coating dissolution occurs as observed from SEM, EDS and XRF results, the coating expands as the electrolyte penetrates and opens up inner active sites located along cracks and pores. Consequently Q increases to maximum before declining as effective electrode surface area decreases with coating dissolution giving rise to the shapes observed for the Q versus t/τ curvese in Figures 81 and 82.

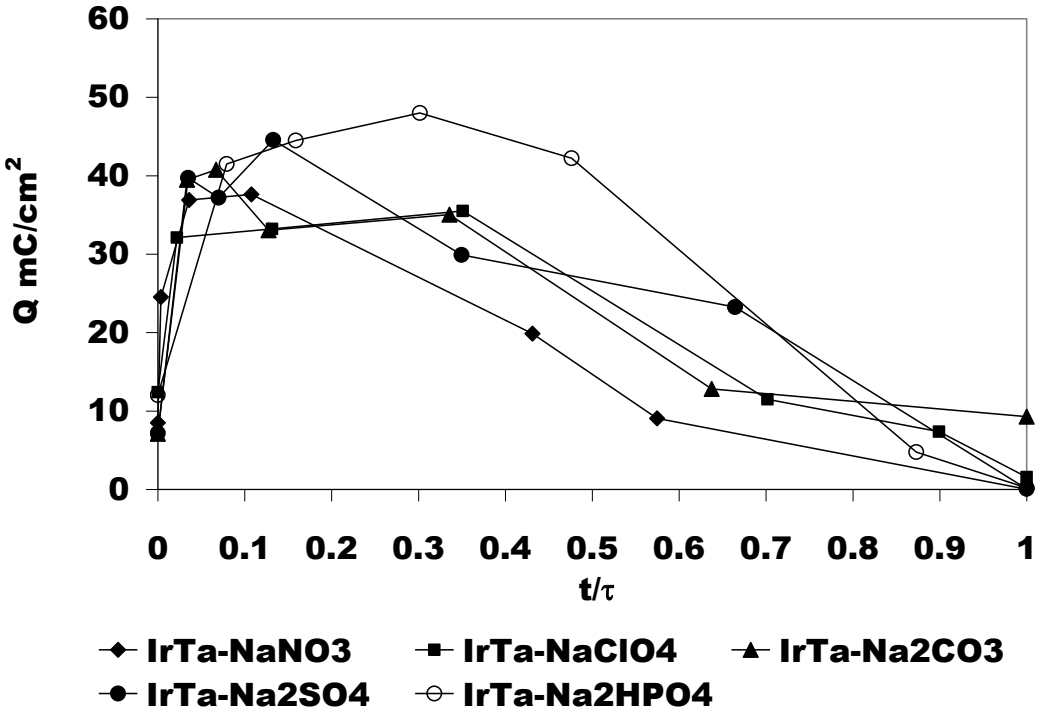

Figure 81 Charge vs t/τ for IrO_2-Ta_2O_5 in 1.2 M electrolytes, 1200 A/m^2, 0.043 M NaCl, 0.1 Hz cycle.

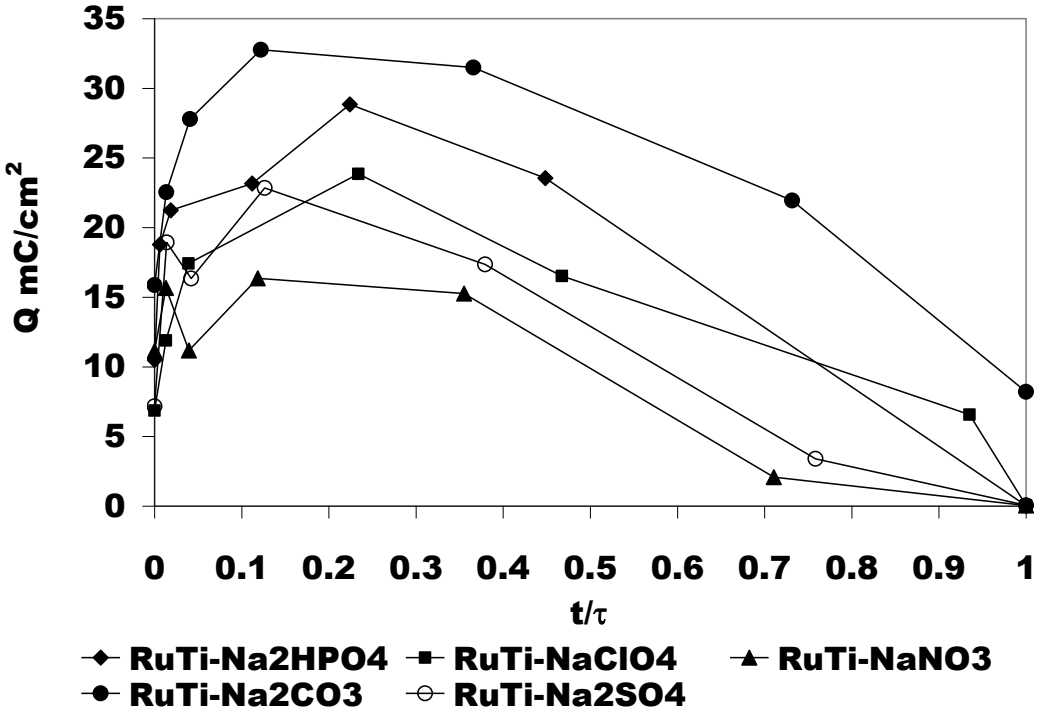

Figure 82 Charge vs t/τ for RuO_2-TiO_2 in 1.2 M electrolytes, 1200 A/m^2, 0.043 M NaCl, 0.1 Hz cycle.

The shapes of the curves appear similar in all the electrolytes examined suggesting that the electrodes may be influenced by the same failure mechanisms in the five electrolytes.

Two [6] mechanisms of charging of oxides surfaces are known. One is driven by electrode potential and the other by pH. The electrode potential mechanism acts on the metal ions where any charge variation is compensated by proton exchange with the electrolyte. The pH driven mechanism tend to act on the surface hydroxocomplexes of the oxide electrodes. Dissociation of the hydroxocomplexes form surface charges which are compensated by adsorption of ions from the electrolyte.

CTEs were examined by cyclic voltammetry in the different electrolytes and the surface redox response was typical of Ir and Ru. The redox response is related to redox reactions at the active sites of the surface of the electrodes, initiated by charge transfer reactions or proton exchange with the electrolytes as shown in equation 27, where M is the metal. A more general description of the surface redox reactions on the CTEs will be as given in equation 28 [6, 193].

$$M^{z} - OH \rightarrow M^{z+1} + O^{-} + H^{+} + e^{-} \tag{27}$$

$$MO_{x}(OH)_{y} + \delta H^{+}\delta e^{-} \leftrightarrow MO_{x-\delta}(OH)_{y+\delta} \tag{28}$$

The surface charge, Q, measures the number of protons exchanged with the electrolyte, and is obtained by integration of the voltammetric curves. Q therefore can be

taken to be proportional to the number of active sites, A, on the coating or the actual surface area of the CTEs, as given in equation 29. Furthermore [100, 207], for intermediates (species and/or complexes) formed in a charge transfer process, the surface coverage, θ, is related to the faradaic charge Q by equation 30.

$$Q = kA \tag{29}$$

$$Q = Q_1\theta \tag{30}$$

where Q is surface charge or faradaic charge, A is number of active sites on coating and k is the proportionality constant, Q_1 is the charge required to form a complete monolayer (or charge at $\theta = 1$).

According to equations 29 and 30, surface charge has a linear dependence on the number of active sites on coating and surface coverage. Equations 29 and 30 explain the trend observed in the plots of Figures 81 and 82 for the IrTa and RuTi electrodes. Surface charge as observed in the plots increases as a function of normalized current reversal time as the coating dissolves and opens inner active sites located along cracks and pores. This increase in surface charge appears to correspond to region I in the cell voltage versus time plot. Surface charge increases as long as more active sites on the electrodes become available for reaction. As the number of active sites are finite in nature, surface charge

eventually decreases as the number of active sites on the coating decreases through coating dissolution. At this point, the CTEs are considered deactivated.

At failure time, surface charge is observed to be nearly zero in the plots for the electrodes in the different electrolytes with the exception of the carbonate ions, indicating complete absence of effective coating area for reaction. However, since the EDS and XRF data indicate the presence of coatings after electrode failure suggests that passivation at substrate/coating interface may have occurred to impede the conduction and/or exchange of charges at the interface. Substrate passivation can set in as soon as coating dissolution occurs and electrolyte reaches the substrate. Even though the electrodes had different lifetimes in all the electrolytes, yet Figures 81 and 82 show the curves of Q versus t/τ plots appear to follow the same trend suggesting that the CTEs may be failing by the same mechanism in the different electrolytes studied.

In summary, surface charge has a linear dependence on the number of active sites on the coating and on surface coverage of the coatings. Surface charge increases as a function of normalized current reversal time to a maximum point before declining. As the number of active sites are finite in nature, surface charge decreases with time as the number of active sites decreases through coating dissolution. The CTEs are deactivated as a consequence.

4.1.1.5 Voltage Time Plots and Pseudocapacitive Effects of Coated Titanium Electrodes

The pseudocapacitance [100] observed for the CTEs in the different electrolytes examined can be explained by changes arising from charging effects with potential. In

addition, the differential capacitance at the electrode/electrolyte interface caused by changes in the coverage of the active sites of the electrode with potential leads to pseudocapacitance. Therefore, the pseudocapacitive behavior [207] of the CTEs is dependent on faradaic charge and surface coverage. During the charging process [208], species in the electrolyte may adsorb or desorb from the interface, and therefore, the structure of the interface may change. The evidence of pseudocapacitance in the present work can be seen by the bands formed by the curves in the voltage-time plots. Pseudocapacitance, Cps, [100, 207] changes as a function of charge and potential, surface coverage also changes as a function of charge and potential, therefore, they can be expressed by equations 30, 31 and 32.

$$Cps = \left(\frac{\partial Q}{\partial V}\right) = Q_1\left(\frac{\partial \theta}{\partial V}\right) \tag{31}$$

$$\theta = \left(\frac{2.303RT}{r}\right)\log(KC) + \left(\frac{F}{r}\right)V \tag{32}$$

where r is the rate of change of free energy with coverage, K is the equilibrium constant for adsorption, C is the bulk concentration of species being adsorbed, V is the potential. All other parameters assume their usual meaning.

A representative sample plot of pseudocapacitive behavior is shown in Figure 83. The band observed in the voltage-time plot which is caused by pseudocapacitance; is

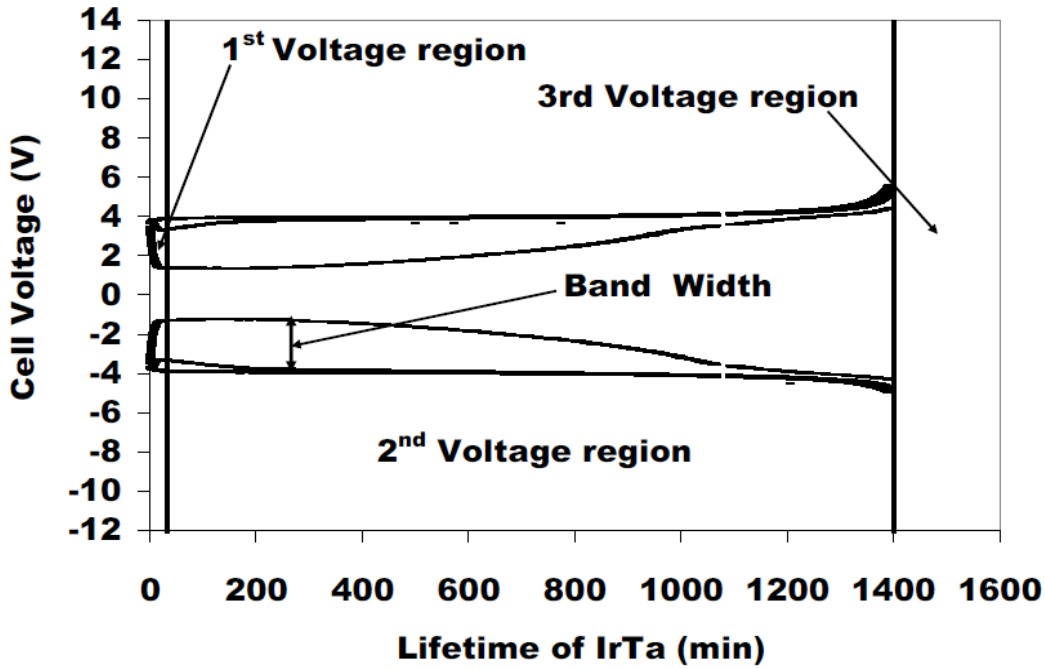

Figure 83 Voltage changes related to pseudocapacitive behavior of CTEs.

seen to broaden along the voltage axis, and becomes narrow as the electrode moves towards failure. Pseudocapacitance is dependent on charge (equation 31), and charge depends on the number of active sites available on the coating for reaction (equation 29). And according to equation 32, surface coverage increases as voltage increases. Pseudocapacitance therefore increases as a function of charge, and decreases as the number of coating active sites decreases by dissolution and/or coverage of the coating.

Three regions of voltage changes are observed for the bands formed in the voltage-time plot shown in Figure 83. The voltage changes also explain the pseudocapacitance changes occurring with time (equation 31). The first region involves an initial drop in the voltage at the start to first few minutes of the experiment. The

second region (covering most of the electrodes lifetime) is where the voltage rises in a fairly constant manner until it reaches a maximum. The third region (last stage of the electrode's life) is where the voltage rises sharply, indicating electrode failure.

The profiles of the Q versus t/τ curves are consistent with the pseudocapacitance and voltage changes observed in the voltage-time plots. As noted in the preceding paragraphs, pseudocapacitance [100, 207, 209] is a faradaic or non faradaic charge transfer reaction, which depends on the number of charges exchanged by the CTEs with the electrolytes. The number of charges exchanged is also dependent on the number of surface active sites available on the oxide coating.

At the start of the experiment, which is considered as the first voltage region, the number of charges exchanged is minimal and so is the pseudocapacitance. Electrolyte penetration to the inner active sites of the coating is also minimal. Faradaic reactions leading to gas evolution begin to occur at the surface of the electrodes in this region. As gas evolution occurs, coating dissolution is initiated in the region thus opening up inner active sites located along cracks and pores to more electrolyte contact. These initial occurrences may explain the reasons for the initial drop in voltage observed in the voltage time plots. In the second voltage region (which covers most of the electrodes lifetime) the number of charges exchanged increases as a function of voltage and electrolysis time as more accesss to the inner active sites of the coating is gained through coating dissolution and electrolyte contact. Pseudocapacitance also increases as a function of surface charge increases. This can be seen by the broadening of the bands along the voltage axis.

Finally, in the third voltage region, the number of charges exchanged decreases as the number surface actives sites on the coating decreases through coating dissolution.

Pseudocapacitance also decreases, and this is reflected in the narrow bands seen in the voltage time plots as the electrode approaches failure. This is supported by equation 31, which shows an inverse relation of pseudocapacitance with voltage.

The preceding discussion suggests that the size (width) of band seen in the voltage-time plot is correlated with amount of charges exchanged at the CTE/electrolyte interface. And the charges exchanged, are in turn correlated with number of active surface sites on the CTE. Therefore, suggesting that the charging behavior of the CTEs as observed in size of the band is related to the lifetime of the CTEs. That is, a wider band indicates larger pseudocapacitance, and for that matter, most probably longer lifetimes for the electrodes. The reverse is true for electrodes with narrower bands. They tend to fail much quicker than electrodes with broader and longer bands, as their pseudocapacitances are much smaller. It must be pointed out here that, the lifetimes (failure time) of the CTEs is made up of plateau time (time used for gas evolution) and charging time (time used for charging effects). Therefore, longer lifetimes of the CTEs do not ultimately result in the production of the desired products (Cl_2, O_2 and H_2 in this instance) as would be expected. This will be discussed in more detail later in the chapter.

An example plot to illustrate band size as it relates to lifetime is shown in Figure 84. The plot compares IrTa electrode in nitrate and hydrogen phosphate ions. The IrTa electrode had a lifetime of 23 hours in nitrate ions and 1 hour in hydrogen phosphate ions. It can be seen from the plot that IrTa has a much wider band in nitrate than in hydrogen phosphate ions. This appears to show that IrTa has much larger pseudocapacitance in nitrate than in hydrogen phosphate ions.

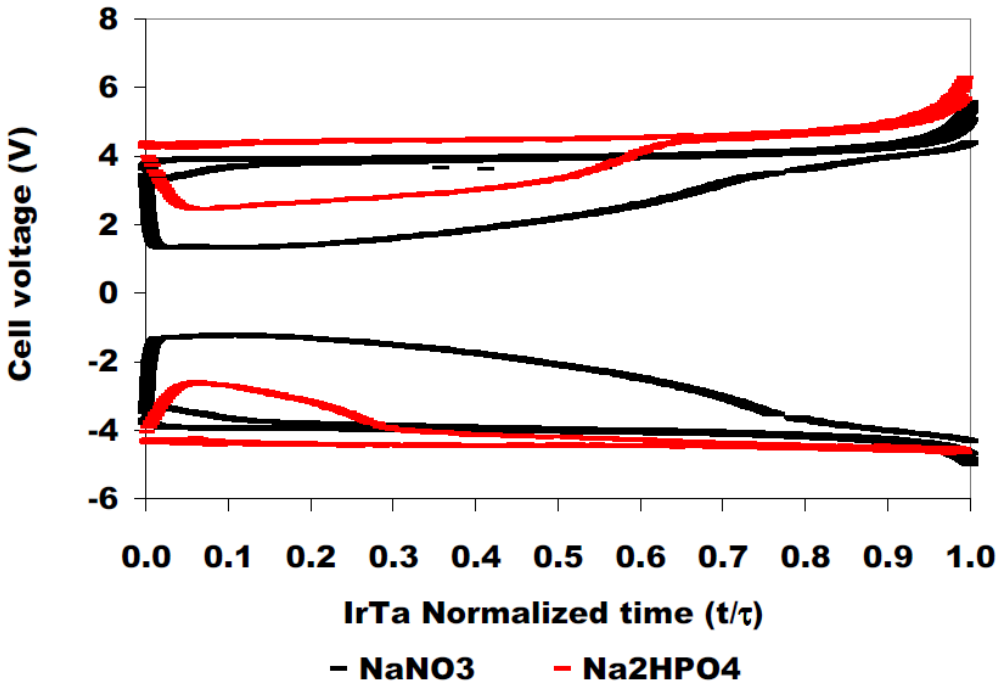

Figure 84 Comparison of cell voltage vs. t/τ for IrTa lifetimes in 1.2 M nitrate and hydrogen phosphate ions.

4.1.1.6 Band Widths from Pseudocapacitive Effects of Coated Titanium Electrodes

The sizes (widths) of the voltage bands observed for the CTEs in the cell voltage versus time plots, and caused by pseudocapacitive effects are plotted against normalized current reversal time (t/τ) in Figures 85 and 86.

The trend and shape of the curves observed in the band widths versus t/τ plots are somewhat similar with the trends seen in the Q versus t/τ plots for the CTEs (Figures 81 and 82). That is, the band widths rise to a maximum value with normalized time. Then

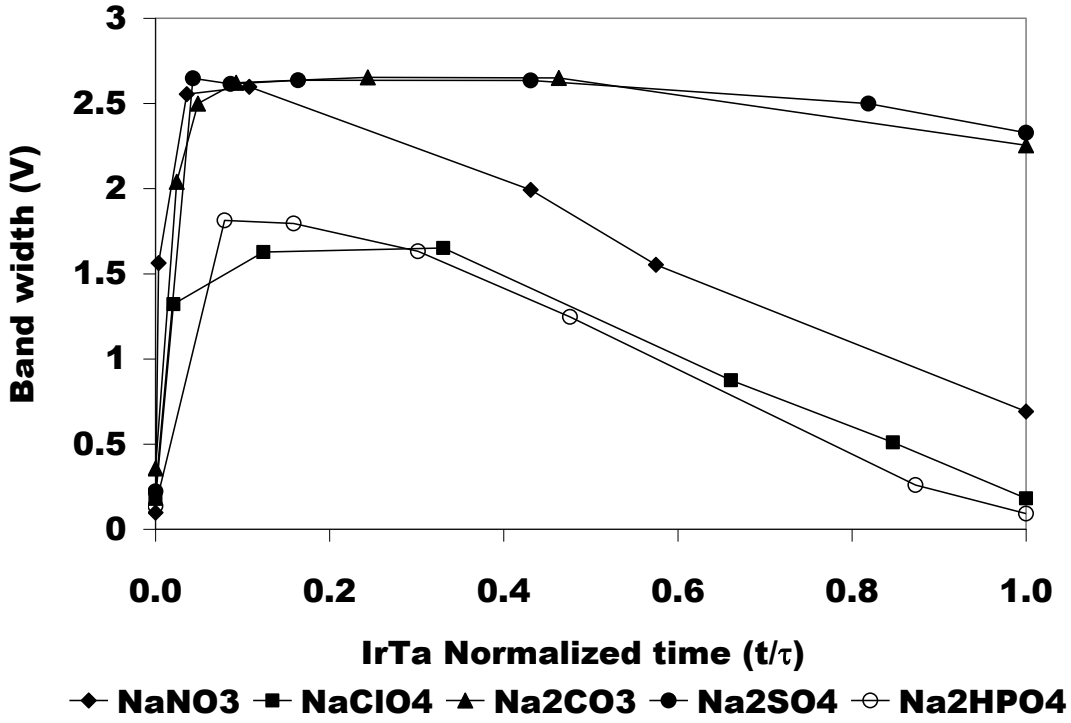

Figure 85 Band widths vs. t/τ for IrTa electrodes in five electrolytes examined.

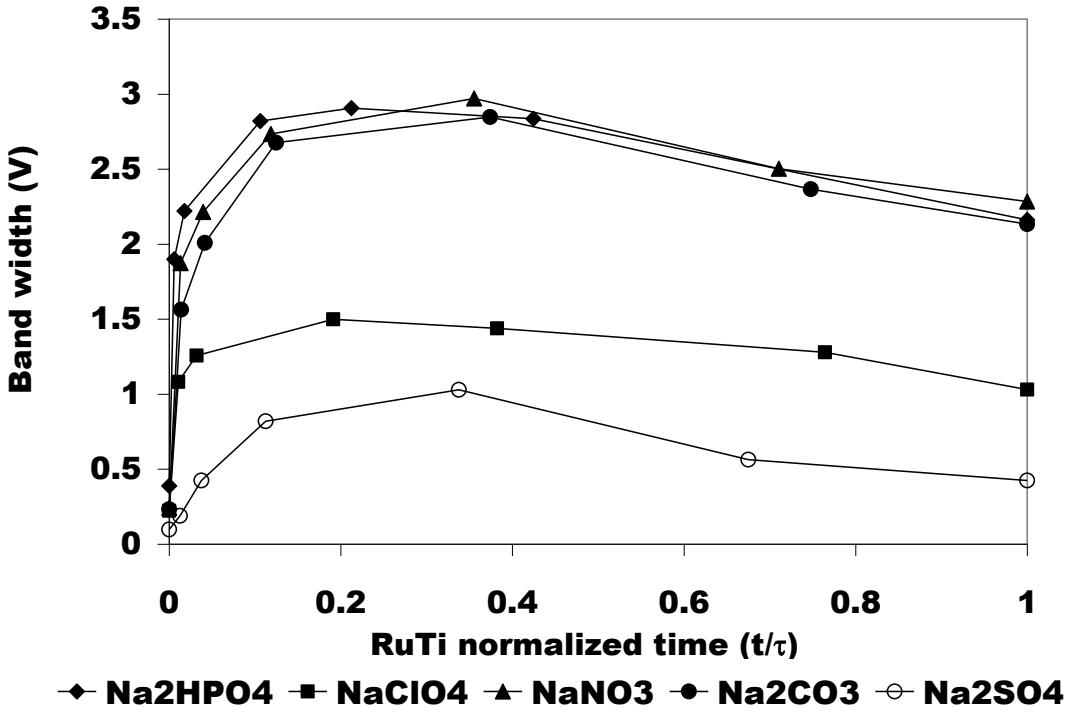

Figure 86 Band widths vs. t/τ for RuTi electrodes in five electrolytes examined.

the band size either stays constant or decline as seen in the plots. The observation reinforces the hypothesis that pseudocapacitance is dependent and/or related to charging reactions, which in turn, is dependent on the effective surface area of the oxide electrode's coating.

Furthermore, the band widths do not get to zero as observed in the plots as a result of the residual coating that remains on the electrodes after failure has occurred. In fact, the electrodes with more residual coating after failure appear to have large band widths as can be seen from the plots. For instance, IrTa anode had more residual coating remaining on it in sulphate and carbonate ions, and they incidentally appear higher in the plots than those with little residual coating. RuTi which had more residual coatings in hydrogen phosphate, nitrate and carbonate ions also show high band widths at failure. Clearly, this supports the notion that residual coating remained on the electrodes after failure.

In summary, pseudocapacitance is dependent on charge and surface coverage. The charges exchanged at electrode/electrolyte interface are a function of the number of active sites available on the coating, and the surface coverage is related to the species adsorbed at the interface. The bands seen in the V-T plots are related to the charging effects occurring at the CTE/electrolyte interface and are related to the pseudocapacitance effects at the interface. And so as charge exchanges increase, pseudocapacitance also increases and vice versa. As the number active sites available decreases, the charge decreases and so is the pseudocapacitance. The active sites decrease by coating dissolution and/or passivation.

4.1.1.7 Influence of Plateau and Charging Times on CTEs Life

Two critical factors, the plateau and charging times are discussed to determine their respective influence on the lifetime of the CTEs examined. The lifetimes of the CTEs reported so far is the total time to failure or failure time (τ_T). The failure time is composed of the plateau or gas evolution time (τ_P) and charging time (τ_C). The plateau time is the actual time used by the CTEs for gas evolution, and is related to the charge transfer redox reactions occurring at the CTE/electrolyte interface. The charging time, however, is the time expended for charging and discharging (adsorption and desorption of species and/or complexes) occurring at the CTE/electrolyte interface. Thus, the time to failure is the sum of plateau and charging times ($\tau_T = \tau_P + \tau_C$).

The τ_P was determined from the current reversal data by choosing the actual voltages (positive and negative) when gas evolution started to occur in the electrochemical cell. Positive voltage times within the time to failure range were summed up. This was repeated for the negative voltage times. The positive and negative voltage times (in seconds) were then added up and divided by 60 to obtain the plateau time in minutes. The τ_C was then determined by subtracting the τ_P from the τ_T ($\tau_C = \tau_T - \tau_P$). Figure 87 shows a schematic of voltage versus time for one cycle (10 seconds) current reversal time to illustrate how the τ_P and τ_C were determined. As can be seen from the plot, positive and negative plateau voltages at which gas evolution occurred were selected and computed to obtain the τ_P. The τ_C was the difference between τ_T and τ_P.

Analysis of the plateau and charging times of the CTEs lifetimes has revealed that the lifetime of a CTE may be longer in a particular electrolyte than another, their plateau times may be nearly the same, or that the electrode with the shorter lifetime may actually

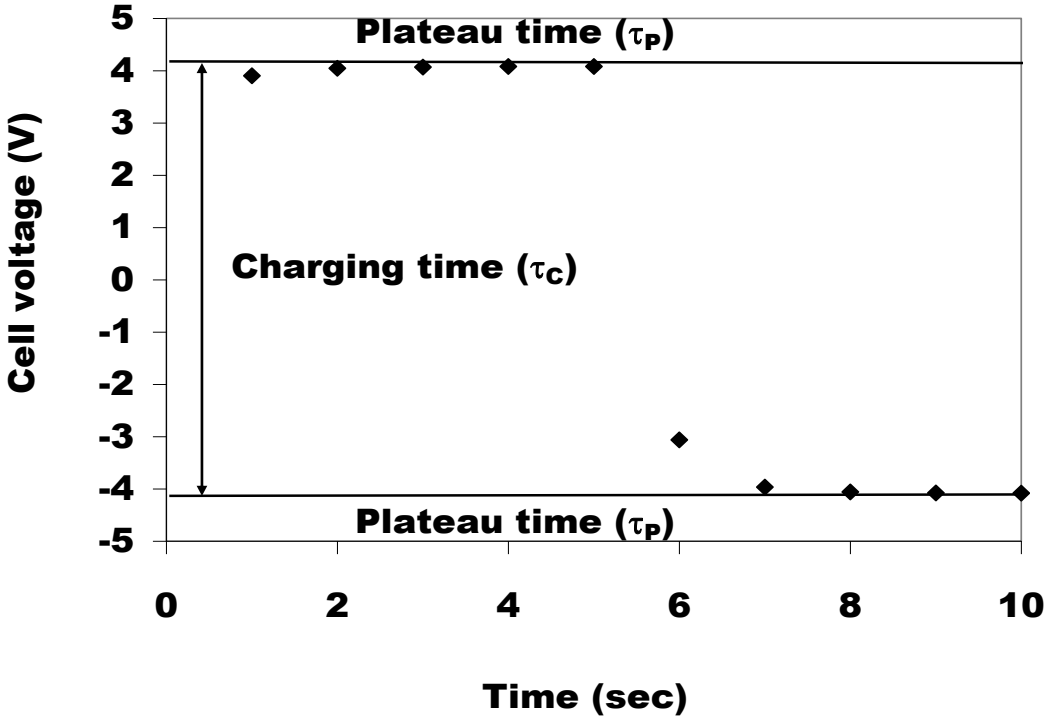

Figure 87 Example plot of voltage vs. time to illustrate the determination of plateau and charging time.

have a longer plateau time. This is illustrated with an example plot in Figure 88. The plot shows that IrTa had a longer lifetime (2050 minutes) in hard water (Mg ions) than IrTa lifetime (1392 minutes) in only nitrate ions. However, comparison of their plateau times reveals IrTa to have a longer plateau time (1135 minutes) in nitrate only ions than in nitrate and Mg ions (1034 minutes).

The total failure, plateau and charging times of the CTEs are presented in Table 11. It is clear from the table that the actual time expended by the electrodes for gas evolution (τ_P) is less than the failure time (τ_T). IrTa electrode which had the longest

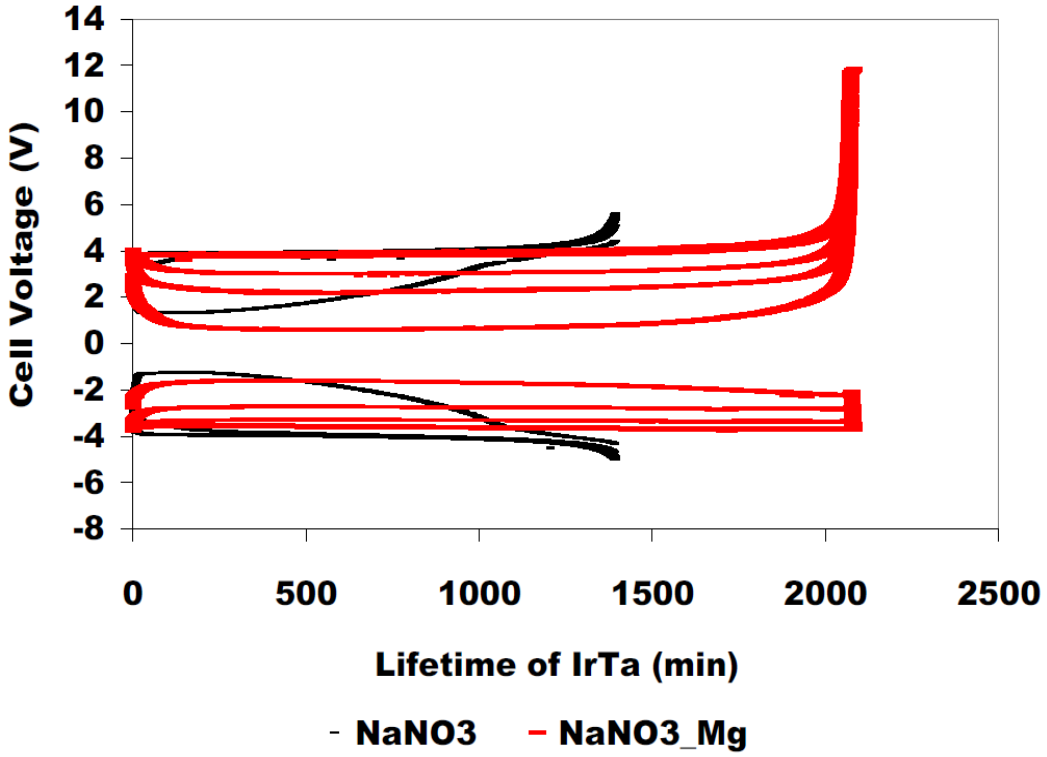

Figure 88 Example plot of cell voltage vs time plot to illustrate plateau and charging time.

Table 11 Comparison of total failure (τ_T), plateau (τ_P) and charging (τ_C) times for IrTa and RuTi electrodes in 1.2 M electrolytes at 1200 A/m^2, 0.043 M NaCl, 0.1 Hz cycle.

IrTa Electrode					
Electrolyte	**τ_T (min)**	**τ_P (min)**	**τ_C (min)**	**% τ_P**	**% τ_C**
$NaNO_3$	1392	1135	257	82	18
$NaClO_4$	242	122	120	50	50
Na_2CO_3	205	103	102	50	50
Na_2SO_4	116	58	58	50	50
Na_2HPO_4	63	55	8	87	13
RuTi Electrode					
Na_2HPO_4	848	387	461	46	54
$NaClO_4$	471	192	279	41	59
Na_2SO_4	400	335	65	84	16
$NaNO_3$	380	162	219	43	57
Na_2CO_3	361	124	237	34	66

lifetime in nitrate expended 1135 minutes of τ_P for gas evolution, while 257 minutes of τ_C was used for charging effects at the interface. IrTa had the lowest lifetime in hydrogen phosphate, of which 55 minutes been τ_P was used for evolving gas and the 8 minutes for charging (τ_C). Moreover, it can be seen from Table 11 that, IrTa used nearly proportionate amounts of times for gas evolution and for charging at the interface in the remaining electrolytes.

The RuTi electrode had the longest lifetime (τ_T = 848 minutes) in hydrogen phosphate ions of which 387 minutes of τ_P was used for evolving gas while the remaining time (461 minutes) was used for charging. RuTi used 335 minutes of τ_P for gas evolution in sulfate ions while 65 minutes was the τ_C. Apart from the sulphate electrolyte where RuTi used 84 % of τ_P for gas evolution, less than 50 % of τ_P was spent evolving gas in the remaining electrolytes. Thus, longer lifetimes of the CTEs do not necessarily translate into equally proportionate times for gas evolution.

Since the main goal was the examination of current reversal effects on CTEs for producing chlorine gas in the five electrolytes studied, the electrolytes in which the CTEs had long τ_P may be considered as the most desirable electrode/electrolyte combination for producing chlorine gas. As the IrTa/nitrate and RuTi/hydrogen phosphate electrolyte combinations produced long τ_P of 1135 and 387 minutes, respectively, IrTa and RuTi may be considered as been effective electrodes for chlorine production in these electrolytes while undergoing current reversal.

4.1.2 Failure Analysis in Hard Water

4.1.2.1 Pseudocapacitive Behavior of CTEs in Hard Water

Pseudocapacitance behavior was also observed for the CTEs in the hard water experiments by the formation of the bands seen in the cell voltage versus current reversal time plots. Evidence that the CTEs exhibited pseudocapacitive behavior in hard water is demonstrated by the representative sample plots of cell voltage versus time shown in Figures 89 and 90. Plots A in the figures show the relationship between voltage and time, while plots B show the dependence of voltage on normalized time (t/τ). The lifetimes and/or normalized times of the two electrodes are compared in the absence of hard water (nitrate ions only) and in the presence of hard water (Ca and Mg ions) under current reversal electrolysis in the figures.

As discussed in preceding sections, the pseudocapacitive behavior [100, 207, 208] observed in the plots is dependent on the charging effects occurring at coating/electrolyte interface. The charging time (τ_C) component of the total time to failure (τ_T) of the electrodes is the time expended for charging at the interface, that is, it involves adsorption and desorption of species at the interface.

In the accelerated lifetime tests for the CTEs (Figure 89A), IrTa electrode had the longest lifetime in nitrate and Mg ions, followed by a lower lifetime in only nitrate ions. The lifetime of IrTa in nitrate and Ca ions appears to be the lowest of the three lifetimes considered. The sizes of the bands in these electrolytes appear to reflect these lifetimes' observations. The magnitude of the pseudocapacitive behavior at the IrTa interface in these electrolytes (nitrate and Mg ions, nitrate and Ca ions and nitrate only ions) which is

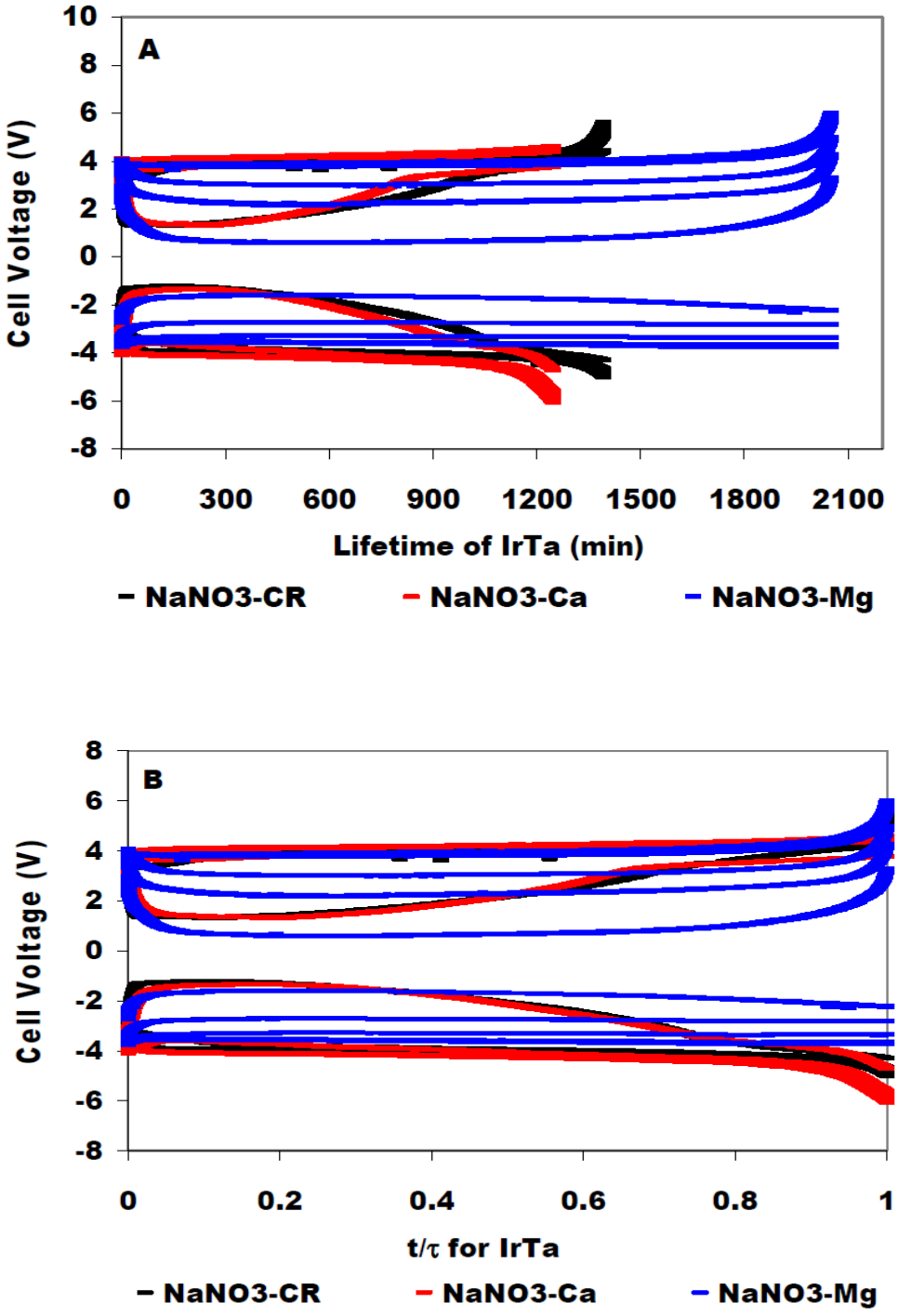

Figure 89 Cell voltage vs lifetime for IrTa electrode at 1200 A/m^2, 857 mg/L Ca and Mg ions, 1.2 M $NaNO_3$, 0.026 M Cl^-, 0.1 Hz. Plot A is lifetime and B is normalized time.

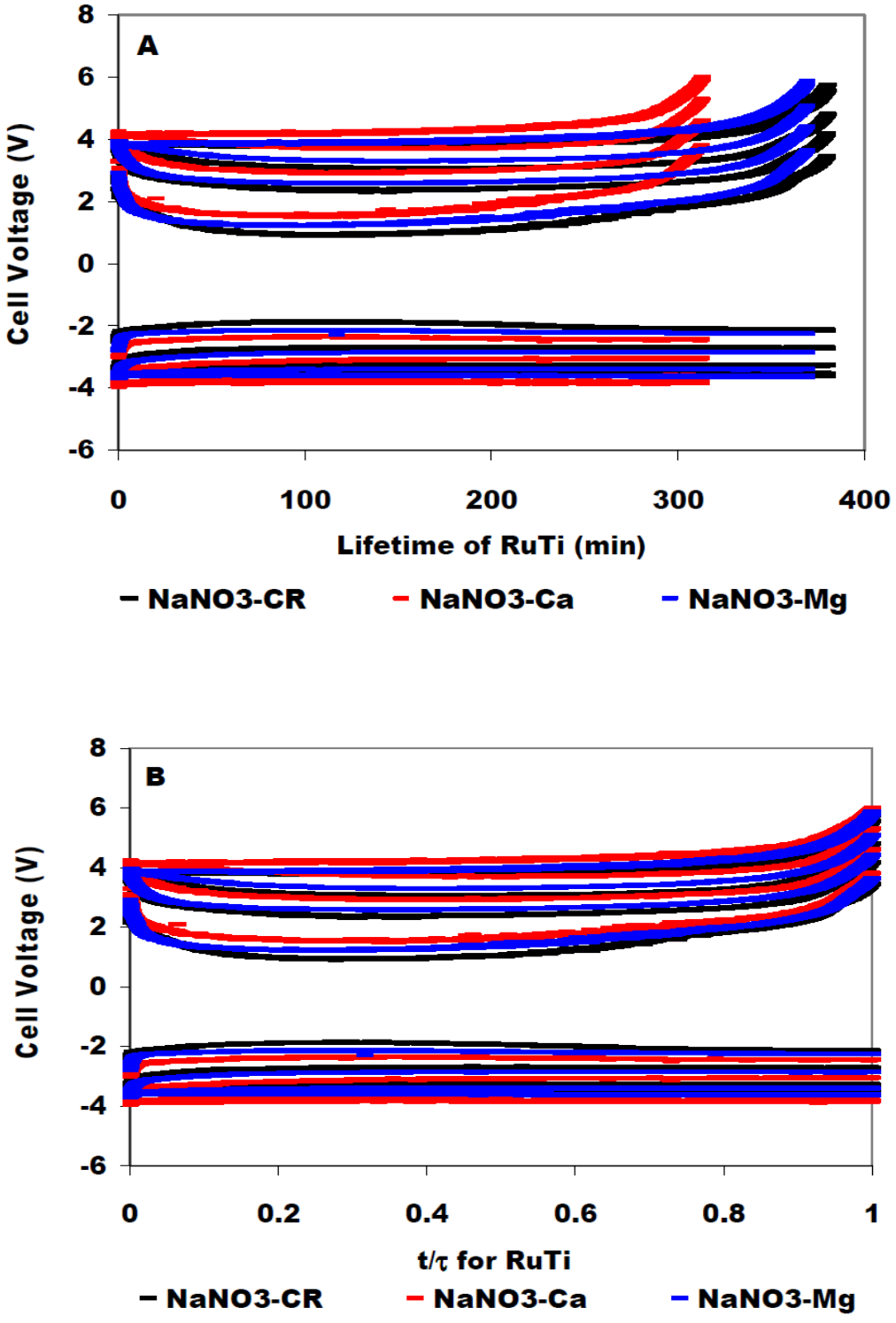

Figure 90 Cell voltage vs lifetime for RuTi electrode at 1200 A/m^2, 857 mg/L Ca and Mg ions, 1.2 M $NaNO_3$, 0.026 M Cl^-, 0.1 Hz. Plot A is lifetime and B is normalized time.

reflective of the band sizes is better observed in Figure 89B on the normalized current reversal time axis. Evidently, the band size for IrTa in nitrate and Mg ions appears much broader than the bands for IrTa in nitrate and Ca ions, and IrTa in only nitrate ions. The band for IrTa in nitrate and Ca ions appears to be of the same size as the band for IrTa in the absence of hard water.

From the preceding discussion, the band size seems to be directly related to the lifetime of the electrodes through the number of charges exchanged at the interface. The charges exchanged depend on the availability of coating active sites, which in turn depends on the surface coverage of the coating. As mentioned in preceding sections, the plateau time (τ_P) is related to the number of charge exchanges occurring at the electrode/electrolyte interface, and is therefore related to the time spent at the interface for gas evolution. IrTa had the longest life in the presence of Mg and nitrate ions, yet there appear to be not much in its τ_P in nitrate and Mg ions, nitrate and Ca ions and nitrate only ions as revealed by Table 12, reinforcing the observation that longer lifetimes do not translate into longer gas evolution times. Also, the wider band size observed for IrTa in nitrate and Mg is supported by the large τ_C of 1016 minutes in Table 12. The τ_P and τ_C for IrTa in hydrogen phosphate and perchlorate ions in the presence of hard water ions (Ca and Mg) also seem similar according to Table 12.

Similarly, the lifetime of the RuTi electrode in the three electrolytes (nitrate and Mg ions, nitrate and Ca ions and nitrate only ions) is reflected by the size of the bands observed in Figure 90A. The band size of RuTi in nitrate only ions and in nitrate and Mg ions appear to be equal. The two seem a little longer than RuTi lifetime in

Table 12 Comparison of total failure (τ_T), plateau (τ_P) and charging times (τ_C) of CTEs examined in hard water at 1.2 M supporting electrolyte concentration and 857 mg/L Ca and Mg ions.

IrTa Electrode						
Electrolyte	**Ions**	**τ_T**	**τ_P**	**τ_C**	**% τ_P**	**% τ_C**
$NaNO_3$	NO_3^-	1392	1135	257	82	18
	Ca	1248	960	288	77	23
	Mg	2050	1034	1016	50	50
Na_2HPO_4	HPO_4^{2-}	63	57	6	90	10
	Ca	116	77	39	66	34
	Mg	58	29	29	50	50
$NaClO_4$	ClO_4^-	242	122	120	50	50
	Ca	191	104	87	54	46
	Mg	176	90	86	51	49
RuTi Electrode						
$NaNO_3$	NO_3^-	380	160	220	42	58
	Ca	314	133	181	42	58
	Mg	369	160	209	43	57
Na_2HPO_4	HPO_4^{2-}	848	387	461	46	54
	Ca	953	320	633	34	66
	Mg	488	172	316	35	65
$NaClO_4$	ClO_4^-	471	192	279	41	59
	Ca	382	155	227	41	59
	Mg	401	163	238	41	59

nitrate and Ca ions. The magnitude of the pseudocapacitive behavior at the RuTi interface in the three electrolytes appear to have similar band sizes as shown in Figure 90B on the normalized time axis. This appears not to be surprising as the plateau (τ_P) and charging (τ_C) times for RuTi in hard water in these electrolytes are similar as well as can be seen in Table. Again, the τ_P and τ_C for RuTi in hydrogen phosphate and perchlorate ions in the presence of hard water ions (Ca and Mg) also appear similar as observed in Table 12.

Visual inspection of the failure times (τ_T) of the two electrodes in hard water ions appears to indicate that failure may have occurred differently in the three supporting electrolytes ($NaNO_3$, Na_2HPO_4 and $NaClO_4$) following Table 12; however, their τ_P and τ_C seem similar. Since the observations made in Table 12 appear to parallel the observations made Table 11 seem to suggest that the CTEs may have failed by the same mechanisms under both current reversal and hard water examinations. Deactivation of the CTE is initiated by coating dissolution. Coating dissolution can either occur electrochemically or chemically under straight polarity conditions [137]. The τ_P (related to gas evolution) is related to the electrochemical dissolution of the coating while τ_C (related to charging) is related to the chemical dissolution of the coating.

Electrochemical dissolution is believed to be the main factor that triggers the electrode deactivation process as the polarity of the electrodes is changed periodically of the CTEs in the three electrolytes in the hard water. Dissolution exposes the substrate to the electrolyte, thus forming a passivating layer at the substrate/coating interface impeding current flow which ultimately deactivates the electrodes.

4.1.3 Failure Mechanisms of CTEs

Two of the four main mechanisms discussed in Chapter 1 are believed to have influenced failure of the CTEs. The surface deposition through adsorbed species mechanism could not be proved to have occurred. Moreover, the τ_C values related to charging and/or discharging of adsorbed species shown in Table 12 did not show any meaningful variability worth considering. The substrate attack mechanism is generally related to processes (such as industrial operations) where F^- ions may be present.

The results and discussion presented reveal that the CTEs examined under current reversal and hard water conditions failed by coating dissolution followed by substrate passivation or by a combination of the two mechanisms. The theory that CTE coating failure was influenced by the dissolution mechanism is supported by SEM/EDS, XRF and CV results. Since all the coating was not consumed at the end of the CTEs lifetimes suggests that passivation of the substrate occurred. The effects of these deactivation mechanisms on the CTE lifetime is discussed next.

4.1.3.1 Failure by Dissolution Mechanism

In the dissolution mechanism, the active components of the coating are systematically dissolved over the course of the current reversal electrolysis time. The physical and electrochemical techniques employed to characterize the CTEs corroborates the occurrence of coating dissolution.

First of all, the SEM images shown in preceding sections of this chapter (and Chapter 3) revealed gradual coating consumption as a function of current reversal time. The occurrence of coating dissolution was verified by visual inspection of SEM images. The SEM images of fresh coatings were compared with images of coatings that have been tested at different times under current reversal electrolysis. The surface morphology of images of the coatings examined under current reversal electrolysis showed obvious areas of coating wear.

Secondly, the EDS results support the theory of coating dissolution with increasing current reversal time. The EDS results indicated that the initial amounts (atomic percent) of Ir, Ru and Ta in the coatings were decreasing as a function of current

reversal time. Furthermore, the XRF results also showed that the percentage of initial Ir, Ru and Ta determined from XRF intensities was decreasing as current reversal time increased.

Deactivation of the CTEs by the dissolution mechanism can occur electrochemically or chemically at low to high current densities under straight polarity [137]. Electrochemical dissolution [137] is related to the number of charges exchanged (ampere-hours passed) at the interface. The coating can be consumed chemically by interactions with electrolyte species.

The CTEs examined are believed to have failed predorminantly by the electrochemical dissolution mechanism under both current reversal and hard water electrolysis. Even though adsorption and desorption of species occurred according to Tables 11 and 12 chemical interactions between adsorbed species and coating leading to dissolution of the coating can not be substantiated as this was not pursued. However, the literature will be cited where possible to support any possible chemical interactions (coating and electrolyte) likely to influence coating dissolution.

The possible dissolution mechanisms for Ir and Ta in IrTa and Ru and Ti in RuTi electrodes can be described by equations 33 to 38 [210, 211]. With continued dissolution as observed under straight polarity conditions a gradual increase in operating cell voltage is observed. This observation parallels what was also observed under the current reversal and hard water experiments. The operating current will shift to the remaining active sites,

$$IrO_2(OH) \leftrightarrow IrO_3 + H^+ + e^- \quad (33)$$

$$IrO_3 + H_2O \leftrightarrow \frac{1}{2}O_2 + IrO(OH)_2 \quad (34)$$

$$RuO_2 + H_2O \leftrightarrow RuO_4 + 4H^+ + 4e^- \quad (35)$$

$$RuO_2 + 4H^+ \leftrightarrow RuO_4 + 2H_2O \quad (36)$$

$$Ta_2O_5 + 6H^+ + 5e^- \leftrightarrow TaO_2^+ + 3H_2O \quad (37)$$

$$TiO_2 \leftrightarrow TiO_2^{2+} + 2e^- \quad (38)$$

locally increasing current density [212] and the operating cell voltage thus deactivating the CTEs. Figure 91 is a schematic diagram of coating dissolution.

When the two electrodes were examined in the five electrolytes, the IrTa electrode had the longest life in $NaNO_3$ and the shortest lifetime in Na_2HPO_4. The RuTi electrode had the longest life in Na_2HPO_4 and the shortest life in Na_2CO_3. The lifetimes of the CTEs in the other electrolytes fall between their longest and shortest lifetimes.

The IrTa electrode is believed to have failed in the presence of nitrate ions by predominantly the electrochemical dissolution mechanism where most of its τ_P was

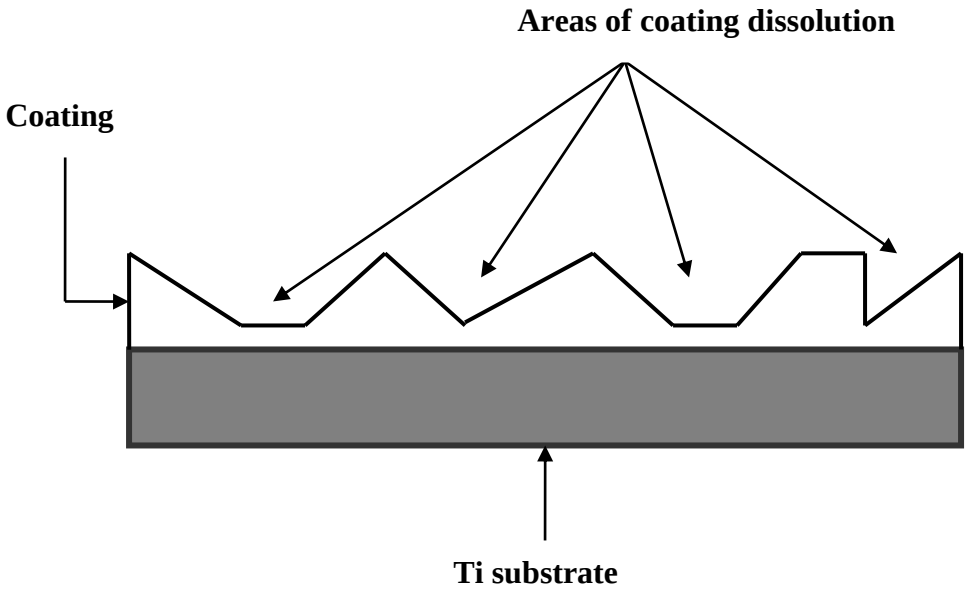

Figure 91 Schematic showing coating dissolution mechanism.

expended evolving gas. Chemical interaction between the nitrate anions and the IrTa coating is likely as NO_3^- anions have been reported to adsorb in outer sphere complexes [213] with hydrous Ir. The effect of the dissolution mechanism on IrTa was confirmed by SEM images showing mostly the Ti substrate after IrTa failure in nitrate electrolyte.

The occurrence of chemical interactions between adsorbed species and/or the coating was not investigated as part of the present investigation, and should be pursued as future work. IrTa also failed predominantly by the electrochemical dissolution mechanism in hydrogen phosphate, given that 55 minutes (out of lifetime of 63 minutes) of τ_P was used for gas evolution and the 8 minutes τ_C was expended adsorbing and/or desorbing of species. Phosphate [137] is reported to selectively react with Ta, thus

accelerating the dissolution process. SEM images support the observation, as the IrTa electrode after failure in hydrogen phosphate showed the Ti substrate devoid of almost any coating.

Electrochemical dissolution was also predominant for IrTa failure in perchlorate, carbonate and sulphate anions as revealed by Table 11. Chemical interactions is also possible between the IrTa electrode and adsorbed ClO_4^-, SO_4^{2-} and CO_3^{2-} anions species as these anions are reported to bind in outer sphere complexes [213] with hydrous Ir.

Electrochemical dissolution mechanism was also the predominant mode of RuTi failure in hydrogen phosphate where 387 minutes τ_P was used for evolving gas while the τ_C for adsorbing and desorbing species was 461 minutes. Hydrogen phosphates ions are reported to strongly adsorb [206] on RuTi under straight polarity conditions to retard chlorine evolution. RuTi failed by electrochemical dissolution mechanism in sulfate where τ_P was 335 minutes for gas evolution and 65 minutes τ_C was for charging. Sulfates [206, 212] have been reported to adsorb on RuTi anode retarding the Cl_2 evolution reaction (ClER). In the remaining three anions (ClO_4^-, NO_3^- and CO_3^{2-}), RuTi equally failed by electrochemical dissolution mechanism. NO_3^-, ClO_4^-, and Cl^- anions have been reported to adsorb on hydrous Ru in outer-sphere complexes [213].

Electrochemical dissolution mechanism seem to be the dorminant mechanism of failure of the CTEs in hard water ions examined in the three supporting electrolytes (NO_3, HPO_4^{2-}, ClO_4^-) as discussed in Section 4.1.1.7. Interactions of the CTEs with the three supporting electrolytes are also possible under hard water electrolysis as was observed under current reversal electrolysis to accelerate dissolution of some form.

In summary, dissolution occurred by predorminantly the electrochemical dissolution mechanim. Chemical interactions of the coating and the supporting electrolytes may have occurred to accelerate dissolution.

4.1.3.2 Failure by Passivation Mechanism

Substrate passivation [206, 212-217] is the growth of a nonconductive oxide layer between the CTE coating and the Ti (valve metal) substrate. Passivation [137] is the most frequent failure mechanism associated with high current density in straight polarity operations. It is [212] the primary mode of failure associated with straight polarity oxygen evolving applications. The passivation [137, 212] failure mechanism is usually preceded by a period of high cell voltage or unstable current distribution, with high amounts of residual coating remaining after electrode failure in straight polarity applications.

In the present investigation, the RuTi electrode had more residual coating remaining on it at failure than the IrTa anode. This seems to suggest that the passivation failure mechanism probably had more influence on the RuTi anode failure than it had on IrTa anode failure. Figure 92 depicts a schematic diagram of CTE failure by the passivation mechanism. The passivation failure mechanism could have caused failure of the CTEs examined by either substrate-electrolyte, substrate-oxygen ions contact [206, 214] or low chloride ions concentration in the case of ClER [212, 214]. For Cl_2 generation, operating at low chloride concentration, as was the case in this investigation, rapidly passivates the electrodes as a result of decrease in current efficiency.

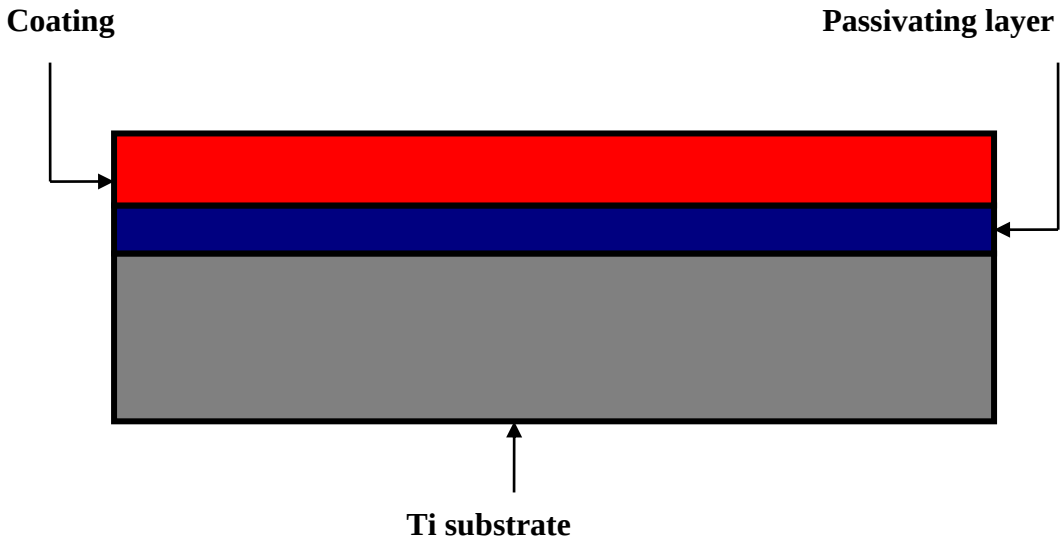

Figure 92 A schematic showing substrate passivation mechanism.

The passivating failure mechanism attributed to substrate-electrolyte and substrate-oxygen ions contact can be described by equations 39 and 40 [214].

$$Ti + 2H_2O \rightarrow TiO_2 + 4H^+ + 4e^- \quad (39)$$

$$Ti + 2O^{2-} \rightarrow TiO_2 + 4e^- \quad (40)$$

The electrolyte and oxygenated ions make contact with the CTE substrate through mud-like cracks in coating, coating pores, and dissolved areas of coating, to form the non-conductive oxide layer (TiO_2) by oxidation. The anode reaction of interest in this work is the ClER, which incidentally, forms the disinfecting species (hypochlorous acid and hypochlorite ions) required for water disinfection applications investigated. Therefore factors (such as low chloride concentration, adsorbed surface species and poor current distribution [212]) that promote the oxygen side reaction over the ClER will increase passivation and electrode failure. The insulating film layer formed at substrate/coating renders the electrode inactive, increase resistance across the interface, and eventual electrode failure.

In summary, the passivating mechanism influenced CTE electrode failure, as corroborated by the high levels of residual coating remaining after electrode failure. Oxidation of the underlying Ti substrate to the non-conductive layer is as a result of the passage of electrolyte solution and/or oxygenated ions through depleted areas of the coating, pores, and cracks. There is increased resistance at the interface resulting in operating cell voltage escalation. This ultimately led to the CTE electrodes deactivation.

CHAPTER 5

CONCLUSIONS

The influence of polarity reversal on two commercially coated titanium electrodes (CTEs) was examined in the presence of various anions and cations. The effects of current density, current reversal cycle length and sodium chloride concentration on the CTEs were also investigated. Current reversal was used to examine lifetimes of the electrodes under accelerated conditions. X-ray fluorescence and energy dispersive spectroscopy, scanning electron microscopy and cyclic voltammetry were used as analytical tools for evaluating data.

Current reversal significantly affected the lifetime patterns and failure times of the electrodes. Cell voltage versus time plots under accelerated conditions showed three characteristic band regions which correspond to the CTEs lifetime patterns. During current reversal, the electrodes experienced periods of faradaic reactions and nonfaradaic charging corresponding to plateau and charging times, respectively. Thus, the total time to failure (τ_T) was comprised of plateau time to failure (τ_P) and charging time to failure (τ_C).

For both electrodes (RuTi and IrTa), lifetime increased with decreasing current density or decreasing reversal cycle frequency. NaCl had no effect on lifetime over the

range studied. The effect of anodic and cathodic current density indicated that if either was decreased to 200 A/m^2, lifetimes became very long (> 1 week). In general, RuTi electrodes have longer lifetimes than IrTa electrodes during current reversal.

Sodium anion compositional and concentration changes had varying extent of influence on coated titanium electrode life in the five anions examined under current reversal electrolysis. IrTa had longer lifetimes in nitrate anions, and the service life of IrTa increased as a function of nitrate concentration. RuTi had longer lifetimes in the remaining four anions. RuTi life increased with increasing hydrogen phosphate concentration. Lifetime of both electrodes seemed to decrease as a function of carbonate ions. Lifetime of the anodes appeared not to change or only slightly decreased as a function of either perchlorate or sulfate anions. Faradaic and nonfaradaic reactions are believed to be responsible for the lifetime patterns exhibited by the anodes in these anions. Consequently, the τ_P and τ_C associated with these reactions are deemed to be critically important to the electrodes life. As τ_P and τ_C determines the amount of time used for gas evolution and charging effects at the CTE/electrolyte interface.

The response of τ_T of the coated titanium electrodes to three sodium electrolytes in the presence of hard water was determined. The lifetime of IrTa was determined to be higher than RuTi in nitrate and hard water. Electrolyte and hard water concentration and compositional changes affected IrTa life more than RuTi under all the water hardness examined, except in Ca and nitrate ions. In the presence of nitrate, increasing Ca concentration did not affect IrTa life. RuTi had longer lifetimes than IrTa in hydrogen phosphate and perchlorate in the presence of Ca and Mg. However, RuTi life in these electrolytes appeared to have been influenced by anion concentration and compositional

changes than by Ca and Mg concentration and compositional changes. A comparison of the τ_T of electrodes in the three electrolytes in the presence of hard water showed in some instances significant differences yet their τ_P showed not much variability. In other words, the plateau times to failure (τ_P) responsible for gas evolution at the electrodes appeared to be same even though the total time to failure (τ_T) for the CTEs indicated otherwise.

From analysis of x-ray fluorescence, energy dispersive, cyclic voltammetry and chronopotentiometric data including scanning electron microscopic images, two failure mechanisms responsible for the CTEs failure in both current reversal and hard water electrolysis were determined. It is believed that coating dissolution and/or substrate passivation mechanisms were responsible for the CTEs failure. The two electrodes seemed to have failed by the same mechanisms. Trends observed in the XRF intensity data, At % metal from EDS, Q from cyclic voltammetry and cell voltage band from accelerated life testing supported this hypothesis. It is believed that coating dissolution is the first mechanism that triggers the CTE deactivation process. Substrate passivation sets in as electrolytes reach the substrate surface.

The decrease in initial metal intensity from XRF and the decrease in At % of metal from EDS data with time, and SEM images showed the coating was systematically consumed with current reversal electrolysis time. Substrate passivation is believed to have occurred based on residual coating that remained on the electrodes after anode failure, especially in the case of the RuTi anode. The two mechanisms acted in combination to deactivate the anodes. However, based on EDS data, IrTa is believed to have failed predominantly by the dissolution mechanism in nitrate, hydrogen phosphate

and perchlorate. RuTi failed predominantly by substrate passivation in hydrogen phosphate, nitrate and carbonate.

REFERENCES

1. A. Kraft, Platinum Metals Review, 52, 3, pp. 177-185, 2008**.**

2. M. Morimitsu, R. Otogawa, M. Matsunaga. Electrochimica ACTE, 46, pp. 401-406, 2000.

3. H. B. Beer, J. Electrochem. Soc., 27, 8, pp. 303-307, 1980.

4**.** S. Trasatti, Electrochimica ACTE, 29, 11, pp. 1503-1512, 1984.

5. D. H. Kroon, L. M. Ernes, Materials Performance, 2007.

6. S. Ardizzone, S. Trasatti, Advances in Colloid and Interface Science, 64, pp. 173-251, 1996.

7. O. De Nora, Chem. Ing. Tech., 42, 222, 1970; 43, 182, 1971.

8. S. Horacek, S. Puschaver, Chem. Eng. Progr. 67, 71, 1971.

9. A. Nidola in Electrodes of Conductive Metallic Oxides (Ed. S. Trasatti), Part B, Elsevier, Amsterdam, pp. 367-658, 1981.

10. A.T. Kuhn, Chemie-Ing-Techn., 47, pp 129-135, 1975.

11. http://ch-www.st-andrews.ac.uk/staff/jac/group/electrocatalysis.html, Nov. 2009.

12. P.C.S. Hayfield, Plat. Met. Rev., 42 (1), pp.27-33, 1998.

13. P.C.S. Hayfield, Plat. Met. Rev., 42 (2), pp. 46-55, 1998.

14. P.C.S. Hayfield, Plat. Met. Rev., 42 (3), pp. 116-122, 1998.

15. S. Trasatti, Electrochimica ACTE, 45, Issue 15-16, pp 2377-2385, 2000.

16. A.T. Kuhn, Chemie-Ing-Techn., 47, pp 129-135, 1975.

17. T.C. Jeffrey, P.A. Danna, H.S. Holden (Eds.), Chlorine Bicentennial Symposium, The Electrochem. Soc., Princeton, New Jersey, 1974.

18. K. Hass, P. Schmittinger. Electrochim. ACTE 21, pp. 1115, 1976.

19. T.C. Jeffrey, P.A. Danna, H.S. Holden (Eds.), Chlorine Bicentennial Symposium, The Electrochem. Soc., Princeton, New Jersey, 1974.

20. K. Hass, P. Schmittinger. Electrochim. ACTE 21, pp. 1115, 1976.

21. H.V.K. Udupa, R. Thangappan, B.R. Yadav, P. Subbiah, Chem. Age India, 23 pp. 545, 1972.

22. http://ch-www.st-andrews.ac.uk/staff/jac/group/electrocatalysis.html, Nov. 2009.

23. S. Trasatti, G. Lodi, Electrodes of Conductive Metallic Oxides (Ed. S. Trasatti), Part B, pp. 521-626, 1981.

24. J. P. G. de Mussy, Ph.D. Thesis, Université Libre de Bruxelles, Belgium, 2002.

25. A. C. C. Tseung, S. Yeh, X. Liu, G. H. Kelsall, P. Dykstra, in Novel Acid-Resistant Oxygen Evolution Electrodes, Commission of The European Communities, EUR 13259 EN, 1991.

26. G. Beni, L. M. Schiavone, J. L. Shay, W. C. Dautremont-Smith, B. S. Scheneider, Nature 282**,** 281, 1979.

27. C. C. Hu, C. H. Lee, T. C. Wen, J. Appl. Electrochem., 26**,** 72, 1996.

28. V. M. Kolotyrkin, V. V. Losev, D. M. Shub and Yu. E. Roginskaya, Elektrokhimiya 15, 291, 1979.

29. U.S. Pat. 5,587,058, 1996.

30. H. S. Holden and J. M. Kolb, in Encyclopedia of Chemical Technology, Metal Anodes 3rd ed., (Ed. K. Othmer), John Wiley and Sons, Inc., New York, 1981.

31. A. Emslie, F. Bonner and L. Peck. J. Appl. Phys. 29, pp. 858–862, 1958.

32. J. Ribeiro, M. S. Moats, A. R. de Andrade, J. Appl Electrochem., 38, pp. 767-775, 2008.

33. J. Ribeiro, P. D.P.Alves, A.R. de Andrade, J. Mater. Sci, 42, pp. 9293-9299, 2007.

34. H. S. Holden and J. M. Kolb, in Encyclopedia of Chemical Technology, Metal Anodes 3rd ed., (Ed. K. Othmer), John Wiley and Sons, Inc., New York, 1981.

35. G. Beni, L. M. Schiavone, J. L. Shay, W. C. Dautremont-Smith, B. S. Scheneider, Nature, 282**,** 281, 1979.

36. J. Krysa, J. Maixner, R. Mraz, I. Rousar, J. Appl. Electrochem., 28**,** 369, 1998.

37. C. Comnimellis, G. P. Vercesi, J. Appl. Electrochem., 21**,** 335, 1991.

38. G. Lodi, A. De Battisti, G. Bordin, C. De Asmundis, A. Benedetti, J. Electroanal. Chem., 277**,** 139, 1990.

39. J. Guang-Way, R. Krishnan, J. Electrochem. Soc., 134**,** 1830, 1987.

40. L. A. da Silva, V. A. Alves, M. A. P. da Silva, and S. Trasatti, Electrochimica ACTE, 42**,** 271, 1997.

41. V. A. Alves, L. A. da Silva, J. F. Boodts, and S. Trasatti, Electrochimica ACTE, 39**,** 1585, 1994.

42. G. P. Vercesi, J. Y. Salamin, C. Comnimellis, Electrochimica ACTE 36**,** 991, 1991.

43. M. Vukovic, Electrochimica ACTE, 34**,** 287, 1989.

44. J. Rolewicz, C. Comnimellis, E. Plattner, J. Hinden, Electrochimica ACTE, 33**,** 573, 1988.

45. R. Kotz, C. Barbero, O. Haas, J. Electroanal. Chem., 296**,** 37, 1990.

46. L. A. da Silva, V. A. Alves, M. A. P. da Silva, S. Trasatti, J. F. Boodts, Electrochimica ACTE, 41, 1279, 1996.

47. G. P. Vercesi, J. Rolewicz, C. Comnimellis, Thermochimica ACTE, 176, 31, 1991.

48. C. J. Kim, W. J. Lee, and K. No, Thin Solid Films, 312, 130, 1998.

49. L. A. de Faria, J. F. Boodts, S. Trasatti, J. Appl. Electrochem., 26, 1195, 1996.

50. C. P. De Pauli, S. Trasatti, J. Electroanal. Chem., 396, 161, 1995.

51. D. T. Shied, B. J. Hwang, J. Electroanal. Chem., 391, 77, 1995.

52. S. M. Lin, T. C. Wen, J. Electrochem. Soc., 140, 2265, 1993.

53. S. Kulandaisamy, J. P. Rethinaraj, S. C. Chockalingam, S. Visvanathan, Mater. Chem. Phys., 35, 176 (1993).

54. R. Otogawa, K. Soda, S. Yamauchi, Y. Nagatoishi, M. Morimitsu, M. Matsunaga, Denki Kagaku Oyobi Butsuri Kagabu, 65, 987, 1997.

55. C. Comnimellis, A. De Bastidi, J. Chim. Phys., 93, 673, 1996.

56. T. Arikawa, Y. Murakami, Y. Takasu, J. Appl. Electrochem., 28, 511, 1998.

57. F. Vicent, E. Morallon, C. Quijada, J. L. Vazquez, A. Aldaz, J. Electrochem. Soc., 28, 607, 1998.

58. D. Cukman, M. Vukovic, M. Milun, J. Electroanal. Chem., 389, 209, 1995.

59. J. Kristof, J. Mihaly, S. Daolio, A. De Bastidi, L. Nanni, J. Electroanal. Chem., 434, 99, 1997.

60. P. Ramachandran, K. V. Venkateswaran, R. M. Meyappan, R. Srinivasan, B Electrochem., 4**,** 67, 1988.

61. L. N. Kulikova, V. N. Fateev, V. D. Rusanov, Russian Journal of Electrochemistry, 34**,** 306, 1998.

62. C. E. Vallet, J. Electrochem. Soc., 138**,** 1234, 1991.

63. M. A. Petit, V. Plichon, J. Electroanal. Chem., 379**,** 165, 1994.

64. A. Brungs, V. Haddadi, M. Skyllas-Kazacos, J. Appl. Electrochem., 26**,** pp 11-17,1996.

65. G. V. Kornienko, T. A. Kenova, Y. V. Saltykov, N. V. Chaenko, V. L. Kornienko, Russian J. Electrochem., 34, pp 561-563, 1998.

66. F. Vergara, Ph.D. Thesis Inst. Polytech. Grenoble, France, 1978.

67. EUR. Patent, 598,517, A1, 1994.

68. EUR. Patent, 0,058,985, A1, 1982**.**

69. EUR. Patent, 0,365,969, A1,1990.

70. U.S Patent, 4,828,653, 1987.

71. U.S Patent, 4,310,391, 1979.

72. U.S Patent, 4, 64,434, 1986.

73. U.S Patent, 4,661,213, 1987.

74. U.S Patent, 5,948,222, 1999.

75. U.S Patent, 5,578,175, 1996.

76. A. J. Scarpellino, G. L. Fisher, J. Electrochem. Soc., 129**,** 515, 1982.

77. U.K Patent, 2,290,553, 1995. **77**

78. Y. L. Lo, S. C. Chou, B. J. Hwang, J. Appl. Electrochem., 26**,** 733, 1996.

79. Y. L. Lo, B. J. Hwang, J. Electrochem. Soc., 143**,** 2158, 1996.

80. K. Izumiya, E. Akiyama, H. Habazaki, N. Kumagai, A. Kawashima, K. Hashimoto, Materials Transactions, 35**,** 308, 1998.

81. K. Izumiya, E. Akiyama, H. Habazaki, N. Kumagai, A. Kawashima, K. Hashimoto, Materials Transactions, 38, 899, 1997.

82. N. Kumagai, S. Jikihara, Y. Samata, K. Asami, K. Hashimoto, Corrosion Electrochemistry and Catalysis of Metals and Intermetallics, 93, 90, pp. 324-333, 1993.

83. Y. Matsumoto, T. Tazawa, N. Muroi, E. I. Sato, J. Electrochem. Soc., 133**,** 2257, 1986.

84. S. Gottesfeld, M. Yaniv, D. Laser in Proc. Int. Symp. 4th Electrochem. Soc., (Ed. R.P. Frankenthal, J. Kruger), Princeton, New Jersey, pp. 134, 1978.

85. EUR. Patent, 0,243,302, A1, 1987.

86. U.K Patent, 2,192,008, 1987.

87. U.K. Patent, 1 583 370, 1967**.**

88. U.K Patent, 1,024,693, 1984.

89. U.S Patent, 4,057,479, 1974.

90. US Patent, 3,330,697, 1967.

91. P. Shrivastava, MS Thesis, University of Utah, 2008.

92. Anodes for Electrowinning, The Metallurgical Society of AIME, (Ed. J. R. Douglas, E. J. Stephen), pp. 69-112,1984.

93. G. Lodi, C. De Asrnundis, S. Ardizzone, E. Sivieri and S. Trasatti, Surf. Techno., 14, 335, 1981.

94. C. Battaglin, A. Carnera, P. Mazzoldi, G. Lodi, P. Bonora, A. Daghetti, S. Trasatti, J. Electroanal. Chem., 135, 313, 1982.

95. R. Garavaglia, C.M. Mari, S. Trasatti, C. De Asrnundis, Surf. Technol., 19, 197, 1983.

96. S. Trasatti and G. Lodi in Electrodes of Conductive Metallic Oxides (Ed. S. Trasatti), Part A, Elsevier, Amsterdam, 1980, pp. 301.

97. G. Lodi, E. Sivieri, A. De Battisti, S. Trasatti, J. Appl. Electrochem., 8, 135, 1978.

98. S. Ardizone, M. Falciola, S. Trasatti, J. Electrochern. Soc., 136, 1545, 1989.

99. D. R. Crow, Principles and Applications of Electrochemistry, 4th Edition, Blackie Academic and professional, Glasgow, pp. 68, 1994.

100. S. Srinivasan, Fuel Cells: From Fundamentals to Applications, 1st Edition, Springer Science, pp. 27-112, 2006.

101 D. N. Furlong, D. E. Yates, T. W. Healy in Electrodes of Conductive Metallic Oxides (Ed. by S. Trasatti), Part B, Elsevier, Amsterdam, 1981, pp. 367.

102. H. Helmholtz, W. Abhandl, Physik. Tech. Reichsanst Alt. 1,925, 1879.

103. A. Gouy, A. Chim., Phys. 29, pp 145, 1903.

104. D. L. Chapman, Phil. Mag. 25, 475, 1913.

105. O. Stem, Z. Electrochem. 30, 508, 1924.

106. O. A. Esin, B. F. Markov, Zh. Fiz. Khim. 13,318, 1939.

107. D. C. Grahame, J Electrochem Soc. 98, 313, 1951.

108. M. A. V. Devanathan, Trans. Faraday Soc., 50, 373, 1954.

109. R. Parsons, Modern Aspects of Electrochem. (Ed. J. O'M. Bockris, B. E. Conway), 1, Butterworths, London, pp. 103, 1954.

110. A. L. Smith in G. D. Parfitt (Ed.), Dispersion of Powders in Liquids, 2nd Ed, Applied Science, London, pp. 86, 1973.

111. L.D. Burke, M. E. G. Lyons in Modern Aspects of Electrochemistry (Ed. R. E. White, J. O'M. Bockris, B. E. Conway), 18, Plenum Press, New York, pp. 169-241,1986.

112. R. M. Reeves, in Modern Aspects of Electrochemistry (Ed. J. O'M. Bockris, B. E. Conway), Plenum Press, New York, 1974.

113. J. Lyklema, J. Th. G. Overbeck, Colloid Set 16, 595, 1961; J. Lyklema, Trans. Faraday Soc. 59, 418, 1963.

114. G. R. Wiese, R. O. James, D. E. Yates, T. W. Healy, in International Review of Science(Ed., A. D. Buckingham, J. O'M. Bockris), Electrochemistry, Physical Chemistry, Series Two**,** 6, Butterworths, London, pp. 54, 1976.

115. S. M. Ahmed, D. Maksimov, J. Colloid Interface Sci., 29, 97, 1969.

116. S. M. Ahmed, Can. J. Chem., 44, pp. 1663-2769, 1966.

117. L. Blok, P. L. de Bruyn, J. Colloid Interface Sci., 32, pp. 518-533, 1970.

118. S. Levine and A. L. Smith, Disc. Faraday Soc., 52, 290, 1971.

119. R. J. Hunter, H. J. L. Wright, J. Colloid Interface Sci., 37, 564, 1971.

120. H. J. L. Wright, R. J. Hunter, Aust. J. Chem., 26, pp. 1183, 1191, 1973.

121. M. Borkovec, J. Westall, J. Electroanal. Chem., 150, 325, 1983.

122. Th. F. Tadros, J. Lyklema, J. Electroanal. Chem., 17, 267, 1968.

123.Th. F. Tadros, J. Lyklema, J. Electroanal Chem., 22**,** 1969.

124. J. Lyklema, J. Electroanal. Chem., 18, 341, 1968.

125. J. Lyklema, Croat. Chem. ACTE, 43, 249, 1971.

126. J. W. Perram, J. Chem. Soc. Faraday II, 2, 993, 1973.

127. J. W. Perram, R. J. Hunter, H. J. L. Wright, Chem. Phys., Lett. 23, 265, 1973.

128. J. W. Perram, R. J. Hunter, H. J. L. Wright, Aust. J. Chem., 27, 461, 1974.

129. M. J. Dignam, Can. J. Chem., 56, 595, 1978.

130. M. J. Dignam, R. K. Kalia, Surf. Sci., 100**,** 154, 1980.

131. T. W. Healy , L. R. White, Adv. Colloid Interface Sci., 9, 303, 1978.

132. D. E. Yates, S. Levine, T. W. Healy, J. Chem. Soc. Faraday I, 70**,** 1807, 1974.

133. J. A. Davis, A. P. James, J. O. Leckie, J. Colloid Interface Sci., 63, 480, 1978.

134. A. Daghetti, G. Lodi, S. Trasatti, Mater. Chem. Phys., 8, 1, 1983.

135. W. Smit, C. L. M. Holten, H. N. Stein, J. J. M. De Goeig, H. M. J. Theelen, J. Colloid Interface Sci., 63, 120, 1978**.**

136. http://en.wikipedia.org/wiki/Ruthenium, November 2009.

137. G. N. Martelli, R. Ornelas and G. Faita, Electrochimica ACTE, 39,11-12 pp 1551-1558, 1994.

138. M. Morimitsu, C. Murakami, K. Kawaguchi, R. Otogawa and Matsinaga, Journal of New Materials for Electrochemical Systems, 7, pp 323-327, 2004.

139. S. V. Evdokimov, Russian J. Electrochem., 37, pp 363-370, 2001.

140. U.S Patent, 3,453,201, 1969.

141. U.S Patent, 3,669,857, 1972.

142. U.S Patent, 3,893,902, 1975.

143. U.S Patent, 3,915,817, 1975.

144. U.S Patent, 3, 974, 051, 1976.

145. U.S Patent, 3,085,014, 1978.

146. U.S Patent, 4,087,337, 1978.

147. U.S pat. 4,088,550, 1978.

148. U.S Patent, 4,255,246, 1981.

149. U.S Patent, 4,345,981, 1982.

150. U.S Patent, 5,807,473, 1998.

151. M. S. Moats, JOM, 60, 10, pp 46-49, 2008.

152. R. S. Alwitt, A. K. Vijh, J. Electrochem. Soc., 116, pp 388, 1969.

153. M. Ihos, G. Bocea , A Lovi, Chem. Bull. Politehnica, 50, pp 64, 2005.

154. M. Valnice , B. Zanoni, J.J. Sene, H. Selcuk, M.A. Anderson, Environ. Sci. Technol., 38, pp. 3203- 3208, 2004.

155. I. Volkov, E. L. Babayan, E. P. Siusheva, Khim. Prom., 46, pp.864, 1970.

156. O. de Nora, Chem. Ing. Techn., 42, 222, 1970.

157. A. C. C. Tseung, S. Jasem, Electrochim. ACTE., 22, 31, 1977.

158. H. H. Walter, H. Kaden, H. Hofmann, Chem. Techn., 29, pp. 212, 1977.

159. H. H. Walter, H. Kaden, H. Hofmann, Phys. Chem., 259, pp. 999, 1978.

160. A. T. Kuhn, C. J. Mortimer, J. Appli. Electrochem., 2, pp. 283, 1972.

161. V. A. Shlyapnikov, Zh. Prikl. Khim., 49, pp. 90. 1976.

162. S. Trasatti, W.E. O'Grady, in Advances in Electrochemistry and Electrochemical Engineering (Ed. H. Gerischer, P. Delahay), 13, Interscience, New York, pp.177-261, 1980.

163. V. I. Eberil', E.A Novikov, A.F.Mazanko, Russian Journal of Electrochemistry, 37, pp. 1218-1222, 2001.

164. E.A. Novikov, V.I. Eberil', A.F. Mazanko, Elektrokhimiya, 36, pp. 976, 2000.

165. V.V. Gorodetskii, V.A. Neburchilov, M.M. Pecherskii, Elektrokhimiya, 30, pp. 1013, 1994.

166. E.A. Novikov, V.I. Eberil', Elektrokhimiya, 33, pp. 620, 1997.

167. A. Kraft, M. Stadelmann, M. Blaschhke, D. Kreysig, B. Sandt, F. Schroder, J. Rennau, J. Applied Electrochem., 29, pp 861-868, 1999.

168. A. Kraft, M. Blaschhke, D. Kreysig, B. Sandt, F. Schroder, J. Rennau, J. Applied Electrochem., 29, pp 895-902, 1999.

169. A. Kraft, M. Blaschhke, D. Kreysig, J. Applied Electrochem., 32, pp 597-601, 1999.

170. B. E. Conway, Electrochemical Capacitors, http://electrochem.cwru.edu/encycl, 2003.

171. K. E. Swider-Lyons, K. M Bussmann, D. Griscom, C.T, Love, D. Rollison, W. Dmoski, T. Egami, Electrohem. Soc. Proceedings, 2000-32, pp 148-150, 2001.

172. T. V. Bommaraju, P. J. Orosz, E. A. Sokol, Brine Electrolysis, Process Technology Optimization Inc., 2007.

173. http://www.controlomatic.com/blog/chlorine-generator-life-span, 2011.

174. U. S Patent, 4, 129,493, 1978.

175. F. Hine, M. Yusada, T. Noda, T. Yoshida, J. Okuda, J. Electrochem. Soc., 126, pp 1439-1444, 1979.

176. http://water.usgs.gov/owq/hardness-alkalinity.html, 2011.

177. http://en.wikipedia.org/wiki/Hard_water, 2009.

178. http://www.lenntech.com/processes/disinfection/chemical/disinfectatants chlorine.html, 2011.

179. C. Comninellis and G.P. Vercesi. J. Appl. Electrochem. 21**,** 1991.

180. R. Otogawa, M. Morimitsu and M. Matsunaga. Electrochim. Acta, 44, 1998.

181. K. Kameyama, K. Tsukada, K. Yahikozawa, and Y. Takasu, J. Electrochem. Soc., 140, 966, 1993.

182. L. A. da Silva, V. A. Alves, M. A. P. da Silva, S. Trasatti, and J. F. C. Boodts, Electrochim. Acta, 42, 271, 1997.

183. M. Ito, Y. Murakami, H. Kaji, K. Yahikozawa, and Y. Takasu, J. Electrochem. Soc., 143, 32, 1996.

184. T. A. F. Lassali, L. O. S. Bulhoes, L. M. C. Abeid, and J. F. C. Boodts, J. Electrochem. Soc., 144, 3348, 1997.

185. L. K. Xu, J. D. Scantlebury, Corrosion Science, 45, pp 2729-2740, 2003.

186. B. V. Tilak, V.I Birss, J. Wang, C. P. Chen, S.K. Rangarajan, J. Electrohem. Soc., pp 112-120, 2001.

187. J. Wen, Z. Zhou, Mat. Chem. And Phy., 98, pp 442-446, 2006**.**

188. T. A.F Lassali, J. F. C. Boodts, L. O. S. Bulhoes, Journal Applied Electrochem., 30, pp 625-634, 2000.

189. A.A.F. Grupioni, E. Arashiro, T.A.F. Lassali, Electrochimica Acta, 48, pp 407-418, 2002.

190. S. Pizzini, G. Buzzanca, C. Mari, Mat Res Bull 7, 449, 1972.

191. N. Wagner, L. Kuhnemund, Cryst Res Technol 24:1009, 1989.

192. K. Kameyama, K. Tsukada, K. Yahikozawa, J Electrochem Soc., 141(3), 643, 1994.

193. J. Wen, Z. Zhou, Mat. Chem. and Phy., 98, pp 442-446, 2006.

194. P. Kurzweil, Journal of Power Sources, 190, pp 189-200, 2009.

195. J. C Forti, P. Olivi, A. R. de Andrade, Electrochimica Acta, 47, pp 913-920, 2001.

196. Y. Kamegaya, K. Sasaki, M. Oguri, T. Asaki, H. Kobayashi, T. Mitamura, Electrochimica Acta, 40, pp 889-895 1995.

197. J.M. M. Millet, A. Sebaoun, Mat. Sc. And Tech, 9, pp 820-826, 1993.

198. U.S Patent 4,461,693, 1984.

199. A. J. Bard, L. R. Faulkner, Electrochemical Methods: Fundamentals and Applications, 1st Ed., John Wiley and Sons Inc., pp 6, 1980.

200. A. S. Pilla, E. O. Cobo, M. M. E. Duarte, D. R. Salinas, J. Applied. Electrochem., 27, pp 1283-1289, 1997.

201. M. Pourbaix, Atlas of Electrochemical Equilibra in Aqueous Solutions, Translated from French by J. A. Franklin, 2nd English Edition, 1974.

202. M. L. Free, Chemical Processing and Utilization of Metals in Aqueous Media, 2nd Ed., XanEdu Original Works, pp 56-69, 2004.

203. M. L. Free, Corrosion Fundamentals Notes, 2007.

204. J. O'M Bockris, S. U. M khan, Surface Electrochemistry: A Molecular Level Approach, 2nd Ed., Plenum Pub. Corp., pp 745-749, 1993.

205. M. Keddam, Corrosion Mechanisms in Theory and Practice (Ed. P. Marcus), 2nd Ed., Marcel Dekker, pp 97-99, 2002.

206. S. Trasatti, Electrochimica ACTE, 32, 3, pp 369-382, 1987.

207. E. Gileadi, Electrode Kinetics for Chemists, Chemical Engineers and Material Scientists, 1st Ed., VCH Publishers Inc., pp 270, 1993.

208. V. Svoboda, Power Sources for Portable, Automotive, and Renewable Energy Systems, pp 1-9, 2010.

209. http://electrochem.cwru.edu, 2010.

210. G. Chen, X. Chen, P. L. Yue, J. Phys. Chem. B, 106**,** pp 4364-4369, 2002.

211. S. Manli, C. Yanxi , Modern Chlor-Alkali Technology, 4, pp 149-157, 1990.

212. R. A. Kus, Effects of Electrolyte Impurities in Chlorate Cells, Eltech Systems Corporation, 16th Annual Chlorine/Chlorate Seminar, pp 1-22.

213. W. Stumm**,** Chemistry of the Solid-Water Interface, 1st Ed: John Wiley & Sons Inc., 1992.

214. L. M. da Silva, L.A. De Faira, J. F. C. Boodts, J. Electroana. Chem., 532, pp 141-150, 2002.

215. S. B. Brummer, K. Cahill, J. Electroanalytical Chem. and Interfacial Electrochem., 16, 2, pp 207-218, 1968.

216. J. O'M. Bockris, A. K. N. Reddy, Modern Electrochemistry, Vol. 2, 1st Ed., Plenum Pub. Corp., pp 632- 639, 1973.

217. S.Goldberg, American Society of Agronomy, (Ed. S. Segoe), 42, 677, 1995.